sid.inpe.br/mtc-m21d/2021/09.24.19.04-TDI

A STUDY ON THE GENERATION AND PROPAGATION OF CONCENTRIC GRAVITY WAVES OVER BRAZIL

Prosper Kwamla Nyassor

Doctorate Thesis of the Graduate Course in Space Geophysics, guided by Drs. Cristiano Max Wrasse, Delano Gobbi, and Igo Paulino da Silva, approved in october 25, 2021.

URL of the original document:
<http://urlib.net/8JMKD3MGP3W34T/45FSAG8>

INPE
São José dos Campos
2021

PUBLISHED BY:

Instituto Nacional de Pesquisas Espaciais - INPE
Coordenação de Ensino, Pesquisa e Extensão (COEPE)
Divisão de Biblioteca (DIBIB)
CEP 12.227-010
São José dos Campos - SP - Brasil
Tel.:(012) 3208-6923/7348
E-mail: pubtc@inpe.br

sid.inpe.br/mtc-m21d/2021/09.24.19.04-TDI

A STUDY ON THE GENERATION AND PROPAGATION OF CONCENTRIC GRAVITY WAVES OVER BRAZIL

Prosper Kwamla Nyassor

Doctorate Thesis of the Graduate Course in Space Geophysics, guided by Drs. Cristiano Max Wrasse, Delano Gobbi, and Igo Paulino da Silva, approved in october 25, 2021.

URL of the original document:
<http://urlib.net/8JMKD3MGP3W34T/45FSAG8>

INPE
São José dos Campos
2021

Cataloging in Publication Data

Nyassor, Prosper Kwamla.

Ny98s A study on the generation and propagation of concentric gravity waves over Brazil / Prosper Kwamla Nyassor. – São José dos Campos : INPE, 2021.

xxxii + 214 p. ; (sid.inpe.br/mtc-m21d/2021/09.24.19.04-TDI)

Thesis (Doctorate in Space Geophysics) – Instituto Nacional de Pesquisas Espaciais, São José dos Campos, 2021.

Guiding : Drs. Cristiano Max Wrasse, Delano Gobbi, and Igo Paulino da Silva.

1. Concentric gravity waves. 2. Deep convective system. 3. Overshooting. 4. Lightning rate. 5. Backward ray tracing. I.Title.

CDU 550.312(81)

MINISTÉRIO DA
CIÊNCIA, TECNOLOGIA
E INOVAÇÕES

INSTITUTO NACIONAL DE PESQUISAS ESPACIAIS

DEFESA FINAL DE TESE DE PROSPER KWAMLA NYASSOR
BANCA Nº 268/2021, REG 141402/2017

No dia 25 de outubro de 2021, por teleconferência, o(a) aluno(a) mencionado(a) acima defendeu seu trabalho final (apresentação oral seguida de arguição) perante uma Banca Examinadora, cujos membros estão listados abaixo. O(A) aluno(a) foi APROVADO(A) pela Banca Examinadora, por unanimidade, em cumprimento ao requisito exigido para obtenção do Título de Doutor em Geofísica Espacial, Área de Concentração: Ciências Atmosféricas. O trabalho precisa da incorporação das correções sugeridas pela Banca Examinadora e revisão final pelo(s) orientador(es).

Título: A STUDY ON THE GENERATION AND PROPAGATION OF CONCENTRIC GRAVITY WAVES OVER BRAZIL

Membros da Banca

Dr. Marcelo Magalhaes Fares Saba	Presidente (INPE)
Dr. Cristiano Max Wrasse	Orientador (INPE)
Dr. Delano Gobbi	Orientador (INPE)
Dr. Igo Paulino da Silva	Orientador (UFCG)
Dr. Kleber Pinheiro Naccarato	Membro da banca Interno (INPE)
Dr. Ricardo Arlen Buriti da Costa	Membro da banca Externo (UFCG)
Dr. Erdal Yiğit	Membro da banca Externo (GMU)

Declaração membro estrangeiro (8417256)

---

sei! assinatura eletrônica

Documento assinado eletronicamente por **Kleber Pinheiro Naccarato**, **Pesquisador**, em 10/11/2021, às 13:32 (horário oficial de Brasília), com fundamento no § 3º do art. 4º do Decreto nº 10.543, de 13 de novembro de 2020.

Documento assinado eletronicamente por **Igo paulino da silva (E)**, **Usuário Externo**, em 10/11/2021, às 19:00 (horário oficial de Brasília), com fundamento no § 3º do art. 4º do Decreto nº 10.543, de 13 de novembro de 2020.

Documento assinado eletronicamente por **Delano Gobbi**, **Pesquisador**, em 12/11/2021, às 11:13 (horário oficial de Brasília), com fundamento no § 3º do art. 4º do Decreto nº 10.543, de 13 de novembro de 2020.

Documento assinado eletronicamente por **Cristiano Max Wrasse**, **Pesquisador**, em 12/11/2021, às 11:25 (horário oficial de Brasília), com fundamento no § 3º do art. 4º do Decreto nº 10.543, de 13 de novembro de 2020.

Documento assinado eletronicamente por **Marcelo Magalhães Fares Saba**, **Pesquisador**, em 03/12/2021, às 12:25 (horário oficial de Brasília), com fundamento no § 3º do art. 4º do Decreto nº 10.543, de 13 de novembro de 2020.

Documento assinado eletronicamente por **Ricardo arlen Buriti da costa (E)**, **Usuário Externo**, em 09/12/2021, às 09:06 (horário oficial de Brasília), com fundamento no § 3º do art. 4º do Decreto nº 10.543, de 13 de novembro de 2020.

A autenticidade deste documento pode ser conferida no site http://sei.mctic.gov.br/verifica.html, informando o código verificador **8416622** e o código CRC **6252E448**.

Referência: Processo nº 01340.007790/2021-07 SEI nº 8416622

*“Show me your **faith** without the **works**, and I will show you my **faith** by my **works**”.*

JAMES 2:18
in *“King James Bible”*, 1611

To my Mother ***Comfort Esi Ghartey*** *and Father* ***Atsianyo***
Kwadzo Addai *of blessed memory*

ACKNOWLEDGEMENTS

First and foremost, I would like to express my sincere gratitude to the Almighty Jehovah for life, health, and strength to embark on this four-year academic pursuit. His divine presence kept me strong through the ups and downs without losing focus.

Next, I would like to thank, Dr. Cristiano Max Wrasse, my supervisor, for his patience, guidance, direction, and support. I have greatly benefited from his wealth of knowledge and meticulous editing. I am extremely grateful that he took me on as a student and continued to have faith in me over the years. I would also like to thank my co-supervisors, Dr. Delano Gobbi and Dr. Igo Paulino, for their diverse support in this Ph.D. work. Also, Dr. Sharon L. Vadas, our collaborator, thank you for your invaluable contributions which helped to steer this work in a new direction.

I am grateful to both the internal and external assessment committee members, Dr. Marcelo Magalhaes Fares Saba, Dr. Kleber Pinheiro Naccarato, Dr. Ricardo Arlen Buriti, and Dr. Erdal Yiğit, who so generously took time off their busy schedules to participate in my thesis defense. Also, my thanks go to the following people who have also contributed to this work: K. P. Naccarato, J. V. Bageston, H. Takahashi, P. P. Batista, R. A. Buriti, and A. R. Paulino.

A big thanks to the hosting institution, the National Institute for Space Research (INPE), for the doctoral opportunity granted to me. Also, my thanks go to the Aeroluminescence (LUME) research group most especially, Dr. C. A. O. B. Figueiredo, Dr. D. Barros, and Dr. P. Essien of INPE. Furthermore, thanks to the Coordenação de Aperfeiçoamento de Pessoal de Nível Superior (CAPES) and the Conselho Nacional de Desenvolvimento Científico e Tecnológico (CNPq) for the financial support during this doctoral studies.

Thanks to my parents (of blessed memory), Comfort Esi Ghartey and Atsianyo Kodzo Addai, for their endless support in all spheres of life since I was born till the time of their demise. Also, my heartfelt thanks go to my dear brother, Sayuti Mohammed Nyassor, for his unwavering support throughout my entire academic life. I am and will be eternally grateful to you for your invaluable contribution to my life.

Also, I would like to thank Dr. Nana Ama Browne Klutse for her support. My appreciation also goes to Georgina Abra Afenyo, Adzo Mansah Adika, Bismark Nyamekye, and Oluwatosin Mariam Junaid for their prayers and support.

Finally, my sincere appreciation goes to the love of my life, Vera Yesutor Tsali-Brown, for being by my side through this long and arduous journey.

ABSTRACT

From airglow images collected at São João do Cariri (7.4°S; 36.5°W), Cachoeira Paulista (22.5°S; 45.0°W) and São Martinho da Serra (29.0°S; 54.3°W), thirty-eight (38) concentric gravity waves (CGWs) in the mesosphere and lower thermosphere were observed. These waves appeared in the OH emission images with different wavefronts such as circular, semi-circular, elliptical, semi-elliptical, or just arc-like. Horizontal wave parameters, thus, wavelength, period, phase speed, and propagation direction were estimated for thirty (30) of these events. The vertical propagations of nine (9) of these CGWs were investigated using the ray tracing model. The database used in the ray tracing model consisted of semi-empirical models such as the HWM-14, MERRA-2, and NRLMSISE-00 that were combined with wind observations by meteor radar and temperatures measured by the SABER instrument aboard the TIMED satellite when available. The ray tracing results suggest that seven (7) CGWs were excited from regions close to intense convection in the troposphere, which were identified with measurements from the GOES satellite based on the estimation of the cloud top temperature. Corroboratively, lightning rates indicated significant amount of lightning close to the positions of the tropospheric deep convection predicted by the ray tracing model. Additionally, spectral analysis was applied to the lightning rate, and the dominant periodicities found were compatible with the observed periods of the CGWs.

Keywords: Concentric gravity waves. Deep convective system. Overshooting. Lightning rate. Backward ray tracing.

O ESTUDO SOBRE A GERAÇÃO E PROPAGAÇÃO DE ONDAS DE GRAVIDADE CONCÊNTRICA NO BRASIL

RESUMO

A partir de imagens da aeroluminescência coletadas em São João do Cariri (7,4°S; 36,5°O), Cachoeira Paulista (22,5°S; 45,0°O) e São Martinho da Serra (29,0°S; 54,3°O) foram observadas trinta e oito (38) ondas de gravidade concêntricas (OGCs) na mesosfera e baixa termosfera. Estas ondas se apresentaram nas imagens da emissão do OH de diferentes formas como circulares, semi-circulares, elípticas, semi-elípticas ou apenas como arcos de circunferências. Parâmetros horizontais das ondas como comprimento de onda, período, velocidade de fase e direção de propagação foram estimados para trinta (30) destes eventos. A propagação vertical de nove (9) destas estruturas foram investigadas a partir da técnica de traçador de trajetórias. O banco de dados utilizado no traçador de trajetórias consistiu de modelos semi-empíricos como o HWM-14 e MERRA-2 e NRLMSISE-00 que foram combinados com observações de ventos por radares meteóricos e temperaturas medidas pelo instrumento SABER a bordo do satélite TIMED quando disponíveis. Os resultados do traçador de trajetórias sugerem que sete eventos advém de regiões próximas a convecção intensa na troposfera, que foram identificadas com medidas do satélite GOES a partir da estimação da temperatura do topo das nuvens. De forma corroborativa foi utilizada a taxa de relâmpagos que mostraram uma quantidade significativa de relâmpagos próximos das posições troposféricas previstas pelo traçador de trajetórias. Adicionalmente, foi aplicado análises espectrais à taxa de relâmpagos, e as periodicidades dominantes encontradas foram compatíveis com os período observados da OGCs.

Palavras-chave: Ondas de gravidade concêntrica. Sistema convectivo. Movimento vertical em nuvem. Taxa de relâmpago. Traçador de raio reverso.

LIST OF FIGURES

LIST OF TABLES

LIST OF ABBREVIATIONS

AGW – Atmospheric Gravity Waves
AIM – Aeronomy of Ice in the Mesosphere
AIRS – Atmospheric Infrared Sounder
BrasilDAT – Brazilian Lightning Detection Network sensors
C – Convective Core
CA – São João do Cariri
CAPE – Convective Available Potential Energy
CCD – Charge-Couple Device
CCL – Cloud Condensation Level
CINE – Convective Inhibition Energy
CGW – Concentric Gravity Wave
COESU – In Portuguese “Coordenação Espacial do Sul”
– In English “Southern Space Coordination”
CPT – Cold Point Tropopause
CP – Cachoeira Paulista
CPTEC – In Portuguese “Centro de Previsões de Tempo e Estudos climáticos”
– In English “Weather Prevision Center and Climate Studies”
CTBT – Cloud Top Brightness Temperature
DNB – Day/Night Band
ECMWF – European Centre for Medium-Range Weather Forecasts
ERA-5 – ECMWF Re-Analysis 5th Generation
EUV – Extreme ultraviolet
FY-2 – Fengyun-2 Satellite
GOES – Geostationary Operational Environmental Satellite
GUVI – Global Ultraviolet Imager
GW – Gravity Wave
HWM14 – Horizontal Wind Model 2014 Version
IC – Intracloud lightning
IDL – Interactive Data Language
INPE – In Prtuguese “Instituto Nacional de Pesquisas Espaciais”
– In English “National Institute for Space Research”
LFC – Level of Free Convection
LNB – Level of Neutral Buoyancy
LT – Local Time
LTE – Local Thermodynamic Equilibrium
IR – Infrared
MCS – Mesoscale Convective System
MSGW – Medium-Scale Gravity Wave
MERRA-2 – The Modern-Era Retrospective analysis for Research and
– Applications, Version 2

MLT	Mesosphere and Lower Thermosphere
MW	Model Wind
NRLMSISE-00	Naval Research Laboratory Mass Spectrometer and Incoherent – Scatter Radar 2000 Version
NaD	Sodium D-Line
NIR	Near Infrared
OH	Hydroxyl radical
OI5577	Atomic Oxygen greenline
OI6300	Atomic Oxygen redline
O_2	Molecular Oxygen
OT	Overshooting Top
PBL	Planetary Boundary Layer
SABER	Sounding of the Atmosphere using Broadband Emission Radiometry
SEE	Solar Extreme Ultraviolet Experiment
SMS	São Martinho da Serra
SNPP	Suomi-National Polar-Orbiting Partnership
SSGW	Small-Scale Gravity Wave
TIDI	TIMED Doppler Interferometer
TIMED	Thermosphere Ionosphere Mesosphere Energetics and Dynamics
UT	Universal Time
VIIRS	Visible/Infrared Imaging Radiometer Suite
ZW	Zero Wind

LIST OF SYMBOLS

A – range of meteor track
$A(\Delta\phi)$ – Airy function
c – speed of light in vacuum
c_g – group velocity
c_{gx} – group velocity in zonal direction
c_{gy} – group velocity in meridional direction
c_{gz} – group velocity in vertical direction
c_H – horizontal phase speed of gravity wave
C_p – heat capacity at constant pressure
c_p – specific heat at constant pressure
c_s – speed of sound
C_v – heat capacity at constant volume
c_v – specific heat at constant volume
$\frac{D}{Dt}$ – substantive derivative
$\frac{d}{dt}$ – total derivative with respect to “t”
$\frac{\partial}{\partial t}$ – partial derivative with respect to “t”
g – gravity acceleration module
$\vec{g}$ – gravitational acceleration
H – scale height
k – zonal wavenumber
k_B – Boltzmann constant
k_H – horizontal wavenumber
$\vec{k}$ – wave vector
k – zonal wave vector
l – meridional wavenumber
m – vertical wavenumber
M – mass of a particle
mer – meridional
n – refractive index
N – Brunt-Väisälä or buoyancy frequency
p – pressure
p_s – pressure at a reference level
Pr – Prandtl number
R – gas constant
R – Radius
R_i – reflection
T – kinetic temperature
T_R – round-trip time of an electromagnetic pulse to a meteor trail
u – eastward or zonal fluid velocity
u_{GW} – horizontal amplitude of the gravity wave

U – zonal wind speed
U_H – horizontal wind
V – meridional wind speed
w – vertical velocity
w_{GW} – vertical amplitude of the gravity wave
W – vertical wind
$\vec{x}$ – zonal wave vector position
x – zonal coordinate
$\vec{X}$ – gravity wave position vector
X_{MW} – average molecular weight
X – vector that locates the gravity wave
y – meridional coordinate
z – vertical coordinate
Z – meteoric track altitude
z_c – altitude of a critical level
zon – zonal
β – zenital angle
Δ – variation
δ – ratio between the product of kinematic viscosity and the vertical wavenumber
– to the product of the scale height and the intrinsic frequency
δ_+ – product of δ_+ and the term $(1 + Pr^{-1})$
ϕ – gravity wave propagation direction
ϕ_x – phase in the zonal direction
ϕ_y – phase in the meridional direction
γ – ratio between heat capacity at pressure to constant volume
κ – thermal diffusivity
$\varkappa$ – thermal conductivity
λ – wavelength
λ_H – horizontal wavelength
λ_x – zonal wavelength
λ_y – meridional wavelength
λ_z – vertical wavelength
μ – molecular viscosity
ν – kinematic viscosity
ν_+ – product of ν and the term $(1 + Pr^{-1})$
θ – potential temperature
θ_i – incidence angle
θ_r – angle of refraction
ρ – fluid mass density
ρ_s – standard reference density
σ – standard deviation of the mean
τ – gravity wave period

ω – observed wave frequency (frequency measured from the ground)

ω_I – intrinsic frequency of the wave

ω_{Ii} – imaginary part of the intrinsic frequency

ω_{Ir} – real part of intrinsic frequency

∇ – gradient operator

$\vec{}$ – vector magnitude

$'$ – disturbance

$\bar{}$ – average

$<>$ – average value

* – complex conjugate

CONTENTS

Page

1 INTRODUCTION

Gravity waves (GWs) are atmospheric waves that are generated when a stably stratified layer is disturbed by gravity and buoyancy (GOSSARD; HOOKE, 1975; NAPPO, 2013). GWs play a very important role in the transport of energy and momentum from their source locations in the lower atmosphere to the middle and upper atmosphere (FRITTS; ALEXANDER, 2003; VADAS et al., 2014; YIĞIT; MEDVEDEV, 2015). The energy and momentum transported by the gravity waves into the upper atmosphere/ionosphere affect the global circulation system (YIĞIT et al., 2009; YIĞIT; MEDVEDEV, 2016).

Several mechanisms such as tropospheric convection, orographic forcing, adjustment of jets, fronts, and wind shear are responsible for the generation of gravity waves. Deep convection among the others is dominant in the tropical and subtropical regions, where convective clouds excite GWs through (a) pure thermal forcing, (b) "obstacle" or "transient mountain" effect, and (c) "mechanical oscillator" effect (FRITTS; ALEXANDER, 2003; KIM et al., 2003). Orographic forcing, on the other hand, is confined to mountainous regions. However, orographic forcing also facilitates convective processes (BROWNING et al., 2007; LEAN et al., 2009; SMITH et al., 2015). Gravity waves with concentric wavefronts are excited when the mechanical oscillator effect tends to overshoot the tropopause.

When a column of rising warm air (known as a convective plume) acts as a vertical mechanical oscillator in a cloud or deep convection and vertically pushes (overshoots) the tropopause into the stratosphere by ~1 - 3 km and then collapses back down to the tropopause, concentric gravity waves (CGWs) can be excited (PIERCE; CORONITI, 1966; YUE et al., 2009; VADAS et al., 2009b). According to Vadas et al. (2009b), CGWs are excited if the overshooting of the tropopause is point-like. The excitation of CGWs through overshooting is analogous to a pebble that is dropped in a pond to generate concentric ripples. CGWs appear arc-like, semi-circular or semi-elliptical, or circular or elliptical when observed in a two-dimensional plane using imaging techniques.

For decades, the observation of CGWs have been made using airglow imagers (SENTMAN et al., 2003; SUZUKI et al., 2007; YUE et al., 2009; YUE et al., 2013) and satellites (YUE et al., 2014; PERWITASARI et al., 2016; XU et al., 2019). However, the field of view of the all-sky imagers is sometimes obstructed by convective systems and as a result, makes it challenging to observed CGW using ground-based imaging instruments. To increase the chances of observing CGWs using all-sky imagers, a network of imagers is necessary to increase the spatial coverage. A typical example of a network of all-sky imagers used to observe CGWs has been reported by Xu et al. (2015). Satellites sensitive to gravity wave perturbation, on the other hand, are not limited by cloud obstruction, thereby making satellites suitable for CGW observations.

Through numerical simulations, Horinouchi et al. (2002), Lane and Sharman (2006), and Vadas and Fritts (2004) describes the morphology and propagation characteristics of the CGWs. These studies showed that a single convective point source-generated gravity wave with circular wavefronts have a conical-shaped phase surface when propagating through the atmosphere with little or no background winds (VADAS; FRITTS, 2004). When observed in a two-dimensional plane, for instance, by using an OH airglow all-sky imager, these CGWs appear as circular rings traveling radially outward away from the center of the cone as observed by Yue et al. (2009), Miller et al. (2012), and Yue et al. (2014). Background winds have been reported by Yue et al. (2009) and Vadas et al. (2009b) to have a directional filtering effect on the propagation of CGWs, which tend to cause them to appear in various concentric wavefronts depending on the strength of the wind. Also, background wind causes a disparity between the centers of the CGWs and their source locations.

It is also important to mention here that CGWs can be excited through another mechanism known as body forces that are created by dissipating or breaking primary GWs (VADAS et al., 2003; VADAS et al., 2018; VADAS; BECKER, 2019). However, this subject is not addressed in this current study, but it is worth mentioning that the understanding of secondary gravity wave generation mechanism is important. This is because phenomena such as Equatorial Spread-F (ESF), Equatorial Plasma Bubbles (EPBs), etc are known to originate from such second-step processes similar to secondary CGWs (TSUNODA, 2010; TAKAHASHI et al., 2018). Also, large-scale waves excited through these secondary processes or generated primarily in the lower atmosphere are capable of initiating or seeding ESF (Tsunoda 2010) and EPBs (TAKAHASHI et al., 2018), and MSTIDs (VADAS; AZEEM, 2020). Therefore, an in-depth understanding of this secondary mechanism will help explain the seeding process of these upper atmospheric phenomena.

1.1 Motivation

Tropospheric convective processes are the main excitation mechanism of gravity waves especially CGWs. However, some questions still persist:

(a) what is the direct relationship between observed CGWs and convective source?

(b) under what condition is deep convection capable of exciting CGW?

(c) is it only background wind that make the atmosphere conducive for the propagation of CGWs to the upper atmosphere?

Perwitasari et al. (2016), showed the statistics of the occurrence probability of CGWs using Visible and near-Infrared Spectral Imager (VISI) of the Ionosphere, Mesosphere, upper Atmosphere and Plasmasphere (IMAP) instrument onboard the international space station using three (3) years of O_2 762 nm airglow data. Their work showed that the global occurrence distribution of CGWs is high in the mid-latitudes, with peaks occurrence around 40°N and 40°S and low occurrence around 10°S. Also, they observed more events in the summer hemisphere mid-latitudes, with a strong transition between the hemispheres taking place around equinoctial months.

A model study by Vadas et al. (2009b) demonstrated that CGWs with phase speed higher than the speed of the wind are capable of propagating to the middle and lower thermosphere (MLT) region with little or no filtering effect and also without significant distortion of the circular wavefronts. In a little or zero wind atmosphere, a CGW must appear circular. Vadas et al. (2009b) further showed that with a stronger background wind, the circular wavefront of CGWs appear elliptical, and even squashed circle or arc-like if filtering occurred. Observational evidence of CGW with elliptical wavefronts was reported by Xu et al. (2015). Using an observed wind from meteor radar, Xu et al. (2015) found that the horizontal wind at the OH emission layer altitude was strong during their observed CGW event. Their result affirms the simulation result of Vadas et al. (2009b).

Sources of CGWs observed in the MLT regions have been reported in litrerature to be overshooting of the tropopause by convective updrafts or plumes within deep convection such as thunderstorms, cyclones, typhoons, etc (YUE et al., 2009; VADAS et al., 2009b; XU et al., 2015). To investigate the propagation of CGWs in the atmosphere and to determine the location of sources of CGWs, two techniques have been reportedly used in previous studies. For instance, Vadas et al. (2009b) used a backward ray tracing model to determine the source location of the CGWs in their work, whereas other researchers use the epicenters of the CGW to approximate the source locations.

To relate an observed CGW directly to the located source by backward ray tracing, Vadas et al. (2012) used the convective plumes parameters of the source to launch spectrum of CGWs with the aid of forward ray tracing model. They then used the modeled parameters in both temperature and airglow intensity perturbation to verify if the model and observed parameters are similar. They observed that the model wave parameters in the temperature and airglow intensity perturbation compared well with that of the observed parameters. This further strengthens the fact that the located source by the backward ray tracing is the source of the observed CGW.

As mentioned before, convective overshoot is the main source mechanism of CGW generation (YUE et al., 2009; VADAS et al., 2009b; XU et al., 2015). Most of the published work on CGW events in literature reported high Convective Available Potential Energy (CAPE) values around the identified convective source prior to the observation of the CGW event (YUE et al., 2009; VADAS et al., 2009b; XU et al., 2015). These CAPE values were related to the updraft velocities, which in turn give a measure of the capability of the updraft to overshoot the tropopause (VADAS et al., 2009b; VADAS et al., 2012). Vadas et al. (2012) used the infrared cloud top brightness temperature images of the geostationary satellite (GOES) as a proxy of overshootings of the tropopause, whereas Yue et al. (2009) used Next Generation Weather Radar (NEXRAD) to determine overshooting before the observation of the CGWs in their respective work. These are the characteristics of the convective source of CGW used as indicators for overshooting.

Besides observing high CAPE values and overshooting as indicators of convective overshooting around the thunderstorm identified to be the source, lightning activity was also used. Sentman et al. (2003) and Xu et al. (2015) observed high lightning activities in the vicinity of the storm that excited the CGW reported in their work. Xu et al. (2019) reported lightning activity near or to some degree around the center of the CGW in their work. In the Brazilian sector, Medeiros (2001a), correlates lightning activity obtained from the Lightning Imaging Sensor (LIS) within a radius of 1000 km centered around Cachoeira Paulista to convective regions in nearby deep convective systems. Also, Wrasse et al. (2003) observed strong lightning activity around the source locations determined by ray tracing. However, studies by Deierling and Petersen (2008), Bedka et al. (2010), and Jurković et al. (2015) showed a direct relationship between CAPE, updraft, lightning, and overshooting.

Studies suggest that irregularities, for instance, ESF, EPBs, etc., in the thermosphere, are due to propagating GWs in those altitudes (TSUNODA, 2010; TAKAHASHI et al., 2018; VADAS; FRITTS, 2004). Tsunoda (2010), showed that even in the absence of a post-sunset rise in plasma on a night of very low solar activity, ESF still developed. The development of ESP under such conditions was suggested to be due to the presence of large-scale wave structures (LSWS), mostly GWs. They further demonstrated that the occurrence of ESF is most probable when this LSWS has concentric phase fronts.

From the scientific point of view, the natural point-like source mechanism of CGWs such as deep convection is prevalent in Brazil. Also, airglow image data and other coincidence data are available to explore the subject of CGWs over Brazil. These two criteria have motivated this doctoral work. Thus, it would be possible to observe CGWs in regions where convective activities are frequent. To study the propagation and generation of CGWs using the available dataset and the scientific basis in literature, an objective was set for this work.

1.2 Objective

The general objective of the present doctoral work is the study on the generation and propagation of concentric gravity waves (CGWs) over Brazil. To achieve this objective, a ray tracing model will be used to study the propagations of CGWs in the atmosphere and also determine the convective source locations of the waves. Furthermore, using the source characteristics a direct link between the source and the observed wave will be established.

More specifically, this doctoral work intends to:

(1) Search, select and classify CGWs events from the years of airglow image data available. Before selecting the events, the raw images will be preprocessed. The classification will be based on the morphology of the concentric wavefronts, that is, circular or elliptical or semi-circle or semi-elliptical or arc-like;

(2) Use spectral analysis to estimate the observed parameters of the CGW events;

(3) Develop methodologies to (i) determine the center and radius of the CGWs, (ii) build wind and temperature database to be used in the ray tracing model, (iii) ray trace the CGWs in the atmosphere, and (iv) study the located convective source characteristics;

(4) Investigate the propagation characteristics of the CGW in the atmosphere and the located CGWs sources by backward ray tracing and the determined centers;

(5) Estimate the convective source parameters such as tropopause temperature and altitude, CAPE, updrafts, overshooting tops, the width of the plume, lightning density, and lightning flash rate;

(6) Contextualize the present work within the current scientific scenario, extract its contributions to literature and present the possibilities for future work.

1.3 Structure of thesis

This thesis was structured to achieve the objectives mentioned above as follows:

- Chapter 2 will give a detailed description of the linear theory of gravity waves including dissipative effects due to molecular viscosity and thermal diffusivity.

After obtaining a dispersion relation that includes the dissipation, the propagation conditions for CGWs will be studied and the concepts of the level of reflection, channeling, absorption, and dissipation of gravity waves will be presented. Also, the theoretical basis of the formation of deep convection is presented. This chapter will be devoted to a literature review of concentric gravity wave studies using airglow imaging and brightness temperature techniques in recent decades;

- Chapter 3 will present details of observations carried from each observation site and a description will be made about the instruments used in this work. That is, this chapter will describe the airglow imager used to detect concentric gravity wave structures; Sounding of the Atmosphere using Broadband Emission Radiometry (SABER) used to measure vertical temperature profiles from the tropopause to the lower thermosphere at $\sim$130 km altitude; meteor radar which measured the horizontal wind in the mesosphere and lower thermosphere; radiosonde which measured temperature and wind in the troposphere up to 30 km and CAPE; lightning sensors used to detect lightning strikes and GOES satellite used to capture cloud top temperatures. Also the semi-empirical models used to complement the observed wind and temperature have described;

- The development of the methodology of the entire thesis will be presented in detail in Chapter 4. The first method is the method used to preprocess the raw image, followed by the method to determine the parameters of concentric gravity waves. Also, the method for construction of the wind and temperature database and that of the ray tracing model used to study the propagations of the concentric gravity waves and determine their source locations are presented. Furthermore, the methodology of the determination of the CGWs centers, the determination of the overshooting tops, lightning densities, and periodicities in lightning flash rate are presented;

- Chapter 5 will present the results of the total number of observed CGW events within the observation years and sites considered. Also, the classification of the CGW based on the morphology of the concentric wavefronts, sample airglow images of CGWs, the parameters of the analyzed CGWs, and events selected for case studies are presented;

- In Chapters 6, 7 and 8, the discussions of the CGW events selected for case studies are presented. For these three chapters, the discussions of the case studies were adapted versions of (i) a published paper for case study 1, (ii) a manuscript to be re-submitted for case study 2, and (iii) a submitted manuscript under revision for case study 3. For Chapters 6 and 7, (i) the propagation characteristics of the CGWs in the atmosphere studied and the source of these waves were located using a ray tracing model; (ii) the effects of the wind on the concentric wave propagation and the wavefronts were investigated, and (iii) the characteristics (i.e., CAPE, tropopause height, and temperature, updraft, overshooting tops, lightning densities, and the lightning flash rate) of the possible identified sources using ray tracing and determined center were also studied. Similar studies were conducted for case study three in Chapter 8 except for the use of lightning activity. Precipitation data were used instead.

- A general conclusions will be presented in Chapter 9. Also, some suggestions for future work will be made.

2 ATMOSPHERIC CONCENTRIC GRAVITY WAVES

In this chapter, we present details of the underlying theoretical background of concentric gravity waves. In this approach, the dispersion relationship will be derived for GWs in a free mode. The conditions that need to be met, in order, for CGWs to be excited as well as the background atmosphere condition that will allow the propagation of CGWs through the atmosphere without distortion of the concentric wavefronts are discussed. The source and its characteristics are also presented as well as some scientific contributions obtained from observations of concentric gravity waves using airglow images and brightness temperature and radiance images.

2.1 Propagation of concentric gravity waves in the atmosphere

Atmospheric concentric gravity waves (GWs) are excited as a result of disturbances that occur in any layer of the atmosphere and are capable of destabilizing the hydrostatic balance of that layer. They are called concentric gravity waves because the main restorative force is gravity and have concentric wavefronts. Observations have shown that GWs appear as complex polychromatic structures or even in the form of solitary pulses. In many cases, a GW can be approximated as a monochromatic structure without losing much of its energy. With this understanding, the mathematical treatment becomes less complex and, in this way, it is possible to quantify the propagation characteristics of this wave. The first simplification that will be used in this work is the assumption of monochromatic GWs.

2.2 Set of basic equations

The atmospheric motion due to concentric gravity waves is principally governed by conservation principles, which are: conservation of mass, momentum, and energy. Since this work is solely the study of CGWs in the neutral atmosphere, the charge conservation is ignored, therefore, the equation of mass conservation or the continuity of mass conservation is given by:

$$\frac{d\rho}{dt} + \rho\nabla.\vec{V} = 0 \tag{2.1}$$

where, $\frac{d}{dt} = \frac{\partial}{\partial t} + \vec{V}.\nabla$ represents the Eulerian derivative with ∇ being the gradient operator, ρ is the density of the fluid and $\vec{V} = (u, v, w)$, with u, v, w being zonal, meridional, and vertical velocities, respectively.

The continuity equation in this form shows that the substantive change in the mass of the fluid per unit volume is equal to the advection of the fluid that is, the mass of the fluid has neither source (generation point) nor sink (dissipation point). The mathematical description of the continuity equation, as well as the expressions for the main forces that act in the atmosphere, can be found in Gossard and Hooke (1975).

The next equation comes from the conservation of momentum, which is described by

$$\left[\frac{d\vec{V}}{dt}\right] = -\frac{1}{\rho}\nabla p + \vec{g} + \vec{F},$$

where, $\vec{F} = \frac{\mu}{\rho}\left[\nabla^2\vec{V}' + \frac{1}{3}\nabla(\nabla.\vec{V}')\right]$, p is the pressure of the fluid, g is the gravitational acceleration, μ is the coefficient of molecular viscosity (VADAS, 2007) and the apostrophes ($'$) represent the disturbed quantities. The first term on the right side is the force (per unit mass) of the pressure gradient and the third term is viscous force (per unit mass). In addition to these three main terms, the fluid undergoes the action of the Coriolis force, frictional forces, hydromagnetic forces, among others. However, for the study of gravity waves, the forces presented in this equation are the most important.

The coefficient of molecular viscosity (μ) is the measure of resistance to the shear stress of a fluid. Mathematically, it is the ratio of the shear stress suffered by the fluid during the flow to its respective speed gradient. The most common unit of measurement is Poise, with 1 Poise $=$ 0.1Nm^{2}s. It is also very common to find the unit of the coefficient of molecular viscosity in “mass/length/time”

Dividing the molecular viscosity by the density of the fluid, we obtain the kinematic viscosity ν, given by $\nu = \mu/\rho$. As the atmospheric density decreases with altitude exponentially, the kinematic viscosity increases with altitude. The term due to the magnitude of the viscosity of the equation above has two terms (KUNDU; COHEN, 2004), the second term $(1/3\nabla(\nabla.\vec{V}'))$ can be neglected in relation to the first for the study of gravity waves (VADAS; FRITTS, 2005). Therefore, the momentum conservation equation is:

$$\left[\frac{d\vec{V}}{dt}\right] = -\frac{1}{\rho}\nabla p + \vec{g} + \frac{\mu}{\rho}\nabla^2\vec{V}' \tag{2.2}$$

The third equation is that of energy conservation, which can be written as follows:

$$\frac{d\theta}{dt} = \frac{\varkappa\theta}{C_p\rho T}\nabla^2 T', \tag{2.3}$$

where $\varkappa$ is the coefficient of thermal conductivity, T is the temperature, C_p is the heat capacity at constant pressure, and θ is the potential temperature that will be defined in Subsection 2.2.1.

The coefficient of thermal conductivity $(\varkappa)$ is a physical property that measures the ability of a fluid to conduct heat. Physically, thermal conductivity is the temporal variation of heat transmitted over a given distance from the fluid, per unit area, due to a temperature gradient. Atmospheric gas is not a good conductor of heat. The unit of the coefficient of thermal conductivity is “power/length/temperature”. As the thermal conductivity is small, the term on the right side of Equation 2.3 can be neglected in the lower and middle atmosphere. However, in the thermosphere, the density decreases a lot and that term becomes important in the dissipative process of gravity waves.

Equation 2.3 can also be represented in terms of thermal diffusivity. Thermal diffusivity is a measure of the temperature variation of a fluid temperature and can be written as:

$$\kappa = \frac{\varkappa}{C_p\rho} = \frac{\mu}{Pr\rho} = \frac{\nu}{Pr},$$

where Pr is the Prandtl number, which is, defined as the ratio of kinematic viscosity to thermal diffusivity. For gases, the Prandtl number is in the order of unity, indicating that the capacity to diffuse heat is practically the same as that of diffuse momentum. For the atmosphere, the Prandtl number is approximately 0.7 (KUNDU; COHEN, 2004) and variations in the Prandtl number with temperature will be neglected in the study of gravity waves (VADAS, 2007).

To complete the set of basic equations, the ideal gas (Equation 2.4) law will be used,

$$p = \rho R T, \tag{2.4}$$

in this case, $R = 8314.5/X_{MW}$ is the specific gas constant, which is defined as the ratio of the universal gas constant to the molar mass of the atmospheric particles (X_{MW}) (VADAS; FRITTS, 2006).

This set of 6 equations listed above, that is, Equations 2.1 - 2.4, and six unknowns does not admit an analytical solution. In addition, numerical solutions are difficult to obtain because the thermodynamic state of the atmosphere and the dissipation terms are not very well known. However, to study the propagation of gravity waves, it will not be necessary to solve this system of equations. Therefore, to extract the characteristics of the wave, simplifications will be made to this system of equations, and plane wave solutions imposed.

2.2.1 Simplifications and linearizations in the basic equations

The potential temperature is defined as the temperature at which a parcel of air would attain if adiabatically brought to a standard reference pressure p_s. In atmospheric studies, the reference pressure level is usually taken to be the Earth's surface. Starting from the first law of thermodynamics and assuming an adiabatic process, one can obtain the expression for the potential temperature to be,

$$\theta = T\left(\frac{p_s}{p}\right)^{\frac{R}{c_p}}, \tag{2.5}$$

where, p_s is the pressure at the reference level.

Using the potential temperature and the ideal gas law, it is possible to eliminate the terms p and θ from Equations 2.2 and 2.3, in order to obtain:

$$\frac{d\vec{V}}{dt} = -\frac{RT}{p}\nabla\rho - R\nabla T + \vec{g} + \nu\nabla^2\vec{V}', \tag{2.6}$$

$$\frac{dT}{dt} = -(\gamma - 1)T\nabla.\vec{V} + \frac{\gamma\nu}{Pr}\nabla^2 T', \tag{2.7}$$

here, $\frac{\gamma}{\gamma-1} \equiv \frac{C_p}{R}$

Another important simplification is to adjust the coordinate system such that the horizontal axis coincides with the direction of propagation of the wave. In this case, one of the system's equations (i.e., Equation 2.2) is suppressed without loss of information. In addition, the solution can be trivially generalized for the three-dimensional case, decomposing only the gravity wave into two horizontal components. Thus, atmospheric fields can be written as the sum of the average value (represented by the over bars or capital letters) and a perturbation (primes):

$$u = U + u', \tag{2.8}$$

$$w = w', \tag{2.9}$$

$$T = \overline{T} + T' \tag{2.10}$$

and

$$\rho = \bar{\rho} + \rho'. \tag{2.11}$$

The average horizontal wind in the direction of the wave is represented by U.

The next step is to linearize Equations 2.1, 2.6 and 2.7. The linearization process involves neglecting the product between two perturbed quantities, that is, the higher-order terms. Linearization does not alter the solution of the system of equations when the perturbation is assumed to be very small relative to the mean value of the atmospheric field. In the present study, the linearization process provides interesting results for the study of gravity waves propagation. However, the inclusion of non-linear terms would certainly make the gravity wave model closer to reality. Through algebraic manipulations, the linearised equations can be described by:

$$\frac{du'}{dt} = -R\frac{\partial T'}{\partial x} - \frac{c_s^2}{\gamma\bar{\rho}}\frac{\partial \rho'}{\partial x} + \nu\nabla^2 u', \tag{2.12}$$

$$\frac{dw'}{dt} = -R\frac{\partial T'}{\partial z} - \frac{c_s^2}{\gamma\bar{\rho}}\frac{\partial \rho'}{\partial z} + \frac{c_s^2}{\gamma H}\left(\frac{T'}{\overline{T}} - \frac{\rho'}{\bar{\rho}}\right) + \nu\nabla^2 w', \tag{2.13}$$

$$\frac{dT'}{dt} = -(\gamma - 1)\bar{T}\left(\frac{\partial u'}{\partial x} + \frac{\partial w'}{\partial z}\right) + \frac{\gamma\nu}{Pr}\nabla^2 T', \tag{2.14}$$

$$\frac{d\rho'}{dt} = \frac{\bar{\rho}}{H}w' - \bar{\rho}\left(\frac{\partial u'}{\partial x} + \frac{\partial w'}{\partial z}\right), \tag{2.15}$$

where, H is the local scale height which is defined by $\frac{d\bar{\rho}}{dz} \equiv \frac{\bar{\rho}}{H}$ and $c_s = \sqrt{\gamma RT}$ is the speed of sound in the atmosphere.

2.2.2 Dispersion relation

Due to decreasing density and increasing gravity wave amplitude with altitude, the same methodology adopted by Pitteway and Hines (1963) is employed to account for the perturbed terms; $\tilde{u}$, $\tilde{w}$, $\tilde{T}$, and $\tilde{\rho}$, hence,

$$\tilde{u} = \left(\frac{\bar{\rho}}{\rho_s}\right)^{\frac{1}{2}} u', \tag{2.16}$$

$$\tilde{w} = \left(\frac{\bar{\rho}}{\rho_s}\right)^{\frac{1}{2}} w', \tag{2.17}$$

$$\tilde{T} = \left(\frac{\bar{\rho}}{\rho_s}\right)^{\frac{1}{2}} T', \tag{2.18}$$

$$\tilde{\rho} = \left(\frac{\bar{\rho}}{\rho_s}\right)^{\frac{1}{2}} \rho', \tag{2.19}$$

in this case, ρ_s is the density at the surface.

The exact solution of this system of equations can only be obtained numerically if small vertical wavelengths ($\lambda_z \leq 2\pi H$) are considered and the coefficients of the system of equations (i.e., Equations 2.16 - 2.19) are assumed to be locally constant hence, the system of equations assumes wave-like solutions:

$$\frac{\tilde{u}}{\tilde{u}_o} = \frac{\tilde{w}}{\tilde{w}_o} = \frac{\tilde{T}}{\tilde{T}_o} = \frac{\tilde{\rho}}{\tilde{\rho}_o} = \exp[i(kx + mz - wt)], \tag{2.20}$$

where ω is the frequency of the wave relative to the ground, k and m are the horizontal and vertical wavenumbers, x and z represent the horizontal and vertical position of the wave at a given time t. Generalizing for the three-dimensional case, k^2 is replaced by $k_H^2 = k^2 + l^2$ and $\omega - kU$ by $\omega - kU - lV$, in this case, the unperturbed wind is $(U, V, 0)$. Considering the non-trivial solution of this system, the dispersion relation for acoustic-gravity waves damped by the molecular viscosity and thermal diffusivity is given by:

$$-\frac{\omega_I^2}{c_s^2}(\omega_I - i\alpha\nu)^2\left(1-\frac{i\gamma\alpha\nu}{Pr\omega_I}\right)(\omega_I - i\alpha\nu)\left(\omega_I - \frac{i\gamma\alpha}{Pr}\right)\left(\vec{k}^2+\frac{1}{4H^2}\right) = k_H^2N^2, \quad (2.21)$$

where $\vec{k}^2 = k_H^2 + m^2$ is the square of the wave vector and ω_I is the intrinsic frequency that is given by

$$\omega_I = \omega - kU - lV, \quad (2.22)$$

N is the Brunt-Väisälä or buoyancy frequency, which is defined mathematically as

$$N^2 \equiv \left(\frac{g}{\theta}\right)\frac{d\bar{\theta}}{dz}, \quad (2.23)$$

which can also be defined as:

$$N^2 \equiv \frac{(\gamma-1)c_s^2}{\gamma^2H^2} = \frac{(\gamma-1)g^2}{\gamma R\bar{T}}, \quad (2.24)$$

in an isothermal atmosphere, and

$$\alpha \equiv -\vec{k}^2 + \frac{1}{4H^2} + \frac{im}{H}. \quad (2.25)$$

At the limit where the molecular viscosity and thermal diffusivity become negligible, the dispersion relation is:

$$-\frac{\omega_I^4}{c_s^2} + \omega_I^2\left(\vec{k}^2+\frac{1}{4H^2}\right) = k_H^2N^2 \quad (2.26)$$

which is the usual dispersion relation for acoustic gravity waves (HINES, 1960). As the interest of this work is to study only internal gravity waves, the terms of the order $(\omega_I/c_s)^2$ in Equation 2.21 are neglected. This gives the desired anelastic dispersion relation for gravity waves under the influence of molecular viscosity and thermal diffusivity, that is,

$$(\omega_I - i\alpha\nu)\left(\omega_I - \frac{i\alpha\nu}{Pr}\right) = \frac{k_H^2 N^2}{\vec{k}^2 + \frac{1}{4H^2}}. \tag{2.27}$$

Below the MLT region, the thermal diffusivity and molecular viscosity terms can be neglected, and Equation 2.27 becomes the well-known anelastic dispersion relation for high-frequency propagating internal gravity waves (GOSSARD; HOOKE, 1975), which is

$$\omega_I^2 \cong \frac{k_H^2 N^2}{\vec{k}^2 + \frac{1}{4H^2}}, \tag{2.28}$$

or in a more usual way,

$$m^2 \cong \frac{k_H^2 N^2}{\omega_I^2} - k_H^2 - \frac{1}{4H^2}. \tag{2.29}$$

This equation is widely used to study gravity waves in the MLT region where dissipation is not so important (GOSSARD; HOOKE, 1975). It is important to mention that in the MLT region, Yiğit et al. (2008) showed using the general circulation model including atmospheric gravity wave parameterization that nonlinear diffusion (or nonlinear interaction) damp gravity waves (YIĞIT et al., 2008; MIYOSHI; YIĞIT, 2019; LILIENTHAL et al., 2020; YIĞIT et al., 2021). However, nonlinear interaction was not included in this current study.

On the other hand, GWs that propagates beyond the turbopause (i.e., $\sim 110\,\text{km}$ altitude), the damping of GWs due to kinematic viscosity and thermal diffusivity becomes very important because atmospheric density decreases with altitude. These two processes are dependent on the parameters of the GWs, so GWs with long vertical wavelengths and high vertical group velocities propagate to higher altitudes in the thermosphere before they dissipate. Here the ion drag is neglected because it does not significantly affect high-frequency GWs (i.e., periods shorter than a few hours) that are of interest in this work (VADAS; FRITTS, 2005). However, ion drag can affect GW propagation in the thermosphere-ionosphere (YIĞIT et al., 2008; MEDVEDEV et al., 2017).

In the classic formulation of the GW dispersion relation with molecular viscosity and thermal diffusivity, Pitteway and Hines (1963) assumed a complex vertical wavenumber. This assumption results in a decrease in the amplitude of the waves with altitude. As the viscosity increases with altitude, the solutions presented are only valid for altitudes beyond which the dissipation is not negligible. On the other hand, Midgley and Liemohn (1966) realized that by disregarding the nonlinear terms of the perturbations, satisfactory results are achieved whenever $\lambda_z < H$.

If a complex intrinsic frequency and a real vertical wavenumber are considered within the dispersion relation, the result will be decreasing GWs amplitude with time, and the solutions can be obtained for any value of kinematic viscosity and diffusivity thermal. In this way, it is possible to describe the trajectory the waves take in the atmosphere during and after dissipation. In addition, this assumption allows the amplitudes of the GWs to decay explicitly with time (implicitly in altitude) or explicitly in altitude (implicitly in time).

Continuing with the assumption that the amplitudes of the GWs decrease with time, the intrinsic frequency is written as the sum of a real and an imaginary part:

$$\omega_I = \omega_{Ir} + i\omega_{Ii}. \tag{2.30}$$

The term ω_{Ir} is the real component and relates the intrinsic frequency to the wave structure. ω_{Ii} is the imaginary component and expresses the inverse of the wave amplitude decay with time due to the kinematic viscosity and thermal diffusivity. The effect of the imaginary component of ω extends to the ground, but below $\sim$100 km of altitude, this term can be neglected because the molecular viscosity and the thermal diffusivity are small. At these levels, the dissipation of gravity waves is not very effective. Substituting Equation 2.30 in Equation 2.27, the inverse of the decay rate is obtained to be:

$$\omega_{Ii} = \frac{\nu}{2}\left(\vec{k}^2 - \frac{1}{4H}\right)\frac{1 + \frac{1+2\delta}{Pr}}{1 + \frac{\delta_+}{2}} \tag{2.31}$$

and this then led to the dispersion relation used in this work,

$$\omega_{Ir}^2 + \frac{\nu^2}{4}\left(\vec{k}^2 - \frac{1}{4H}\right)^2\left(1 - \frac{1}{Pr}\right)^2\frac{1 + \delta_+\frac{\delta^2}{Pr}}{\left(1 + \frac{\delta_+}{2}\right)^2} + \frac{\nu_+ m\omega_{Ir}}{H} + \frac{\nu^2 m^2}{PrH} = \frac{k_H^2 N^2}{\vec{k}^2 + \frac{1}{4H^2}}, \tag{2.32}$$

where $\delta_+ = \delta(1 + Pr^{-1})$, $\nu_+ = \nu(1 + Pr^{-1})$ and $\delta = \nu m / H\omega_{Ir}$. This dispersion relation is non-hydrostatic and compressible, but excludes acoustic waves, similar to that of Marks and Eckermann (1995).

Equation 2.32 will be very useful in the ray tracing model for two reasons: (1) to directly calculate the intrinsic frequency that should be derived in relation to spatial coordinates and (2) to determine the vertical wavenumbers (m) that will be evaluated in the stopping conditions of the ray tracing (more details are giving in Section 4.3).

2.2.3 Propagation of gravity wave

Base on the characteristics of GWs, they can be classified as propagating or evanescent. Propagating waves are waves that propagate both horizontally and vertically, whereas evanescent waves are waves that do not propagate vertically but rather only horizontally. The propagating waves, in which internal gravity waves are included, propagate vertically upward with increasing amplitude due to a decrease in density with altitude (See left panel of Figure 2.1). The dispersion diagram for varying ω and k_x at constant k_z shown in the right panel of Figure 2.1) illustrate the regions of acoustic, evanescent, and gravity waves. If no dissipation occurs, the wave amplitude becomes so great that it can undergo the process of breaking and transfer of momentum and energy to the background atmosphere, thereby accelerating or decelerating the mean flow and causing turbulence.

Figure 2.1 - Propagation of gravity waves in the atmosphere.

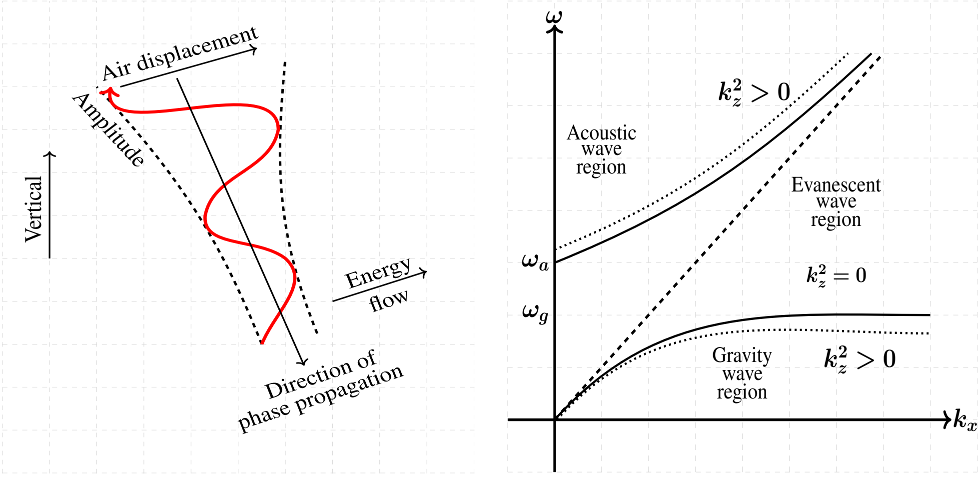

In the left panel is a schematic diagram illustrating propagating gravity wave with increasing amplitude. In the right panel, the dispersion diagram showing the regions of existence of acoustic, evanescent, and gravity waves at constant k_z but varying ω and k_x is presented.
Source: Left panel - Hargreaves (1992) and right panel - Gossard and Hooke (1975).

To analyze the effects of propagation, reflection, and absorption of gravity waves in the atmosphere, the dispersion relation (Equation 2.29) of Gossard and Hooke (1975) will be analyzed for simplification reasons. This is because the extra terms in Equation 2.32 are most importantly related to the dissipation processes of the wave. For vertical propagation of gravity waves, the vertical wavenumber must be real with the adapted orientation defined as:

i. $m < 0 \rightarrow$ upward propagation

ii. $m > 0 \rightarrow$ downward propagation

For complex m, part of the wave is refracted whereas the other part does not satisfy the propagation conditions.

2.2.4 Gravity wave reflection, absorption and ducting

One very important and necessary condition for gravity wave propagation is that the Brunt Väisäla frequency must be greater than the intrinsic frequency of the wave or N/ω_{Ir} should be greater than unity. Gravity waves that satisfy this propagation condition suffer reflection when they encounter turning (reflection) level (PAULINO, 2012; FRITTS; ALEXANDER, 2003). These levels appear in the atmosphere at the interface between a propagating region (which satisfy the conditions of $m^2 > 0$) and an evanescent region ($m^2 < 0$). At this level, $m \rightarrow 0$ ($\lambda_z \rightarrow \infty$), which then cause the wave to undergo total internal reflection where the vertical group velocity changes sign.

The left panel of Figure 2.2 shows a graphic illustration of reflection. In physical terms, gravity waves encounter reflection level through (i) increment of the intrinsic frequency of the wave and (ii) reduction of the Brunt Väisäla frequency of the medium. The vertical variation of the horizontal wind modifies the intrinsic frequency of gravity wave (FRITTS; ALEXANDER, 2003; PAULINO, 2012). Horizontal wind in opposite direction to the wave propagation direction tends to increase the intrinsic frequency of the wave (i.e., decreases intrinsic period). If the Brunt Väisäla frequency approaches the intrinsic frequency, the vertical wavenumber approaches zero and the wave will be reflected.

Also, the Brunt Väisäla frequency depends inversely on the potential temperature and directly on its vertical gradient. The potential temperature in the atmosphere increases practically with altitude as shown in Figure 2.3. In panel (a), the temperature profile from 0 to 300 km at 02:55:02 UT on March 24, 2018, at São Martinho da Serra is represented by the black solid line and the density profile by the blue solid line. Using Equation 2.5, the potential temperature represented by the black solid line in panel (b) was estimated and its derivative with altitude depicted by the red solid line.

Another condition propagating gravity waves encounter in the atmosphere is absorption. Absorption of gravity waves is encountered in the atmosphere when the horizontal wind

Figure 2.2 - A schematic diagram of reflection and critical/absorption levels of propagating gravity waves.

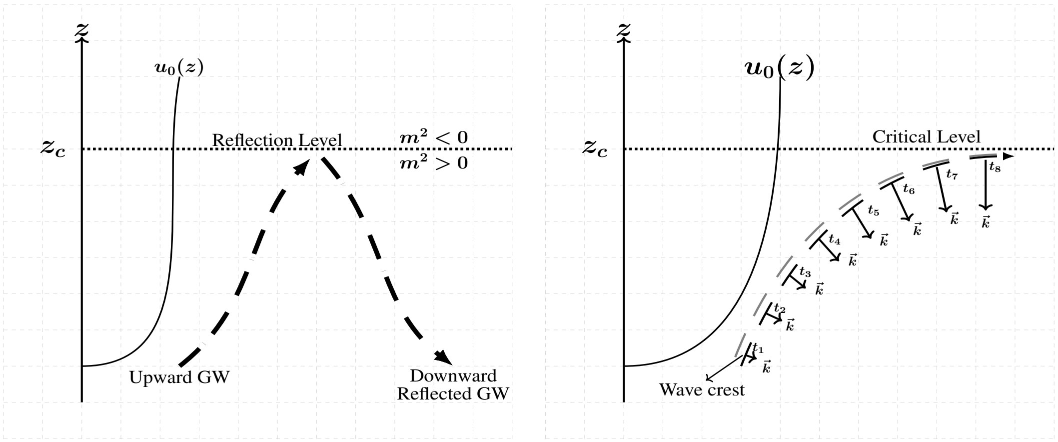

The left panel shows a schematic diagram of a reflection level for a gravity wave. An evanescent region is the top ($m^2 < 0$) and a propagating region at the bottom ($m^2 > 0$). The dashed lines show the direction of propagation of the wave. The dotted line separating the evanescent and propagating regions represents the reflection level. An arbitrary wind profile labeled $u_0(z)$ is shown solid profile. The right panel illustrates the progression of gravity wave packet toward a critical level (represented by the dotted lines labeled z_c) at successive times t_1.........t_8 with each wave packet vector direction shown by $\vec{k}$. The arbitrary wind profile of the wind is the solid black line with the $u_0(z)$ on it.
Source: Left panel - Paulino (2012) and right panel Gossard and Hooke (1975).

is equal to the horizontal phase velocity of the wave. This causes the intrinsic frequency to approach zero or the intrinsic period to infinity ($\tau \to \infty$). The level where this occurs is known as the critical or absorption level. The right panel of Figure 2.2 illustrates the scenario of gravity waves approaching a critical level. The vertical propagation of the wave becomes very slow and also unable to propagate horizontally because $m \to 1$. In this condition, the wave will be quickly absorbed. Note that when the GW approaches the critical level, the phase structures tend to be parallel to the horizontal.

Besides reflection and absorption of gravity waves, trapping or ducting of gravity waves also occurs where there are reflection/turning levels above and below. In other words, ducting occurs when a gravity wave is trapped between two reflection levels. The configuration of a duct in the atmosphere is illustrated in Figure 2.4. To know whether or not there is a duct, the vertical wavenumber squared profile is used. The $m^2 > 0$ region between two $m^2 < 0$ is the region where the GW can be trapped.

Ducting happens when an upward propagating gravity wave reaches a reflection level, is reflected, and propagate downwards until it reaches another level of reflection at a lower

Figure 2.3 - In panel (a), the temperature profile (black solid line) and density (blue solid line) obtained at 02:55:02 UT on March 24, 2018, at São Martinho da Serra are presented. In panel (b), the potential temperature (black solid line) and its respective derivative with altitude (red solid line) are shown.

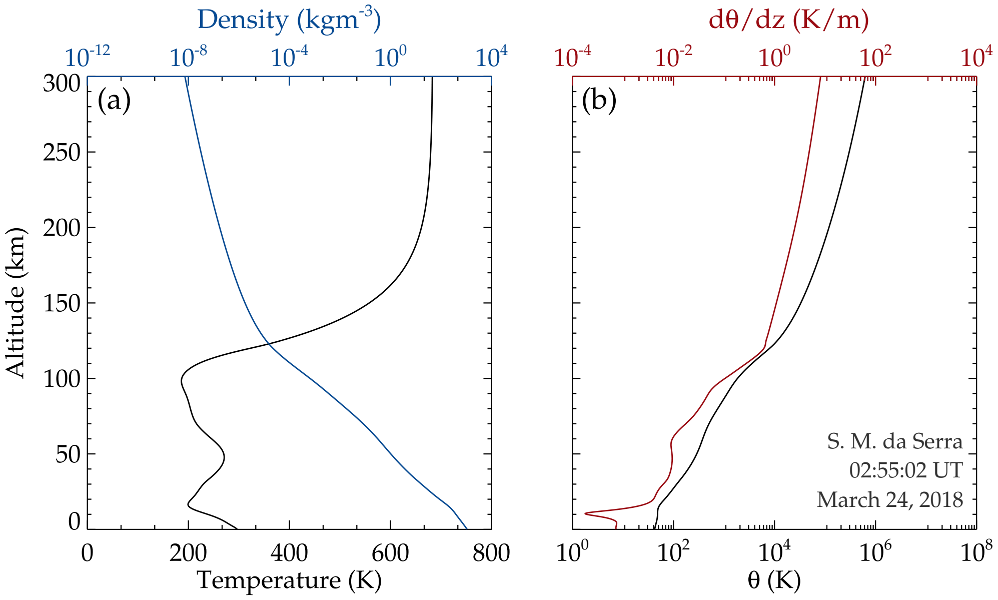

altitude where it will be reflected and propagate upwards again. This situation is characterized as a duct and is illustrated in the shaded region of Figure 2.4. A duct that exists for a longer period of time with relatively longer horizontal extension compared to the horizontal wavelength favors a longer horizontal propagation of the wave. Constructive interference between incident and reflected wave may occur if the width of the duct is multiple the vertical wavelength. This causes the ducted wave to propagate even longer horizontally (See the shaded region of Figure 2.4). However, the ducted wave may suffer destructive interference if the duct is not of the order of the vertical wavelength (PAULINO, 2012; NAPPO, 2013).

Two distinct mechanisms are responsible for the formation of ducts in the atmosphere: 1) inversion in the temperature profile which is technically called “thermal duct” and 2) vertical gradient in the horizontal wind also favors the formation of duct, which is, termed as “doppler duct”. It is also possible to have both thermal and doppler ducts occur at the same altitude and time. Such kind of duct is known as “dual duct” (ISLER et al., 1997).

Figure 2.4 - Profile of the vertical wavenumber in the case of a duct.

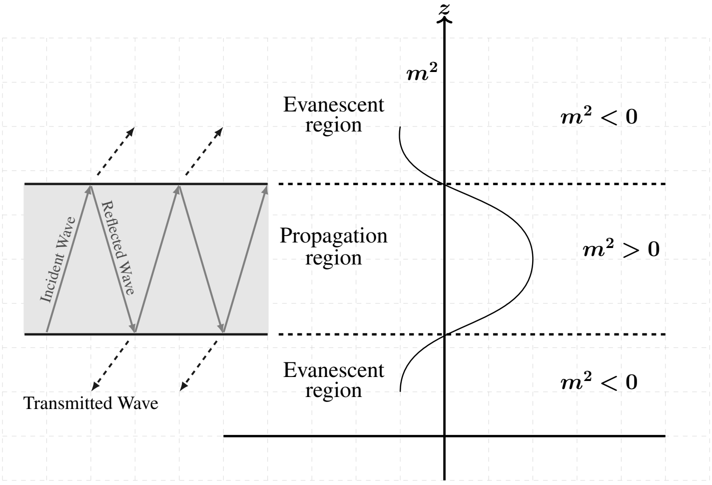

The regions where the wave is propagating ($m^2 > 0$) and evanescent ($m^2 < 0$) are shown. The gray shaded region emphasizes the reflection and transmission two $m^2 < 0$. The regions where the wave is propagating ($m^2 > 0$) and evanescent ($m^2 < 0$) are shown in this panel.
Source: Paulino (2012).

2.2.5 Gravity wave filtering

The presence of critical and reflection levels in the atmosphere considerably limits the spectrum of gravity waves that propagate from their source position in the troposphere to the mesosphere and lower thermosphere (MLT) region. Therefore, the critical and reflection levels act as natural filters for gravity waves, responsible for the selection of GWs packets at any given altitude in the atmosphere. Gravity waves with low horizontal phase velocities are more susceptible to absorption (MEDEIROS et al., 2003).

Small-scale Gravity waves with faster phase speed tend to suffer reflection more easily (FRITTS; ALEXANDER, 2003). Medium-scale gravity waves (MSGWs), that is GWs with intermediate characteristics, are better candidates for reaching higher altitudes. MSGWs have vertical wavelengths from several tens to hundreds of kilometers and periods longer than 30 minutes (TAYLOR et al., 2009).

2.2.6 Dissipation and breaking of gravity waves

We now look at GW dissipation and breaking in the atmosphere. As mentioned earlier, atmospheric density decreases with increasing altitude. As a result, above the turbopause ($\sim$110 - 120 km in altitude), molecular viscosity and thermal diffusivity begin to be important in the dissipation process of gravity waves. Below the turbopause, eddy diffusion and other turbulence (mixing) processes play an important dissipation role. However, the

GWs wave theory used in this work did not include the effect of eddy diffusion. The momentum flux per unit mass for a gravity wave generated at an altitude $z = z_i$ and at time $t = t_i$ is given by Vadas and Fritts (2009) as:

$$\tilde{u}_{GW}\tilde{w}^*_{GW}(\vec{x}, t) = |\overline{\tilde{u}_{GW}\tilde{w}^*_{GW}}|_{t_i} \frac{\bar{\rho}(z_i)}{\bar{\rho}(z)} e^{-2\int_{t_i}^{t} |\omega_{Ii}| dt'}, \tag{2.33}$$

where $|\overline{\tilde{u}_{GW}\tilde{w}^*_{GW}}|_{t_i}$ is the module of the average momentum flux (per unit mass) of a gravity wave at an instant t_i, $\vec{x}$ indicates the position of the wave, * represents the complex conjugate, and ω_{Ii} is the inverse of the decay rate due to molecular viscosity and the thermal diffusivity that is given by Equation 2.31.

Equation 2.33 reveals that the momentum flux is related to two important terms: (1) $1/\bar{\rho}(z)$ and (2) $e^{-2\int_{t_i}^{t} |\omega_{Ii}| dt'}$. Here the density decrease exponentially with altitude, and the first term causes an increase in the momentum flux with altitude. However, due to the exponential growth of ω_{Ii} with altitude, the second term tends to reduce the momentum flux. The overall effect of these two terms causes the momentum flux to reach a maximum at a given altitude within the thermosphere-ionosphere and then decrease rapidly above the altitude where the momentum flux was attained. The graphical illustration of Equation 2.33 obtained from ray tracing result of CGW event at São Martinho da Serra is shown in Figure 2.5.

Figure 2.5 illustrates the vertical momentum flux profile for the CGW event observed on March 23-24, 2018, at São Martinho da Serra. The altitude at which the momentum flux is maximum is called the effective dissipation altitude, above which the amplitude of the gravity wave will effectively decrease. The altitude at which the momentum flux is reduced to less than 10% of the value calculated at the maximum momentum flux altitude is shown by the open red square in the zero wind profile. However, the model wind profile showed that the wave did not propagate further after maximum momentum was attained, suggesting all momentum was deposited. Beyond the altitude where the momentum flux is reduced to less than 10% the maximum momentum flux, the wave practically dissipates, thereby giving an idea of how the GW is losing energy in the atmosphere.

It can also be seen in Figure 2.5 that in addition to density, the momentum flux depends on the influence of the wind on the waves (Equation 2.33). This shows clearly that the wind can considerably modify the altitude at which effective dissipation begins.

Figure 2.5 - The vertical profiles of density, imaginary component of intrinsic frequency, and momentum flux per unit mass.

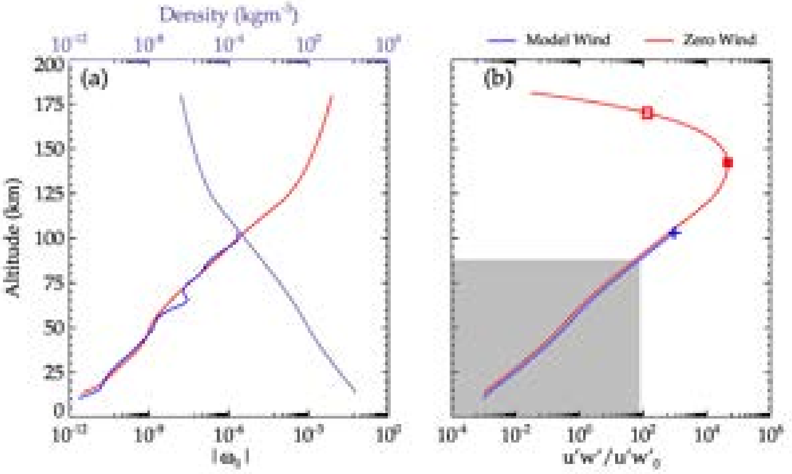

In panel (a), the vertical density profile (purple solid line) and ω_{Ii} profiles for zero wind in the atmosphere (solid red line) and model wind (solid blue line). In panel (b), the momentum flux per unit of mass for a CGWs event on the night of March 23-24, 2018. Similarly, the solid blue line depicts model wind conditions and the solid red line represents zero wind. The plus (‘+’) and filled square symbols represent the altitudes at which the maximum momentum flux was attained for model and zero wind conditions. The unfilled square represents the altitudes at which momentum flux is 10% less than the maximum. The gray shaded region emphasizes momentum flux within the altitude range from 0 - 87 km.

2.2.7 Propagation of concentric gravity waves in the atmosphere

Convectively generated atmospheric gravity waves (with concentric wavefronts) at the tropopause are capable of propagating vertically upward. Some of these excited CGWs having small-scale characteristics with large amplitudes may become nonlinear or reach critical levels below the stratopause. Also, they cannot survive the critical level and wave filtering and hence, are most likely unable to reach higher altitudes (FRITTS; ALEXANDER, 2003; LANE et al., 2003; LANE; SHARMAN, 2006). CGWs with small initial amplitudes are capable of propagating to the upper atmosphere. A three-dimensional simulation of CGWs excited by a single-point source has shown that (see Figure 2.6) they have conical-shaped phase surfaces when little or zero background wind condition is assumed.

Figure 2.7 shows a simulation result of the propagation direction of CGWs above mesoscale convective complexes to the middle/upper atmosphere (VADAS; FRITTS, 2004). In this result, the horizontal cross-section (left and center) and vertical cross-section (right) of their propagation show the wave fields arising from simulated convective plume with multiple updrafts after 30 minutes (top), 60 minutes (middle), and 90 minutes (bot-

Figure 2.6 - Propagation of concentric gravity waves in the atmosphere.

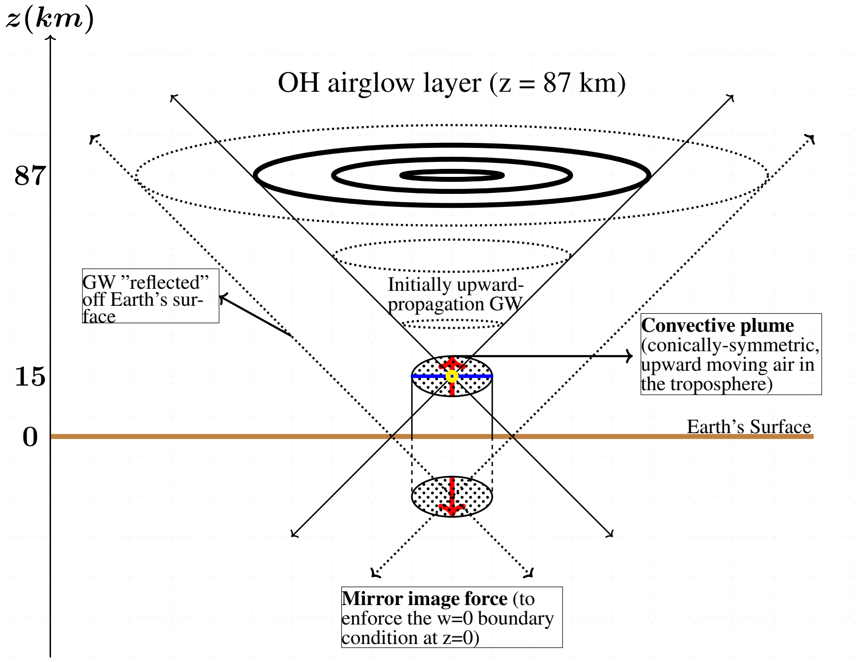

A sketch showing the components of the convective plume model with an upward-moving body force above the Earth's surface (labeled as a convective plume) and an identical downward-moving image of the body force "below" the Earth's surface (labeled as mirror image force). The body forces are shown as hatched ellipses, and the red arrows in the body forces show the direction of air movement. The thick horizontal brown line represents the Earth's surface. A few of the excited CGWs are shown as thin solid lines with arrows.
Source: Vadas et al. (2009b).

tom) following the initiation of convective excitation. In the left and center columns, the horizontal cross-sections were set at altitudes of 25 km, and 50 km, respectively, and in the right column, the vertical (x, z) cross-sections, that is, y-component is set to zero.

At lower altitudes at initial times, it is observed that the wave fields are broader. This occurs because of the shallower propagation of lower frequency waves with small vertical group velocities and also as a result of the reflection of waves excited earlier from the Earth's surface which were initially propagating downwards. The vertical cross-sections (right column) show vertical velocities in the Boussinesq model as well as their vertical propagation morphology (conical shape as shown in Figure 2.6). The vertical velocities are considered to be actual velocities scaled by the multiplication factor ,$[\bar{\rho}_i/\bar{\rho}]^{1/2}$, with $\bar{\rho}_i$ being the background density. This multiplication scaling factor is used to offset the exponential increase in wave amplitudes resulting from decreasing density with altitude (FRITTS; ALEXANDER, 2003; VADAS; FRITTS, 2004; NAPPO, 2013).

Figure 2.7 - Simulation result of horizontal and vertical cross-section showing the vertical velocity of the wave field after the initiation of convective excitation.

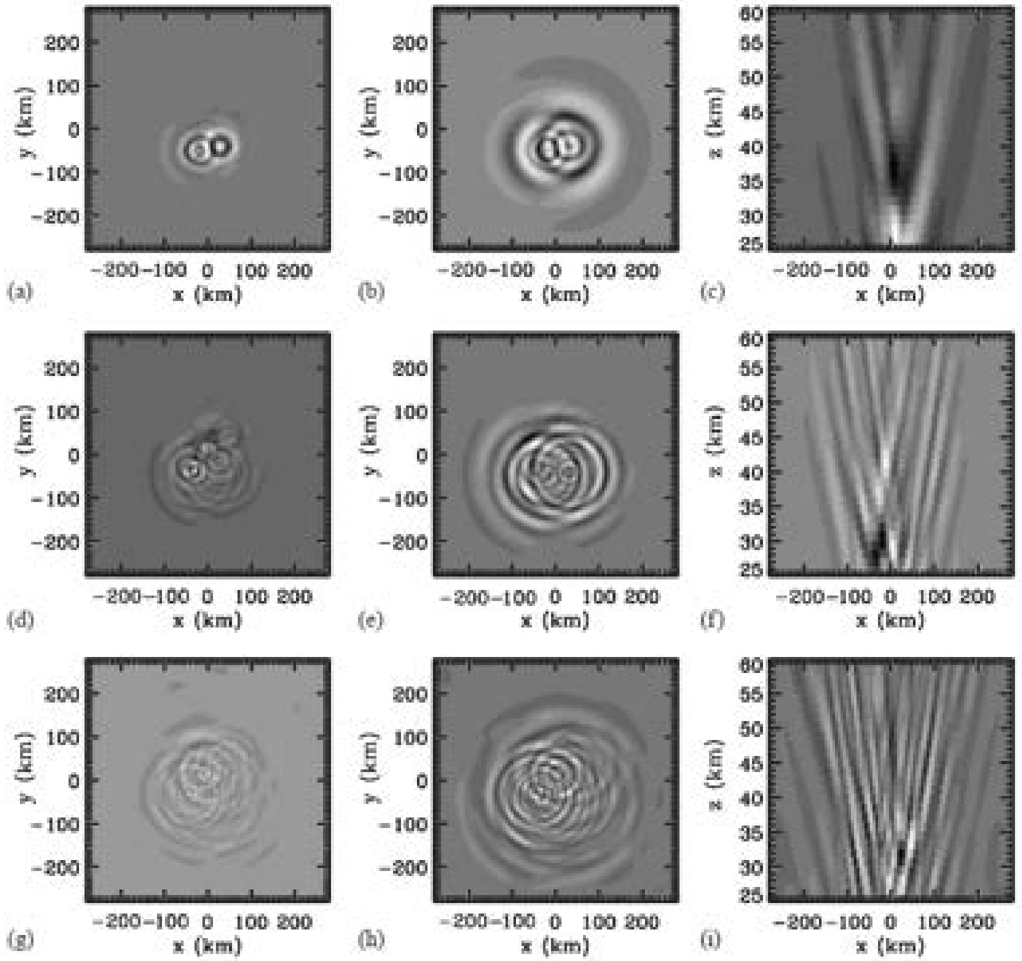

Horizontal (left and center) and vertical (right) cross-sections of vertical velocity showing wave fields arising from simulated mesoscale convective complexes at 30 minutes (top), 60 minutes (middle), and 90 minutes (bottom) after initiation of convective excitation. The left and center horizontal cross-sections are at altitudes of 25 and 50 km, and the vertical (x,z) cross-sections are at $y = 0$. The broader wave fields seen at lower altitudes at later times are due to both the shallower propagation of lower-frequency waves having smaller vertical group velocities and also reflections from the Earth's surface of waves excited earlier and propagating downward initially.
Source: Vadas and Fritts (2004).

The schematic diagram in Figure 2.6 was developed by Vadas and Fritts (2009) to further explain the excitation and propagation morphology of CGWs in the atmosphere. Therefore, although the gravity waves are actually propagating upward and horizontally with respect to time and altitude, the waves and associated perturbations in trace species, such as the OH airglow, appear as outward, horizontally propagating concentric rings in a 2D plane under the condition of zero background wind (VADAS; FRITTS, 2009).

2.3 Observation of concentric gravity waves using airglow

Despite the numerous gravity wave observation techniques used over the last half-century, only imaging techniques in a two-dimensional plane could be used to observe concentric GWs. The ground-based imaging technique is employed by the use of airglow all-sky cameras. In the case of space-borne instruments, the airglow technique, as well as radiance/brightness temperature, have been in use to date. Table 2.1 give a summary of some concentric GWs observation using both ground-based and satellite imaging techniques.

Table 2.1 - Summary of concentric gravity waves observation, technique, and instrument.

Authors/Year	Location	Technique	Instrument
Taylor and Hapgood (1988)	Switzerland	OH Airglow	OH TV Camera
Dewan et al. (1998)	Calcutta	CO_2 4.3 μm	MSX Satellite
Sentman et al. (2003)	Bear Mt.	OH Airglow	Photometric Camera
Yue et al. (2009)	Fort Collins	OH Airglow	All-sky imager
Vadas et al. (2012)	Fort Collins	OH Airglow	All-sky imager
Yue et al. (2014)	Fort Collins	albedo & 4.3 μm	CIPS/AIM & AIRS Satellite
Xu et al. (2015)	Northern China	Airglow & 4.3 μm BT	All-sky imager, AIRS & VIIRS
Perwitasari et al. (2016)	Global survey	O_2 Airglow	IMAP/VISI & ISS
Kogure et al. (2020)	Andes Mountains	10.76 μm, 4.3 & 15 μm BT	DNB/VIIRS & AIRS
Vadas and Azeem (2020)	CONUS	TEC	GPS
Nyassor et al. (2021)	Southern Brazil	OH Airglow	All-sky Imager

A review of selected CGWs observation from 1988 to 2021 observed in the stratosphere, mesosphere, and ionosphere is presented in Table 2.1. The complete review of all CGWs can be found in the above-cited works in Table 2.1 and references therein. The observation of CGWs in the stratosphere, mesosphere, and lower thermosphere (SMLT) indicates that these waves propagated from the lower atmosphere to the SMLT region and even to higher altitudes. In this section, a brief review of CGWs observations using the airglow imaging technique and its instruments in Brazil and other parts of the globe will be presented. Also, the brightness temperature imaging technique used to observed CGWs has as well be reviewed.

2.3.1 Airglow imaging

Airglow is an atmospheric optical phenomenon in which physically or chemically excited atoms and molecules emit photons. This causes the atmosphere to emit light in a broad spectrum ranging from ultraviolet to infrared. Nighttime airglow (nightglow) are easily differentiated from the celestial spectrum, thereby making nightglows attain peak concentrations in the mesosphere and lower thermosphere (MLT) region. The main nightglow emissions in the MLT region are summarized in Table 2.2.

Table 2.2 - Summary of Atmospheric nightglow, emissions, wavelengths, and peak altitudes.

Atmospheric Layer	**Airglow Emission**	**Wavelength (nm)**	**Peak Altitude (km)**
Ionosphere/ Thermosphere	Atomic Oxygen (OI)	777.4	250 - 300
	Atomic Oxygen (OI)	630.0	250 - 300
Mesosphere	Atomic Oxygen (OI)	557.7	96
	Molecular Oxygen (O_2(0 - 1))	865.5	94
	Sodium D-Line (NaD)	598.2	92
	Hydroxyl (OH)	715 - 930	87

Source: Chamberlain (2016).

In the ionosphere-thermosphere region, the OI777.4 nm, and OI630.0 nm have significantly high intensities, thereby making it suitable for wave studies in this region. In the mesospheric heights, the OI557.7 nm, O_2(0 - 1), NaD, and OH are the emissions present, with the OH emission having the highest intensity, hence the use of OH emission for most mesospheric gravity waves studies.

The OI 557.7 nm and the NaD airglow emissions were the first airglow measurements made back in the 1930s. In an attempt to explain the OI 557.7 nm (green line) emission, a theory was developed by Chapman (1951) which is a reference till now. A parallel study by Meinel (1950) showed that the strongest emission of the airglow spectrum is the hydroxyl near-infrared [OH NIR]. Details of these emissions can be found in the works of Buriti (1997) and Medeiros (2001b).

The thickness of the emission layers in the MLT are typically 6 - 10 km which makes it possible to study gravity waves with vertical wavelengths greater than these thresholds. Furthermore, if a photographic image covers a considerable horizontal extent of the sky, it is possible to detect and study GWs of large horizontal dimensions (horizontal wavelengths from tens to hundreds of kilometers).

The development of equipment capable of imaging the sky at the wavelengths of these airglow emissions has considerably contributed to the scientific knowledge of GWs characteristics, their effects on the Earth's atmosphere, and interactions with other atmospheric phenomena. Furthermore, airglow observations are fundamental for understanding the propagation process of GWs excited in the lower atmosphere and its effects on the upper atmosphere. The important hierarchical works carried out on airglow imaging (PETERSON; KIEFFABER, 1973; CRAWFORD et al., 1975; MOREELS; HERSE, 1977; PETERSON; ADAMS, 1983; HERSÉ, 1984; TAYLOR et al., 1987) over the decades have been discussed in detail by Taylor (1997) and Paulino (2012).

2.3.2 Radiance and brightness temperature imaging

Brightness temperature or radiance is the temperature at which a black body in thermal equilibrium with its surroundings would have to be in order to duplicate the observed intensity of a grey body object at a frequency (ν). In terms of satellite application, brightness temperature is a measurement of the radiance of the radiation traveling upward from the top of the atmosphere to the satellite, expressed in units of the temperature of an equivalent black body. This concept is used in radio astronomy, planetary science, and materials science.

In most atmospheric applications, radiance and brightness temperature are used interchangeably, since the two quantities are inversely related through the Planck's function (TRISHCHENKO, 2006). Currently, most satellite observations in the troposphere and stratosphere use this concept to obtain spatial and temporal information about cloud top temperature, precipitation, ozone, CO_2 etc.

For the observation of GW activities in the stratosphere, the Atmospheric Infrared Sounder (AIRS) instrument onboard the Aqua satellite has been mostly used in the 4.3 and 15 μm channels (YUE et al., 2014; KOGURE et al., 2020). Also, cloud top activities are observed in the AIRS 8.1 μm channel (YUE et al., 2014). The concept of brightness temperature is also used in the infrared and near-infrared channels of the geostationary satellite (GOES), which is designated for weather studies. In the absence of visible images, the infrared and near-infrared channels are used for the observation of cloud top activities. Convective overshooting of the tropopause by deep convection that excites CGWs can be observed as the minimum brightness temperature of the cloud top in the infrared images.

2.3.3 Examples of CGWs observations and their sources

Vadas et al. (2009b), reported CGWs event observed by OH imager in Yucca Ridge Field Station (40.7°N, 104.9°W) on the night of May 11, 2004 at 04:00 UT. The left panel of Figure 2.8 shows the unwarped normalized OH airglow image with concentric rings centered at 102.8°W and 40.0°N. In the right panel of Figure 2.8, the convective overshooting top observed by GOES-12 visible image at 01:32 UT prior to the CGWs observation in the OH emission altitude is presented. This CGW event lasted for about an hour and a half starting from 03:40 to 05:10 UT.

Figure 2.8 - In the left panel is the Concentric gravity waves (CGWs) with circular wavefronts observed at Yucca Ridge Field station on the night of May 11, 2004, at 04:00 UT and the overshooting top observed prior to the CGWs event by GOES-12 visible satellite image at 01:32 UT in the right panel.

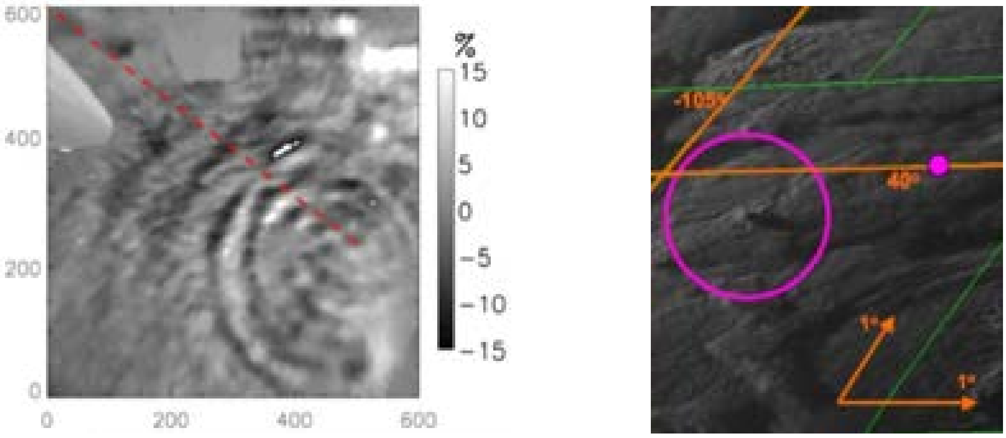

Source: Vadas et al. (2009b).

The Thermosphere-Ionosphere-Mesosphere-Electrodynamic General Circulation Model (TIME-GCM) and Denver balloon soundings on the same night, revealed weak meridional wind ($\sim$10 m/s) and variable zonal wind ($\sim$30 m/s at the tropopause, $\sim$-10 m/s at 80 km and $\sim$-5 m/s at $\sim$87 km). They use the variations observed in the zonal wind component to explain the disappearance of part of the circular pattern.

Xu et al. (2015), on the night of August 13, 2013, around 22:00 LT at the Shuozhou station in Northern China observed concentric GWs with elliptical wavefront. This is shown in the left panel of Figure 2.9. A 30 minutes resolution Fengyun-2 (FY-2) satellite cloud top brightness temperature (CTBT) image from 20:00 - 00:30 LT showed intense convective activities centered around the estimated center of the ellipse. The CTBT image at 21:00 LT with the white arrow pointing to the minimum BT region close to the center of the ellipse is shown in the right panel of Figure 2.9. The green squares represent the crest of the gravity wave in the airglow. The black line represents the fitted ellipse with the red dot representing the center of the fitted ellipse. They further demonstrated using a hodograph of the wind which varied from 58 m/s at 20:00 LT to 10 m/s at 04:00 LT) at 87 km to explain the observed elliptical wavefront. This observational result agrees well with the simulation result of Vadas et al. (2009b) that demonstrated the effects of background winds on the concentric shape of CGWs.

Figure 2.9 - CGWs with ellipse shape observed over Shuozhou station on August 13, 2013 at 22:00 UT and possible source.

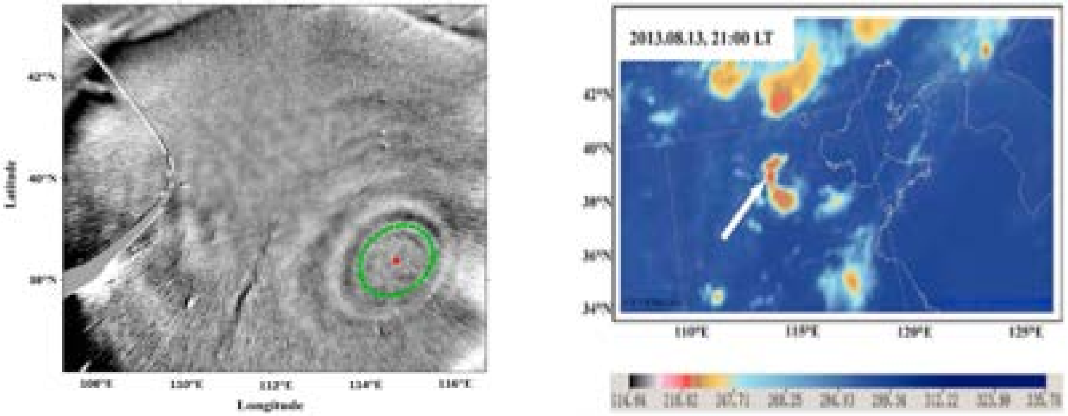

CGWs with elliptical shape observed over Shuozhou station on August 13, 2013, at 22:00 UT is presented in the left panel and the right panel showing the respective possible source. The green squares represent the crest of the gravity wave in the airglow whereas, the ellipse fitting is represented by the black line represents. The center of the ellipse fitting is indicated by the red dot. Source: Xu et al. (2015).

An example of a satellite observation of CGWs excited by tropical cyclone (TC) Mahasen over the Indian Ocean was reported by Yue et al. (2014). Concentric rings of small- and medium-scale gravity wave characteristics were observed in the mesosphere in the Day/Night Band channel of the Visible/Infrared Imaging Radiometer Suite (VIIRS) on-board the Suomi National Polar-orbiting Partnership (S-NPP) satellite. During the same night, the AIRS (AUMANN et al., 2003) also observed concentric ring perturbations in the stratosphere. The authors further showed that the CGWs observed in the DNB of VIIRS and 4.3 μm radiance channel in AIRS were generated by the TC Mahasen. Figures 2.10 and 2.11 show the CGWs observed in the DNB and AIRS, respectively.

On this night, $\sim$60 km and 150 km horizontal wavelength concentric gravity waves were observed in the mesospheric nightglow emission by the VIIRS/S-NPP satellite on the nights of May 13 and 14, 2013, respectively. The epicenters of these CGWs (red cross) in the upper panels of Figure 2.10 corresponded to the center (white cross) of the TC Mahasen infrared (IR) 10.76μm band CTBT image in lower-panels of Figure 2.10. This suggests that the cyclone is the possible source of the CGWs. The left side of each panel

Figure 2.10 - Day night band (DNB) observations of Typhoon generated mesospheric concentric gravity waves (CGWs) and their respective tropospheric convective overshooting top.

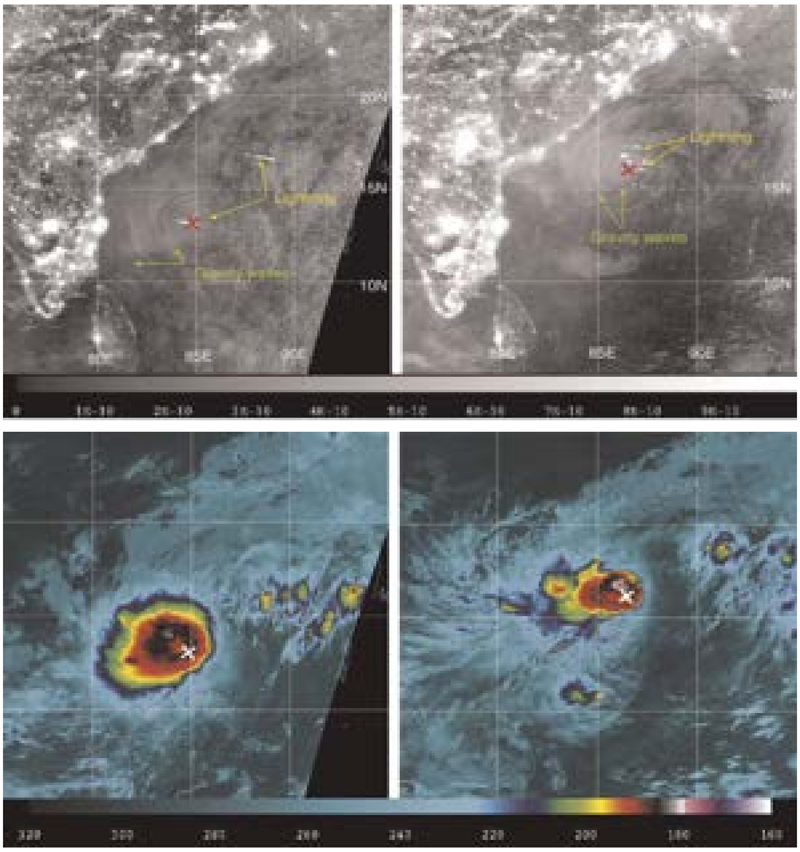

Day/night band (DNB) observations of mesospheric Typhoon generated concentric gravity waves (CGWs) are presented in the upper panels and in the lower panels their respective cloud top brightness temperature observations of tropical cyclone (TC) Mahasen on May 13, 2013, around 20:10 UT are shown. The red and white crosses in both panels represent the determined center of the CGWs. Source: Yue et al. (2014).

of Figure 2.10 is the CGWs and TC Mahasen overshooting event on May 13, 2013, and the right side is that of May 14, 2013. This further indicated that the CGWs captured by the DNB channel were propagating towards the westward and northward directions.

On this same night (May 13, 2013, to specific), concentric patterns were seen in the AIRS 4.3 μm radiance perturbation shown in the left panel of Figure 2.11 and were propagating in the eastward, northward, and westward directions with wavelengths of ~ 60 km and ~ 150 km. The epicenter of the wave indicated by the black circle with a white dot in left panel Figure 2.11 was found close to the coldest region of the cloud top brightness temperature observation in the AIRS 8.1 μm radiance of tropical cyclone Mahasen around 20:10 UT. The image of the CTBT observation is shown in the right panel of Figure 2.11.

Figure 2.11 - AIRS observations of Typhoon generated stratospheric concentric gravity waves (CGWs) and tropospheric convective overshooting top.

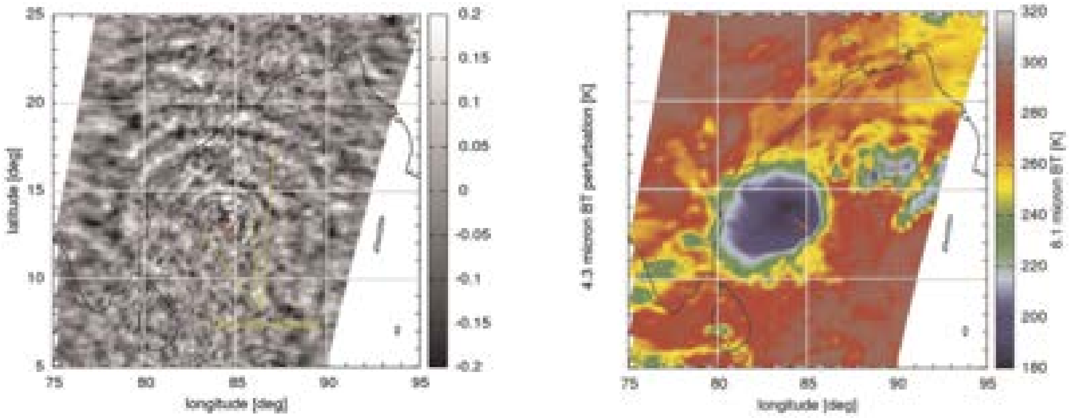

AIRS observations of (left-panel) stratospheric Typhoon generated concentric gravity waves (CGWs) in 4.3 μm radiance and (right-panel) cloud top brightness temperature observations in 8.1 μm radiance of tropical cyclone (TC) Mahasen on May 13, 2013, around 20:10 UT. The red cross in both panels represents the determined center of the CGWs. Source: Yue et al. (2014).

Comparing the left panel of Figure 2.11 and upper panel of Figure 2.10, the small-scale CGWs with horizontal wavelength of ~60 km in the stratosphere and mesosphere are approximately co-located between 83-85° E, 12 - 15°N. The AIRS-observed CGWs in the left panel of Figure 2.11 were mainly propagating eastward, northward, and westward, while the DNB CGWs in the upper left panel of Figure 2.10 was found to be heading toward only the west and north. The authors attributed the disappearance of the eastward component of the CGWs in the DNB to the vertical wavelength of the eastward part of the wave since DNB can only observe mesospheric GWs having vertical wavelengths longer than ~10 km (YUE et al., 2013). The AIRS on the other hand can only detect stratospheric GWs having vertical wavelengths longer than ~20 km.

Aside from using the center of the concentric shape to locate the source position of the CGWs, a ray tracing model was also used. In addition, the ray tracing model was further used to study the CGW propagation from the source location in the troposphere through the stratosphere to the airglow layer (~90 km) (ALEXANDER; ROSENLOF, 1996; YUE et al., 2013; YUE et al., 2014). It was observed that the vertical wavelengths of eastward propagating CGWs (which were not visible in the DNB/VIIRS) were substantially reduced near the airglow layer, while the vertical wavelengths of the westward CGWs were enlarged. This facilitated the observation of westward CGWs in the airglow, especially for the small-scale CGWs. Also from the ray tracing result, the estimated period of propagation for the small-scale CGWs with 60 km horizontal wavelength (i.e., in Figures 2.11

and 2.10) traveled ∼50 km horizontally and ∼ 10 - 20 minutes from the stratosphere to the mesosphere. They concluded that the ray tracing simulations further provided evidence that the CGWs observed by both AIRS and VIIRS originated from the same source.

2.3.4 Gravity waves (planar/concentric) observed over Brazil by airglow imager

This section presents a brief review of advances in airglow observation of planar/concentric gravity wave in Brazil.

Numerous gravity waves studies using airglow have been reported by various works over the Brazilian sector (TAKAHASHI et al., 1986; TAKAHASHI et al., 1998; BURITI et al., 2001; MEDEIROS et al., 2003; MEDEIROS et al., 2004; WRASSE, 2004; WRASSE et al., 2004; BAGESTON et al., 2009; BAGESTON, 2010; VARGAS, 2007; VARGAS et al., 2009; PAULINO, 2012; PAULINO et al., 2012b). All these studies were focused on characteristics of linear gravity waves: their source, propagation, and dissipation/breaking. A brief review of some of the GWs using airglow over Brazil is outlined in the next paragraph.

Using an all-sky imager installed at Cachoeira Paulista (22°S;45°W) (BATISTA et al., 2000), Medeiros (2001b) used airglow data obtained from the routine observations of this equipment to characterized gravity waves in this location. Besides the observed GWs events such as bands and ripples, bore events for the first time in Brazil were observed (BATISTA et al., 2000; MEDEIROS, 2001b). Figure 2.12 shows a gravity wave event observed on the night of January 19, 1999, in Cachoeira Paulista. Panels (a) to (c) in Figure 2.12, illustrate the process carried out to obtain the desired wave parameters. These pioneering works have motivated a series of interesting studies on GWs in Brazil over the past two (2) decades.

Using a backward ray tracing technique, Wrasse (2004) investigated the propagation characteristics and sources of GWs observed in the OH airglow over Cachoeira Paulista and São João do Cariri. The ray tracing result revealed that 16% of the observed GWs have tropospheric origins associated with cold fronts, deep convection, and orographic effects. The source positions of these gravity waves in the troposphere identified by the ray tracing are shown in Figure 2.13. In the case of identified GWs sources in São João do Cariri, 23% were found to have tropospheric origin (WRASSE et al., 2006). It is important to note that there were intense lightning activities associated with the convective sources of the GWs reported by Medeiros (2001b) and Wrasse (2004).

The source and dissipation positions and altitudes of medium-scale gravity waves (MSGWs) observed in the OH and OI630.0 nm emission layers over São João do Cariri during

Figure 2.12 - Gravity wave event observed in Cachoeira Paulista on the night of January 19, 1999.

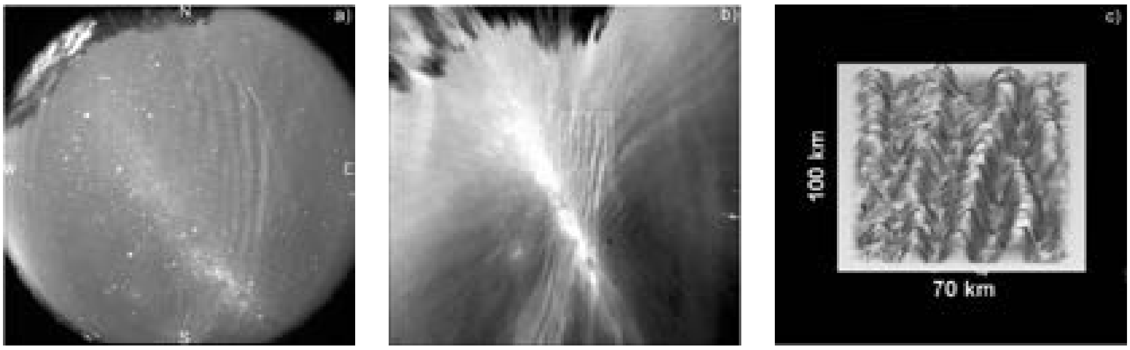

A gravity wave event observed in Cachoeira Paulista on the night of January 19, 1999, is presented. In panel (a) the original airglow image is shown and panel (b) the linearized image without stars, the region within the square highlights gravity wave structures of interest. The three-dimensional structure referring to the square selected region in (b) is shown in panel (c).
Source: Medeiros et al. (2003).

the Spread-Fex campaign were studied by Paulino (2012). He used a ray tracing model to investigate the source and the breaking/dissipation altitudes of the waves as well as their source locations. The ray tracing model used by Paulino (2012) follow the works of Vadas and Fritts (2005) and Vadas (2007) in which the dispersion relation incorporate kinematic viscosity and thermal diffusivity. The ray tracing result identified nearby deep convection as a possible source of one of the MSGWs (event #5) that occurred on September 23 - September 24, 2009. The result of the ray tracing for this event is shown in Figure 2.14. The season when this wave was observed, however, coincides with the season of strong convective activities. On the other hand, the ray tracing of some of the MSGWs studied showed that most of the waves do not have their origins in the troposphere.

These three (3) studies reviewed above and the references therein discussed the sources of GWs with plane wavefronts observed in the OH and OI630.0 nm airglow emission layers. However, no cases of concentric gravity waves (CGWs) have been recorded. The current study, for the first time, will investigate the sources of CGWs over Brazil. The details of the observed CGWs are presented in the results chapter (i.e., Chapter 5) and discussed in Chapters 6, 7, and 8 following the adopted published paper (NYASSOR et al., 2021), manuscript under review (NYASSOR et al., Under Review) and manuscript under revision (NYASSOR et al., Under Revision), respectively.

Figure 2.13 - Seasonal distribution of the final positions of the gravity waves backward ray traced to the troposphere.

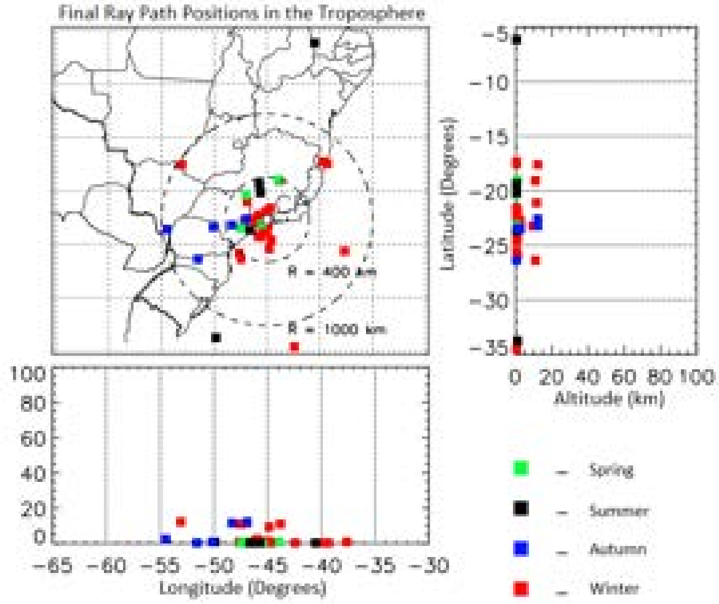

The symbols represent the final positions of gravity waves for each of the seasons of the year.
Source: Wrasse et al. (2004).

2.4 Source of CGWs

This section addresses the underlying theoretical concept governing the convective sources of observed primary CGWs reviewed in Subsection 2.3.3.

Atmospheric gravity waves are generated by various mechanisms that cause vertical displacements of air parcels at equilibrium mostly in the lower atmosphere. Mechanisms such as tropospheric meteorological disturbances or deep convection, wind shear, and orographic forcing are known to excite GWs. Other mechanisms, for example, adjustment of jet streams, frontal systems, body forcing accompanying localized wave dissipation, and wave-wave interactions (FRITTS; ALEXANDER, 2003; TSUDA, 2014) also generate GWs. Medium- and large-scale gravity waves are mostly noted to be generated in the troposphere (LANE et al., 2003).

Among the above-mentioned mechanisms, deep convection is dominant in the tropical and subtropical region where convective clouds excite a broad spectrum of gravity waves (VADAS et al., 2009a; VADAS et al., 2012) through (a) pure thermal forcing, (b) “obstacle”, or “transient mountain effect”, and “mechanical oscillator” effect (FRITTS; ALEXANDER, 2003; KIM et al., 2003). Using the convective plume model, Lane et al. (2001), Lane et al.

Figure 2.14 - Gravity wave event observed in São João do Cariri on the night of September 23 - 24, 2009.

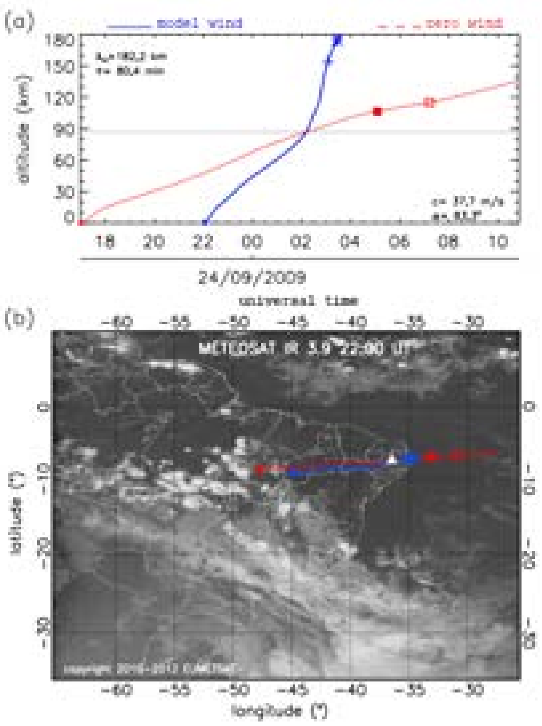

In panel (a) the vertical ray paths of the observed MSGW on the night of September 23 - 24, 2009 (event #5) for zero wind (dashed red lines) and modeled wind (blue solid lines). In panel (b), the horizontal trajectories superimposed on the infrared satellite METEOSAT image observed at 22:00 UT is shown. The black triangle indicates the location of the observation site. The '+' symbols and filled squares represent the maximum momentum flux (MMF) condition. The asterisks and empty squares show where the momentum flux is less than 10% the MMF, respectively. Wave parameters are shown in the upper-left corner and lower-right corners of the panel (a).
Source: Paulino (2012).

(2003), Lane and Sharman (2006), studied the time evolution of a thunderstorm and how they excite GWs. The plume theory has been widely used to relate the vertical "mechanical oscillator" mechanism of convective overshooting by deep convection to observed CGWs. In most CGWs cases, convective overshooting tops are mostly seen around the observation site and some minutes or hours before the observation of the waves. Ray tracing results showed strong agreement between GWs and deep convection (VADAS et al., 2009a; PAULINO et al., 2012a; VADAS et al., 2012). Using plume model and ray tracing, Vadas et al. (2012) simulated CGWs radiated by deep convection and forward ray traced these waves to the upper atmosphere. The characteristics of the simulated wave in the airglow layer were similar to the characteristics of the observed waves in the OH images. In the following subsections, the formation of thunderstorms and how it excites CGWs will be described. Also, the condition of the atmosphere that supports the formation of a thunderstorm will be reviewed.

2.4.1 Conditional instability

A plume is a type of flow generated by the convection of a less dense fluid (a fluid with a higher temperature) released from a localized source into a more dense (lower temperature) environment. The difference in the densities (temperatures) generates buoyancy that drives this flow. For an air parcel to undergo buoyancy leading to the formation of clouds, the potential temperature of the air parcel in the atmosphere must increase with height. In adiabatic lapse rate representation, if the lapse rate (Γ) between the dry adiabatic (Γ_d) and pseudo-adiabatic (Γ_s) values satisfy the condition: $\Gamma_s < \Gamma < \Gamma_d$, then the atmosphere is said to be stably stratified with the adiabatic displacement but unstable with respect to pseudo-adiabatic displacement (HOLTON; HAKIM, 2012). Such a state of the atmosphere is referred to as conditional instability.

To express this condition in terms of variation in equivalent potential temperature with height (θ_e^*), the conditional stability criterion for saturated parcel becomes,

$$\frac{\partial \theta_e^*}{\partial z} \begin{cases} < 0, & \text{conditionally unstable} \\ = 0, & \text{neutrally saturated} \\ > 0, & \text{conditionally stable} \end{cases}$$

Equivalent potential temperature (θ_e^*), is the potential temperature that would be obtained, if all of the water in air parcels were condensed and rained out by upward raising air and then lowering the air parcel adiabatically to a standard reference pressure

Conditional instability is a very important mechanism by which thunderstorm clouds and other meteorological phenomena are formed. When conditional instability is favorable, parcels are lifted from the lower levels of the troposphere to a level sufficient enough for condensation to occur and latent heat released. This level is known as the *cloud condensation level*, CCL. The air parcel at this level eventually finds itself positively buoyant with respect to its surroundings. The *convective inhibition energy* (CINE) which is the amount of energy needed to warm the *planetary boundary layer* (PBL) in order for surface parcels of air to reach the *level of free convection* (LFC) causes this to occur. At the LFC, the air parcel becomes upwardly buoyant. The magnitude of this upward buoyancy is determined by the *convective available potential energy* (CAPE) which eventually causes the air parcel to reach the level of neutral buoyancy (LNB) where the buoyancy vanishes. At LNB, the plume has the capability to overshoots beyond the level of neutral buoyancy to a maximum height due to its momentum.

2.4.2 Convective available potential energy (CAPE)

The convective available potential energy (CAPE) is defined as the maximum kinetic energy per unit mass that a buoyant parcel is determined, by the rising of a parcel from a state of rest at the level of free convection to the level of neutral buoyancy near the tropopause as shown in Figure 2.15. The development of convective storms depends on the presence of environmental conditions favorable for the occurrence of deep convection. A way to predict this possibility is by the use of CAPE. Figure 2.15 shows the skew-T diagram which summarizes the conditional instability description given in Subsection 2.4.1.

Mathematically, Holton and Hakim (2012, p. 54) defined CAPE as

$$CAPE = \frac{w_{max}^2}{2} = \int_{z_{LFC}}^{z_{LNB}} g\left(\frac{T_{parcel} - T_{env}}{T_{env}}\right) dz \equiv B \quad [Jkg^{-1}] \tag{2.34}$$

from which the maximum updraft velocity at any height (z) is given by:

$$w_{max}(z) = \sqrt{2.CAPE(z)} \quad [m/s] \tag{2.35}$$

Severe weather conditions are classified according to the CAPE. The classification of CAPE according to the Storm Prediction Center (SPC) (NOAA, 2019) of National Oceanic and Atmospheric Administration (NOAA) forecast is shown in Table 2.3.

Table 2.3 - Classification of CAPE.

CAPE/Jkg	STATUS
CAPE < 1000	Weak Instability
1000 < CAPE < 2500	Moderate Instability
2500 < CAPE < 4000	Strong Instability
CAPE > 4000	Extreme Instability

Source: NOAA (2019).

CAPE, therefore, provides a measure of the maximum possible kinetic energy that a statically unstable parcel can acquire, assuming that air parcel ascends without mixing with

Figure 2.15 - An illustration of factors of conditional instability in a thermodynamical system.

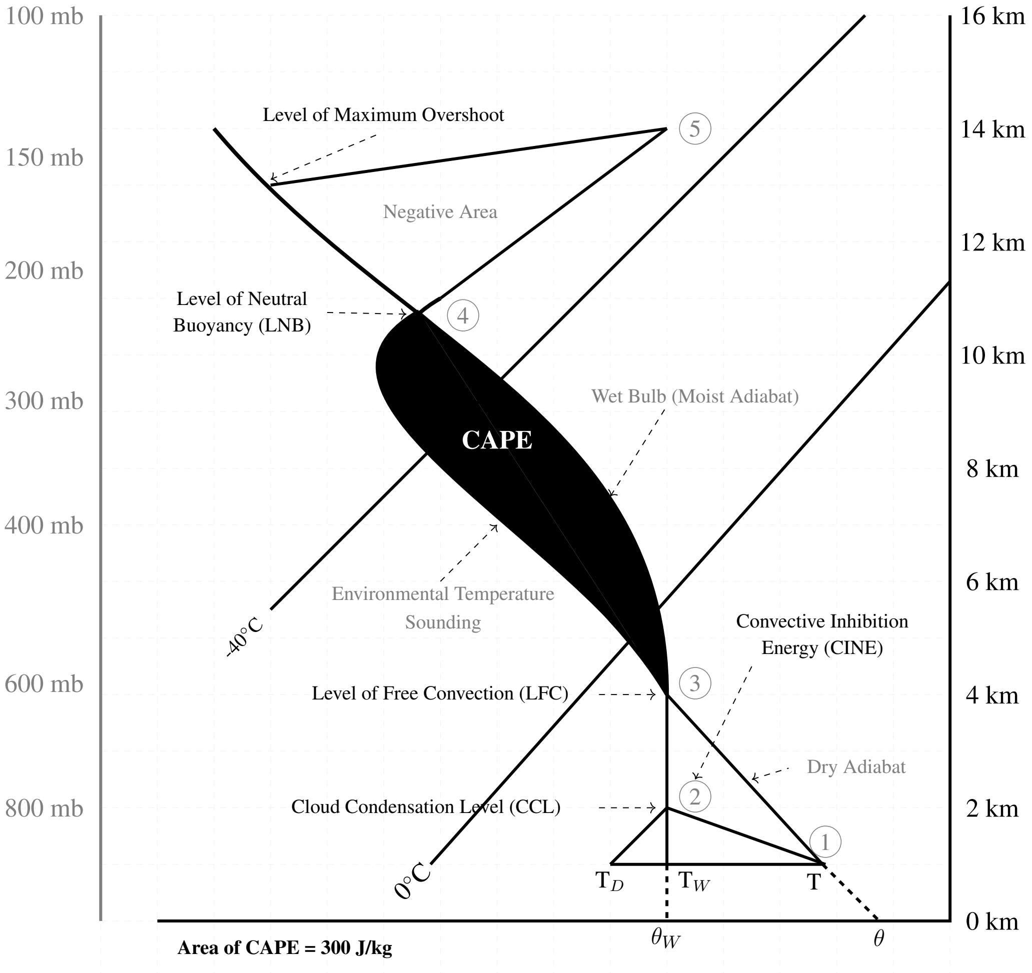

This diagram (Skew-T diagram) is a quantitative representation of parcel theory based on atmospheric observations of pressure, temperature, and water vapor. Horizontal lines represent constant pressure (or altitude). Straight lines upward to the right at 45° are isotherms.
Source: Adapted from Volland (2017, p. 33).

the environment and instantaneously adjusts to the local environmental pressure (VOLLAND, 2017). On the other hand, the value of CAPE is reduced when air mixing and entrainment are considered.

Entrainment describes the process of engulfment and mixing of fluid (air parcel) from the environment into the cloud by large eddies, thus increasing its volume with respect to height, as shown in Figure 2.16. When estimating CAPE, it is assumed that the convective cells do not mix with the environmental air in order to keep the θ_e constant during their ascension. But in reality, ascending saturated parcel of air tends to mix up with environmental air through entraining thereby diluting the air parcel. In the case where the

Figure 2.16 - Air model showing an entraining environmental air into an ascending air parcel.

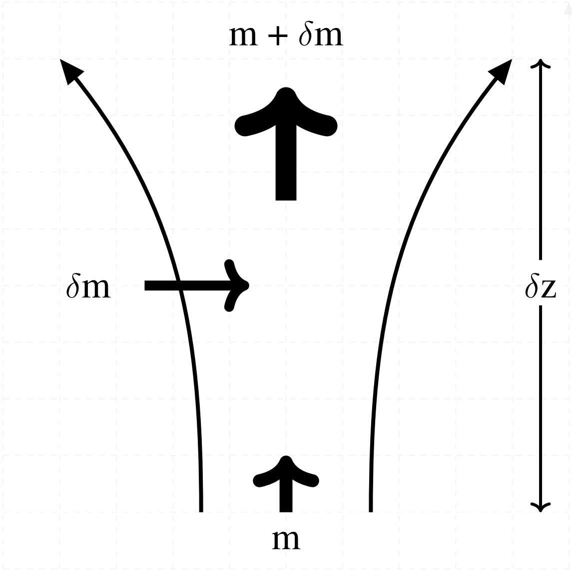

Source: Adapted from Holton and Hakim (2012, p. 295).

environmental air is unsaturated, there must be an evaporation of the rising air in order to maintain the state of saturation within the convective cell due to the entraining of the surrounding air. As a result of this evaporative cooling, the buoyancy of the convective parcel (i.e., the θ_e) is diminished causing θ_e to decrease with height instead of being constant. The effect of entrainment affects other conservable variables as well within the rising air parcel thereby modifying the overall in-cloud vertical profile. By including the contribution of the entraining environmental air on all conservable variables, the altitude variation of CAPE is given by Holton (1992) as:

$$\frac{d}{dz}\left(\frac{w^2}{2}\right) = g\left(\frac{T_{cld} - T_{env}}{T_{env}}\right) - \alpha w^2 \tag{2.36}$$

where α is a constant of proportionality which relates the entraining mass to the rising air parcel. g is the gravitational acceleration and w is the speed of ascent of the parcel.

Understanding entrainment is important because it provides powerful predictive properties of the cloud. In summary, an entraining cell will experience less acceleration than a non-entraining cell, not only due to buoyancy but also due to the drag exerted by mass entrainment. Entrainment helps in the determination of the vertical profile of cloud variables.

Figure 2.17 - Schematic diagram of a plume in the atmosphere.

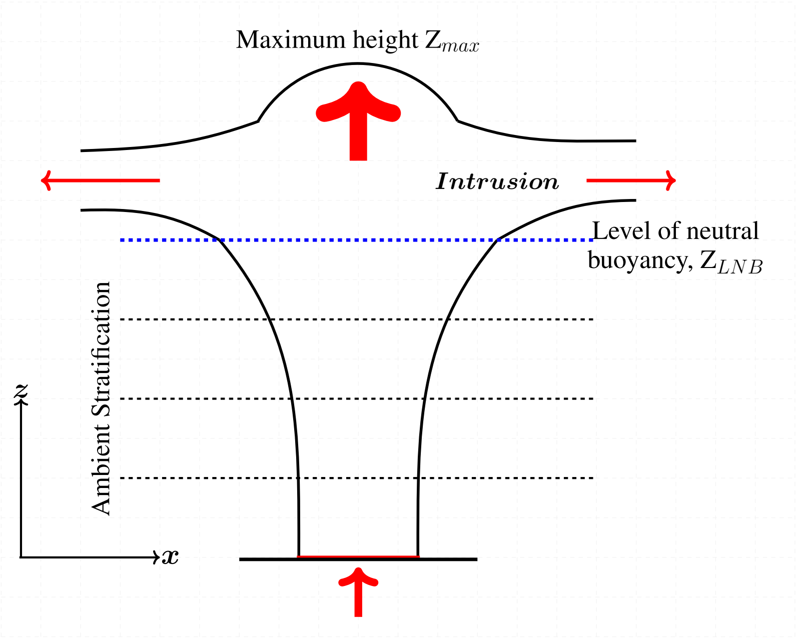

An ideal plume in a stratified environment is presented. The black dashed lines indicate the stratification, whereas the blue dashed lines show the level of neutral buoyancy. The red arrows pointing vertically upwards show the direction of movement of the air parcel within the plume. The eastward and westward red arrows indicate the direction of parcels down drafting after overshooting to the maximum height (Z_{max}).
Source: Adapted from Kotsovinos (2000).

When a warm rising air or a plume in a cloud with sufficient CAPE (w) reaches its level of neutral buoyancy (LNB) (as described in Section 2.4.1), a plume in a stratified fluid first overshoots this level and then falls back to spread radially as an intrusive gravity current. Such radial currents undergo different spreading regimes as they propagate outward (KOTSOVINOS, 2000), forming an anvil shape as shown in Figure 2.17. The level of neutral buoyancy (z_{LNB}) is attained at the height where the buoyancy flux vanishes and the maximum penetration height Z_{max} is estimated at the point where the momentum flux goes to zero. The frequency of overshooting can have n+1 cycle depending on the CAPE. To study numerically the generation of GWs via overshooting by deep convection, the convective plume model is mostly used.

2.4.3 Convective plume model

Several linear, non-linear and 3-D numerical models of GWs excited by deep convection have been developed by Lane et al. (2001), Lane et al. (2003), Piani et al. (2000), Horinouchi et al. (2002), Vadas and Fritts (2004), Vadas and Fritts (2009), and Vadas et al.

(2009b). These models demonstrated that GWs with concentric rings are excited from vertically oriented, point-like overshooting deep convective plumes. The concentric rings of these GWs propagate in the atmosphere if the background intervening winds are small.

The description of convective sources of gravity waves is made analytically and equivalently as heating or momentum sources since these sources are coupled through the vertical momentum equation. Walterscheid et al. (2001) used such a heating model to describe a spectrum of gravity generated by a deep convective source. On the other hand, Vadas et al. (2009b) used the vertical body forces to describe CGWs generated by a deep convective plume. A shown in Figure 2.6, Vadas et al. (2009b) describes the plume as a cylindrically symmetric, upward-moving air in the troposphere. They modeled the upward acceleration of the envelope of air parcel as a "vertical body force" in the momentum equation.

A single convective overshooting by the body forces according to Vadas and Fritts (2009) evolves in time $\mathcal{F}(t)$ as $\sin^2(\pi/\sigma_t)$ over the during of the forcing from $t = 0$ to $t = \sigma_t$. The spatial features of the body forces are represented as a Gaussian function in the horizontal and vertical directions. Details on the mathematical formulation of the convective plume model considering the vertical body force can be found elsewhere in Vadas and Fritts (2009) and references therein. Convective overshootings by convective plumes can be observed using groud-base and space-borne instruments.

2.4.4 Observation of convective overshooting tops

An overshooting convective cloud top or overshooting tops according to the American Meteorological Society's *Glossary of Meteorology* (GLICKMAN; WALTER, 2000) is defined as "a dome-like protrusion above a cumulonimbus anvil, representing the intrusion of an updraft through the equilibrium level." Overshooting tops (OTs) indicate the presence of a deep convective storm with sufficient energy to penetrate through the tropopause and into the lower stratosphere (BEDKA et al., 2010). The tropopause is said to be a boundary in the Earth's atmosphere between the troposphere and the stratosphere. It is a thermodynamic gradient stratification layer demarcating the end of the troposphere and the beginning of the stratosphere. Averagely, the tropopause extends from 9 km in the polar regions to 17 km in the equatorial region.

OTs have been identified as one of the localized sources of atmospheric gravity waves among the three GW generation mechanism by deep convection (LANE et al., 2003). Thunderstorms with OTs produce severe weather-associated activities such as heavy rainfall, gust winds, large hail, and tornadoes (ADLER et al., 1985; BRUNNER et al., 2007). Also, thunderstorms with OTs are often associated with lightning discharges through charge separation and accumulation in the storm updraft region (ZIEGLER; MACGORMAN, 1994; WIENS et al., 2005).

As shown in Figure 2.8 (VADAS et al., 2009b), Figure 2.9 (XU et al., 2015), Figure 2.10 (YUE et al., 2014), and Figure 2.11 (YUE et al., 2014) in Subsection 2.3.3, convective overshooting were seen in the cloud top brightness temperature (CTBT) prior to the observation of all the observed primary CGWs reviewed. This implies observation of OTs are mostly made using satellite imagery in the infrared wavelength. OTs in the CTBT infrared images appear to be the regions with the coldest BT. Visible satellite imagery (VADAS et al., 2009b) can as well be used to observe OTs. Ground-based Next Generation Weather Radar (NEXRAD) can also be used to observed OTs of deep convective systems within the coverage region of the instrument (YUE et al., 2009). Due to the direct link between updraft, overshooting, and lightning, some studies used spatial lightning densities to locate OTs (DEIERLING; PETERSEN, 2008; BEDKA et al., 2010).

3 OBSERVATION, INSTRUMENTATION, AND MODELS

This chapter discusses the details of the principal and co-located instruments used to observe concentric gravity waves and other related data. Both ground-based and space-borne instruments will be discussed. Part of this chapter will discuss the observation schemes of the instruments and also the observation periods at the various sites. The semi-empirical models used to complement the observation are also discussed.

3.1 Observation

The study of CGWs was conducted in the equatorial and tropical regions of Brazil using airglow observational data from various observation sites. We used 18 years of hydroxyl (OH) airglow data from São João do Cariri - CA (7.39°S, 36.53°W), 20 years from Cachoeira Paulista - CP (22.66°S, 45.00°W), and 3 years from São Martinho da Serra - SMS (29.48°S, 53.87°W). The geographical locations of the observation sites are shown in Figure 3.1(A). In panel (B) of Figure 3.1 shows a summary of observed airglow datasets from 1998 - 2019 using the all-sky imagers. The red squares indicate the observation years.

Figure 3.1 - Observation sites used in the study of CGWs.

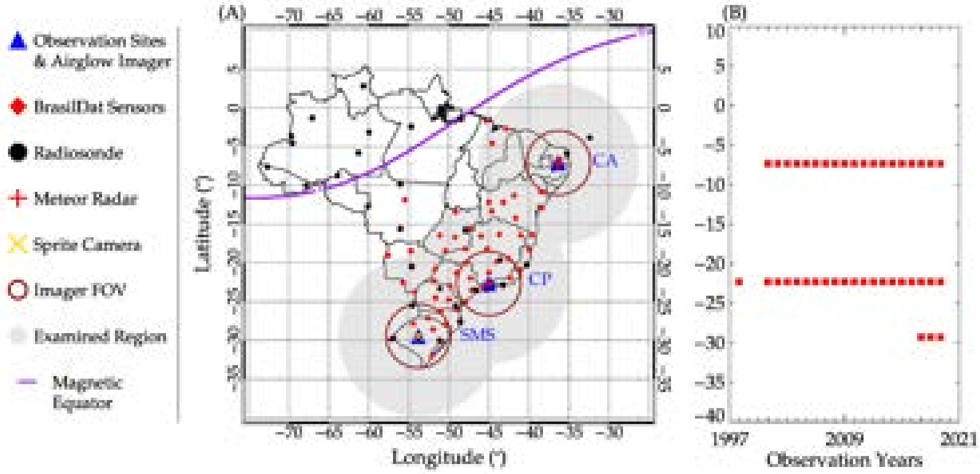

Panel (A) shows the locations of the sites where all-sky imagers were used to observe CGWs. The blue triangles indicate the location of the observation site/all-sky imager and the dark red circles show the field of view of the all-sky image. The ground-based co-located instruments: the BrasilDat lightning sensors, the radiosonde, meteor radar, and camera for sprite observation are depicted by red diamond, black filled circle, red plus sign, and cross sign, respectively. TIMED/SABER, GOES-R CTBT, and lightning data within the light gray region were examined. In panel (B), the available observed airglow data from 1998 to 2019 were used in this study. The purple solid line depicts the magnetic equator. Each red square represents an observation year.

The locations of the ground-based instruments are presented in Figure 3.1(A). The location of the instruments: all-sky imager, BrasilDAT sensors, radiosonde, meteor radar, sprite camera are represented by the blue triangles, red squares, black filled circles, red plus sign, and light blue, respectively. The red circles show the field of view (FOV) of the all-sky imagers and the light gray shaded regions show the region within which the Sounding of the Atmosphere using Broadband Emission Radiometry (SABER) instrument onboard the Thermosphere Ionosphere Mesosphere Energetics Dynamics (TIMED) satellite were examined. Also, within the gray shaded region, the cloud top brightness temperature (CTBT) images obtained from the Geostationary Operational Environmental Satellite (GOES) were examined. The radiosonde positions over entire Brazil are presented but the ones within the light gray shaded regions were used in this work.

Observation of gravity waves using airglow imagers began in 2000 to date at São João do Cariri (CA). At Cachoeira Paulista (CP), observations started in 1998 to date except 1999 and 2000. However, observations in São Martinho da Serra (SMS) began in April 2017 to date. The summary of the observation periods from the various site is shown in Figure 3.1(B). From all the three observation sites, 19, 20, and 3 years from CA, CP, and SMS, respectively of airglow observations resulted in 6,732 observation nights. 3,525 airglow observation nights were recorded at São João do Cariri, 2,743 nights at Cachoeira Paulista, and 464 nights at São Martinho da Serra. The clear sky nights out of the total observation nights for the respective observation sites are 1,586 nights, 1,125 nights, and 325 nights.

Airglow observations using all-sky imagers at these sites were made when the Sun and Moon elevations are lower than -12° and 10°, respectively. This allows 28 nights of observation per month center at new moon and also helps to combine the optical airglow observations with the radio observations (PAULINO, 2012). The time interval between each observation cycle was approximately 100 seconds. Regular observations can sometimes be interrupted by artificial light sources which tend to limit the length of the observation period. Natural sources such as the moonlight and galactic lights also limit the observation period. These sources reduce the quality of the image which in turn affects the accuracy of the parameters obtained from the analysis of the images (MEDEIROS et al., 2005; NYASSOR et al., 2018). Also, this creates large intensity variation in the image which makes it difficult to see well-defined wave signatures at the portion of the image with wave activities.

Other co-located and complementary ground-based and space-borne observations were considered in this work. Ground-based observation: wind from meteor radar, lightning activity from BrazilDAT lightning sensors, tropospheric meteorological data from radiosonde, and low-light camera for sprite observations. For space-borne observations, the GOES-R imagery was used to observed convective overshooting in the infrared cloud-top brightness temperature (CTBT) images. Also, temperature profiles and airglow intensity profiles were observed using the SABER instrument onboard the TIMED satellite. The positions of the co-located ground-based instruments are presented in Figure 3.1A. The gray shaded region in Figure 3.1A is the region within which convective and lightning activities data, as well as data from SABER sounding, are examined.

Wind and temperature model data were obtain from the Modern-Era Retrospective analysis for Research and Applications, Version 2 [MERRA-2] (GELARO et al., 2017), Horizontal Wind Model [HWM14] (DROB et al., 2015) and Naval Research Laboratory Mass Spectrometer and Incoherent Scatter Radar 2000 [NRLMSISE-00] (PICONE et al., 2002) to complementary the observation. A pictorial summary of the instruments and models with their corresponding altitude range within which measurement are made or taken are presented in Figure 3.2. In table 3.1, the instruments, class of instrument with their respective observed variables/parameters are presented.

Figure 3.2 - Instruments and models with their respective altitude range within which measurements were made.

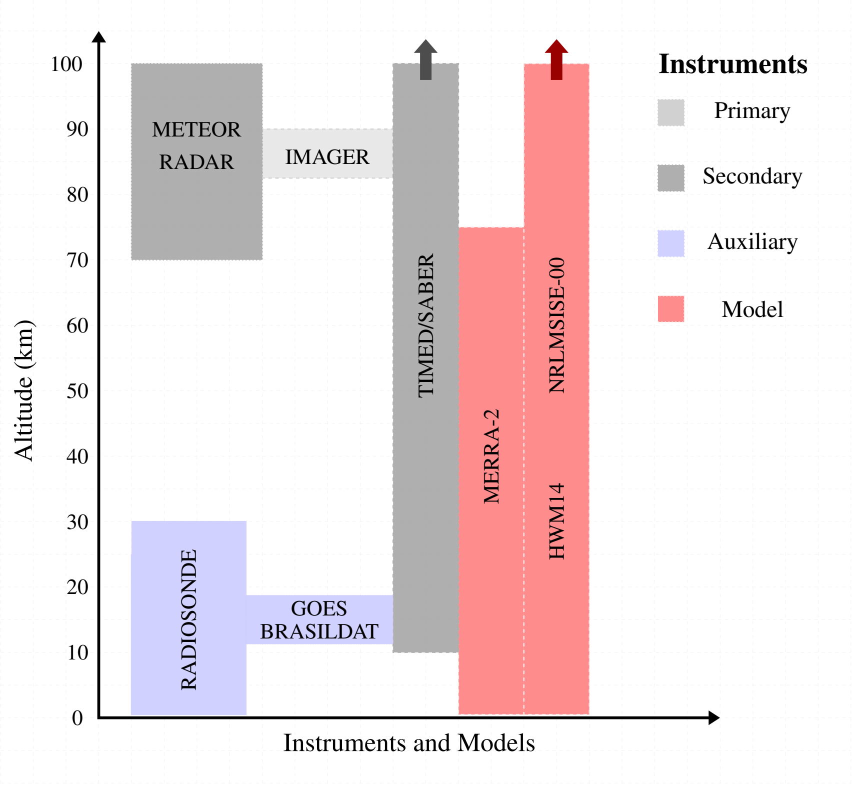

Table 3.1 - Classification of instruments based on the parameters each instrument observes.

Instrument	Instrument Classification	Observed Parameters
All-sky imager	Primary	OH gravity waves
Meteor radar SABER	Secondary	Mesospheric wind Neutral temperature
Radionsonde GOES BrasilDAT	Auxiliary	Wind and temperature Cloud top activity Lightning activity
HWM-14 NRLMSISE-00 MERRA-2	Semi-empirical models	Wind Temperature Wind and temperature

The primary instrument, OH NIR all-sky imagers were used to acquire spectra information of the concentric GW. The secondary instruments: meteor radar and SABER were used to obtain the real background conditions of the atmosphere, whereas semi-empirical (atmospheric numerical) models were used to complement the observed background conditions of the atmosphere in the cases, where no observations were available. The background conditions (i.e., wind and temperature) were used to build the database used in the ray tracing model to study the propagation of CGWs and to locate their source positions. The auxiliary instruments, on the other hand, were used to observe deep convection phenomena to further investigate identified convective sources of the CGW in the troposphere. The deep gray and red vertical arrows on top of the TIMED/SABER, and HWM14 and NRLMSISE-00 data-altitude region indicate that the altitude range of these data exceed 100 km

The above-listed co-located ground-based and space-borne instruments together with the models were used to complement the gravity wave observation by the all-sky imager. This helps in the investigation of the propagation of the observed gravity waves back to the likely source using ray tracing and to identify the source locations of the waves studied in this work.

3.2 Instrumentation

In this section, we will discuss the details of the main instruments used to observe concentric gravity waves. Also, the co-located instruments, both ground-based and space-borne will be discussed. The instruments that were used in this work are: (i) all-sky imager; (ii) Meteor radar; (iii) SABER instrument on TIMED satellite; (iv) GOES satellite; (v) BrazilDAT sensors; (vi) Radiosonde and (vii) Low-light sprite camera. The altitude and phenomena they measure/observe will as well be highlighted. Models such as Modern-Era Retrospective and analysis for Research and Application-version 2 (MERRA-2), Horizontal Wind Model 2014 version (HWM-14), and Naval Research Laboratory Mass-Spectrometer-Incoherent-Scatter (NRLMSISE-00) are discussed.

3.2.1 All-sky imager

The All-Sky Imager managed by the Atmospheric Luminescence (LUME) group of the National Institute for Space Research ("Instituto Nacional de Pesquisas Espaciais - INPE") is composed primarily of an optical system with a fisheye lens having a field of view of 180°, a CCD camera, a computer system, meteorological station (MetStation) and a power supply system (NoBreak). The “All-Sky” imager can detect variations in the intensity of airglow of the nighttime and saving them as images. The schematic diagram of the components of the airglow imager used in Cachoeira Paulista (CP) and São João do Cariri (CA) observation sites are shown in Figure 3.3 whereas that of São Martinho da Serra (SMS) observation site is shown in Figure 3.4.

The SMS imager is installed at the Southern Space Observatory (SSO) and coordinated by the Southern Space Coordination (COESU/INPE). The CP imager at the Atmospheric Luminescence Laboratory, Cachoeira Paulista is coordinated by the LUME group of INPE, whereas the CA imager is installed at the Paraíba Atmospheric Luminescence Observatory and coordinated by the AEROLUME group under the Department of Physics (UAF) of the Federal University of Campina Grande (UFCG). Sample OH images of concentric GWs by the SMS imager on March 24, 2018 are shown in Figure 3.5.

All-sky imagers capture and store images of the sky in several airglow emissions, thereby monitoring in real-time the variations that occur in airglow. The skylight passes through a telecentric lens system and then through filters arranged in sequence. The filters are used to select the spectrum of light of interest, which is OH emission in this case. Note that the imager installed at the SMS observation site has only an OH filter. Finally, the filtered skylight passes through an image reconstruction system (made up of lenses) which reconstructs the image onto a Charged-Couple Device (CCD). The left panel of Figure 3.6

Figure 3.3 - Schematic of the imager used to measure the emissions of nighttime aeroluminescence in São João do Cariri and Cachoeira Paulista.

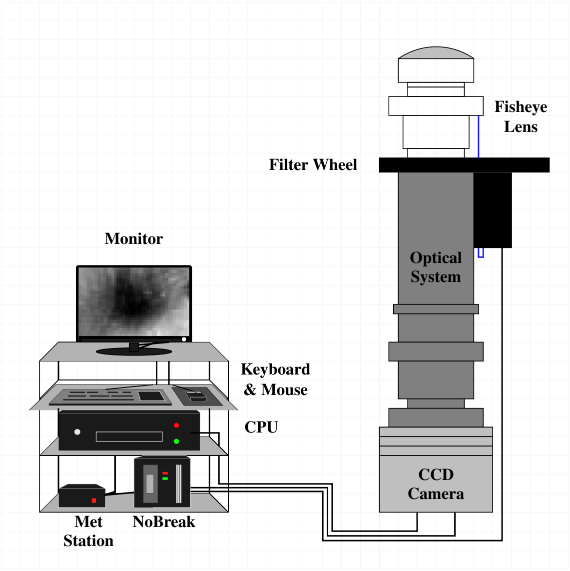

The imager is composed of an optical system, interference filters, CCD camera, computer system, power supply and the instrument's meteorological station (MetStation).
Source: Adapted from Wrasse (2004).

shows a photo of the recent "All-Sky" imagers used by the LUME group of INPE.

The component of the All-Sky Imager that captures all the lights from the sky to form an image is the FISHEYE lens. The fisheye lens has a wide-angle (180°) lens that produces strong visual distortion intended to create a hemispherical image (HORENSTEIN, 2005). A ray diagram of the optical imager system used in observing airglow emissions is shown in the right panel of Figure 3.6

Incident light that passed through the fisheye lens (L_1) traveled through a telecentric lens (L_2) system. The system of telecentric lenses causes the light rays coming from the primary image obtained by the fisheye lens to be parallel to the axis of the optical system of the imager. This maintains the size of the image irrespective of the distance from which the image is being taken. During airglow observation, the distance from which the image is taken corresponds to an emission altitude. Based on the interest of the studies, these emission altitudes are selected using filters. The filters permit the bandwidth of interest. Table 3.2 presents the main characteristics of the interference filters, the wavelengths of the photochemical species, and the altitude of the emission layers used in the imaging of atmospheric airglow.

Figure 3.4 - Similar to Figure 3.3 but installed at São Martinho do Serra with only OH interference filter.

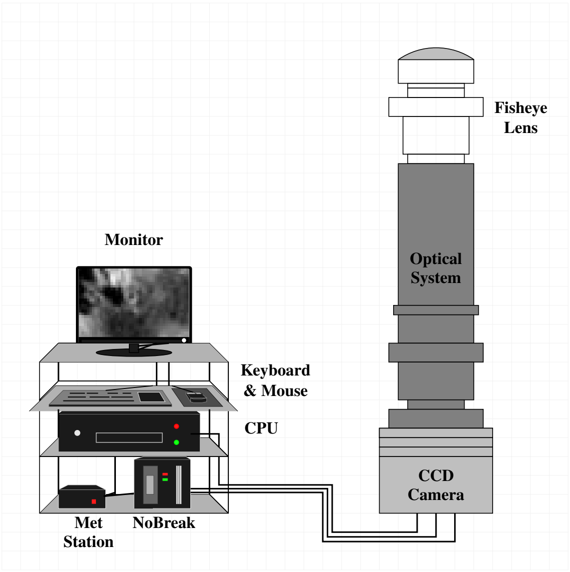

Source: Adapted from Wrasse (2004).

Figure 3.5 - Sample OH images of concentric GWs observed at SMS.

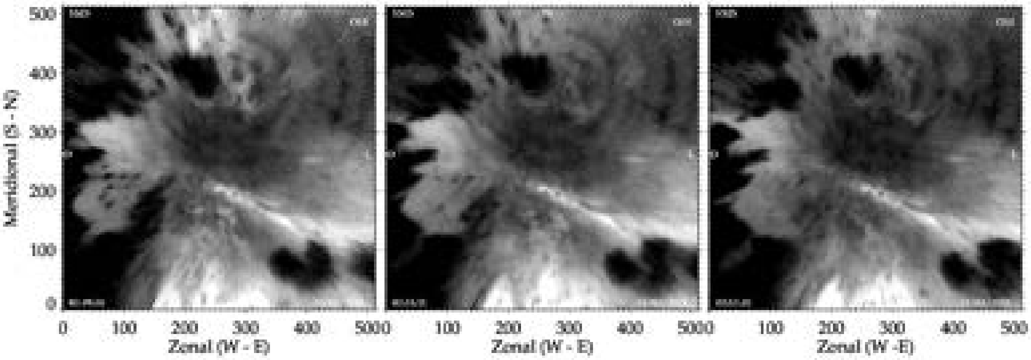

A mechanical system causes the wheel to rotate to the positions of the filters. The most common filters used for MLT dynamics and morphology studies are OI557.7 nm, OI630 nm, OI777.4 nm, OH NIR; O_2 (0.1), and luminous background ("background"). The details of the filters are shown in Table 3.2. In this work, only the OH NIR and luminous background filters were used.

After filtering, the signal goes to the lens system in charge of reconstructing the image

---

[1] With intercept at 865.5 nm, which corresponds to the emissions of the atmospheric band of O_2 (0-1)

Figure 3.6 - Photo and optical diagram of an all-sky imager.

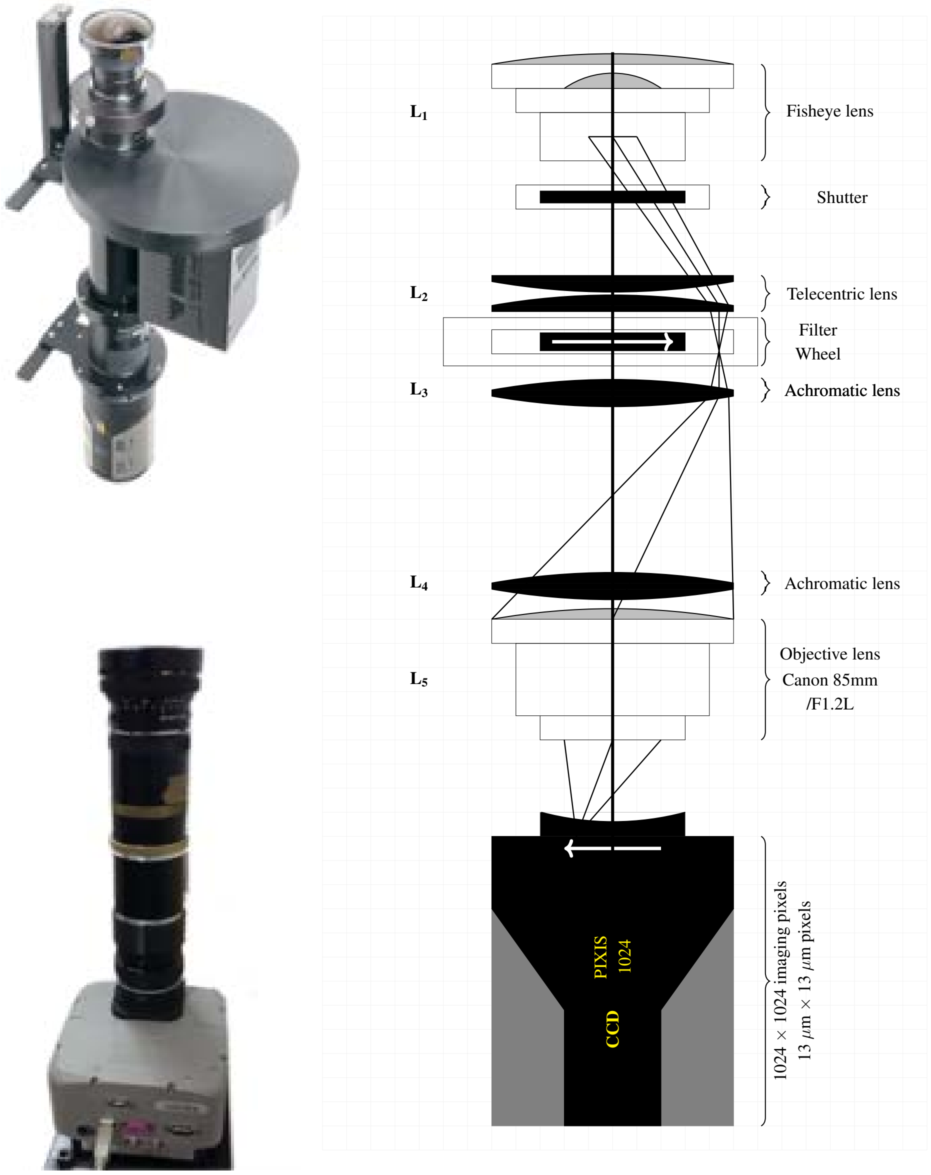

Upper left panel is the operational all-sky imager at São João do Cariri and Cachoeira Paulista and imager at São Martinho da Serra in the lower left panel. An optical Schematic diagram of the all-sky imager is shown in the right panel.
Source: Adapted from Wrasse (2004).

on the charge couple device (CCD) camera. This optical system is called the image reconstruction system. Finally, the light is projected onto the CCD detector. The integration time of the image depends directly on the average intensity of each emission, for example, it is customary to use fifteen (15) seconds of exposure to obtain the images of OH and ninety (90) seconds for the OI6300 nm.

Table 3.2 - Characteristics of interference filters used in airglow observations.

Emission Wavelength (nm)	Assumed Centroid Height (km)	Filter Transmission Wavelength (nm)	Filter bandwidth (nm)
OI	~250	630.0	2.40
OI	~96	557.7	2.67
Background		578.0	10
O_2 (0-1)	~94	865.5	12
OH	~87	715 - 930[1]	215

Source: Keoscientific (2018).

The images captured by the camera are then transferred to the microcomputer to be stored in physical memories. A detailed description of how the all-sky imager optic system works can be found in Wrasse (2004), including the function of each component shown in the optic system's scheme (right panel of Figure 3.6). The function of the CCD is to convert the luminous information into electrons that are then converted to a color system that corresponds to the intensity of the airglow in the image. The CCD operation process can be summarized in four steps:

- Generate and store electrical charges;
- Transfer these electrical charges to the reading process;
- Convert the analog signal from counting electrical charges to digital;
- Store digital data in matrix form to compose the images.

The CCD camera allows the capturing of high-resolution images of the sky with relatively short integration times. The CCD device used in the Cachoeira Paulista and São João do Cariri imager has a 6.45 cm^2 area, a high resolution of 1024×1024 pixels encoded in 14 bytes, a high quantum efficiency (~70% visible), low thermal noise (~0.5 electrons/pixel/second), low reading noise (15 electrons/pixel) and high linearity (0.05%). In addition, the images are projected to a resolution of 512×512 pixels to decrease the signal/noise ratio. Details of the mode of operation of the CCD camera used in the imager of Cachoeira Paulista and São João do Cariri can be found elsewhere in Wrasse (2004), Paulino (2012) and Nyassor et al. (2018).

The SMS all-sky imager has a single filter for Hydroxyl-Near Infrared (OH-NIR) observations (715 - 930 nm with notch at 865.5 nm) and an objective lens. The incoming light is recorded by a Charge Coupled Device (CCD) camera (SBIG, STL-1001E model) with an array size of 1024×1024 pixels and 24.6×24.6 mm and 50% of quantum efficiency in the near-infrared. The image was not binned but cropped to 512×512 pixels producing a final image size of 12×12 mm on the CCD chip. Each image has an integration time of 20 s with a sampling rate of 38 s since the imager does not have a filter wheel (BAGESTON et al., 2009; NYASSOR et al., 2018).

The light from the previous system of lenses undergoes an image reconstruction process (using L_3 and L_4) and then passes onto the Canon-type objective lens (L_5). The CCD detector finally measures the detected light and performs the final image formation. The basic function of a CCD detector is to convert light into incident electrons. These electrons are stored up in the detector to be read, thereby producing data that can be presented as images.

To obtain the intrinsic parameters of the gravity waves understudy as well as the background atmospheric conditions (e.g., pressure, density, temperature, etc.), other co-located instruments were used. These instruments provide the necessary measurement to further complement the investigation of the observed wave parameters by the all-sky imager. These co-located measurements reveal the condition imposed by the background atmosphere on the propagation of the wave. Some of these instruments were used to investigate the identified convective sources of the wave. Details on these instruments are given below.

3.2.2 Meteor radar

Meteor radar is used in electrically neutral atmospheric wind measurement between the altitudes of 80 and 100 km. This region is affected daily by a large number of dust particles (meteoroids) coming from the interplanetary medium. Within this altitude range, the effects of the magnetic field on the dynamics of the particles can be neglected. The meteor trails move mainly due to the action of the neutral winds. Transmitted very-high frequency (HF/VHF) radio waves reflected by the meteor trails are detected by receiving antennas and its characteristics are recorded by the meteor radar. The signal reflected by the meteor trails undergoes a Doppler shift caused by the meteor trail drifts with time. Using the Doppler shift, the radial speed of the meteor trail can be determined and subsequently the speed and direction of the atmospheric wind at the altitude at which the meteor was observed.

The meteor radar used in this work is a transceiver composed of a transmitting antenna, five receiving antennas, and modules for transmitting, receiving, acquiring, and processing data. The radial distance of the trail is calculated from the travel time of the electromagnetic signal. The horizontal location of the meteoric trail is obtained using the interferometric configuration of the receiving antennas (CLEMESHA et al., 2001).

Among the three observation site considered in this work, only São João do Cariri CGWs Cases had simultaneous meteor radar wind observation. The meteor radar installed in São João do Cariri is a SKiYMET model. SKiYMET is a system that has a view of the whole sky and operates at a frequency of 35.24 MHz, with a rate of 2144 pulses per second and transmitted power of 12 kW. It measures wind velocity from 82 to 100 km at a height interval of 3 km and with a temporal resolution of 1 hour. The high frequency makes it possible to reduce the ambiguity of the detection of the meteor echo (HOCKING et al., 2001). In perfect working condition, the radar operates 24 hours a day, measuring meteor echoes, which vary between 1000 and 5000 useful echoes per day. Thus, it allows studying the winds continuously for long periods of time.

The antenna system of this radar is composed of a three-element Yagi transmitting antenna (T) and five receiving antennas ($R_{1,2,3,4,5}$) arranged in the shape of an asymmetric cross. This arrangement is established to minimize the ambiguity in the received signal. The distance between the two pairs of antennae at the ends and the central antenna measures 2.0 and 2.5 wavelengths, respectively.

In Figure 3.7, a schematic diagram of the distribution of the transmitting and receiving antennas of the SKiYMET meteor radar is shown. The main parameters provided by the SKiYMET system are summarized in Table 3.3. The SKiYMET software records daily files with all the parameters listed in Table 3.3 for all the meteor echoes detected during the observation period.

The echo range is determined by half the time it takes the transmitted pulse to travel to the meteor and return (T_R). As it is an electromagnetic pulse, the velocity of the pulse is equal to the speed of light (c), thus, the range (A) is expressed mathematically as follows: $A = \frac{cT_R}{2}$. Using the echo range and the zenith angle, the height of the meteor can be determined. Based on Figure 3.8 it can be written that the height of the meteor is $Z = A\cos\beta$, where β is the zenith angle.

The angular position of the meteor can be determined from the arrival direction (or phase) of the wavefront reflected by the meteor's track, which is calculated using the interferometric system. Regarding speed, there are two speeds associated with a meteor; radial

Figure 3.7 - Schematic diagram of SKiYMET meteor radar transmitting and receiving antennas.

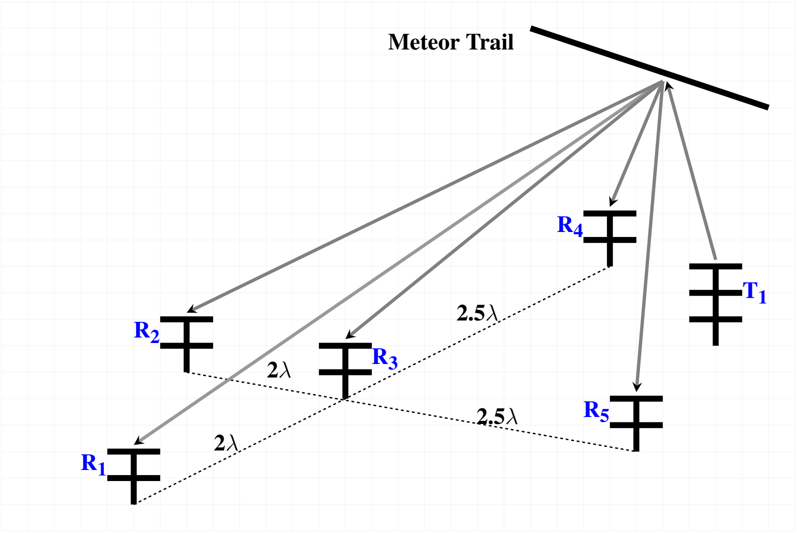

Figure 3.8 - Diagram showing the height of the meteor (Z) and the range (A).

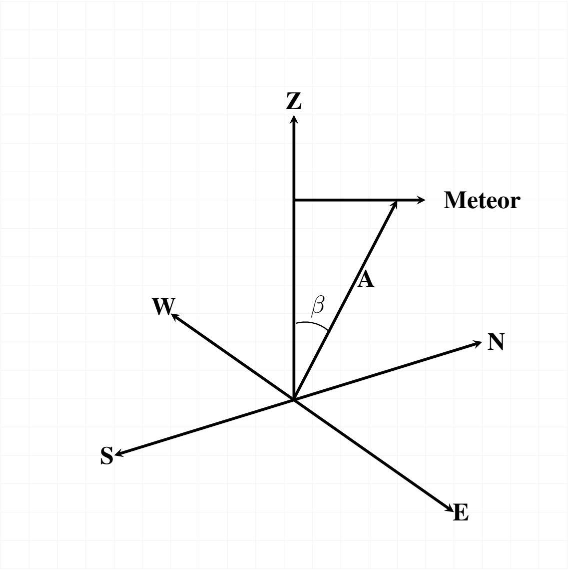

speed, and geocentric speed. The first speed is determined by measuring the Doppler shift between the transmitted and received signals by reflecting the electromagnetic signal through the meteor track. The second is the speed at which the meteoroid enters the atmosphere.

With the radial velocity, the zenith angle, and the azimuthal angle of a minimum number of meteor echoes (generally more than 5 echoes), the zonal (east-west), meridional (north-south), and vertical components of the wind can be determined. The decay time

Table 3.3 - Parameters provided by SKiYMET Meteor Radar.

Data	Description
Date	date of meteor detection
Time	hour of meteor detection
Rge	detection range
Ht	corrected height above ground
Vrad	radial velocity of the trail in m/s
DelVr	deviation from the measured radial velocity obtained by the 5 pairs of antennas on the interferometer
θ	zenital angle of detection in degrees
ϕ	azimuthal angle of detection in degrees counterclockwise from the east
Ambig	number of locations from which the detection may have originated
Delphase	worst phase error between the antennas in degrees
Ant-pair	antenna pair with the worst phase error
IREX	receiver channel used in test quality analysis and always "1" during normal operation
amax	peak value of the amplitude of the echo of the meteorological radar
τ	decay time in seconds
vmet	meteor entry velocity in km/s
snrdb	relation to the signal-noise of the meteor echo

Source: Lima (2004).

is a measure of the time it takes the echo amplitude to reach a value of $\frac{1}{e}$ its maximum amplitude.

Figure 3.9 presents a sample contour plot of zonal and meridional wind observed by Meteor radar in São Martinho da Serra between the hours of 18:00:00 UT on March 23, 2011, and 06:00:00 UT on March 24, 2011. The wind components were estimated using the above mathematical description. The color bar shows the speed of the wind.

Figure 3.9 - Sample result of zonal and meridional wind observed at São Martinho da Serra by a meteor radar.

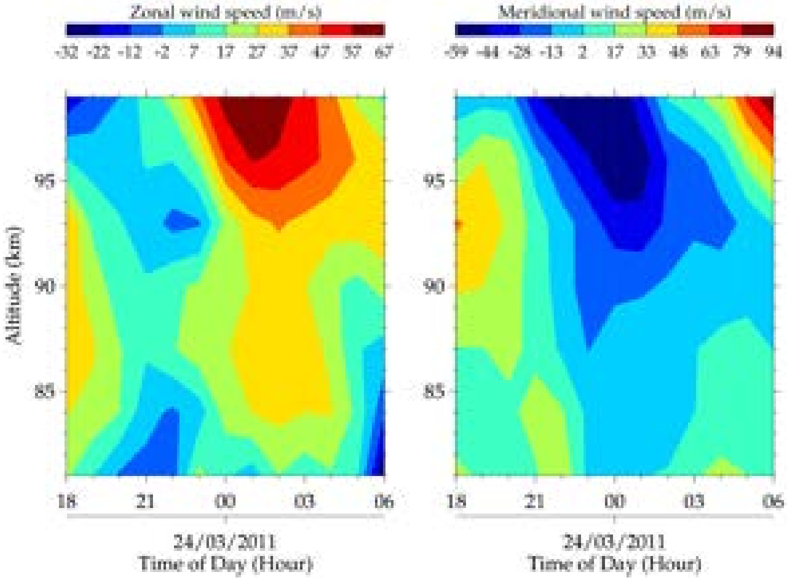

3.2.3 Radiosonde

Radiosondes are mainly used for in situ upper-air measurements of meteorological variables (pressure, temperature, relative humidity (RH), wind speed, and direction) in the atmosphere up to about 36 km. The radiosondes and associated tracking systems provide simultaneous measurements of the vertical structure of temperature, relative humidity, and wind speed and direction over the height range required.

The variation of these meteorological variables in the vertical contains the majority of the critical information for weather forecasting. The radiosonde systems are the only meteorological observing systems able to regularly provide the vertical resolution that meteorologists need for all four variables. Identification of the heights where sudden changes in a variable occur is vital. Thus, continuity of reliable measurements must be sustained throughout the deployment cycle of the radiosonde.

Observations are made by radiosondes carried by ascending balloons launched from land stations. Special meteorological balloons made of high-quality neoprene rubber are filled with helium gas. When employed, they elevate the radiosonde to altitudes as high as 50 km.

Two basic systems are used for data collection and coding for transmittal. These systems consist of mechanical and electrical components. The mechanical component consists of a bimetallic strip thermometer, a goldbeater's skin hygrometer, and an aneroid-type pressure system. The electrical system is made up of mechanical bellows that are responsive to atmospheric pressure changes. This change causes the bellows to switch arrangements to alternately transmit measurements of temperature and humidity. The temperature is indicated by a temperature-sensitive resistor and the humidity by a humidity-sensitive arrangement consisting of a strip of polystyrene coated with lithium chloride. Wind velocities are determined by tracking the radiosonde with a theodolite or with an automatic tracking antenna.

Radiosonde observations are carried out routinely by almost all countries, two to four times a day. The observations are then disseminated immediately to all other countries within a few hours. The observing systems and data dissemination are all organized under the framework of the World Weather Watch Programme of the World Meteorological Organization (WMO). The description of the parameters observed by the radiosonde is given in Table 3.4. In the left panel of Figure 3.10, an artistic diagram with labeled components is shown whereas, in the right panel, a photo of an ascending radiosonde is shown.

Table 3.4 - Data observed by the Radiosonde.

Parameter	Description	Units
PRES	Atmospheric Pressure	hPa
TEMP	Temperature	celsius
RELH	Relative Humidity	%
SKNT	Wind Speed	knot
DRCT	Wind Direction	degrees true

Source: Wyoming (2019).

From the direct measurements, that is, pressure, temperature, relative humidity, and wind (speed and direction), other derived quantities of interest are estimated. Samples of derived parameters estimated from the observed parameters summarized in Table 3.4 are listed in Table 3.5. Detailed information on other derived quantities from radiosonde measurement can be found in Wyoming (2021). In panels (A) and (B) of Figure 3.11, a sample plot of the radiosonde wind (zonal and meridional) and temperature profile taken at Santa Maria (53.81°W, 29.69°S) at 00:00:00UT on March 24, 2018 is shown.

Figure 3.10 - The left panel is the artistic diagram of ascending radiosonde with labeled components whereas, the right panel shows the photo of an ascending radiosonde.

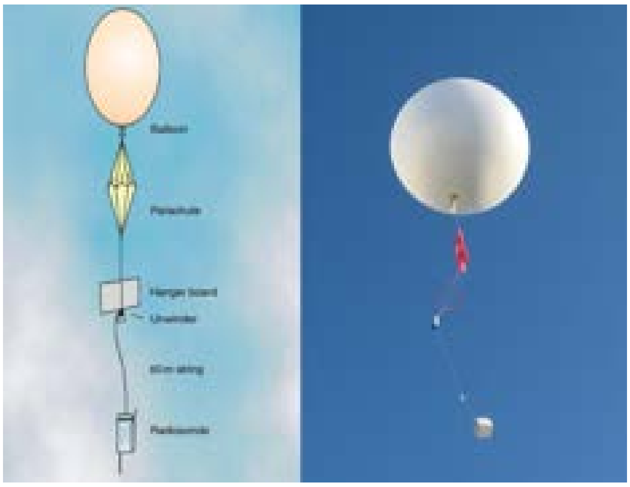

Source: Cole et al. (2003) and Radiosonde (2021).

Table 3.5 - Derived parameters from radiosonde measurements.

Parameter	Description	Units
HGHT	Geopotential Height	meter
DWPT	Dewpoint Temperature	celsius
FRPT	Frost Point Temperature	celsius
MIXR	Mixing Ratio	gram/kilogram
THTA	Potential Temperature	kelvin
THTE	Equivalent Potential Temperature	kelvin
THTV	Virtual Potential Temperature	kelvin

Source: Wyoming (2019).

Figure 3.11 - Radiosonde wind and temperature profile taken at 53.81°W, 29.69°S at 00:00:00UT on March 24.

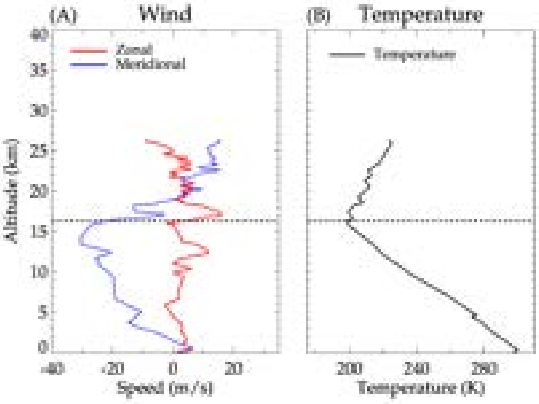

3.2.4 BrasilDAT sensor

The Brazilian Total Lightning Network ("BrasilDAT") network is an integrated intra-cloud (IC) and cloud-to-ground (CG) lightning detection system that combines wide-band sensors and relatively dense network deployment of Earth Networks technology. The combination of the advanced lightning detection technologies with modern electronics, an Earth Networks Lightning sensor ("ENLS") can acquire detailed signals emitted from both IC and CG (LIU; HECKMAN, 2012). A complete ENLS system consists of an antenna, a global positioning system (GPS) receiver, a GPS-based timing circuit, a digital signal processor (DSP), and onboard storage and internet communication equipment. Currently, the BrazilDAT network is made up of 65 active lightning sensors distributed all over Brazil except the Amazon basin (NACCARATO et al., 2014). A schematic labeled diagram and image of the ENTLS which form the BrasilDAT network is shown in the left and right panels of Figure 3.12, respectively.

Figure 3.12 - In the left panel is a schematic labeled diagram of the Earth Networks Total Lightning System (ENTLS) whereas, the right panel is the image of the ENTLS.

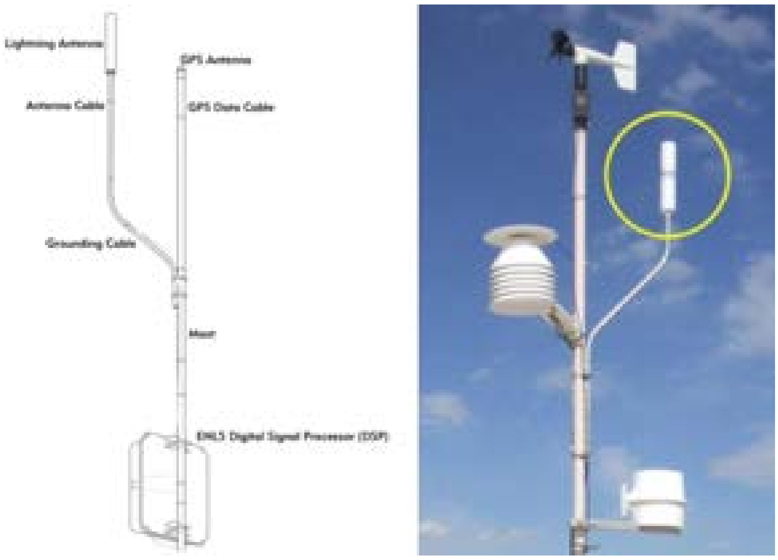

Source: EarthNetworks (2021) and Naccarato et al. (2014).

The sensors use a time of arrival (TOA) method of detection which enables simpler calibration than direction-finding since it is much easier to calibrate timing than bearing. Time-of-arrival is the absolute time taken by a radio signal originating from a transmitter to reach a receiver. The difference between the transmitted and receiving time is the time of arrival. The time of arrival (TOA) method helps to reduce potential errors in locating lightning events and improves detection efficiency and location accuracy. Besides locations, the system also provides a polarity of charge lowered to the ground, peak current estimates, and classification of a flash as IC or CG (NACCARATO et al., 2014). Also, the sensors produce a time and location for each pulse of a flash including in-cloud components and multiple return stroke components for CG flashes.

Exceptional efforts were made to reduce system noise and to broaden the frequency range. As a result, these efforts help to create an integrated unit capable of detecting both CG and IC discharges with high detection efficiencies. The sensors operate in the 1 Hz to 12 MHz range. The CG lightning has been found to radiate at lower frequencies, while IC activity radiates at medium and higher frequencies. Current estimates show that BrasilDAT has 85 to 90% CG detection efficiency, about 50 to 60% IC detection efficiency, and about 500 m CG location accuracy.

Figure 3.13 is a sample plot of observed lightning at São Martinho da Serra during a CGW event between the hours of 21:00 UT on the night of October 1, 2019, and 04:00 UT on October 2, 2019. In panel (A), the lightning density (i.e., the number of lightning strikes at a given longitude and latitude) is presented. In panel (B), the upper left and right panels show the temporal variation in the peak current emitted by the IC and CG lightning, respectively. The lower panel shows the peak current of the total lightning. The temporal range is the same for the upper and lower panels of Figure 3.13. The methodology used to estimate the lightning densities is discussed in Section 4.6.

Figure 3.13 - Panel (A) shows the lightning density at a given longitude and latitude, whereas in panel (B), the temporal variation of the peak current is shown.

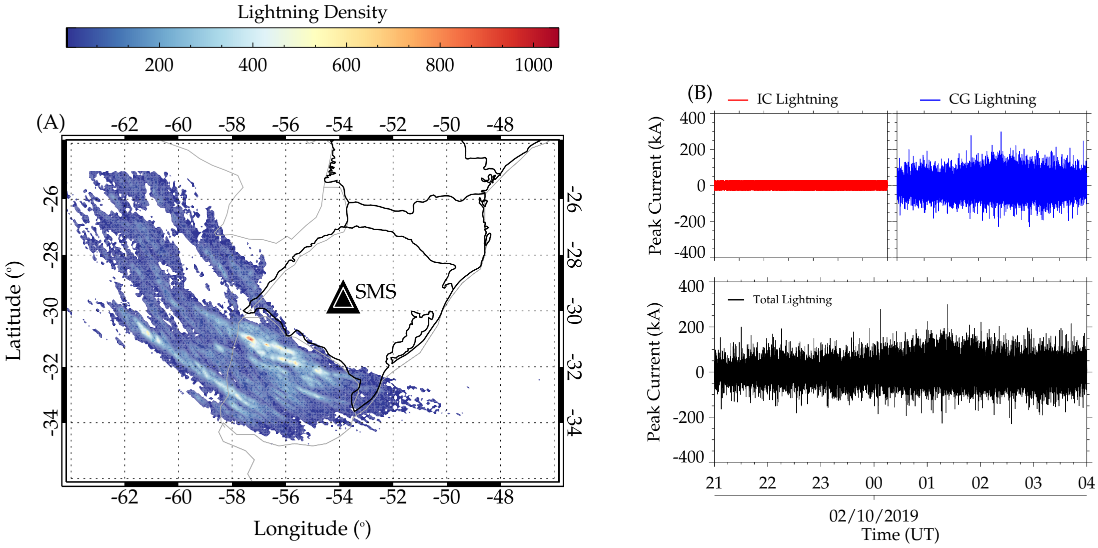

3.2.5 TIMED/SABER

The Sounding of the Atmosphere using Broadband Emission Radiometry “SABER ” is an instrument onboard the Thermosphere Ionosphere Mesosphere Energetics and Dynamics (TIMED) satellite. The TIMED/SABER was launched on December 7, 2001, and began observations in January 2002. The TIMED satellite consists of four instruments: “Solar Extreme Ultraviolet Experiment” (SEE), “TIMED Doppler Interferometer” (TIDI), “Global Ultraviolet Imager” (GUVI), and SABER. The SEE instrument measures solar radiation between 60 and 180 km, TIDI measures wind and temperature profiles in the region between 60 and 180 km, GUVI measures composition, temperature and energy input, and SABER measures atmospheric emissions over a wide spectral range of altitude. Figure 3.14 shows an artistic conception of the TIMED satellite in orbit on Earth. The technical and physical characteristics of the TIMED satellite can be seen in Yee et al. (2003).

Figure 3.14 - Artistic conception of the TIMED satellite in orbit on Earth.

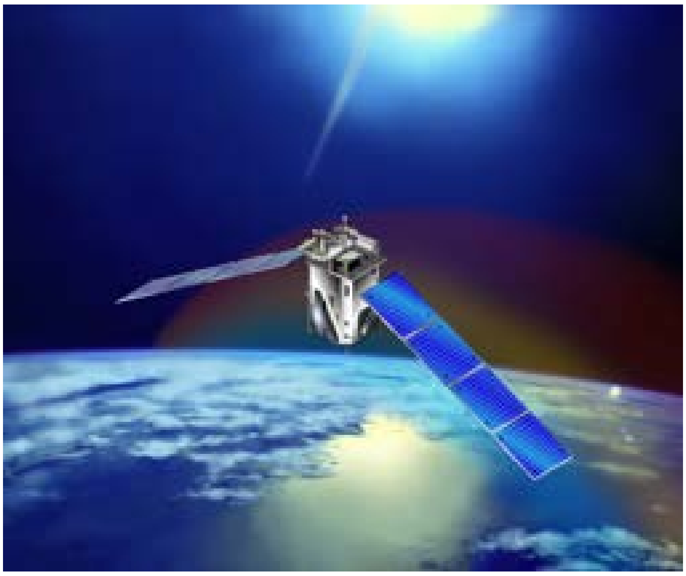

Source: TIMED/SABER (2021).

SABER is a multi-spectral radiometer operating in the infrared band between 1.27 μm and 17 μm. It is capable of measuring vertical emission profiles of various gases in the Earth’s atmosphere. This instrument has a limbo sight and performs continuous sounding during the day and night. The limb sounding has an along track sampling at 400 km interval with a global coverage every day for cells of 580 km average. SABER has a horizontal resolution of 400 km and a vertical resolution of 2 km in the altitude range of 10 to 180 km.

This makes it possible to study globally the variability of atmospheric parameters. Table 3.6 shows the parameters measured by SABER and their scientific applications.

Table 3.6 - Emissions observed by SABER and their respective scientific applications.

Parameter	λ (μm)	Scientific Application	Altitude (km)
CO_2	15	Kinetic temperature, pressure and altitude measurements, cooling rates by infrared emission, study of the nature of non-LTE and LTE CO_2.	10 - 135
O_3	9.6	Concentration of O_3, rate of cooling, rate of solar heating, basic studies of the chemistry and dynamics of the atmosphere.	15 - 100
O_2 ($^1\Delta$)	1.27	Daytime O3 concentration, energy loss, inference of atomic oxygen at night.	50 - 105
CO_2	4.3	CO2 concentration and solar heating in the upper mesosphere, dynamic tracer over 90 km.	85 - 140
OH (υ)	2.0 & 1.6	Emission used to infer [H] and [O], energy loss due to dynamic chemiluminescence of the mesosphere, polar mesospheric clouds, chemical heating.	80 - 100
NO	5.3	Thermospheric cooling and NOx chemistry.	90 - 100
H_2O	6.9	Hydrogen source, dynamic tracer, cooling of the lower mesosphere.	15 - 80

Source: Paulino (2012).

The temperature provided by SABER is the kinetic temperature, which is obtained using CO_2 emissions measurements from two-channel bandpass (650 - 695 cm^{-1}) and (580 - 760 cm^{-1}). Both channels are used to record pressure with altitude in the stratosphere and to infer kinetic temperature assuming local thermodynamic equilibrium (LTE) conditions. However, above 50 km, LTE conditions are not satisfactory for the CO_2 band at 15 μm. There, a recovery algorithm considering non-LTE conditions is used to infer the kinetic temperature in the mesosphere and low thermosphere using radiance measurements of the spectral channel (650 - 695 cm^{-1}) of CO_2.

The non-LTE model for obtaining the kinetic temperature is mainly composed of two components: (1) radiance model and (2) inversion model. The radiance model is composed of two sub-parts: (i) vibrational temperature model and (ii) limb radiance model. A detailed description of the algorithm for obtaining the kinetic temperature can be found in Mertens et al. (2001).

Figure 3.15 shows a kinetic temperature profile retrieved using this algorithm (red solid line). In addition, the temperature profile measured by radiosonde is shown in black solid line. The SABER sounding was taken around 01:00 UT on March 24, 2018, at 54.44°W, 29.65°S. It can be noted that the measurements of the algorithm used by SABER are very consistent with the measurement between the altitudes of 10 - 30 km.

Figure 3.15 - A sample plot of kinetic temperature profile (red solid line) from SABER sounding around 01:00 UT on March 24, 2018, at 54.44°W, 29.65°S and radiosonde temperature profile in black solid line.

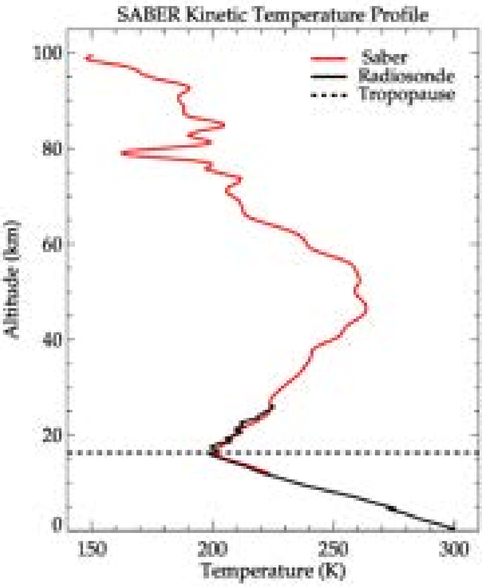

3.2.6 GOES satellite

The GOES-R ("Geostationary Operational Environmental Satellites - R Series") is a collaborative development and acquisition effort between the National Oceanic and Atmospheric Administration (NOAA) and National Aeronautics and Space Administration

(NASA). The GOES-R is launched in November 2016 and is in operation to date. The GOES-R satellite, the first of the series provide continuous imagery and atmospheric measurements of Earth's Western Hemisphere and space weather monitoring.

The GOES-R primary instrument is the Advanced Baseline Imager (ABI). In addition, GOES-R also has onboard other instruments: Extreme Ultraviolet and X-ray Irradiance Sensor (EXIS), Space Environment In Situ Suite (SEISS), Magnetometer, Geostationary Lightning Mapper (GLM), and Solar Ultraviolet Imager (SUVI). The ABI and GLM are nadir-point, EXIS and SUVI are solar-point whereas, SEISS and Magnetometer are in-situ. The ABI is an imaging radiometer with 16 different spectral bands, including two visible channels, four near-infrared channels, and ten infrared channels. Figure 3.16 shows an artistic design of the GOES-R satellite with the six instruments well indicated.

Figure 3.16 - Artistic view of the GOES-R spacecraft in orbit on Earth.

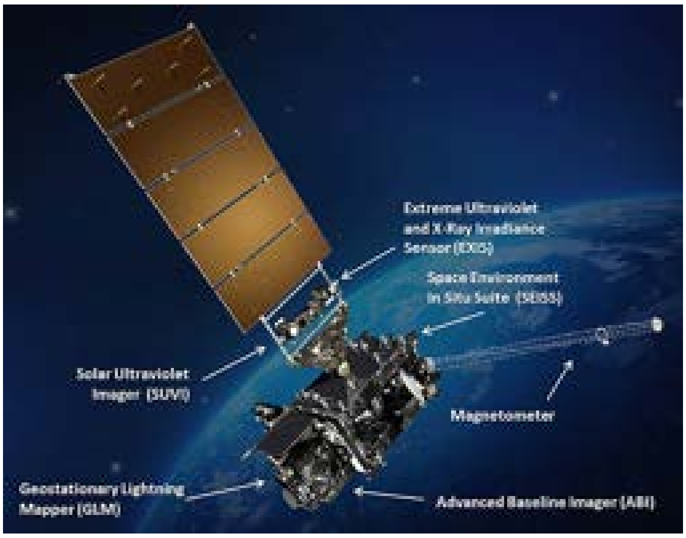

Source: NOAA (2021b).

The 16 channels of GOES 16 have a spatial resolution of 0.5 km to 2 km. These channels cover visible and infrared wavelength regions that allow the generation of dozens of critical weather (including thunderstorms, tornadoes, fog, flash floods) and climate products. The cloud top brightness temperature (CTBT) product is derived from the 11 μm, 12μm, and 13.3μm infrared observations and is produced every 15 minutes for Full Disk, and every 5 minutes for Mesoscale. The characteristics of ABI is summarized in Table 3.7 and a sample result of the observation of cloud top brightness temperature captured by the 13.3μm IR channel at 03:00 UT on October 2, 2019 over South America in Figure 3.17.

Table 3.7 - Characteristics of ABI of GOES-R.

Requirement	ABI of GOES-R
Number of spectral band	16
Spatial Resolution:	
VIS	0.5 km
VNIR (2 $<$ μm)	1.0 km
VNIR (2 $>$ μm)	2.0 km
Time for full disk scan	15 minutes
Time for mesoscale scan	5 minutes

Source: Schmit et al. (2005).

Figure 3.17 - Cloud top brightness temperature infrared image taken by GOES-16 on the night of October 2, 2019 at 03:00 UT over South Amenrica.

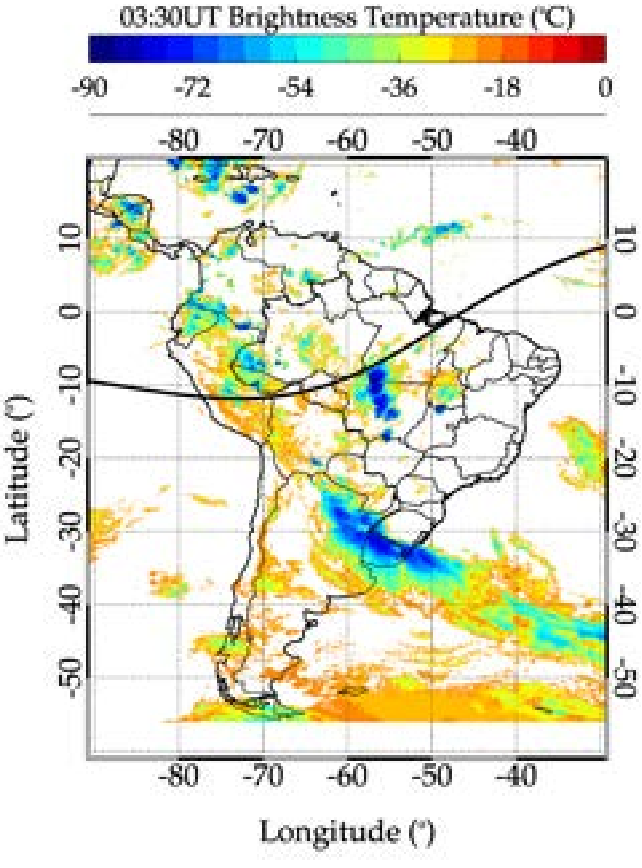

3.3 Models

To complement temperature and horizontal wind observation data (i.e., in the case, where there are no observation data available) semi-empirical models were used. The semi-empirical models used in this work are:

- NRLMSISE-00;
- MERRA-2;
- HWM14.

The parameters obtained from each of these models are discussed in detail in the subsequent subsections, that is, Sections 3.3.1, 3.3.2, and 3.3.3.

3.3.1 NRLMSISE-00

The NRLMSISE-00 is an empirical model of the atmosphere adapted by the "Naval Research Laboratory" (NRL) from the "Mass Spectrometer and Incoherent Scatter Radar" (MSIS) model (PICONE et al., 2002). The letter "E" in the acronym indicates that the model extends from the ground to space. This model calculates the composition, temperature, and total mass density of the neutral atmosphere.

The model includes the main parameters of the upper atmosphere, which are the solar flux in the extreme ultraviolet (EUV) and the warming of the atmosphere due to the effects of magnetic activities. The solar flux at 10.7 cm ($F_{10.7}$) is used as the standard for the EUV while the daily geomagnetic index (Ap) indicates the magnetic activity. This model was developed based on previous versions of the MSIS-86 and MSISE-90 models. The dataset of this model includes measurements from ground-based instruments, satellites, and rockets (PICONE et al., 2002).

The inputs of the model are: year, day, hour, altitude, geodetic latitude, geodetic longitude, apparent local solar time, 81-days average of $F_{10.7}$, daily $F_{10.7}$ solar flux of the previous day, and daily magnetic index. The model outputs are vertical profiles of numerical density of He, O, O_2, N, N_2, Ar, and H constituents. Also, total mass density, exospheric temperature, and neutral temperature, and density scale height are output profiles. In this work, only neutral temperature, total mass density, and density scale height

A sample vertical profiles of temperature (T), total mass density (ρ) and density scale height (H) obtained from the NRLMSISE-00 model is presented in Figure 3.18. These profiles extend from the Earth's surface to an altitude of ~500 km at São Martinho da Serra on March 24, 2018, at 02:00 UT. The dark red squares show the profile at each 1 km.

Figure 3.18 - Vertical temperature profile obtained from NRLMSISE-00 model for March 24, 2018, at 02:00 UT.

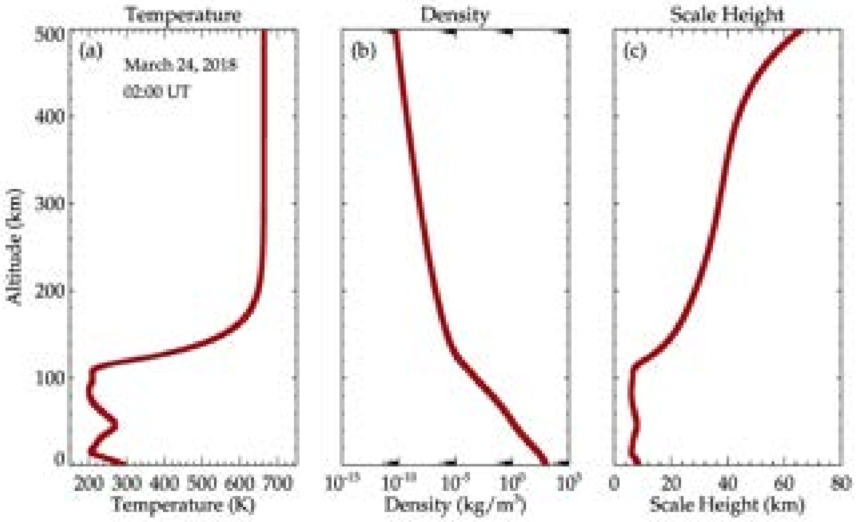

3.3.2 MERRA-2

The Modern-Era Retrospective analysis for Research and Applications, Version 2 (MERRA-2) is the advanced version of the original MERRA dataset. MERRA-2 is a global reanalysis data that assimilates space-based observations of aerosols and their interaction with other atmospheric physical processes in the climate system. In Version 2 of MERRA, advances are made in the assimilation system that enables the assimilation of observation datasets such as, modern hyperspectral radiance and microwave and GPS-Radio Occultation.

In addition, ozone profile observations from the National Aeronautics and Space Administration (NASA) were also included. The Goddard Earth Observing System Version 5 (GEOS - 5) Model and Gridpoint Statistical Interpolation (GSI) assimilation system have been improved and included in MERRA-2. The GEOS - 5 is an integrated Earth system model and data assimilation system developed at the Global Modeling and Assimilation Office. The components of the model use the Earth System Modeling Framework (ESMF), enabling them to be connected flexibly and supporting the investigation of many different aspects of Earth science. The GSI is a public domain variational data assimilation system that flexibly and efficiently run on various parallel computing platform.

MERRA-2 products, for instance, temperature and wind have a temporal resolution of 3 hours. On a spatial scale, MERRA-2 has horizontal (longitude × latitude) resolution of 0.500° × 0.625° (55 km × 68 km). On the vertical scale, MERRA-2 has 72 model levels which correspond to pressure height ranging from 0.01 to 985 hPa and altitude range from the Earth's surface up to ∼75 km. Many atmospheric data can be obtained from MERRA-2 among which, we have temperature and wind. To access these data, the following input information needs to be defined: Refine Date Range [$\mathrm{yyyy_i}$ - $\mathrm{mm_i}$ - $\mathrm{dd_i}$ - $\mathrm{yyyy_f}$ - $\mathrm{mm_f}$ - $\mathrm{dd_f}$], Refine Region [$\mathrm{lon_i}$, $\mathrm{lat_i}$, $\mathrm{lon_f}$, $\mathrm{lat_f}$], Variables [e.g., T = air temperature, U = eastward wind, V = northward wind], Dimensions [1, 2, 3,...,72], Time of Day [00:00 - 21:00], and Grid [[interpolation type],[grid type]]. The 'i' means initial and 'f' means final. Based on the defined input information, the output is given in a default NetCDF format.

To obtain temperature profile at São Martinho da Serra, the following input fields were defined:

i. Refine Date Range: 2018-03-24 - 2018-03-24

ii. Refine Region: -58.85, -29.25, -58.85, -29.25

iii. Variables:

    a. T = air temperature

    b. U = zonal wind

    c. V = meridional wind

iv. Dimensions: [1, 2, ... , 71, 72]

v. Time: 00:00 - 21:00

vi. Grid: [Default, Default]

The vertical temperature (panel (a)) and horizontal wind (panels (b) and (c)) profile for the input fields of the MERRA-2 model that extends ∼0 km to ∼75 km at São Martinho da Serra on March 24, 2018, at 03:00 UT is illustrated in Figure 3.19.

Figure 3.19 - Vertical horizontal wind profile obtained from MERRA-2 model for March 24, 2018, at 03:00 UT.

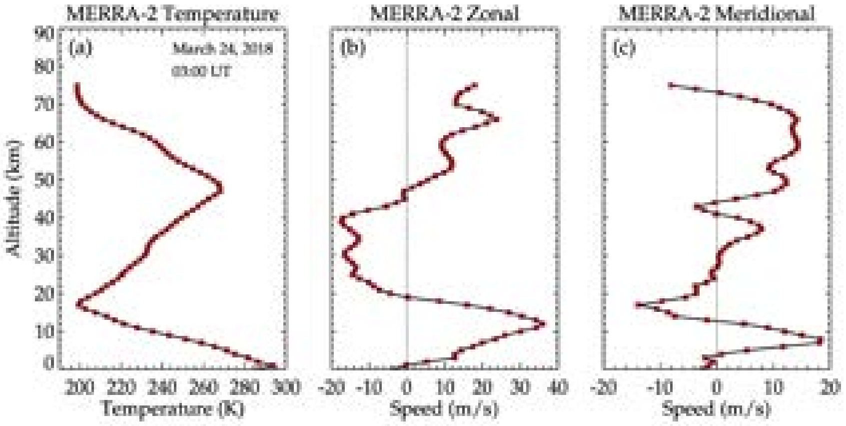

The dark red square sign shows the profile at each 1 km. In panels (a), (b), and (c) the temperature, zonal and meridional wind are presented, respectively.

3.3.3 HWM14

The HWM is an empirical model of the horizontal neutral wind in the upper thermosphere. The model is based on wind data obtained from the Atmosphere Explorer-E (AE-E) and Dynamics Explorer-2 (DE-2) satellites. The zonal and meridional wind components are described by a set of vector spherical harmonics. The spherical harmonics $Y_l^m(\theta, \phi)$ are the angular portion of the solution to Laplace's equation in spherical coordinates where azimuthal symmetry is not present.

The first edition of the model released in 1987 (HWM-87) was intended for winds above 220 km. HWM evolves as time progresses and more upgrades were made by including ground-based observations such as incoherent scatter radar and Fabry-Perot optical interferometers in 1990. Also, the influence of solar and magnetic activities has been included. In the 1993 version (HWM-93), observed winds from meteor and medium frequency (MF) radars were included (HEDIN et al., 1996) and as a result, the altitude range of the model was extended to the Earth's surface.

The HWM-93 depicts the transition from the predominance of diurnal variations in the upper thermosphere to semidiurnal variations in the lower thermosphere. It also depicts the transition from summer to winter current above 140 km and from winter to summer current below 140 km. Significant vertical wind gradient extends up to 300 km in some hours of the day. The model also depicts the main temporal mean variations and tidal components in the lower, middle, and upper atmosphere.

The HWM-14 is the current and updated version of HWM-07. In this version, more observational data are included, thereby producing a more realistic output wind profile. The details on the HWM, from the 1987 version to the 2014 version can be found in Drob et al. (2008) and Drob et al. (2015) and references therein.

The model inputs include day of year (doy), local time, latitude, longitude, altitude, solar flux ($F_{10.7}$), and geomagnetic activity (Ap). The output of the model is the horizontal wind in two components: zonal and meridional. In panels (a) and (b) of Figure 3.20, the vertical profile of the HWM-14 zonal and meridional winds are presented, respectively. These profiles were obtained for São Martinho da Serra on March 24, 2018, at 02:00 UT.

Figure 3.20 - Vertical horizontal wind profile obtained from HWM14 on March 24, 2018, at 03:00 UT.

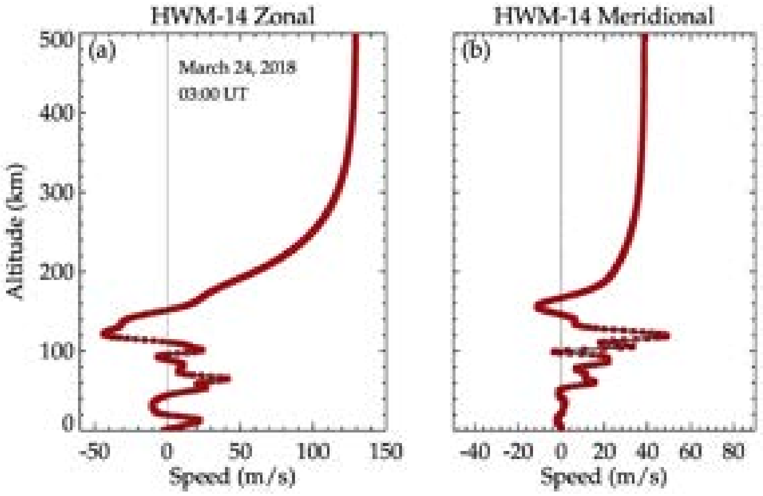

The dark red squares shows the profile at each 1 km. In panel (a) the zonal wind is shown whereas the meridional wind is shown in panel (b).

4 GENERAL METHODOLOGY

In the present chapter, the methodology developed to estimate the concentric gravity waves parameters will be discussed, as well as the determination of the center and radius of CGWs observed. The database needed for the ray tracing and the implementation of the ray tracing model used to study the propagation of gravity waves in the atmosphere and to locate their possible source location will also be discussed. Also, in this chapter, discussions on the methodologies employed to analyze other co-located observations will be made.

4.1 All-sky image preprocessing

An airglow image can be described in terms of an equally spaced array of pixels where each pixel can be identified as a matrix. The value corresponding to each pixel quantifies the luminous intensity associated with grayscale in the position of the image (WEEKS, 1996). To analyze original airglow images and extract gravity waves parameters, image preprocessing is required. The technique used in the preprocessing of all-sky airglow images in this work is similar to the technique described by Garcia et al. (1997), Maekawa (2000), Vargas (2003), Wrasse (2004), Vargas et al. (2007), and Bageston (2010). A detailed step-by-step description of airglow image preprocessing is illustrated in Section 4.1.1.

4.1.1 Image preprocessing

The following procedures outline the step-by-step preprocessing of original airglow images.

a. The first step in airglow image preprocessing is the alignment of the top of the image to the geographic north. In this case, the image undergoes a rotational transformation under a suitable angle such that the top of the image corresponds to the geographical north. The images are calibrated by using the stars in each image as a known reference point in the sky. In this way, a series of star positions from the sky map and their corresponding positions in the airglow image is used to determine the lens function. The lens function is then used to map each pixel from the original image to a new spatial coordinate called the geographic coordinate.

   The complete algorithm for this coordinate transformation can be found in Appendix B of Medeiros (2001a). Wrasse and Rodrigues (2008) developed computer software using the above-described procedure presented by Medeiros

(2001a). This software performs all steps of airglow image calibration, making the process more fast and easy to run.

b. After the alignment of the image to the geographic north, the stars are removed from the images. The removal of the stars is necessary due to their accentuated luminosities which cause possible contamination in the wave spectrum at high frequencies (MAEKAWA, 2000).

c. Next to steps **a** & **b**, the original images are unwarped. Unwarping is the process of projecting a dome-like shape of the airglow images to a square-like planar projection. Unwarping is necessary because the projection of the night sky over the CCD camera is distorted due to the shape of the fisheye lens. The unwarping is used in this case to make zenithal adjustment and also correct the edge distortion effect introduced by the fisheye lens. However, the CCD camera distortion problem had been resolved by Hapgood and Taylor (1982) and Garcia et al. (1997) through an algorithm that maps the original image onto new coordinates that relate distances between pixels in the image to physical distances in the airglow layer. To unwarped the images, the peak of the hydroxyl (OH) emission layer is assumed to be around an altitude of 87 km. In this new coordinate system, the zenith is located at the origin of the image, with x and y being the axes in the east-west (zonal) and north-south (meridional) coordinates, respectively.

d. The fluctuation fraction of the intensity of the unwarpped images in step **c** is estimated. The fluctuation fraction provides a relative percentage measure of how much the intensity in a given pixel varied in a given instant. Since the imager does not provide absolute values of luminous intensity, the fraction of the intensity fluctuation is a good parameter as far as we know the variation of the luminosity of the airglow layers. The fraction calculation of the intensity fluctuation is determined using Equation 4.1 (GARCIA et al., 1997):

$$\frac{\Delta I}{\bar{I}} = \frac{I - \bar{I}}{\bar{I}}, \tag{4.1}$$

where I represents the luminous intensity contained in any image of the night sky and $\bar{I}$ is the average image of the whole night.

e. The images are then filtered using bandpass filters. Conveniently, the application of digital filters to images is made to emphasize gravity waves of a certain scale. For example, to observe small-scale gravity waves, high-pass filters (i.e., wavelengths greater than 100 km) can be used to remove medium-scale gravity waves and other large-scale spectral contamination.

The construction of algorithms to carry out the above-described procedures does not necessarily need to follow this order. The step-by-step image preprocessing steps are illustrated in Figure 4.1. Panel (a) of Figure 4.1 is the calibrated original airglow image taken on the night of March 24, 2018, at 02:51:11 UT. The image in Figure 4.1(a) after the star removal procedure (item **b**) is presented in panel (b). In panel (c), the unwarped (linearised) image (item **c**) is shown.

Figure 4.1 - Illustration of airglow image preprocessing sequence.

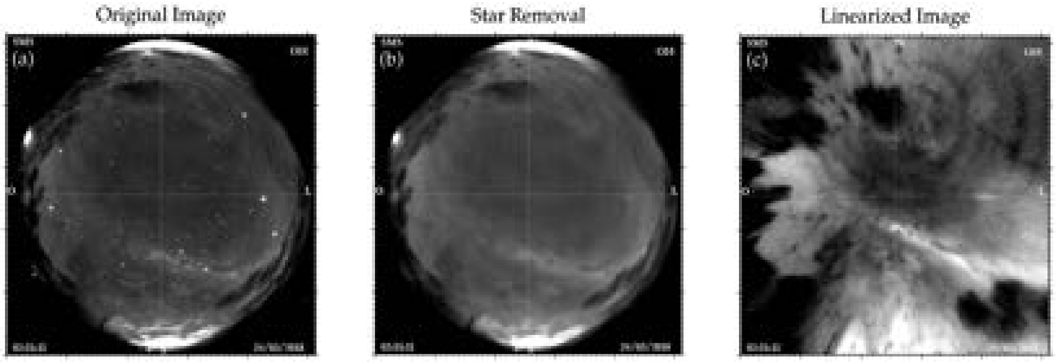

The step-by-step preprocessing technique was applied to OH images on the night of March 24, 2018, at 02:51:11 UT. Panels (a), (b), and (c) show the original image, image without stars, and unwarped image, respectively.

Figure 4.1(a) shows the OH airglow image in the standard coordinate, aligned with geographic north together with the observed stars and planets, which appear to be the small white dots. The Milky Way is the cluster of stars (which appear as a white strand) extending across the entire image from the southeast to the northwest direction. The cloud passing over the field of view of the imager are the dark structures at the western, southeastern, and northern parts of the image. As a result of these structures, the contrast of the image has been adjusted. In panel (b), the image after the star removal process is presented. It can be seen that the small white dots have been removed almost entirely. Finally, in panel (c), the same image as panel (b) but the unwarped (linearized) version. The white lines extending vertically and horizontally illustrate north-south and east-west directions.

4.1.2 Spectral analysis

The spectral analysis is a two-dimensional discrete Fourier transform (2D-DFT) based technique. In this work, the technique is mostly applied to regions on OH images with visible propagating waves across the zenith of the all-sky imager to extract the parameters of the wave. Wave parameters such as propagation direction (ϕ), phase speed (c_H), horizontal wavelength (λ_H), and period (τ) are obtained.

The left panel of Figure 4.2 shows a linearized OH image with CGW observed on the night of March 24, 2018 at 02:51 UT. In the right panel, regions of interest (ROI) with dark and bright visible concentric bands are depicted.

Figure 4.2 - Preprocessed airglow image with concentric wavefronts and regions selected for spectral analysis application.

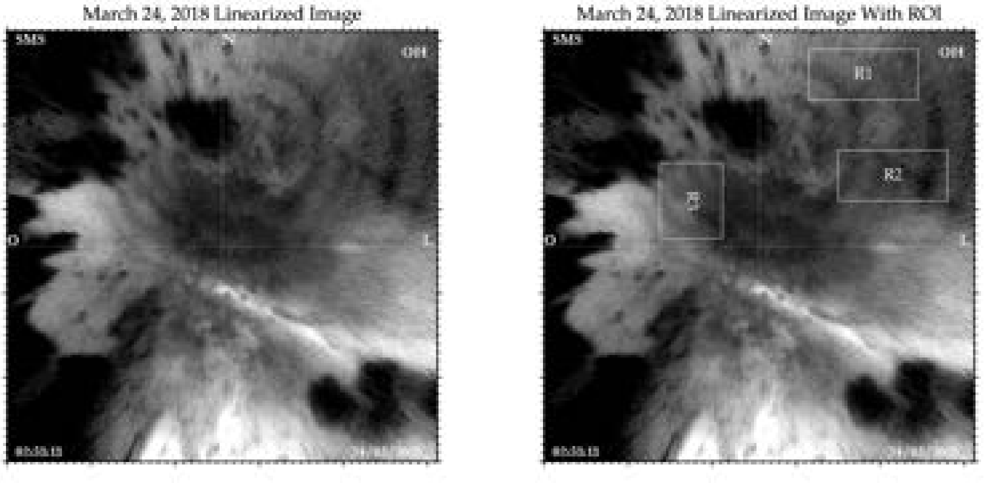

Illustration of all-sky images with visible concentric dark and bright bands (left panel). In the right panel, regions of interest (R_1, R_2, and R_3) selected to be used in the spectral analysis.

As seen in Figure 4.2, there are visible circular dark and bright bands present in the northeastern and the northwestern part. The southern part of the image has been contaminated by the Milky Way and clouds. This contamination has significantly altered the contrast of the image in that part, therefore the visibility of the concentric bands is reduced. The selected ROI where spectral analysis will be applied is also shown. Regions 1, 2, and 3 are labeled R_1, R_2, and R_3, respectively.

To apply spectral analysis, the identified regions of interest with visible concentric bands in the Figure 4.2 are used to construct time-series images. The time-series images constructed in this study contain 10 images in a time sequence. As mentioned earlier the temporal resolution of the images is $\sim$1 minute. So, using 10 images imply observation of 10 minutes of CGW activities.

Figure 4.3 shows a time series of images of 10 minutes images at a time interval of $\sim$1 minutes. It is important to mention that the spectral analysis is applied to a region at a time. For instance, to extract wave parameters from R_1, the spectral analysis was applied to only R_1 without selecting R_2 and R_3.

Figure 4.3 - Time series of 10 OH images used for spectral analysis.

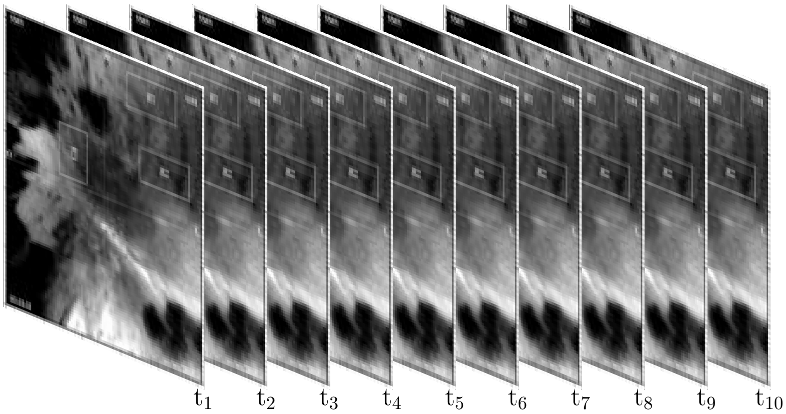

After constructing the image time series from 02:40:23 UT to 02:52:32 UT on March 24, 2018, we applied the spectral analysis. First, a two-dimensional discrete Fourier transform (2D-DFT) is applied to the selected regions in the image time series using

$$\mathcal{F}(k,l) = \sum_{x=0}^{M-1}\sum_{y=0}^{N-1}\left[exp\left(-i\frac{2\pi xk}{M}\right)\right]\left[exp\left(-i\frac{2\pi yl}{N}\right)\right]f(x,y), \tag{4.2}$$

where $\mathcal{F}(k,l)$, is the Fourier transform of the function $f(x,y)$, k, l are the zonal and meridional wavenumbers, $M \times N$ is the dimension of the analyzed image.

Next, the power spectrum in two dimensions was computed by the quadratic module, $\left|\mathcal{F}(k_x,k_y)\right|^2$, of the 2D-DFT estimated using Equation 4.2. The computed power spectrum is shown in Figure 4.4

A property of power spectrum is its symmetrical nature about the origin, that is, $\left|\mathcal{F}(k,l)\right|^2$ = $\left|\mathcal{F}(-k,-l)\right|^2$. As a result, there is an ambiguity of 180° in the direction of wave propagation. Therefore, only half of the resulting spectrum contains the desired information whereas, the other half is redundant. Hence, the propagation direction of a wave can not be determined directly through the power spectrum. A simple way to solve this problem is through the animation of a sequence of images that contains the wave event (WRASSE, 2004).

Figure 4.4 - Two-dimensional power spectrum result obtained from 10 images time series obtained from the Hydroxyl (OH) airglow on March 24, 2018 between 02:40:23 and 02:52:32 UT.

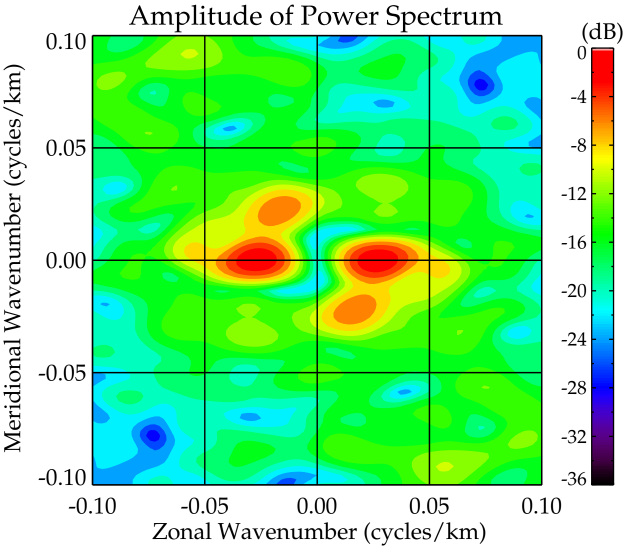

Positive wavenumbers represent the northward propagation direction for the meridional component and the eastward direction for the zonal component.

The ambiguity in the propagation direction using the power spectrum can be resolved by computing the cross-spectrum between two successive images. Contrary to the power spectrum, the cross-spectrum provides a complex value that contains information on the amplitude and phase of the two signals (BLOOMFIELD, 2004). Considering two successive images, $f(x, y)$ and $g(x, y)$, the cross-spectrum between the two images is given by:

$$\mathcal{C}(k,l) = \mathcal{F}(k,l)\mathcal{G}^*(k,l) \tag{4.3}$$

where $\mathcal{C}(k,l)$ is the cross-spectrum between the two images, $\mathcal{F}(k,l)$ and $\mathcal{G}(k,l)$ represent the discrete Fourier transform of the images respectively. $\mathcal{G}^*(k,l)$ represents the complex conjugate of $\mathcal{G}(k,l)$. If (n) images are selected, the cross-spectrum will be computed for $n-1$ images, and the resultant spectrum will be the average of the set of $n-1$ computed spectra. The amplitude and phase computed from the average cross-spectrum of the image time series presented in Figure 4.3 are shown in Figure 4.5.

In the left and right panels of Figure 4.5 show the amplitude and phase, respectively after applying cross spectrum to the image time series shown in Figure 4.3. We observe that

Figure 4.5 - In the left panel, the amplitude estimated from the cross-spectrum is shown whereas, the resultant phase is shown in the right panel.

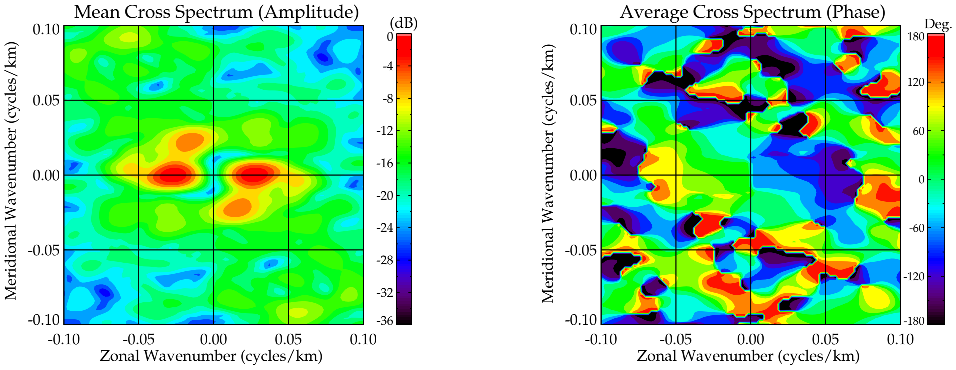

the amplitude of the cross-spectrum is the same result as the power spectrum shown in Figure 4.4. In addition to the amplitude, the cross-spectrum also provides the phase of the spectrum shown in right panel of Figure 4.5. In the case where $\Delta\varphi < 0$ for k_{max} and l_{max}, the unambiguity in the gravity waves propagation direction is shown in Figure 4.6.

Figure 4.6 - The amplitude of unambiguous cross-spectrum.

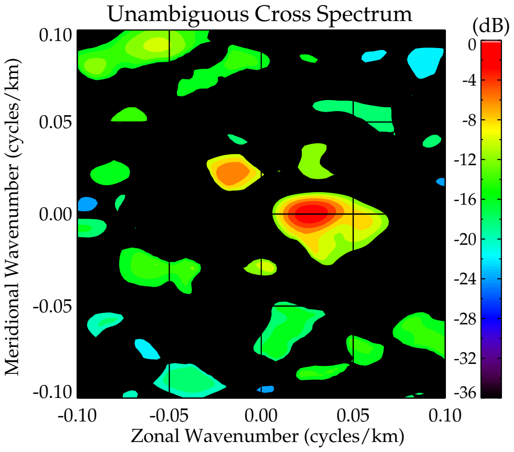

The amplitude of the wave was estimated from the modulus of the cross-spectrum using $\left|\mathcal{C}(k,l)\right|$ and the phase is computed by:

$$\varphi_{(k,l)} = arctg\left\{\frac{Im\mathcal{C}(k,l)}{Re\mathcal{C}(k,l)}\right\}, \qquad -\pi \leq \varphi \leq \pi \tag{4.4}$$

The determination of wave parameters (λ_H, τ, c_H, and ϕ) using cross-spectrum had been described by Maekawa (2000). From the cross-spectrum:

i. The zonal (k) and meridional (l) wavenumbers of gravity waves are the k and l corresponding to the maximum amplitude of the cross-spectrum.

ii. Using the zonal (k) and meridional (l) wavenumbers, and the phase ($\varphi_{(k,l)}$), the observed phase velocity is given by

$$c_H = \frac{1}{\sqrt{k^2 + l^2}} \times \frac{\Delta\varphi_{(k,l)}}{360^\circ} \times \frac{1}{\Delta t}, \tag{4.5}$$

where Δt is the time difference between two successive images.

iii. The horizontal wavelength λ_H of the wave was determined directly from the zonal (k) and meridional (l) wavenumbers using the relation:

$$\lambda_H = \frac{1}{\sqrt{k^2 + l^2}}. \tag{4.6}$$

iv. Next, to estimate the observed period of the gravity wave, the phase velocity and the horizontal wavelength are used as inputs in

$$\tau = \frac{\lambda_H}{c_H}. \tag{4.7}$$

In the case of availability of simultaneous gravity wave and background wind measurements in the OH emission layer altitude, the intrinsic period and phase velocity can be estimated. The intrinsic phase velocity can be estimated using $c_{H_I} = c_H - \vec{u}$, where $\vec{u}$ is the wind in the propagation direction of the wave. Using c_{H_I}, the intrinsic period is

$$\tau_I = \frac{\lambda_H}{c_{H_I}} \tag{4.8}$$

v. Finally, the propagation direction of the wave can be determined from

$$\phi = tan^{-1}\left[\frac{l(l_{max})}{k(k_{max})}\right], \tag{4.9}$$

where k_{max} and l_{max} are the maximum wavenumbers in the x and y directions.

Table 4.1 shows the wave parameters determined using the above described spectral analysis procedure. The horizontal wavelength (λ_H), propagation direction (ϕ), phase velocity (c_H), an period (τ) of the circular gravity waves parameters were obtained using spectral analysis.

Table 4.1 - Parameters of circular gravity waves determined using spectral analysis.

Region (R)	# of images	λ_H (km)	τ (min)	c_H m/s	ϕ (°)
R_1	10	30.80 ±1.30	6.90 ±0.3	74.40 ± 4.3	031.0
R_2	10	31.32±1.05	7.20±0.5	72.50± 2.7	095.5
R_3	10	30.56±1.00	7.06±0.3	70.63± 3.1	198.0

4.2 Composition of database for ray tracing model

A ray tracing model is a numerical tool used in conjunction with observed wave parameters and background wind and temperature to study the propagation of CGWs in the atmosphere and also to locate the possible source locations of CGWs. The ray tracing technique is used in this work because of its capability of incorporating background conditions to simulate a more realistic atmosphere through which the propagation of the wave will be studied. Therefore, using the ray tracing model to investigate the propagation of CGWs to their sources, it is necessary to know:

i. the physical characteristics of the observed CGWs at a given position and time;
ii. the spatial and temporal evolution of thermodynamic variables of the atmosphere and;
iii. the spatial and temporal dynamics of the background wind.

As discussed in Chapter 3, the simultaneous observation of several phenomena such as wind and temperature during the individual CGW event allowed the creation of database to extensively investigate the source of each CGW event. Regarding ray tracing, the temperature, and wind are important background parameters needed to study the CGWs propagation in the atmosphere. Base on this, observed and model winds and temperatures during each CGW event were used to create a database in space and time, which will be used in the ray tracing model.

Two different wind and temperature model data were used to create the database in this work. The model winds were obtained from the Modern-Era Retrospective and analysis for Research and Application - Version 2 [MERRA-2] (GELARO et al., 2017) and Horizontal Wind Model 2014 (HWM-14) (DROB et al., 2015). The model temperatures on the other hand were obtained from MERRA-2 and the Naval Research Laboratory Mass-Spectrometer-Incoherent-Scatter 2000 (NRLMSISE-00) empirical atmospheric model (PICONE et al., 2002). However, observed wind from meteor radar and temperature from TIMED/SABER, and radiosonde soundings were also included in the database if there are data available.

The database created using the wind and temperature profiles from these models has an altitude range from 0 - 500 km. However, the altitude range for MERRA-2 wind and temperature extended from 0 - 75 km, so we concatenated the MERRA-2 wind with HWM-14 wind. The concatenated wind and temperature were interpolated at each 1 km altitude ranging from near the surface of the ground to 500 km. The MERRA-2 and NRLMSISE-00 temperatures were only concatenated if the variations in their profiles are large. For a CGW event with SABER and radiosonde temperature observation, the SABER, radiosonde, and NRLMSISIE-00 temperatures were concatenated.

There are sometimes discontinuities present at the concatenation altitude of the two or three different profiles, which may be due to the dynamics in space and time of each profile. To minimize these discontinuities at the altitude of concatenation, the following steps were taken:

i. an altitude range of 10 km is set. This range extends from the point where the two profiles will be concatenated. This range for the two profiles must be within the same altitude range.

ii. the two profiles are interpolated at each kilometer to avoid the bias caused by different vertical resolutions.

iii. the difference between the profile at each kilometer within the set range was estimated, then the altitude with the smallest difference is chosen as the concatenation altitude.

iv. finally, the concatenated profile was smooth at every three points.

A pictorial description of the above-listed concatenated procedures is shown in Figure 4.7 using observed temperature profiles on March 24, 2018, from radiosonde and SABER. The radiosonde profile was taken at Santa Maria [53.79°W, 29.69°S] at 00:00 UT whereas the SABER profile sounding was at -62.44°W, 29.65°S around 01:00 UT. The black solid line in panels (a) and (b) of Figure 4.7 shows the observed temperature profiles of radiosonde and SABER, respectively. Their interpolated profiles at each one kilometer are shown in the red dashed lines. In panel (c), the concatenated profile of the observed and interpolated profiles are presented. The final concatenated profile smoothed at every three-point is shown in panel (d) of Figure 4.7.

Figure 4.7 - A pictorial description of the concatenation procedure of observed temperature profile of radiosonde and SABER.

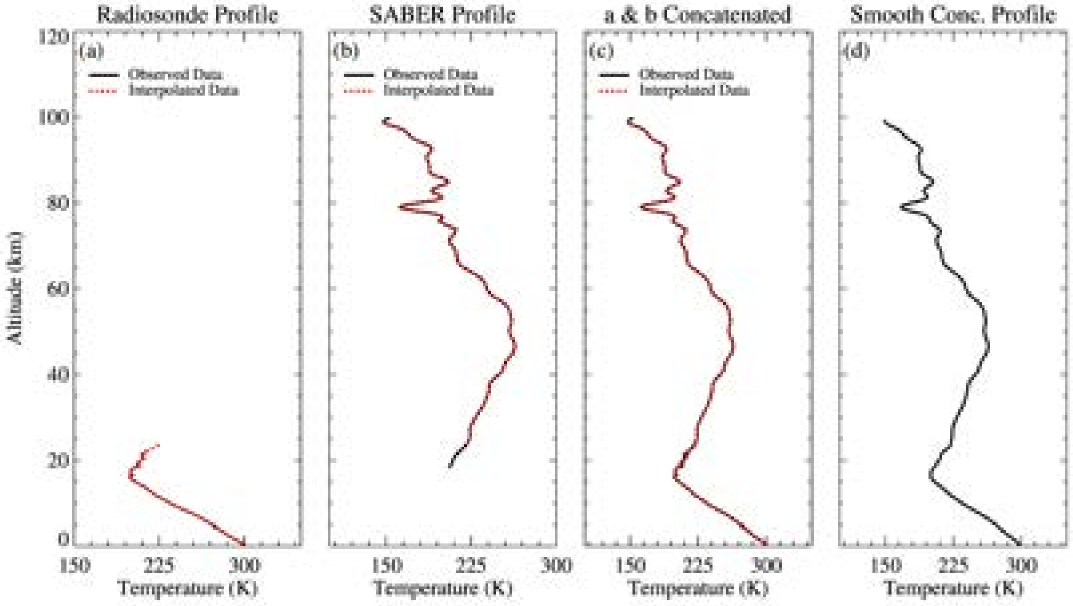

In panel (a) is the radiosonde profile, panel (b) is the SABER profile, and panel (c) is the concatenated profiles from (a & b). In panel (d) the final concatenated profile smooth at each three-point is shown. The black solid line and the red dashed lines in panels (a), (b), and (c) show the observed and interpolated profiles. respectively.

Note that MERRA-2 has a temporal resolution of 3 h, but since temporal resolution of an hour is needed in the database, interpolation in time was performed. This makes the temporal resolution of the wind and temperature database used in the ray tracing model to be an hour and vertical spacing of one kilometer. These variables are longitude and latitude dependent. Here, the vertical wind were assumed to be zero. Since the temporal resolution of the meteor radar wind profile is one hour, the same resolution was used for the database. It is also important to mention that during the iteration process, when running the model, the spatial and temporal resolution of the wind and temperature changes depending on the temporal step size of the model. The temporal step size is described in the ray tracing methodology (see Section 4.3)

Similarly, the concatenation procedure applied to the temperature profiles was employed for the horizontal wind profiles. The horizontal wind from MERRA-2 and HWM-14 is divided into two components, zonal (east-west) and meridional (north-south) directions. The complete database was set up to cover the entire year with a 1 hour temporal resolution, 0.5° × 0.625° horizontal resolution, and 1 km vertical resolution. The horizontal resolution of 0.5° × 0.625° was adopted from the MERRA-2 model. Vertically, the database extends from the surface to an altitude of 500 km.

The methodology used to obtain the temperature and wind profiles used in the ray tracing model will be discussed in the Sections 4.2.1 and 4.2.2.

4.2.1 Temperature profile

The temperature profiles include measurements from the TIMED satellite by the SABER instrument and radiosonde. The CGW events where there are no observations, the temperature profiles were obtained from MERRA-2 and NRLMSISE-00. The methodology used to create the temperature database is described in detail in this Section (i.e., Section 4.2.1). Note that during the CGW event when there are temperature observations, the model data were not used.

4.2.1.1 SABER temperature

The SABER instrument takes temperature measurements from ∼12 km to altitudes close to 120 km. However, the exact altitude of the top and bottom of the profile varies according to the limb measurements performed by the instrument. To standardize the measurements of all temperature profiles from this instrument, the cutting altitudes were chosen below ∼12 km and above 110 km. In this way, the temperature profiles measured by the SABER instrument used in this work are between these thresholds.

Figure 4.8 illustrates an average temperature profile used in the database for the CGW event on September 8 - September 9, 2016. The average profile is indicated by the solid thick black line. The error bars represent the standard deviation of the mean, calculated from six selected profiles on that day (thin solid lines in red, dark red, orange, green, blue, and dark blue). The largest variations in the measurements are observed in the MLT region because the atmospheric fields in this region are affected by short-term changes. Small variations are observed in the lower part of the profiles when compared to the MLT region.

The selection of the profiles used to estimate the average profile followed the temporal criterion of ± 6 hours the observation time of the CGW. Regarding the distance from

Figure 4.8 - Preprocessing of SABER kinetic temperature profiles.

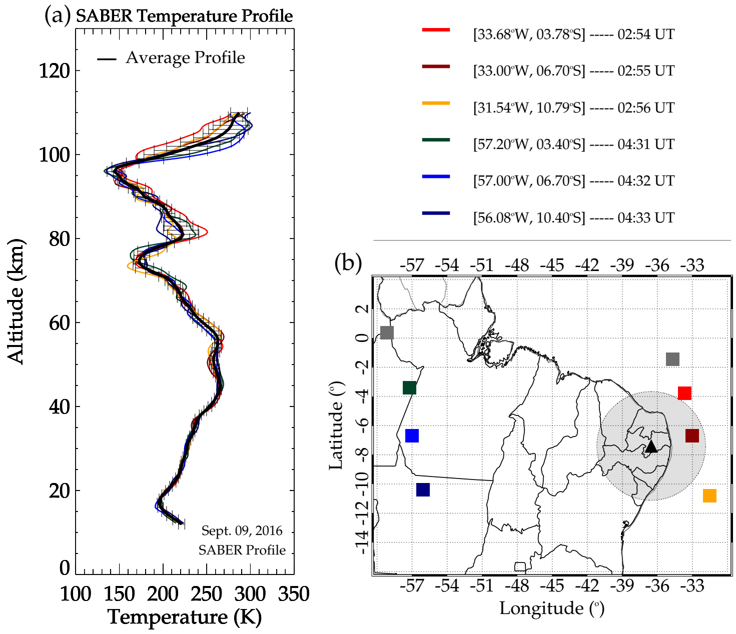

Panel (a) is the kinetic temperature profile from six SABER soundings. The position of each profile is shown by the corresponding colored squares in panel (b). The position and time of the sounding are defined in the legends. The gray squares are not considered in the temperature profile in (a). The black solid profile in panel (a) is the average profile of the six with the error bars being the standard deviation of their mean.

the observatory, temperature measurements taken within a grid of 15° longitude × 15° latitude centered at São João do Cariri were taken. The spatial range also depends on the variations in temperatures.

In panel (b) of Figure 4.8, the spatial grid used to select the temperature profiles is presented, where each corresponding colored square represents the location of the satellite sounding during the wave event. The universal time for each sounding is shown in the legends corresponding to each color of the squares. The triangle represents the location of the São João do Cariri airglow observatory and the gray shaded region is the field-of-view of the all-sky imager.

4.2.1.2 NRLMSISE-00 temperature

The NRLMSISE-00 model was used to obtain neutral temperature, total mass density, and density scale height as described in Section 3.3.1. However, among these three parameters, the temperature was considered in the databank where the NRLMSISE-00 and MERRA-2 temperature profiles were concatenated.

Figure 4.9 illustrates a vertical temperature profile of the NRLMSISE-00 model that extends from the Earth's surface to an altitude of ~500 km at São Martinho da Serra on March 24, 2018, at 02:00 UT. The temperatures calculated by this model were included in the temperature database for altitudes above 65 km altitude. This altitude range between 65 to 500 km is indicated by the gray shaded region. This gray shaded region emphasizes the altitude range for the NRLMSISE-00 temperature to be used for the concatenation and below this altitude (i.e., the white region) will be the range for the MERRA-2 temperature. In this profile, the model does not predict significant changes in temperatures throughout the day, however, the model predicted good day-to-day variation during the individual CGW events.

Figure 4.9 - Vertical temperature profile obtained from NRLMSISE-00 model for March 24, 2018, at 02:00 UT.

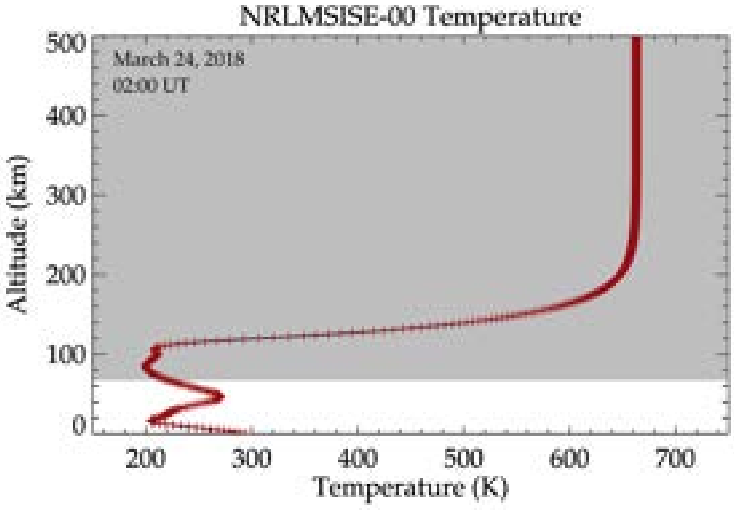

The dark red plus sign shows the profile at each 1 km. The gray shaded region ranges from 65 to 500 km which emphasizes the range of NRLMSISE-00 temperature profile to be used for the concatenation.

4.2.1.3 MERRA-2 temperature

The temperature profile, which is one of the MERRA-2 output parameters (described in Section 3.3.2) used in this work. The MERRA-2 temperature was concatenated with the NRLMSISE-00 temperature profile. The vertical temperature profile for the input fields defined in Section 3.3.2 of the MERRA-2 model that extends ~0 km to ~75 km at São Martinho da Serra on March 24, 2018, at 03:00 UT is illustrated in Figure 4.10. The gray shaded region emphasizes the altitude range of the MERRA-2 temperature profile that will be concatenated with the NRLMSISE-00 temperature profile. The dark red plus ('+')

sign shows the profile at every 1 km.

Figure 4.10 - Vertical temperature profile obtained from MERRA-2 model for March 24, 2018, at 03:00 UT.

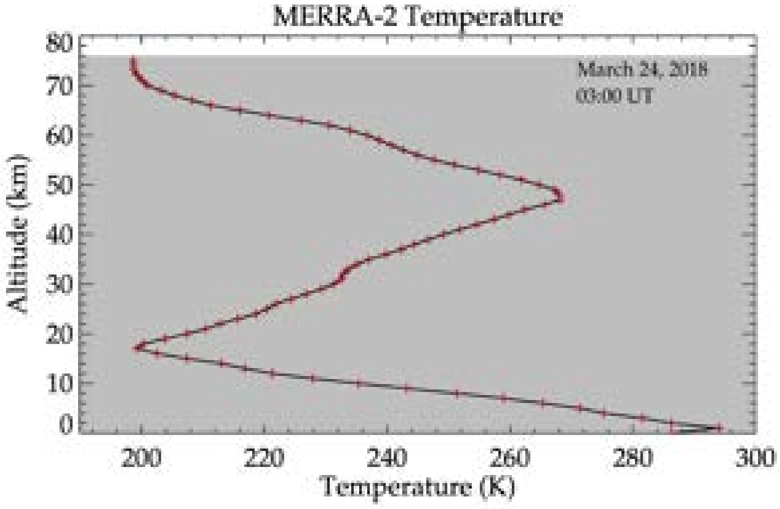

The dark red plus sign shows the profile at each 1 km. The gray shaded region indicates the altitude range of the MERRA-2 temperature profile to be used for the concatenation.

4.2.2 Wind profile

To compose the wind database, measurements from the meteor radar installed at São João do Cariri were used when observations between 80 and 110 km are available. For altitudes between the surface of the ground and 75 km, MERRA-2 winds were used. Between 75 and 80 km and above 100 km, the Horizontal Wind Model 2014 Version was used. It is important to note that for the wind database in this work, only the MERRA-2 and HWM-14 winds were used unless there are observations. In the case of observations during the night of the CGWs event, the database is modified to include the observed winds if necessary.

4.2.2.1 MERRA-2 horizontal wind

Similarly, using the same input field defined for the MERRA-2 temperature in Section 3.3.2, the horizontal winds for the same location and time were obtained. The output horizontal wind profile is shown in Figure 4.11. In panels (a) and (b), the vertical profile of MERRA-2 zonal and meridional winds are shown, respectively. The gray shaded regions indicate the altitude range for the MERRA-2 winds. The vertical dotted lines at zero are used to demarcate the directions of the wind. For zonal wind directions: positive values are eastward and negative values are westward. For the meridional wind, the positive values for northward and the negative values for southward. The dark red plus sign shows the profile at each 1 km.

Figure 4.11 - Vertical horizontal wind profile obtained from MERRA-2 model for March 24, 2018, at 03:00 UT.

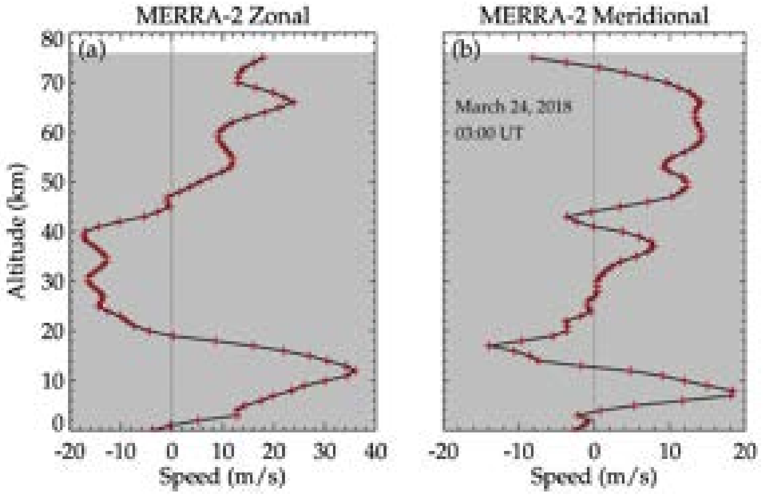

The dark red plus sign shows the profile at each 1 km. In panel (a) the zonal wind is shown whereas the meridional wind is shown in panel (b). The gray shaded region ranging from 0 to 75 km highlights the altitude range for the MERRA-2 wind profile that will be used in the concatenation.

4.2.2.2 HWM-14 horizontal wind

Similarly, the output profile of the horizontal (zonal and meridional) wind presented in Figure 3.20, under the description of the HWM14 (in Section 3.3.3), Figure 4.12 presents the vertical profile of the horizontal wind.

In panels (a) and (b) of Figure 4.12, the vertical profile of the HWM-14 zonal and meridional winds are presented, respectively. These profiles were obtained for São Martinho da Serra on March 24, 2018, at 02:00 UT. The altitude range between 65 to 500 km is indicated by the gray shaded region. The gray shaded region emphasizes the altitude range of the HWM-14 wind profile to be used for the concatenation with the MERRA-2 horizontal wind. Here, the dark red plus sign shows the profile at each 1 km. The vertical dotted line in each panel is used to demarcate the direction of each wind component.

Figure 4.12 - The vertical profile of the horizontal wind obtained from the HWM-14 model for March 24, 2018, at 03:00 UT is presented.

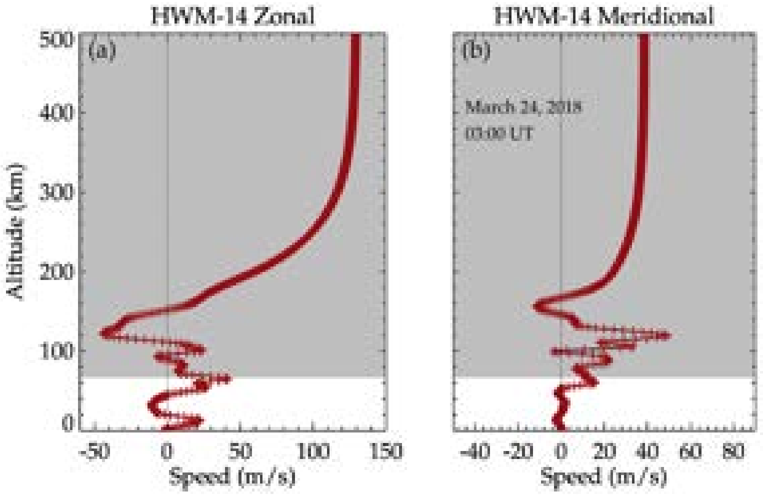

The dark red plus sign shows the profile at each 1 km. In panel (a), the zonal wind is shown whereas the meridional wind is shown in panel (b). The gray shaded region ranging from 65 to 500 km indicate the altitude range of the HWM-14 wind profile to be used in the concatenation. The vertical dotted lines demarcate the direction of the winds. Positive for north and east, and negative for south and west.

4.2.2.3 Wind measured by meteor radar

The meteor radar carried out wind measurements in the mesosphere and lower thermosphere region, approximately between the altitudes of 80 and 100 km at São João do Cariri. There were observations from 2001 to 2008 and 2019 up to date. Between 2009 and 2018, the radar has been disabled due to technical problems, therefore no meteor wind data were available during these years. The wind used in this work was calculated using all meteors that were detected by the radar in a given time interval and altitude as discussed in Section 3.2.2.

The average wind is estimated using the least-squares method considering all echoes from this particular region in the considered time interval (PAULINO, 2012). The time interval used to calculate the wind was two hours and the meteor region was divided into five layers of four kilometers centered on 82, 86, 90, 94, and 98 km, and with overlapping of one kilometer between the layers.

Panel (a) of Figure 4.13 illustrates an example of wind observation on March 11, 2008, at 00:00 UT. The solid dark red line corresponds to the zonal (east-west) wind, while the solid dark blue line represents the meridional (north-south) wind. To obtain wind profile at every one kilometer, linear interpolation and smoothing were performed as it can be seen in panel (b) of Figure 4.13.

Figure 4.13 - Observed meteor radar wind on March 11, 2008, at São João do Cariri.

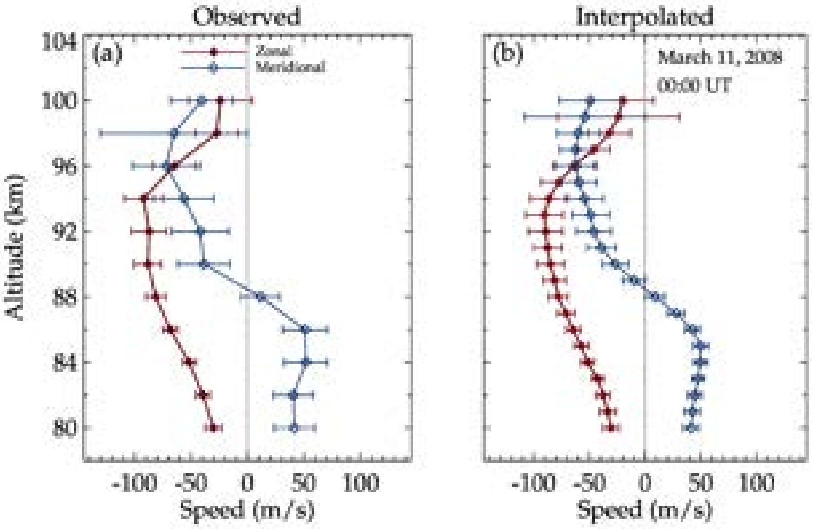

Panel (a) is zonal (solid dark red line) and meridional (solid dark blue line) winds observed on March 11, 2008, at São João do Cariri at 00:00 UT. In panel (b) is the interpolated and smoothed wind presented in panel (a). The error bars represent the standard deviation of the wind at 00:00 UT relative to the mean value.

The main objective of this procedure is to increase the number of points in the database thereby, ensuring realistic wind information. It is also important to reduce the problems in calculating the vertical wind derivatives in regions where there are sudden changes in the wind with altitude.

It is important to mention that there are days where there are no observations at certain times thereby creating gaps in the data. Such a situation is presented in Figure 4.14.

Figure 4.14 - An example of meteor radar wind measurements in the MLT region on March 11, 2009.

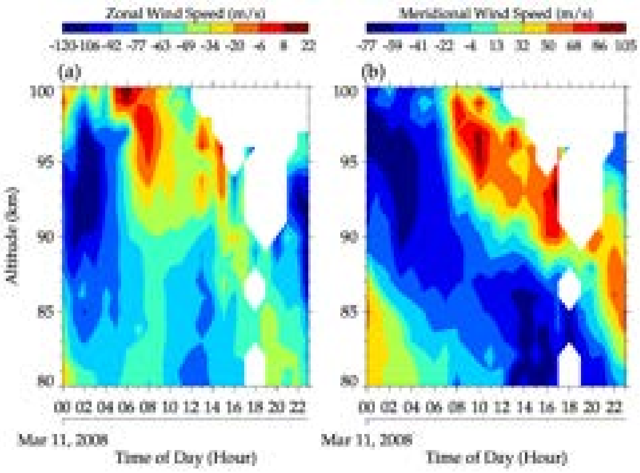

In panel (a), the zonal wind obtained by meteor radar is presented and in panel (b), the observed meridional wind is presented.

In panels (a) and (b), gaps can be seen in the winds between 13 and 21 hours. These gaps were filled by a bilinear interpolation (BOVIK, 2009) (in time and altitude). The result after the interpolation is shown in Figure 4.15. The final result has a resolution of one kilometer in altitude and a temporal resolution of one hour.

Figure 4.15 - Interpolated and smooth horizontal wind presented in Figure 4.14.

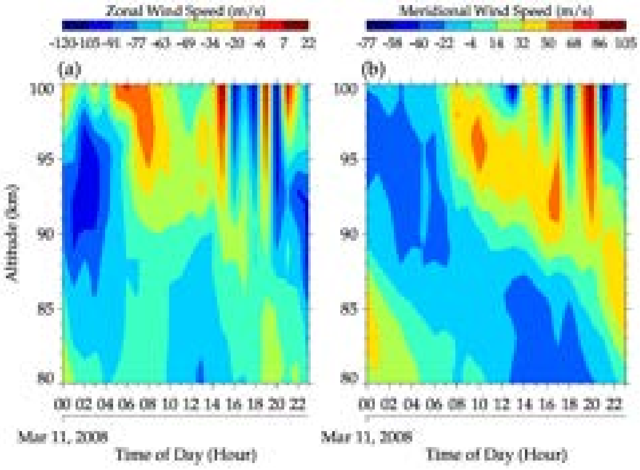

Panel (a) is an interpolated and smoothed zonal wind in panel (a) of Figure 4.14. The interpolated and smoothed meridional wind in panel (b) of Figure 4.14 is shown in panel (b). The same type of interpolation used in Figure 4.13 was used in all profiles in this contour plot.

4.2.3 Construction of database

The above-described methodology for each profile of temperature and wind was used to organize the data for concatenation and subsequently for creating the matrix that forms the database. Figure 4.16 shows the constructed database of temperature profiles from MERRA-2 and NRLMSISE-00 for March 2018 at São Martinho da Serra. The lower panel is the contour plot of the MERRA-2 temperature from 0 to 75 km at every hour and 1 km. The middle panel is the NRLMSISE-00 temperature from 65 to 500 km using the same vertical and temporal resolution of MERRA-2. Implementing the concatenation procedure described in Section 4.2, the concatenated profiles of NRLMSISE-00 (gray shaded region in Figure 4.9) and MERRA-2 (gray shaded region in Figure 4.10) for March 2018 from 0 to 500 km was obtained as shown in the upper panel. The color bars show the temperature scale.

With the same order of arrangement as Figure 4.16, the zonal and meridional components of the MERRA-2, HWM-14, and concatenated horizontal wind are presented in Figures 4.17 and 4.18.

Figure 4.16 - Contour plot of MERRA-2 (lower panel), NRLMSISE-00 (middle panel), and Concatenated (upper panel) temperature for march 2018 at São Martinho da Serra.

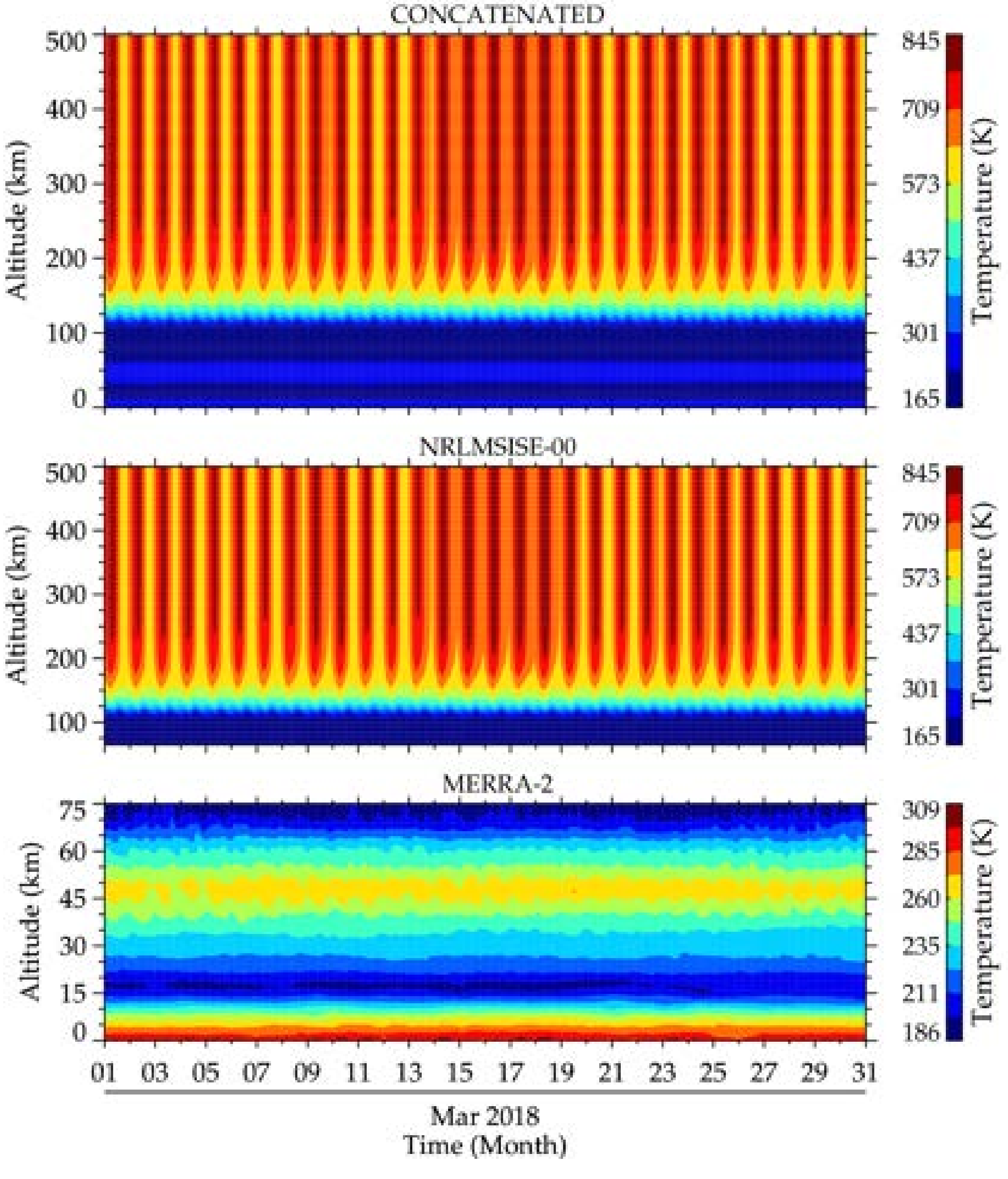

Each profile has a vertical and temporal resolution of 1 km and 1 hour, respectively. The color bars show the temperature scale.

Figure 4.17 - Contour plot of MERRA-2 (lower panel), HWM-14 (middle panel), and Concatenated (upper panel) zonal wind for March 2018 at São Martinho da Serra.

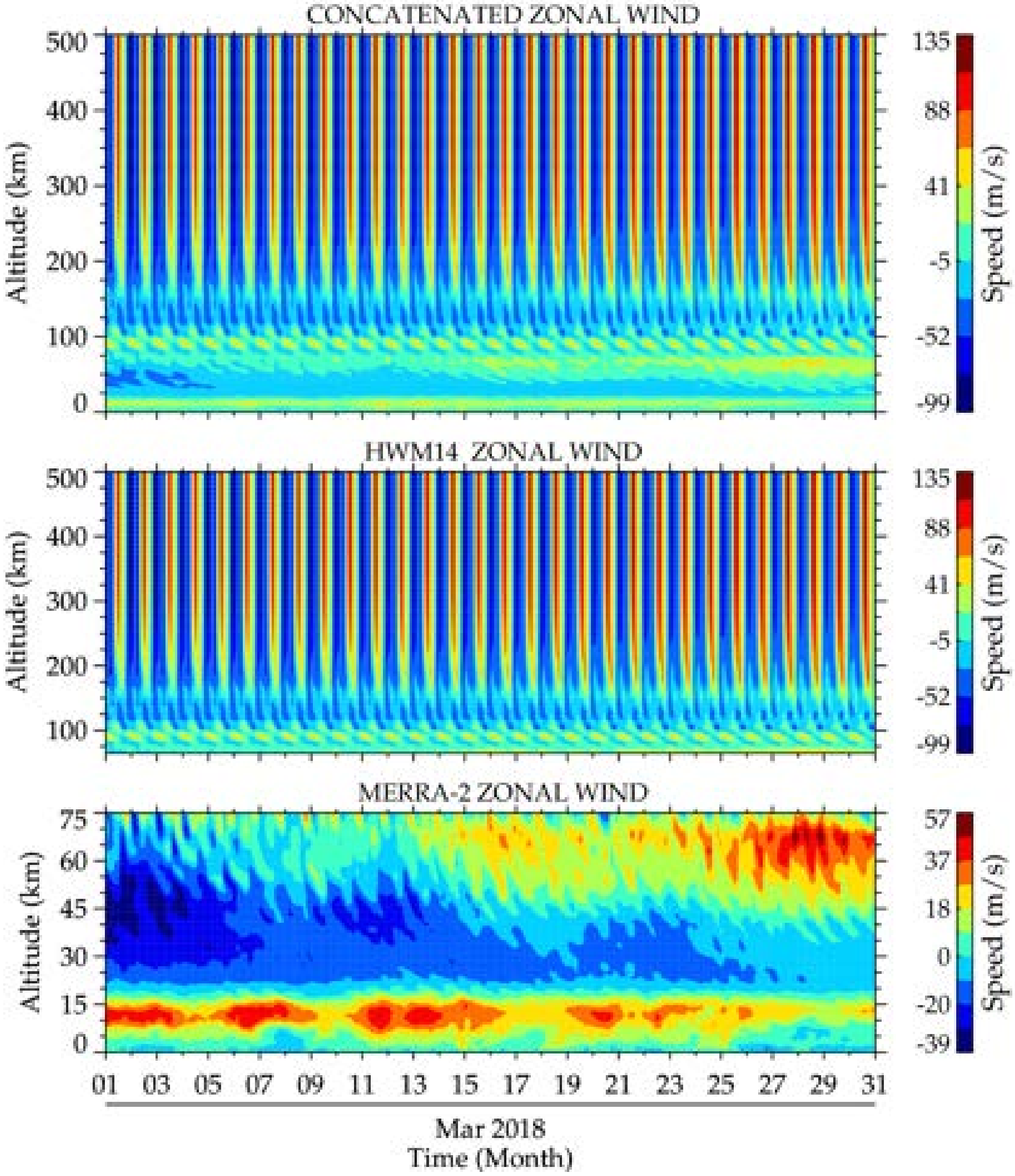

Each profile has a vertical and temporal resolution of 1 km and 1 hour, respectively. The color bars show the wind speed.

Figure 4.18 - Contour plot of MERRA-2 (lower panel), HWM-14 (middle panel), and Concatenated (upper panel) meridional wind for March 2018 at São Martinho da Serra.

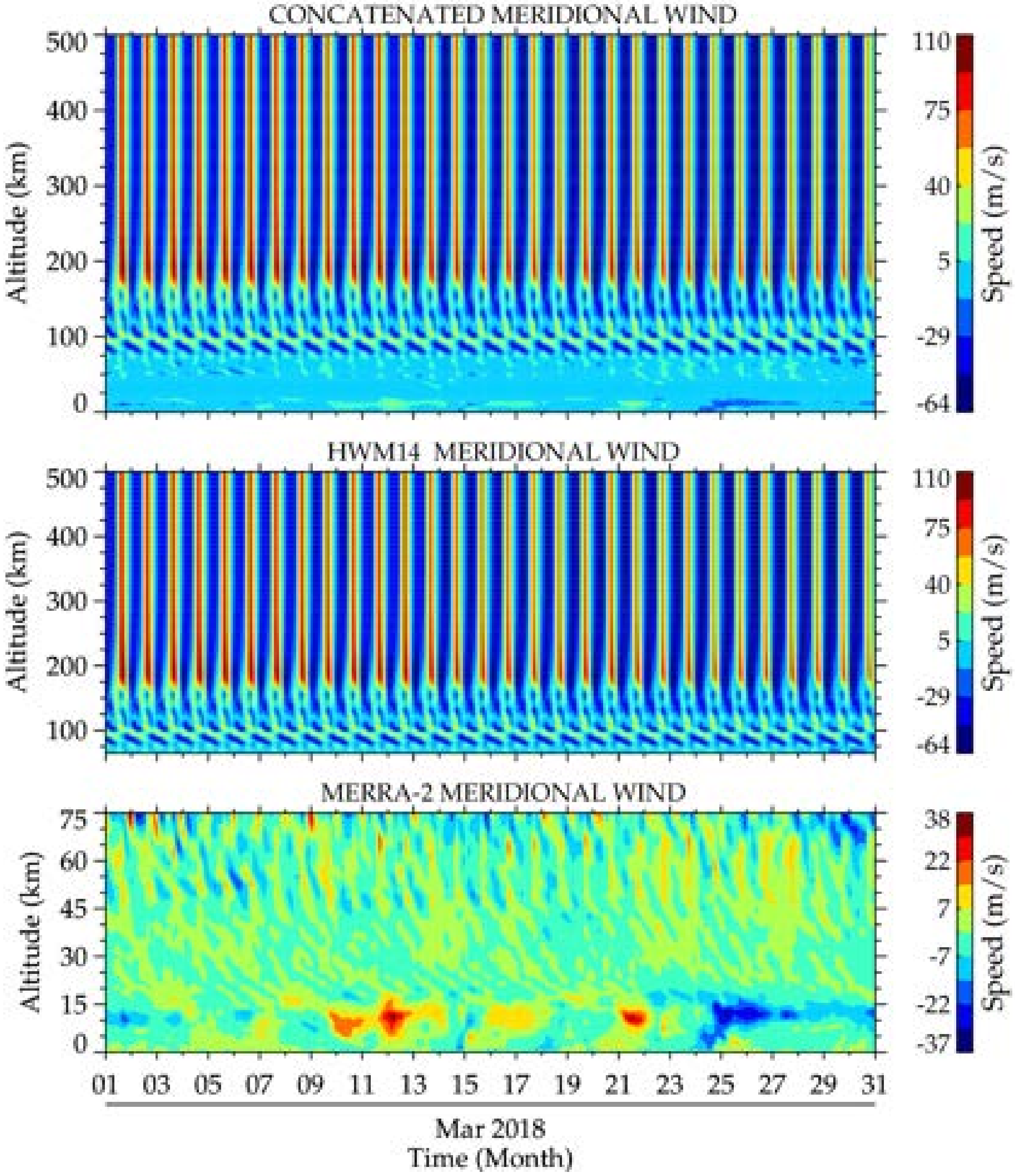

Each profile has a vertical and temporal resolution of 1 km and 1 hour, respectively. The color bars show the wind speed.

4.3 Mathematical description of ray tracing

The ray tracing model used in the studies of wave propagation and the identification of source positions of waves is based fundamentally on the work of Lighthill (1978). If gravity wave (GW) with wavenumber $\vec{k} = (k, l, m)$ is propagating in the atmosphere relative to a background wind, $\vec{V} = (V_1, V_2, V_3)$, then the equations that describe its temporal and spatial evolution are (LIGHTHILL, 1978)

$$\frac{dx_i}{dt} = V_i + \frac{\partial \omega_{ir}}{\partial k_i} = V_i + c_{g_i} \tag{4.10}$$

and

$$\frac{dk_i}{dt} = -k_j \frac{\partial V_j}{\partial x_i} - \frac{\omega_{Ir}}{\partial x_i} \tag{4.11}$$

where $i, j = 1, 2, 3$, indicate the components of the quantities; positions ($\vec{x}$), wavenumber ($\vec{k}$), velocity ($\vec{V}$), $\vec{c_g}$ is the group velocity of the wave and repeated indices imply summation. $\omega_{Ir} = \omega_r - kU - lV$ is the real part of the intrinsic frequency and the dispersion relation given by Equation 2.32 (VADAS; FRITTS, 2005) is:

$$\begin{aligned} \omega_{Ir}^2 + \frac{\nu^2}{4}\left(\vec{k}^2 - \frac{1}{4H}\right)^2 \left(1 - \frac{1}{Pr}\right)^2 \frac{1 + \delta_+ + \frac{\delta^2}{Pr}}{\left(1 + \frac{\delta_+}{2}\right)^2} \\ + \frac{\nu_+ m \omega_{Ir}}{H} + \frac{\nu^2 m^2}{PrH} = \frac{k_H^2 N^2}{\vec{k}^2 + \frac{1}{4H^2}}. \end{aligned} \tag{4.12}$$

Using this dispersion relationship one can estimate the group velocity components (c_{gx}, c_{gy}, c_{gz}) of the wave. These components are given as the derivatives of the Equation 4.12 with respect to the wave vectors (k, l, m), and wave positions (x, y, x) and solving for $\partial \omega_{Ir}/\partial k_i = c_{g_i}$, and $\partial \omega_{Ir}/\partial x_i$, Equations 4.13, 4.14, 4.15 and 4.16 are obtained:

$$c_{gx} = \frac{k}{\omega_{Ir} B}\left[\frac{N^2(m^2 + \frac{1}{4H^2})}{(\vec{k}^2 + \frac{1}{4H^2})^2} - \frac{\nu^2}{2}\left(1 - \frac{1}{Pr}\right)^2 \left(\vec{k}^2 - \frac{1}{4H^2}\right) \frac{(1 + \delta_+ + \frac{\delta^2}{Pr})}{(1 + \frac{\delta_+}{2})^2}\right], \tag{4.13}$$

$$c_{gy} = \frac{l}{\omega_{Ir} B}\left[\frac{N^2(m^2 + 1/4H^2)}{(\vec{k}^2 + \frac{1}{4H^2})^2} - \frac{\nu^2}{2}\left(1 - \frac{1}{Pr}\right)^2\left(\vec{k}^2 - \frac{1}{4H^2}\right)\frac{(1 + \delta_+ + \frac{\delta^2}{Pr})}{(1 + \frac{\delta_+}{2})^2}\right], \tag{4.14}$$

$$\begin{aligned} c_{gz} = &-\frac{m}{\omega_{Ir} B}\frac{k_H^2 N^2}{(k^2 + \frac{1}{4H^2})^2} - \frac{m}{\omega_I B}\frac{\nu^2}{2}\left(1 - \frac{1}{Pr}\right)^2\left(\vec{k}^2 - \frac{1}{4H^2}\right)\frac{(1 + \delta_+ + \frac{\delta^2}{Pr})}{(1 + \frac{\delta_+}{2})^2} \\ &+\frac{m}{\omega_I B}\frac{\nu^4(1 - \frac{1}{Pr})^4}{16H^2\omega_{Ir}^2}\frac{(\vec{k}^2 - \frac{1}{4H^2})^2}{(1 + \frac{\delta_+}{2})^3} - \frac{m}{\omega_I B}\frac{\nu^2}{PrH^2}\frac{1}{\omega_I B}\frac{\nu_+\omega_{Ir}}{2H}, \end{aligned} \tag{4.15}$$

$$\begin{aligned} \frac{\partial \omega_{Ir}}{\partial x_i} = &\frac{1}{\omega_{Ir} B}\frac{k_H^2 N^2}{(\vec{k}^2 + \frac{1}{4H^2})^2}\left(\frac{\partial N}{\partial x_i}\right) + \frac{1}{\omega_{Ir} B}\frac{k_H^2 N^2}{4(\vec{k}^2 + \frac{1}{4H^2})^2}\left(\frac{1}{H^3}\frac{\partial H}{\partial x_i}\right) \\ &-\frac{1}{\omega_{Ir} B}\frac{\nu}{8}\left(1 - \frac{1}{Pr}\right)^2\left(\vec{k}^2 - \frac{1}{4H^2}\right)\frac{(1 + \delta_+ + \frac{\delta^2}{Pr})}{(1 + \frac{\delta_+}{2})^2}\left(\frac{1}{H^3}\frac{\partial H}{\partial x_i}\right) \\ &-\frac{1}{\omega_{Ir} B}\frac{\delta^2\nu^2 H^2(1 - \frac{1}{Pr})^4}{16}\frac{(\vec{k}^2 - \frac{1}{1/4H^2})^2}{(1 + \frac{\delta_+}{2})^3}\left(\frac{1}{H^3}\frac{\partial H}{\partial x_i}\right) \\ &+\frac{1}{\omega_{Ir} B}\left(\frac{\nu_+ m\omega_{Ir} H}{2} + \frac{\nu^2 m^2}{Pr}\right)\left(\frac{1}{H^3}\frac{\partial H}{\partial x_i}\right) \\ &-\frac{\nu(1 - \frac{1}{Pr})^2}{16\omega_{Ir} B}\frac{(\vec{k}^2 - \frac{1}{4H^2})^2}{(1 + \frac{\delta_+}{2})^3}\left[4 + 6\delta_+ + \left(1 + \frac{10}{Pr} + \frac{1}{Pr^2}\right)\delta^2\right. \\ &\left.+\frac{2(1 + \frac{1}{Pr})}{Pr}\delta^3\right]\left(\frac{\partial \nu}{\partial x_i}\right) - \frac{1}{\omega_{Ir} B}\left[\frac{m\omega_{Ir}(1 + \frac{1}{Pr})}{2H} + \frac{\nu m^2}{PrH^2}\right]\left(\frac{\partial \nu}{\partial x_i}\right), \end{aligned} \tag{4.16}$$

$$B = \left[1 + \frac{\delta_+}{2} + \frac{\delta^2\nu^2}{16\omega_{ir}}^2\left(1 + \frac{1}{Pr}\right)^4\frac{(\vec{k}^2 - \frac{1}{4H^2})^2}{(1 + \frac{\delta_+}{2})^2}\right]. \tag{4.17}$$

The solutions to this set of equations (4.12 - 4.16) describe the evolution of a gravity wave in space and time. Equations 4.12 - 4.16 can be found in Appendix C of Vadas and Fritts (2005). To follow the GWs trajectory at each next step in time, a fourth-order Runge-Kutta routine is employed to solve the ray equations (i.e., Equations 4.10 and 4.11) in time. The entire ray tracing model was implemented using the Interactive Data Language (IDL). Since IDL has a built-in fourth-order Runge-Kutta library, it makes IDL a suitable computational language for the ray tracing implementation. However, in this work, only the source positions were investigated. Hence the waves were backward ray traced.

To use the fourth-order Runge-Kutta routine it is necessary to know:

a) the dependent variables at a given time;

b) the respective derivatives at that time instant;

c) the desired time increment;

d) a function that calculates the respective derivatives.

The initial dependent input variables are the position of the wave and the wave vector. At the initial start time of the ray tracing, the position (longitude, latitude, altitude) of the GW is the longitude and latitude of the first visible innermost concentric wavefront in the OH image and the altitude of the OH layer (i.e., 87 km). On the other hand, the wave vectors were obtained from the decomposition of the GW horizontal wavelength into the zonal (east - west) and meridional (north - south) directions. The vertical component of the wavenumber was obtained from Equation 4.12.

The derivatives of the wave position and the vertical wavenumber are estimated directly by Equations 4.12 to 4.16. The derivatives are then passed onto the fourth-order Runge-Kutta routine to determine the new positions and wave vectors for the next time increment.

The determination of the time increment has been well tested, discussed, and validated before the algorithm was obtained. For example, Wrasse et al. (2004) used a temporal increment with a fixed maximum limited of 100 m for GW, whereas Paulino (2012) used 200 m. According to Paulino (2012), for backward ray tracing, the 100 m limit does not cause any computational discontinuity in the vertical profile. However, Paulino (2012) stated that care needs to be taken when forward ray tracing GWs to the Thermosphere-Ionosphere (TI) in order to minimize these discontinuities. For this reason, Paulino (2012) used 200 m. In the model used in this work, the 200 m limit was adapted.

Background conditions of the atmosphere, such as wind, temperature, etc., are included in the model. This is because these conditions control the propagation of gravity waves in the atmosphere. Details of the background atmosphere and their effects on wave propagation had been discussed in Chapter 2. Also, the details of the background wind and temperature profiles used in the model had been given in Section 4.2.

When gravity waves approach the critical level, their vertical propagation becomes slow due to kinematic viscosity and thermal diffusivity. So, by imposing a constant increment in altitude, the temporal increments will be very large. This might cause changes in the variables more than 25% every time increment. To minimize these changes, the GW is not allowed to travel more than 200 m. To proceed to the next time step, two conditions were tested and imposed using the velocity relation, $\Delta z = c_{gz}\Delta t$, to see whether the estimated Δz for the next time step is greater or less than 200 m. If the estimated Δz is less than 200 m, then the new Δz is taken as the next step, but if the estimated Δz is greater than 200 m, then the imposed 200 m step is maintained. The conditions tested to control the time step are similar to the approach adopted by Vadas (2007) and Paulino (2012). Before performing the iteration for the next step, stopping conditions were tested and imposed if any of the conditions are violated. These stopping conditions are:

1. the group velocity should be less than or equal to 0.9 times the speed of sound $c_g \leq 0.9C_s$,
2. the real component of the intrinsic frequency must be greater than zero ($\omega_{Ir} > 0$),
3. the momentum flux at all points of the wave trajectory must satisfy the expression:

   $$R_m > 10^{-15}R_0, \tag{4.18}$$

   where R_m is the momentum flux at each altitude and R_0 is the momentum flux at the reference altitude. The factor 10^{-15} was arbitrarily chosen.
4. the module of the vertical vertical wavelength must be less than viscosity scale $\left(|\lambda_z| < 2\pi[(d\nu/dz)/\nu]^{-1}\right)$. Because $[(d\nu/dz/\nu)]^{-1} \sim H$, a GW must approximately satisfy $\lambda_z < 2\pi H$ where dissipation becomes important in the thermosphere; this is found to be satisfied for GWs of most importance in the thermosphere (VADAS, 2007).

It is important to note that items 3 and 4 are important when forward ray tracing the waves into the thermosphere. To determine the next time increment of the ray equation, the GWs must satisfy all the above-listed conditions. If any of these conditions is violated, the procedure will be interrupted and all calculations automatically saved. The wave positions and vectors together with all relevant calculated variables are saved at the end in a binary file format with a "*.rt*" extension. The results are graphically represented later. Further details on the stopping conditions are discussed in Vadas (2007) and Paulino et al. (2012b).

The above procedure repeats until the GWs encounter a stopping condition, that is, it does not achieve physical conditions to propagate or lose its energy through dissipation due to molecular viscosity and thermal diffusivity. The model can be set to run two modes, (a) zero wind (ZW) and (b) model wind (MW). In the ZW mode, the model is run without the wind, whereas in the MW mode, the model is run with the database winds. The ray tracing model can be run backward to determine the location of the source position of GWs in the lower atmosphere. On the other hand, the model is run forward to the upper atmosphere to determine where the GWs dissipate.

In addition to the wavenumbers (estimated from the horizontal wavelength and Equation 4.12), wind, and temperature profiles, the period and phase speed of the gravity waves are also part of the input parameters. Dependent and independent variables with their vertical derivatives are computed using the input parameters after which the ray tracing procedure initiates. The procedure of the ray tracing model described above is summarized in the flowchart as shown in Figure 4.19.

As shown in the flowchart in Figure 4.19, the ray tracing model is divided into stages. Stage one is where the GWs parameters, constants, and the wind and temperature datasets are called into the main program file through the file root path. At the initiation stage (i.e., stage two), the defined inputs in stage one are fed into the virtual memory and are organized in a matrix. The initial altitude step is then set, after which other dependent variables are estimated. Next, the stopping conditions are tested and if none is violated, the next time step is computed. Note that so far as none of the stopping conditions is violated, stage two repeats until the GW achieves no physical conditions to propagate or lose its energy. From here, the third stage is implemented when all calculations performed are saved, and the processes are completed. It is important to mention that the white rectangular region in stage two emphasizes the stopping conditions. A sample result of ray tracing results is presented in Figure 4.20. The profiles of the background atmosphere and the ray path of the estimated parameters for this ray tracing result are presented in Figures A.1 and A.2, respectively in the Appendix.

In Figure 4.20, a sample ray tracing result of the concentric gravity waves (CGWs) observed at São Martinho da Serra on March 24, 2018 is presented. The variations of the ray paths in longitude and latitude are presented in panel (a). In panel (b), the variations of ray paths in altitude and latitude are shown, whereas variations in ray paths of longitude and altitude are presented in panel (c). The variations in the ray paths in time relative to altitude are shown in panel (d). The color bar shows the temperature scale of the cloud top brightness temperature image overplotted in panel (a). The input wave parameters of the gravity waves are shown in the lower right-hand corner. The meaning of each symbol is defined in the legends. In all panels, the red dashed-dotted line, red solid line, and blue

Figure 4.19 - Ray tracing model flowchart showing the stages of both backward and forward ray tracing.

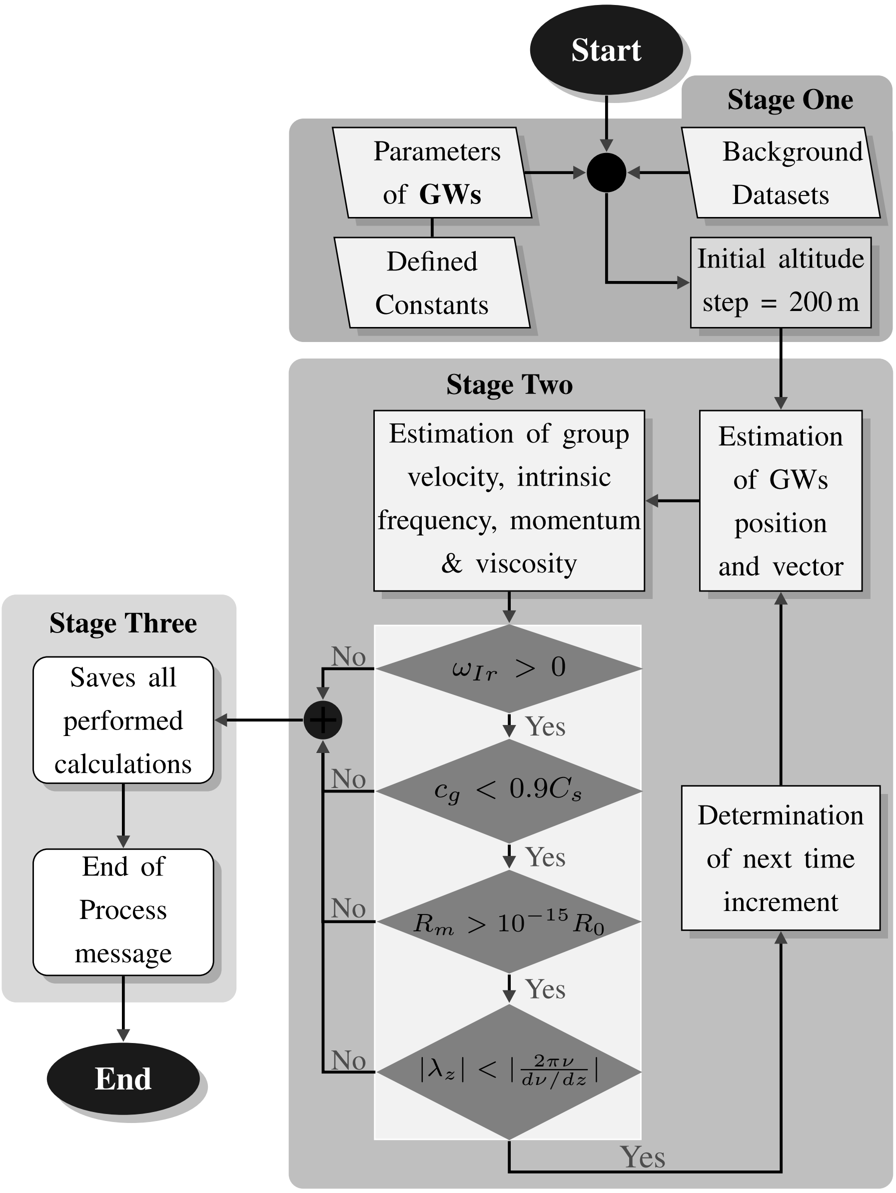

solid line represent the ray paths of the zero, HWM-14, and concatenated MERR-2 and HWM-14 winds, respectively. As it can be observed in Figure 4.20 that no significant variations were seen in the zero, HWM-14, and concatenated MERRA-2 and HWM-14 winds. Also, no significant difference was observed in the final positions of the ray paths (red and blue filled circles) and the center (black diamond) of the red dashed circle. The red dashed circle represents the first concentric wavefront in the OH image. The convergence of all the three ray paths at the CGW center indicate weak background wind during this event and also affirming that the wave was excited by the convective system.

Figure 4.20 - A sample ray tracing results of March 24, 2018 CGW event observed at São Martinho da Serra.

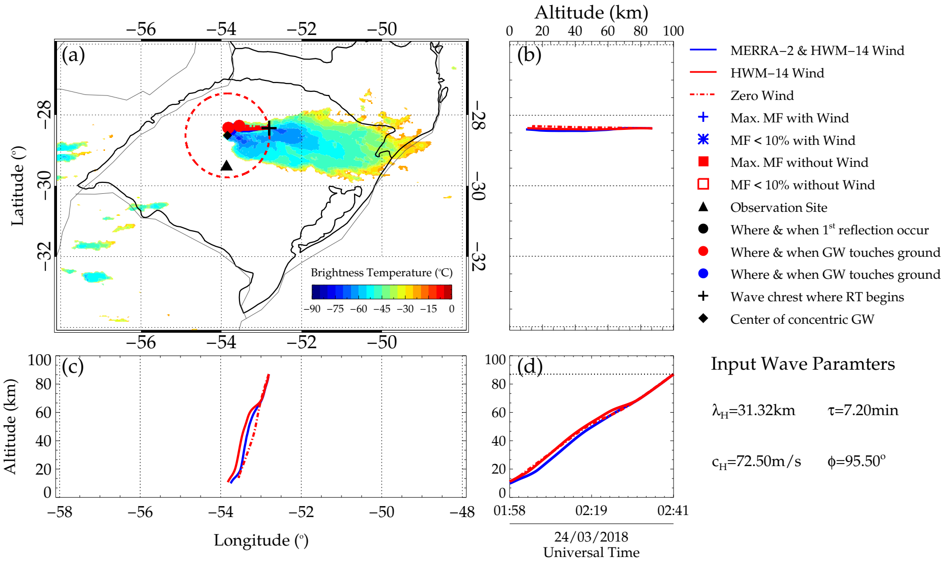

The variations of the ray paths in longitude and latitude, the variations of ray paths in altitude and latitude, variations in ray paths of longitude and altitude, and the variations in the ray paths in time relative to altitude are shown in panels (a), (b), (c), and (d), respectively. The color bar shows the temperature scale of the cloud top brightness temperature image overplotted in panel (a).

Before the ray tracing model became operational, it went through a careful validation process to calculate both backward and forward ray paths of gravity waves in the atmosphere. Gravity wave reflections on the surface and critical layers due to winds are included and validated as well. The atmospheric background database used in the model is position and time dependent. In this model, the absolute amplitude of GWs in the wind, temperature, and density fields at all levels are computed as well.

4.3.1 Considerations on the ray tracing model

To ray trace GWs using this ray tracing model, the inputs are:

1. The parameters (λ_H, τ, c_H, ϕ) of the gravity waves of interest. Also, the spatial coordinates (longitude, latitude, altitude) where the GWs were observed and the respective time of observation (hour, day, month, year);
2. Wind and temperature database for the day on which the GWs was observed;
3. Physical constants such as the gas constant, average radius of the Earth, among others, and a set of constants to calculate the average molecular mass of the atmosphere at all altitudes. These constants were determined semi-empirically

by Vadas (2007) and will be discussed in this section;

4. Two root file paths are provided:

    i. the root path to the GW parameters, wind, and temperature database files;

    ii. the root path to where the final ray tracing results will be saved

The first computation performed by the model is the calculation of the thermodynamic variables using the wind and temperature profiles provided through the database. In this calculation, the hydrostatic equation $d\overline{p} = dz = -g\overline{\rho}$ and the gas law $\overline{p} = \overline{\rho} R\overline{T}$ were used to calculate the pressure (VADAS, 2007):

$$\overline{p}(z) = p_0 e^{-\frac{1}{R}\int_0^z \frac{g}{T}dz'}, \tag{4.19}$$

where $\overline{\rho}$ is the mean density and $p_0 = p(z = 0)$. Using the pressure estimated from Equation 4.19 and the ideal gas law, the density is estimated. Recalling that $R = 8314.5/X_{MW}$ m^{-2}s^{-2}K^{-1}, the average molecular mass is calculated by:

$$X_{MW} = \frac{1}{2}(X_{MW_0} - X_{MW_1})\left[1 - tanh\Big(\frac{s-a}{\Delta_a}\Big)\right] + X_{MW_1} \tag{4.20}$$

The numerical values of the constants X_{MW_0}, X_{MW_1}, a and Δa are defined in Table 4.2 with $s = ln\rho$. The calculation of density, pressure, and molecular mass was done assuming the density value at the surface of 1.21 kgm^{-3}.

Table 4.2 - Constants for calculating the average molecular mass and the ratio of specific heats at constant pressure and volume.

Constants	Value
X_{MW_0}	28.90
X_{MW_1}	16.00
a	14.00
Δ_a	4.20
γ_1	1.40
γ_1	1.67
b	15.10
Δ_b	1.40

Source:Vadas (2007)

With the density known, the scale height (H) can be easily obtained using

$$H = -\frac{\overline{\rho}}{d\overline{\rho}/dz}. \tag{4.21}$$

The kinematic viscosity (ν) is

$$\nu = \mu/\rho \tag{4.22}$$

and molecular viscosity (μ) are defined to be

$$\mu = 3.34 \times 10^{-4}\overline{T}^{0.71}, \tag{4.23}$$

in units of gm^{-1}s^{-1}. The Prandtl number is assumed to be constant and equal to 0.7 throughout the atmosphere (KUNDU et al., 2016). The Prandtl number gives the measure of the efficiency of momentum transport to thermal transport.

The potential temperature is given as

$$\theta = \overline{T}\left(\frac{p_o}{p(z)}\right)^{R/C_p} \tag{4.24}$$

where $\gamma = C_p/C_v$ and $C_p = \gamma R/(\gamma - 1)$. The values of γ were defined by Vadas (2007) using

$$\gamma = \frac{1}{2}\left(\gamma_0 - \gamma_1\right)\left[1 - tanh\left(\frac{s-b}{\Delta_b}\right)\right] + \gamma_1, \tag{4.25}$$

where the constants γ_1, γ_0, b and Δ_b are also given in Table 4.2.

Knowing γ, and consequently the potential temperature, the Brunt Väisälä frequency is derived using Equation 2.23. Also, using γ, R, and $\bar{T}$, the speed of sound in air is $c_s = (\gamma R\overline{T})^{1/2}$. c_s undergoes modifications throughout the atmosphere, especially in the thermosphere - ionosphere.

The results of the estimation of thermodynamical variables described above are presented in Figure 4.21. The temperature profile in panel (a) was obtained from NRLMSISE-00 at

02:55:02 UT on March 24, 2018 at São Martinho da Serra. Using the temperature profile in Equation 4.19, the density profile was estimated as shown by the light blue solid line in panel (a). The density scale height profile shown in panel (b) was estimated using Equation 4.21. In panel (c), the vertical profile of the average molecular mass (X_{MW}) in the black solid line and the ratio of specific heat at constant pressure and volume (γ) in the red solid line are presented. The X_{MW} and γ were estimated using Equations 4.20 and 4.25. In panel (d) the speed of sound which was estimated using $c_s = (\gamma R\overline{T})^{1/2}$ is shown. It can be observed that both the scale height and speed of sound profile are similar.

Figure 4.21 - The estimated thermodynamic and thermodynamic-related profiles.

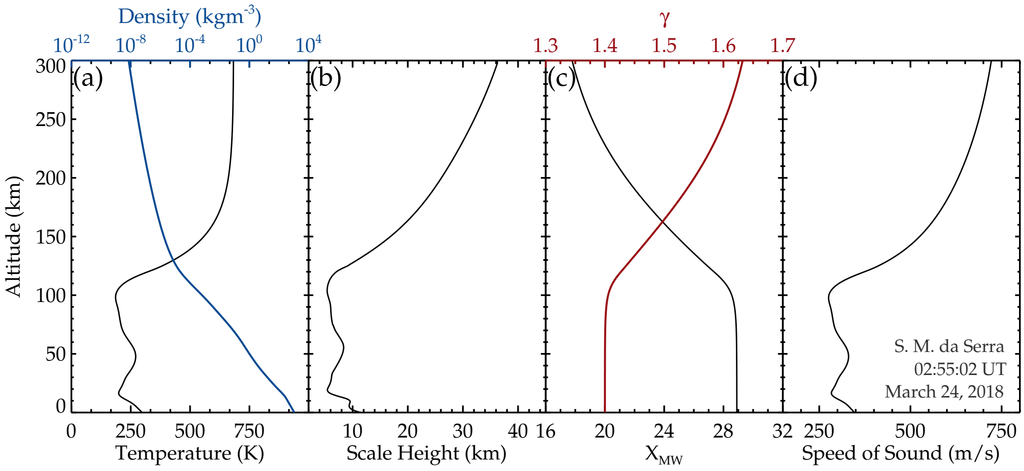

In panel (a), the temperature profile (black solid line) and calculated atmospheric density profile (dashed blue line) are presented. Panel (b) shows the scale height profile calculated from the density profile. The mean molecular mass profile (black line) and the ratio of specific heats at constant pressure and volume (dashed blue line) are presented in panel (c). In panel (d) the vertical profile of the speed of sound is presented.

4.3.2 Underlying concepts of stopping conditions

One very important effect of the thermosphere is the increase in the speed of sound in the air due to increasing temperature. The speed of sound practically doubles from the mesosphere to ~ 400 km. The effect of the thermosphere on the speed of sound is important because the speed of sound is the threshold between acoustic and internal waves. The higher the speed of sound, the greater the permitted range of internal waves. Since the dispersion relation (Equation 4.12) neglects acoustic waves (VADAS, 2007; PAULINO, 2012) and also, a GW propagates at the group velocity (PAULINO, 2012); the first ray tracing stopping condition adopted here is that each GW must propagate slower than the speed of sound:

$$c_g = 0.9C_s, \tag{4.26}$$

where the factor 0.9 is chosen arbitrarily, $c_g = \sqrt{c_{gx}^2 + c_{gy}^2 + c_{gz}^2}$. If a GW violate Equation 4.26, it is excluded from the spectrum and the ray tracing procedure for that wave will end.

As discussed earlier in Chapter 2, when a propagating GW approaches a critical or absorption level, the intrinsic frequency of the wave approaches zero. When this happens, a GW cannot propagate, therefore, a GW must have an intrinsic frequency greater than zero (VADAS, 2007):

$$\omega_{Ir} > 0 \tag{4.27}$$

Dissipation process due to molecular viscosity and thermal diffusivity causes a rapid decrease in GW momentum flux. During the ray tracing procedure, the momentum flux per unit mass at each step is computed using Equation 2.33. As demonstrated in Chapter 2, the momentum flux attains its maximum value in the lower thermosphere after which it decreases rapidly with altitude.

The rapid decrease is due to the increase in temperature and decrease in density which are the determining factors of molecular viscosity and thermal diffusivity inverse decay rate of dissipating GW. Therefore, when forward ray tracing GW into the thermosphere - ionosphere, the momentum flux per unit must satisfy the condition:

$$\tilde{u}_{GW}\tilde{w}_{GW}^*(z,t) \geq 10^{-15}\tilde{u}_{GW}\tilde{w}_{GW}^*(z = 87\,km, t = 0), \tag{4.28}$$

else the ray tracing procedure comes to an end. The factor 10^{-15} was also arbitrarily chosen.

To ensure that the viscosity does not change significantly over with altitude and over time, the module of the vertical wavelength needs to be smaller than the viscosity scale:

$$\lambda_z < \frac{2\pi}{\frac{d\nu/dz}{\nu}}. \tag{4.29}$$

This condition is necessary because only GWs with these characteristics must satisfy the simplifications made to obtain the dispersion relation presented in Equation 2.32. According to Vadas and Fritts (2006), this condition is almost always satisfied during high solar activity when the density in the thermosphere is higher. During low solar activity, it is necessary to use this condition to filter the permitted spectrum of GW. More details on the underlying concept of the four stopping conditions in Equations (4.26 - 4.28) can be found in Vadas and Fritts (2005), Vadas and Fritts (2006), and Vadas (2007).

4.3.3 Reflections of GW ray paths

When a GW ray path encounters the $m \rightarrow 0$ condition, that is a reflection level, or when it reaches the Earth's surface, reflection occurs. The ray tracing model indicates reflection using the signs on the vertical wavenumber (m). The change of sign of m is the feature that indicates whether a GW is downward or upward propagating. When m is negative a GW is upward propagating whereas it is downward propagating when m is positive. Under such conditions, the model responds well.

An indication before the occurrence of reflection is the progressive decrease in the time step of the GW ray path until the exact moment of reflection. So, to carefully handle reflection, especially, the position of the GW after reflection. This is done by using the last time interval right after the reflection.

To determine the reflection point on the Earth's surface, the following conditions were imposed:

i. Since GW cannot be transmitted to the interior of the Earth, the vertical velocity of the wave is zero at the Earth's surface;

ii. The reflection must occur such that the angle of reflection of the wave relative to the zenith must equal the angle of incidence;

iii. The horizontal propagation direction of the wave must be conserved.

The reflection of GWs on the surface of the Earth is an important concept since it can be used to investigate possible sources of GWs.

For instance, Vadas et al. (2009a) used this concept to look for tropospheric sources of MSGWs that could be present both before and after the reflection. On the other hand, Takahashi et al. (2011) also used the concept of wave reflection on the Earth's surface to discuss the possibility of gravity wave generations by thermospheric body forces. However, in the present work, the ray paths of GWs after the reflection on the Earth's surface were not investigated. Also, none of the GW events studied in this work met such a condition.

4.3.4 Gravity waves amplitudes in atmospheric fields

The GWs amplitudes of the relative airglow intensity perturbations, $I'/\overline{I}$, in airglow images were estimated using the spectral analysis procedure in Section 4.1.2. The intensity perturbation is related to the relative amplitude of temperature by the cancellation factor, CF (LIU; SWENSON, 2003):

$$\frac{T'}{\overline{T}} = \frac{I'/\overline{I}}{CF} \tag{4.30}$$

Using the GW wavelength at the emission altitude, Vargas (2007) defined the cancellation factor as:

$$CF = 3.68 - 3.41e^{-0.0053(\lambda_z - 6)^2}, \tag{4.31}$$

where λ_z is in km. For medium-scale GW, CF depends on λ_z and ranges between 1.9 - 3.6. According to Vadas et al. (2009a), the dependence of CF on λ_z is due to the finite thickness of the OH layer. This is because the intensity perturbations in the OH airglow partially cancel out for $\lambda_z < 20 - 30$ (VADAS et al., 2009a).

Assuming adiabatic motions, Fritts and Alexander (2003) defined the GW horizontal wind perturbations as

$$u'_H = \frac{mg\omega_{Ir}}{k_H N^2}\frac{\theta'}{\overline{\theta}}. \tag{4.32}$$

For GW satisfying the hydrostatic approximations: $\omega_{Ir}^2 \ll N^2$, $m/k_h \sim N/\omega_{Ir}$, and $\theta'/\overline{\theta} = T'/\overline{T}$, Equation 4.32 then becomes

$$u'_H = \frac{g}{N}\frac{T'}{\overline{T}}. \tag{4.33}$$

For the GW vertical perturbation (w'), the Boussinesq continuity equation yields (VADAS et al., 2009a)

$$w' \sim \frac{k_H u'_H}{m} \tag{4.34}$$

and mean momentum flux (VADAS et al., 2009a) of

$$\overline{u'_H w'} \sim \frac{1}{2}\frac{k_H}{m}(u'_H)^2. \tag{4.35}$$

This mean momentum flux is the initial momentum flux estimated in the OH layer. The momentum flux at every time or altitude step can be estimated using Equation 2.33. This methodology to determine the momentum flux at the altitude of the OH emission layer was also used in the work of Vadas et al. (2009a).

To determine GW amplitudes in wind, temperature, and density fields, we followed the methodology of Vadas et al. (2009a). The GW amplitude in the vertical wind at a given point of the ray path is given by:

$$\tilde{w}\tilde{w}^* = \left(\frac{\tilde{w}}{\tilde{u}_H}\right) u'_H \tilde{w}^*, \tag{4.36}$$

where $\tilde{w}$ is the vertical spectral perturbation of the GW.

The spectral perturbation on the horizontal (VADAS; FRITTS, 2009) is given as:

$$\tilde{u}_H \tilde{u}_H^* = \left[\left(\frac{\tilde{w}}{\tilde{u}_H}\right)^{-1}\right] u'_H \tilde{w}^*. \tag{4.37}$$

The zonal and meridional components of the horizontal perturbation are given respectively as:

$$\tilde{u} = \frac{k}{k_H} u'_H, \tag{4.38}$$

$$\tilde{v} = \frac{l}{k_H} u'_H. \tag{4.39}$$

The density and temperature perturbations are determined using the polarization relations defined in Appendix B of Vadas and Fritts (2005):

$$\tilde{T} \simeq \frac{(\gamma-1)\bar{T}}{H\mathcal{D}}\left(im + \frac{1}{2H}\right)\tilde{w}_0, \tag{4.40}$$

$$\tilde{\rho} \simeq \frac{(\gamma-1)\bar{\rho}_0}{H\mathcal{D}}\left(im - \frac{1}{2H}\right)\tilde{w}_0, \tag{4.41}$$

where

$$\mathcal{D} = \left[i\omega_I\left(\gamma im + \frac{1}{H} - \frac{\gamma}{2H}\right) + \frac{\gamma\alpha\nu}{Pr}\left(im - \frac{1}{2H}\right)\right],$$

$$\alpha = \vec{\mathrm{k}}^2 + \frac{1}{4H^2} + \frac{im}{H}$$

$$\frac{\tilde{w}}{\tilde{u}_H} = -\frac{k_H m}{m^2 + \frac{1}{4H^2}}\left[1 - \frac{i(\vec{\mathrm{k}}^2 + \frac{1}{4H^2})(\omega_I - i\alpha\nu)}{2mHk_H^2N^2}\left[\left(\frac{2}{\gamma} - 1\right)\omega_I - \frac{i\alpha\nu}{Pr}\right]\right].$$

4.3.5 Validation of ray tracing model

To validate the current ray tracing model, we compared the results obtained in the current computational code to the results of the event obtained from the code of Paulino (2012) and references therein. During the validation process, all discrepancies in the final results due to the wind and temperature profiles used were analyzed.

4.3.6 Estimation of error in the ray tracing model

It is necessary to specify the error in the final position of the ray path of a gravity waves, especially for small-scale gravity waves (SSGW). In most cases, the final positions of the zero wind and model wind ray paths were used, since their differences are mostly within the error margin of the wind. This approach has been adopted by Wrasse (2004) and Vadas et al. (2009a) to discuss the error in determining the final position of the GWs backward ray traced when they were investigating the source locations.

The error estimation method of SSGW mentioned above was applied to medium-scale gravity waves (MSGW) by Paulino (2012) whose sources were investigated. More detail on the error estimation using this method can be seen in Paulino (2012).

4.4 Determination of the center of CGWs

To determine the center of the circular gravity waves, the geometry technique based on the concept of intersection between three circles was employed. The main aim of using the intersection points of the circles is to determine a line perpendicular to a point on the circumference. The intersecting lines between the circles that touches a point on any part of the circumference perpendicularly defines the new points to be use in determining the center of the circle. The following is the step by step description of the procedure for estimating the center of the CGWs according to Pedoe (1995). The pictorial representation is given in Figure 4.22.

Figure 4.22 - Schematic diagram showing how to determine the center of CGWs and an airglow image of CGW observed on March 24, 2018.

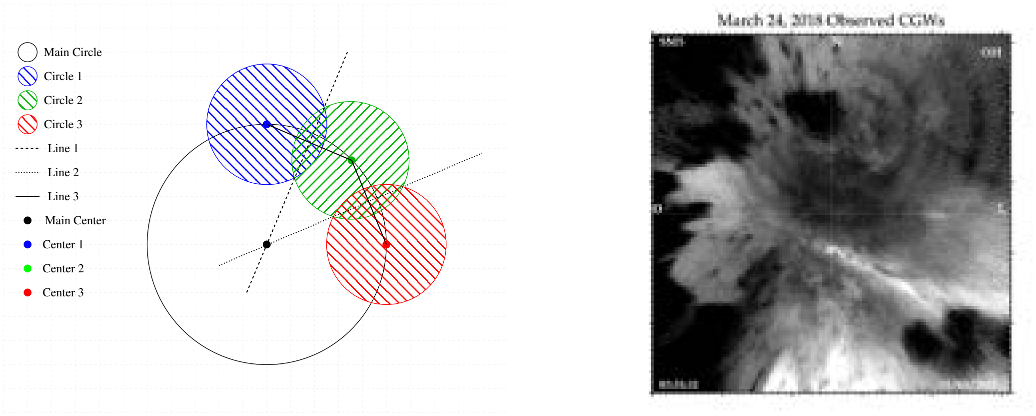

Left panel shows a diagram illustrating how the center and radius of a concentric (circle, ellipse and arc) pattern are determined using geometry technique. In the right panel, an observed CGWs on the night of March 24, 2018 at São Martinho da Serra is presented.

Considering a circle with an unknown center, "main circle" as shown in right panel of Figure 4.22 (the ideal case) and right panel of Figure 4.22 in the case of the observed CGWs on the night of March 24, 2018.

In estimating the center of this concentric shape, three arbitrary points are selected on the arc/circle (main circle), where each point is considered as a center of the circles to be drawn. These three circles (i.e., circle 1, circle 2 and circle 3) must all satisfy the equation of a circle of the form;

$$\left.\begin{aligned}(x-x_1)^2+(y-y_1)^2 &= r_1^2\\(x-x_2)^2+(y-y_2)^2 &= r_2^2\\(x-x_3)^2+(y-y_3)^2 &= r_3^2\end{aligned}\right\} \tag{4.42}$$

where, x, y and r respectively are the x-position, y-position and radius.

An arbitrary radius was chosen to construct circle 1 (blue), circle 2 (green) and circle 3 (red) with their respective centers denoted by the dot. The distance (D) between circle 1 and circle 2, and circle 2 and circle 3 was then estimated using Equation 4.43.

$$D = \sqrt{(x_2-x_1)^2+(y_2-y_1)^2}. \tag{4.43}$$

In order to obtain the a line perpendicular to the circumference of the circle, the intersection points of each pair of circles were determined. For this to be carried out, it is important that:

i) the sum of the two radii must be greater than the distance between the two circles ($r_0 + r_1 > D$) and

ii) their difference must be lesser than the distance between the two circles ($|r_0 - r_1| < D$).

With the aid of Equation 4.43, the intersection points of the first and second circles was estimated as well as that of second and third circles. Equations 4.44 and 4.45 were then used to estimate the X and Y positions.

The intersection points between circle 1 and circle 2 were estimated using Equation 4.44, whereas that of circle 2 and 3 by Equation 4.45.

$$X_{1,2} = \frac{x_1+x_2}{2} + \frac{(x_2-x_1)(r_1^2-r_2^2)}{2D^2} \pm 2\frac{y_1-y_2}{D^2}\delta \tag{4.44}$$

$$Y_{1,2} = \frac{y_1+y_2}{2} + \frac{(y_2-y_1)(r_1^2-r_2^2)}{2D^2} \mp 2\frac{x_1-x_2}{D^2}\delta \tag{4.45}$$

where δ is define by

$$\delta = \frac{1}{4}\sqrt{(D + r_1 + r_2)(D + r_1 - r_2)(-D + r_1 + r_2)} \tag{4.46}$$

The dashed line (line 1) denotes the connecting line between the intersection points of circle 1 and circle 2. For circle 2 and circle 3, the connecting line of their intersection point is denoted by the dotted line (line 2). These connecting lines were constructed using Equation 4.47.

$$c = \frac{x_1 - x_3}{y_2 - y_1}x + \frac{(r_1^2 + r_2^2) + (x_2^2 - x_1^2) + (y_2^2 + y_1^2)}{2(y_2 - y_1)} \tag{4.47}$$

We next determined the intersecting point of the two intersection lines using Cramers rule (CRAMER, 1750). Before applying the Cramers rule, the lines connecting the two intersection points of the circle were calculated using Equation 4.48,

$$\left.\begin{aligned} y_1 &= m_1 x + a \\ y_2 &= m_2 x + b \end{aligned}\right\} \tag{4.48}$$

where, a and b are the intercept and m is the slope.

From Cramer's rule (CRAMER, 1750), the x and y positions of the intersection of the already determined intersecting lines, that is, lines 1 and 2 were obtained using

$$\left.\begin{aligned} x &= \frac{\begin{bmatrix} -a & -1 \\ -b & -1 \end{bmatrix}}{\begin{bmatrix} m_1 & -1 \\ m_2 & -1 \end{bmatrix}} = \frac{a - b}{m_2 - m_1} \\ y &= \frac{\begin{bmatrix} m_1 & -a \\ m_2 & -b \end{bmatrix}}{\begin{bmatrix} m_1 & -1 \\ m_2 & -1 \end{bmatrix}} = \frac{am_2 - bm_1}{m_2 - m_1} \end{aligned}\right\} \tag{4.49}$$

Finally, the radius of the circle was then estimated by considering the distance between the center of the circle to one of the three points. Applying Pythagoras theorem (SALLY, 2007), the radius using Equation 4.50,

$$Radius = \sqrt{\Delta x^2 + \Delta y^2}, \tag{4.50}$$

was obtained.

The above described procedure was applied to other regions on the circumference of the circle as shown in Figure 4.23.

Figure 4.23 - The quadrant within which the procedure to determine the center of a circle was repeated.

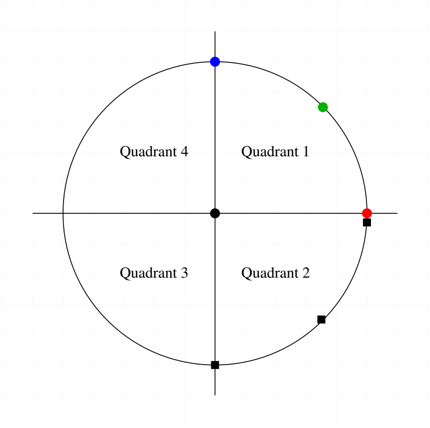

To validate the accuracy of the procedure describe above, we repeated the steps considering various points on the main circle (in the case of real CGWs, either the bright or dark band). Figure 4.23 shows an example of the selected points where the procedure has been repeated. The square black points are the points selected in the second quadrant.

The geometrically determined center gives a zeroth-order approximation of the possible location of the wave. This approach does not consider the effect of the background wind. To determine the source of the wave considering the influence of background wind, the ray tracing technique is used.

4.5 Estimation of overshooting tops (OTs) height

As mentioned in Chapter 2, point-like convective overshooting of the tropopause by ∼1 - 3 km into the stratosphere can generate concentric gravity waves. Therefore, it is necessary to know to what extent the tropopause is overshoot into the stratosphere. To do this, two different methods were adopted from (i) Griffin et al. (2016) and (ii) São Sabbas et al. (2009).

4.5.1 Method of Griffin et al. (2016)

The overshooting tops using the method of Griffin et al. (2016) can be estimated using

$$OT_{Height} = H_{Trop} + \frac{OT_{BT} - T_{Trop}}{OT_{LR}}, \tag{4.51}$$

where H_{Trop} is the tropopause height, OT_{BT} is the brightness temperature of the OT, T_{Trop} is the tropopause temperature and OT_{LR} is the OT lapse rate. The OT lapse rate is difference between the lapse rate at the tropopause and that of the OT height.

To estimate the OT height using Equation 4.51, the tropopause temperature and height were first determined using the lapse rate definition (XIAN; HOMEYER, 2019). The lapse rate definition for tropopause determination is an efficient way to estimate thermal tropopause (LIU et al., 2020). This definition was introduced by the World Meteorological Organization (WMO) in 1957. WMO defines the lapse rate tropopause as the lowest level where the value of the temperature lapse rate decreases to 2 K/km or 2°C/km or less, provided the average lapse rate between this level and all higher levels within 2 km does not exceed 2 K/km or 2°C/km. In panel (a) of Figure 4.24, the tropopause determined using the lapse rate tropopause definition is presented. The temperature profile used to determine the tropopause was obtained from radiosonde measurement taken at Santa Maria on March 24, 2018 at 00:00 UT.

Figure 4.24 - Illustration of determination of tropopause altitude.

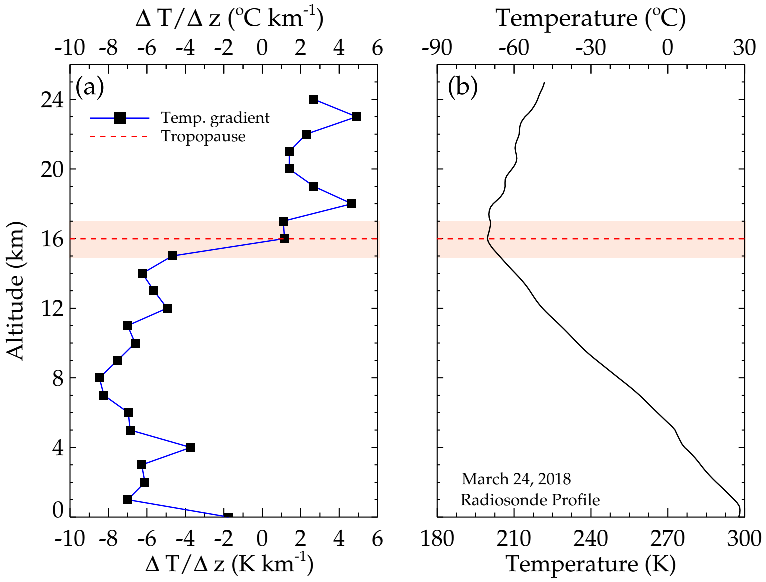

In panel (a), the determined tropopause using the lapse rate tropopause definition is shown, whereas panel (b) is the determined tropopause using the cold-point tropopause definition.

In panel (a) of Figure 4.24, the blue solid line with the black squares shows the profile of the temperature gradient. The black squares show each 1 km mark. The red dashed line is the tropopause height. The light red shaded region around the tropopause emphasizes the error range of the tropopause height. Using the lapse rate tropopause definition, the determined tropopause height and temperature, the OT_{BT}, and the OT lapse rate are used as input parameters in Equation 4.51 to estimate OT height.

4.5.2 Method of São Sabbas et al. (2009)

On the other hand, the method of São Sabbas et al. (2009) uses the cold-point definition to determine the tropopause. The cold point tropopause is defined as the level between the stratosphere and troposphere where the temperature is coldest. Panel (b) of Figure 4.24 shows the radiosonde temperature profile. The tropopause altitude is shown by the horizontal red dashed line. The tropopause height determined by the two methods is similar. Based on this definition, the tropopause height, and temperature were considered as the reference height and temperature for the OT estimation. To estimate the OT height adopting the method of the São Sabbas et al. (2009), the following procedures were employed:

i. a threshold temperature $T \leq -70°C$ was set and used to identify the general convective core cloud cover;

ii. the average temperature ($\bar{T}$) was determined by adding the temperature of all pixels whose values were lower than a threshold ($T \leq -70°C$) and divided by the total number of pixels;

iii. the temperature difference (ΔT) between the temperature of each pixel (T_{pixel}) and the average ($\bar{T}$), $\Delta T = T_{pixel} - \bar{T}$ was then calculated;

iv the pixel with the lowest ΔT was selected as the "center" of the convective cores (T_{core});

v the area or width of the convective core was estimated by adding the area of surrounding pixels until $\Delta T = T_{core}/2$.

In most cases, the temperature gradient around the convective core center was rather sharp, the number of pixels with $\Delta T \leq T_{core}/2$ was small, and in such cases, all pixels were included. For the few convective cores that extended to larger areas and/or merged with other convective cores, only a few pixels outward in each direction from the coldest spot were included. Now having obtained the temperature of the convective core center (i.e., the coldest cloud top temperature), we then estimated the height of the convective core centers. Since the temperature of the convective core center, the tropopause height, and temperature are known, the height of the convective core center ($T_{core}\ Height$) is estimated using

$$T_{core}\ Height = \frac{T_{temp} \times T_{core}}{T_{height}}, \tag{4.52}$$

where T_{temp} is the tropopause temperature, T_{core} is the temperature of the convective core and T_{height} is the tropopause height.

Obtaining the maximum height of the convective core (T_{core}) from Equation 4.52, and the tropopause height from the radiosonde soundings (ADLER; FENN, 1979; HEYMSFIELD; JR, 1988), the OT height is simply estimated by subtracting the tropopause height from the maximum height of the convective core (T_{core}).

4.6 Determination of spatial and temporal characteristics of lightning activities

BrazilDAT lightning sensors take the position, time, and peak current of Lightning activities in the vicinity of thunderstorms. The instrument as well distinguishes intracloud and cloud-to-ground lightning. Two main information were retrieved from lightning activities:

i. determination of the spatial distribution of the lightning strikes;

ii. determination of the lightning rate per minute (i.e., lightning strokes per minute).

4.6.1 Determination of spatial distribution

The spatial distribution of the position (in longitude and latitude) of lightning strokes are determined by binning in 0.06° × 0.06° (6.6 km × 6.6 km) grid boxes. This is done to determine their spatial densities within a given longitude and latitude. This methodology is employed in order to compare the region with high density to the region with minimum cloud top brightness temperature (a proxy for convective overshooting) since there is a positive correlation between the two phenomena (BEDKA et al., 2010).

4.6.2 Determination of temporal variation

In this study, time-series of lightning rates are used to investigate lightning jumps, since lightning jumps can be used to infer overshooting due to updraft. To construct a lightning rate time series, the lightning strokes per minute are computed within a time range of ± 1 hour centered around the time when the observed wave was excited, as indicated by the ray tracing result. Also, the lightning rate was computed for every minute in order to achieve a temporal resolution of one minute, which is equivalent to the temporal resolution of the airglow images. Next, Lomb Scargle and Wavelet analysis are applied to the lightning rate to obtain the periodicities. The periods in the lightning flash rate are compared to the periods of the observed waves.

5 RESULTS

This chapter presents and discusses the main results of concentric gravity wave (CGW) observations made from 2000 to 2019. The total number of CGWs events observed at São João do Cariri (36.50°W, 07.40°S), Cachoeira Paulista (45.00°W, 22.66°S), and São Martinho da Serra (53.85°W, 29.54°S) will be presented.

5.1 Statistics of CGWs observation

Airglow observation at São João do Cariri (CA) began from 2000 to date, while at Cachoeira Paulista (CP), observation started in 1998 up to date, and at São Martinho da Serra (SMS), it began in April 2017. In this study, airglow data from 2000 to 2019 from São João do Cariri and Cachoeira Paulista were used, whereas for São Martinho da Serra, data from 2017 to 2019 were considered. The statistics of the years of airglow observation and the number of CGW events observed are presented in Figure 5.1.

Figure 5.1 - The number of concentric gravity wave events observed over Brazil from 2000 to 2019.

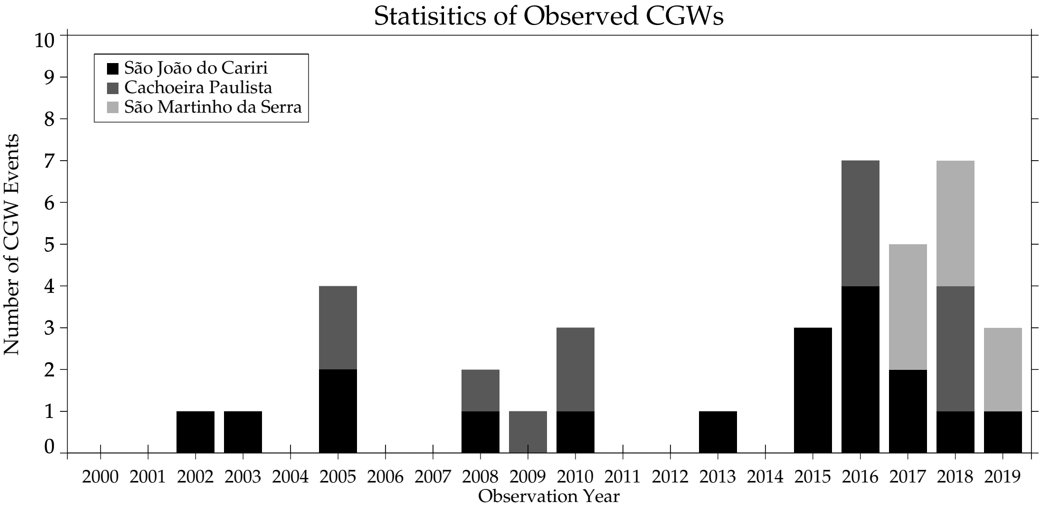

The black, dark gray, and gray bars represent the CGW events observed over São João do Cariri, Cachoeira Paulista, and São Martinho da Serra, respectively.

From Figure 5.1, a total of thirty-eight (38) CGW events were observed. Twenty-five (25) events were observed at São João do Cariri, twelve (12) events at Cachoeira Paulista, and eight (8) events at São Martinho da Serra. It is necessary to mention that even though twenty-five (25) CGW events were observed in São João do Cariri, 18 of the events have well-defined concentric structures. Therefore, for this work, only the 18 CGWs events were presented as part of the record observations. This is because the 18 events satisfy the criteria used to index the CGWs for further analysis.

In Figure 5.1, the number of CGW events observed in airglow image data from 2000 to 2019 are presented. For each year, the bar shows the accumulated number of CGW events from all observation sites. The black, dark gray, and gray bars represent the number of CGW observed at São João do Cariri, Cachoeira Paulista, and São Martinho da Serra, respectively.

5.2 Indexing CGW events

To select the best CGW event for detailed investigation, indexes were used to classify them, based on the morphology of the concentric wavefronts in the airglow images. The CGWs are classified as:

i. index 1, if the CGW have at least three visible concentric wave crest/trough on the image with more than 50% of the concentric wavefront visible;

ii. index 2, if the CGW have at least three visible concentric wave crest/trough on the image with ~25% to 50% of the concentric wavefront visible;

ii. index 3, if the CGW have at least three visible concentric wave crest/trough on the image with less than 25% of the concentric wavefront visible;

In Figure 5.2, the images corresponding to the indexes are presented with stars in order to visualize the wave perturbations without filtering. Index 1, 2, and 3 CGWs are presented in the left, middle, and right panels of Figure 5.2.

Figure 5.2 - The indexes used to classify CGW events for further investigations.

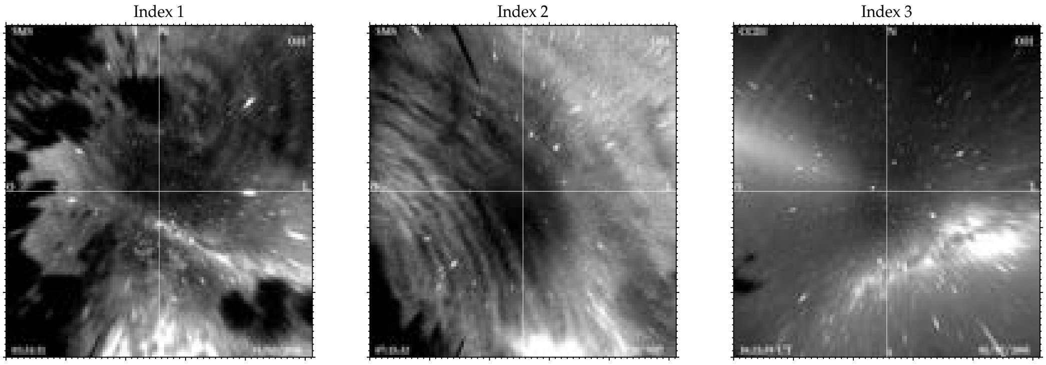

Index 1 Index 2 Index 3

After the classification of the CGW, the waves presented in Figure 5.1 have been grouped into their respective observation sites and years, and then finally grouped according to the indexes. The indexed classified CGW events from each observation site are presented in Figure 5.3.

In panels (a), (b), and (c) the classified CGW events for São João do Cariri, Cachoeira Paulista, and São Martinho da Serra are presented, respectively. In the legends, the black square is Index 1, the dark gray square is Index 2, and the gray square is Index 3. In São João do Cariri, out of the 18 events, six (6) of them are Index 2 whereas, twelve (12) events are Index 3. For Cachoeira Paulista (panel (b)), two (2) out of the twelve (12) events were Index 2 whereas, the remaining ten (10) are in Index 3. However, the events in São Martinho da Serra have one (1) Index 1 and seven (7) Index 2 out of the total of eight (8) events observed. The statistics used to make the plot in Figure 5.3 are further summarized in Table 5.1.

Figure 5.3 - The classification of CGW events for each observation site using indexes.

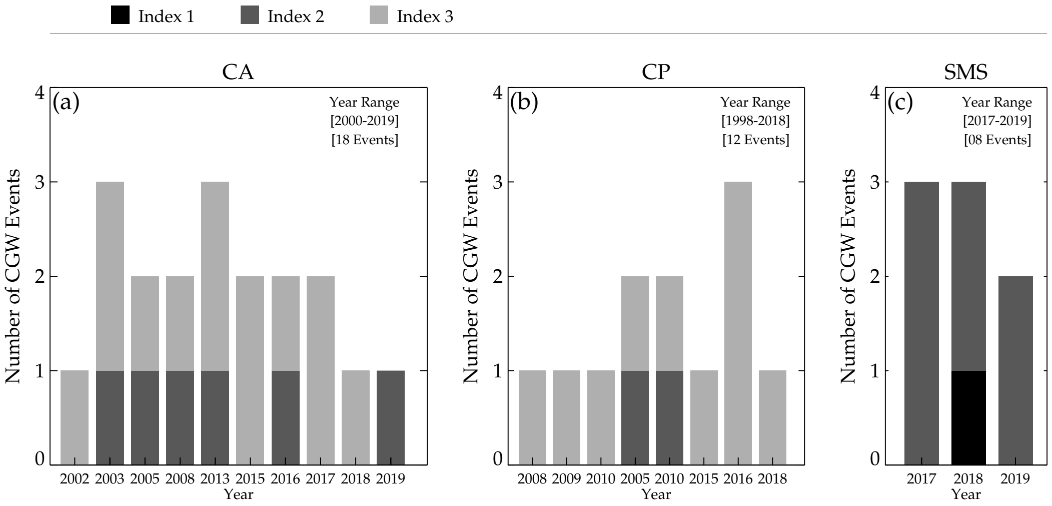

Panels (a), (b), and (c) show the classification of the events for São João do Cariri, Cachoeira Paulista, and São Martinho da Serra, respectively.

Table 5.1 - The summary of CGW events classification using indexes.

Observation Site	Index 1	Index 2	Index 3	Total Cases
CA	0	6	12	
CP	0	2	10	38
SMS	1	7	0	

5.3 Observed CGW

In this section some examples of CGW observed at the three observatories will be presented, in order to show their morphologies. Figure 5.4 presents nine (9) different concentric gravity waves observed at São João do Cariri, Cachoeira Paulista, and São Martinho da Serra with their respective date of observation. The parameters of the waves, presented in Figure 5.4, are highlighted in light red as shown in Table 5.2.

Figure 5.4 - Samples of airglow images with concentric wavefronts observed at São João do Cariri, Cachoeira Paulista and São Martinho da Serra.

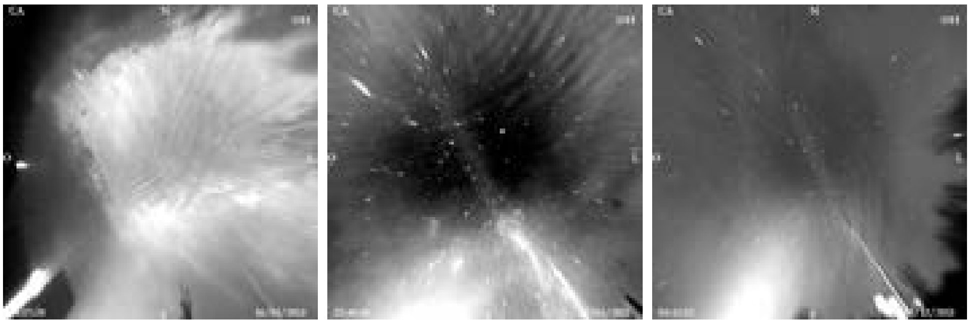

CA - 03/16/2013 CA - 03/15/2015 CA - 12/05/2015

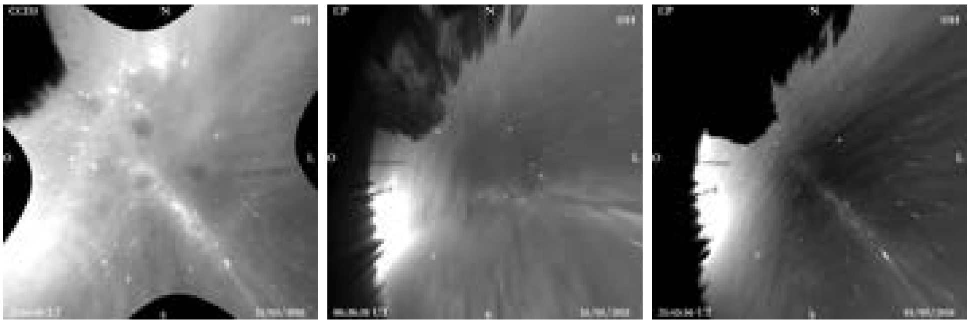

CP - 03/11/2010 CP - 05/15/2015 CP - 05/01/2016

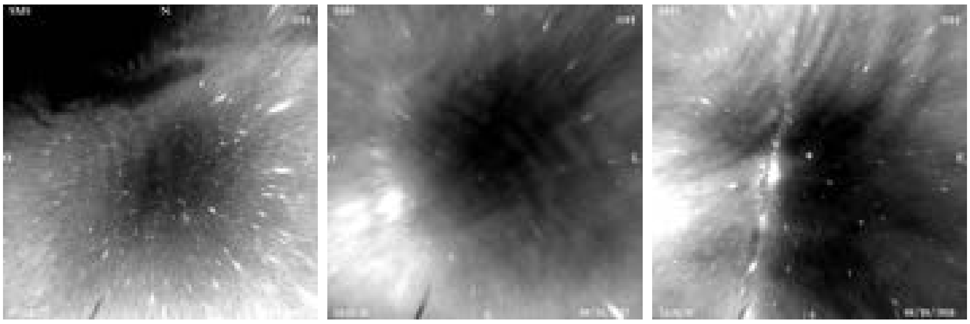

SMS - 08/28/2017 SMS - 11/08/2017 SMS - 10/08/2018

The parameters of the CGW events based on the Indexes were obtained using the spectral analysis technique discussed in Section 4.1.2. The horizontal wavelength (λ_H), period (τ), and phase speed (c_H) are presented in Table 5.2 and graphically illustrated in Figure 5.5. The date of the observed CGW events presented in Table 5.2 and subsequent tables follow the [MM/DD/YYYY] format.

Table 5.2 - Observed parameters of concentric gravity waves selected using indexes.

Event #	Observation Site	Date	I. H	# of Images	Layer	λ_H (km)	τ (min)	c_H (m/s)
01	CA	08/02/2002	19:29	10	OH	40.9 ± 1.3	6.4 ± 11.8	99.8 ± 19.4
02		12/17/2003	18:46	10	OH	25.8 ± 0.1	10.1 ± 0.4	42.5 ± 1.6
03		04/02/2005	18:29	10	OH	23.3 ± 0.5	6.8 ± 0.3	57.4 ± 2.5
04		02/11/2005	03:57	10	OH	23.7 ± 0.3	06.9 ± 0.2	57.5 ± 1.9
05		03/11/2008	21:52	10	OH	31.9 ± 2.1	10.8 ± 1.3	49.2 ± 5.1
06		03/13/2010	00:51	10	OH	27.3 ± 1.9	41.2 ± 10.3	11.0 ± 27.6
07		03/16/2013	04:26	10	OH	28.6 ± 1.5	8.2 ± 0.9	58.2 ± 5.5
08		05/15/2015	00:31	10	OH	22.90 ± 0.5	48.9 ± 2.7	7.8 ± 0.4
10		03/15/2015	22:49	10	OH	36.9 ± 0.9	8.6 ± 0.7	71.3 ± 5.1
09		12/05/2015	03:14	10	OH	29.3 ± 1.6	6.5 ± 6.5	75.5 ± 76.4
11		02/15/2016	03:13	10	OH	25.5 ± 0.6	16.1 ± 0.8	26.4 ± 1.2
12		05/01/2016	21:40	10	OH	23.8 ± 0.5	25.0 ± 2.3	15.9 ± 1.4
13		08/25/2016	23:35	10	OH	51.7 ± 2.1	6.9 ± 0.5	124.7 ± 6.5
14		09/09/2016	04:59	10	OH	42.5 ± 0.8	12.3 ± 3.9	57.3 ± 10.6
15		12/17/2017	22:06	10	OH	95.3 ± 16.6	25.1 ± 17.5	63.4 ± 42.9
16		09/12/2017	23:40	10	OH	21.4 ± 0.8	6.2 ± 0.4	57.5 ± 3.0
17		01/13/2018	23:22	10	OH	58.9 ± 1.4	13.8 ± 1.2	71.1 ± 6.2
18		05/25/2019	21:16	10	OH	30.9 ± 0.9	7.0 ± 0.4	74.1 ± 4.8
19	CP	02/11/2005	03:57	10	OH	23.7 ± 0.3	6.9 ± 0.2	57.5 ± 1.9
20		03/11/2010	21:49	10	OH	24.2 ± 0.2	9.7 ± 0.8	62.5 ± 1.6
21		05/15/2015	00:31	10	OH	25.9 ± 1.0	59.2 ± 6.8	7.3 ± 0.8
22		05/01/2016	22:19	10	OH	53.3 ± 1.0	32.7 ± 3.5	27.0 ± 2.8
23	SMS	08/28/2017	07:22	10	OH	23.1 ± 01.2	5.6 ± 0.5	68.0 ± 4.9
24		10/01/2017	08:09	10	OH	48.2 ± 1.6	13.3 ± 0.6	60.2 ± 5.8
25		11/08/2017	23:42	10	OH	32.8 ± 3.0	9.1 ± 1.2	60.1 ± 5.9
26		03/24/2018	02:39	10	OH	31.3 ± 0.4	7.2 ± 0.1	72.5 ± 1.9
27		08/10/2018	23:26	10	OH	48.2 ± 0.5	11.8 ± 1.6	68.3 ± 9.0
28		10/18/2018	05:55	10	OH	44.9 ± 0.8	9.8 ± 0.5	76.1 ± 4.3
29		10/02/2019	00:27	10	OH	50.3 ± 4.6	11.4 ± 1.9	73.9 ± 10.9
		10/02/2019	00:55	10	OH	54.9 ± 5.0	10.0 ± 3.0	91.0 ± 9.0
		10/02/2019	04:04	10	OH	30.5 ± 4.1	7.0 ± 0.9	72.9 ± 8.6
30		10/28/2019	23:23	10	OH	31.2 ± 2.7	7.1 ± 1.1	73.0 ± 9.4

I. H - Initial Hour

In Table 5.2, a total of 30 CGW parameters are presented. Eighteen (18) wave events for São João do Cariri and eight (8) for São Martinho da Serra. For Cachoeira Paulista, even though twelve (12) events were observed, the parameters of only four (4) events including the two (2) “Index 2” CGW events were presented. This is due to time constraints to analyze further the other events. As a result, the entire events observed at Cachoeira Paulista are reserved for future work. Henceforth, the other eight (8) Events of Cachoeira Paulista will not be included in the subsequent statistical results.

Figure 5.5 - The distribution of concentric gravity waves (CGW) with small-scale characteristics.

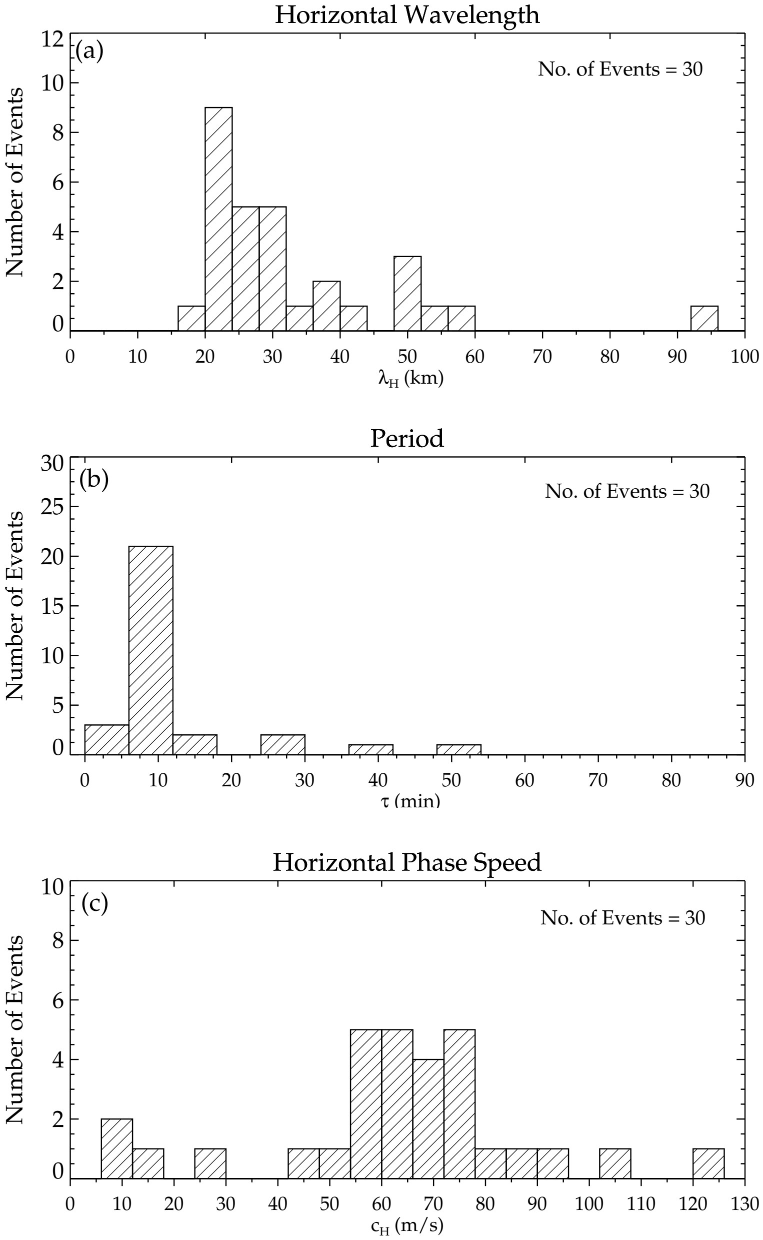

In panels (a), (b), and (c), the horizontal wavelength, period, and horizontal phase speed are shown.

Figure 5.5(a) shows the distribution of horizontal wavelength of the 30 observed CGW events (three CGWs for the CGW event on October 2, 2019). The distribution of the horizontal wavelength is mainly between 15 and 40 km, with an average value of around

33±16 km.

In panel (b) of Figure 5.5, the distribution of the observed CGW period is presented. The periods are principally distributed within the range of 5 to 20 minutes. The mean period ($< \tau >$) was ∼11±10 minutes.

On the other hand, the observed phase speed distribution of the CGWs is shown in Figure 5.5(c) . It was observed that majority of waves have phase speeds between 40 and 100 m/s, with a mean value of ∼63±25 m/s.

It has been mentioned earlier that 8 CGW events were observed at São Martinho da Serra. However, in Table 5.2, 10 CGW events are presented. On October 2, 2019 the CGW event was composed of three different GWs with concentric wavefronts at different times. Hence, these three (3) CGWs were considered as one event. Detail on this event will be given in Section 5.4 and further discussed in Chapter 7.

5.4 CGW events for case studies

Based on the objective of this work, some of the CGW events were selected for case studies to further investigate their propagations in the atmosphere and identify their source locations. In Table 5.2, the selected CGW events for the case studies are highlighted in light gray. The case studies are divided into three because of (a) the geographic location where the CGW events were observed and (b) the morphology of the wavefronts.

5.4.1 Case study one

The wave characteristics presented in Table 5.3 are used for case study one. Three CGW events, that is, Event # 24, 26, and 28 from São Martinho da Serra highlighted in gray in Table 5.2 were used. These CGW events were considered for this case study because these waves occurred on different nights and with different wavefronts morphologies.

Table 5.3 - Observed concentric gravity waves in São Martinho da Serra selected for case study one.

Event #	Date	Index	λ_H (km)	τ (min)	c_H (m/s)	Observatory
1	10/01/2017	2	48.20 ± 1.6	13.3 ± 0.6	60.2 ±5.8	SMS
2	03/24/2018	1	31.32 ± 0.4	7.2 ± 0.1	72.5 ±1.9	SMS
3	10/18/2018	2	44.9 ± 0.8	9.8 ± 0.5	76.1 ±4.3	SMS

In Figures 5.6, 5.7, and 5.8, a time sequence of three (3) images of the CGW events selected for the case study one are presented. Figure 5.6 for October 1, 2017 CGW event, Figure 5.7 for March 24, 2018 CGW event, and 5.8 for October 18, 2018 CGW event.

Figure 5.6 - The sequential OH images of the October 1, 2017 CGW event from 07:12:50 to 07:15:32 UT.

Figure 5.7 - The sequential OH images of the March 24, 2018 CGW event from 02:48:29 to 02:51:11 UT.

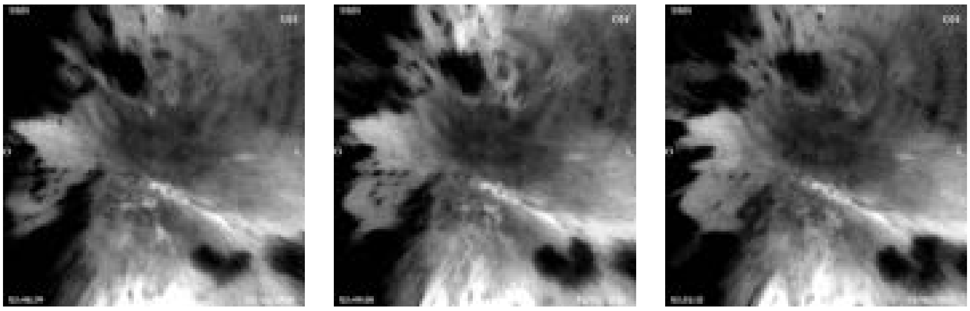

Figure 5.8 - The sequential OH images of October 18, 2018 CGW event from 05:55:43 to 05:58:44 UT.

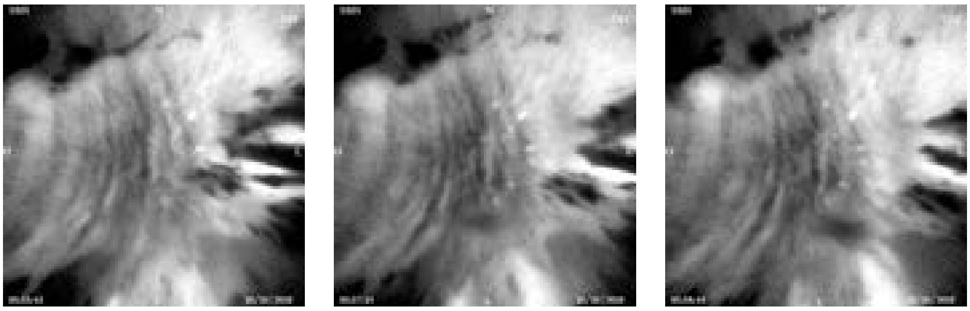

5.4.2 Case study two

The CGW event on October 2, 2019 with three (3) different concentric waves excited at different times is the second case study. The observed parameters of the three waves and their initial excitation times are presented in Table 5.4. The characteristics of these waves corresponds to Event # 29 in Table 5.2, highlighted in gray. For this study, the October 2, 2019 CGW event was selected because this is a single event with different concentric waves occurring at different times on the same night.

Table 5.4 - Observed concentric gravity waves in São Martinho da Serra selected for second case studies.

Event #	Date	I. H	Index	λ_H (km)	τ (min)	c_H (m/s)	Observatory
1	10/02/2019	00:27:53	2	50.30 ± 4.6	11.40 ± 1.9	73.90 ± 10.9	SMS
2	10/02/2019	00:55:56	2	54.90 ± 5.0	10.00 ± 3.0	91.00 ± 9.0	
3	10/02/2019	04:04:50	2	30.50 ± 4.1	7.00 ± 0.9	72.90 ± 8.6	

I. H - Initial Hour

Figure 5.9 shows the first images with visible concentric wavefronts for each of the three CGWs on the night of October 2, 2019 at São Martinho da Serra. In the left panel is the first concentric wave observed at 00:27:53 UT. The middle panel shows the first image of the second concentric wave at 00:55:56 UT and the first image of the third concentric wave at 04:04:50 UT is shown in the right panel.

Figure 5.9 - The visible images with observed concentric wavefronts for each of three CGWs at São Martinho da Serra. The left, middle, and right panels show the CGWs at 00:27:53 UT, 00:55:56 UT, and 04:04:50 UT, respectively.

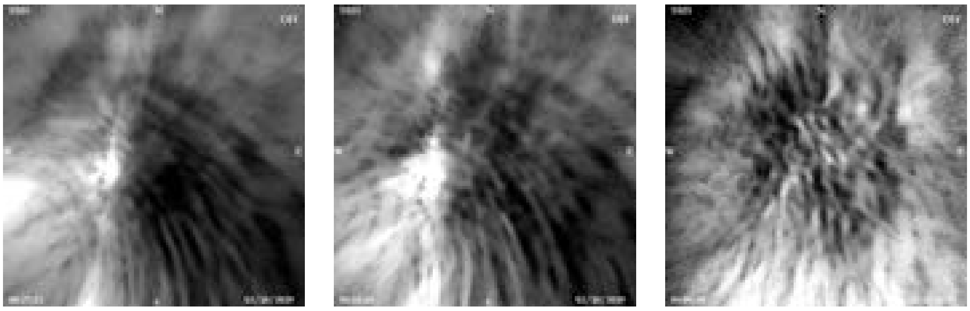

5.4.3 Case study three

The third case studies of this work comprise the three (3) CGWs events highlighted in gray corresponding to Events # 05, 14, and 18 in Table 5.2. These CGW events were observed in São João do Cariri. The selection of this case study is based on the location (i.e., CA), where the CGW events were observed, which is different from the location of case studies 1 and 2. Also, this case study comprises of CGWs events with different concentric wavefronts. The characteristics of these events have been summarized in Table 5.5.

Table 5.5 - Observed concentric gravity waves in São João do Cariri selected for third case studies.

Event #	Date	Index	λ_H (km)	τ (min)	c_H (m/s)	Observatory
1	03/11/2008	2	31.90 ± 2.10	10.80 ± 1.30	49.20 ± 5.10	CA
2	09/09/2016	2	42.50 ± 2.50	12.30 ± 1.10	57.60 ± 5.40	CA
3	05/25/2016	2	30.90 ± 2.05	7.00 ± 1.56	74.10 ± 4.90	CA

A time sequence of three (3) images of the CGW events selected for the third case study are presented in Figures 5.10, 5.11, and 5.12. Figure 5.10 for March 11, 2008 CGW event, Figure 5.11 for September 9, 2016 CGW event, and 5.12 for May 25, 2019 CGW event.

Figure 5.10 - The sequential OH images of the March 11, 2008 CGW event from 21:55:00 to 21:59:14 UT.

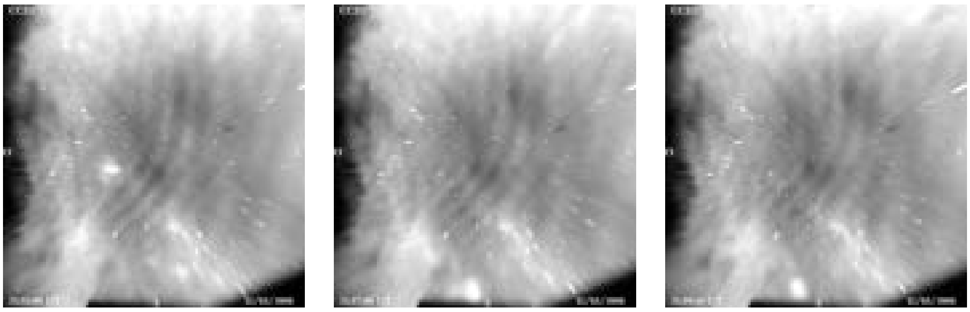

Figure 5.11 - The sequential OH images of the September 9, 2016 CGW event from 05:13:50 to 05:17:56 UT.

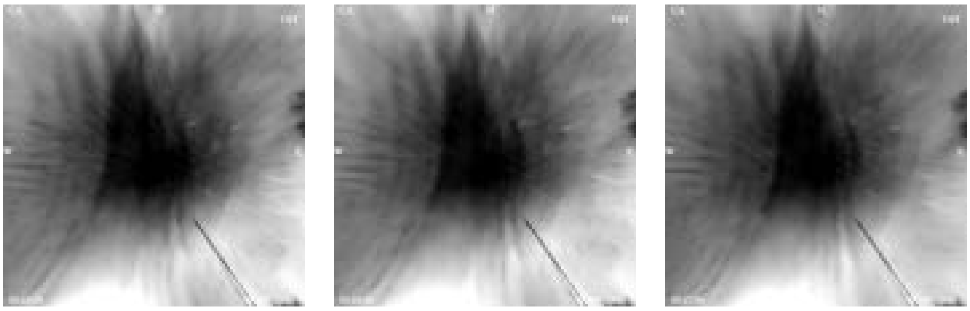

Figure 5.12 - The sequential OH images of the May 25, 2019 CGW event from 21:37:42 to 21:41:17 UT.

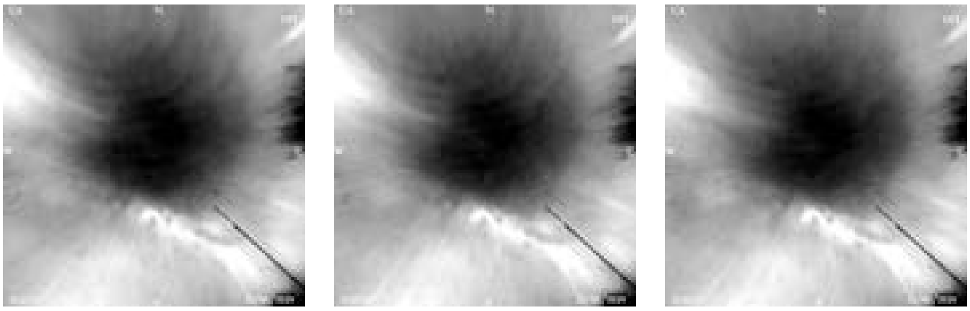

Case studies: one (1), two (2), and three (3) are discussed in Chapters 6, 7, and 8, respectively adapted from a published paper (NYASSOR et al., 2021) and a manuscript under review (NYASSOR et al., Under Review) and a manuscript under revision (NYASSOR et al., Under Revision).

6 CASE STUDIES ON CONCENTRIC GRAVITY WAVES SOURCE USING LIGHTNING FLASH RATE, BRIGHTNESS TEMPERATURE AND BACKWARD RAY TRACING AT SÃO MARTINHO DA SERRA (29.44°S, 53.82°W)[1]

6.1 Introduction

Concentric gravity waves (CGWs) as mentioned earlier in Chapter 2 are generated through the overshooting of the tropopause by a point-like source (YUE et al., 2009; VADAS et al., 2009b). Naturally, sources such as deep convections, earthquakes, and volcanic eruptions (also known as convective plume) are known to have point-like overshooting nature on the tropopause. Analogous to circular ripples generated when a pebble dropped in a pond with a still surface, point-like (pebble-like) overshooting generates CGWs. Propagation of CGWs into the upper atmosphere follows a conical configuration when viewed in a three-dimensional (3D) plane. Viewing CGW in a two-dimensional (2D) horizontal plane, it propagates radially out from the center (VADAS et al., 2009b; VADAS et al., 2012). A 3D description of the generation, propagation, and observation is shown in Figure 6.1.

Figure 6.1 - 3D diagram illustrating the generation, propagation, and observation of concentric gravity waves.

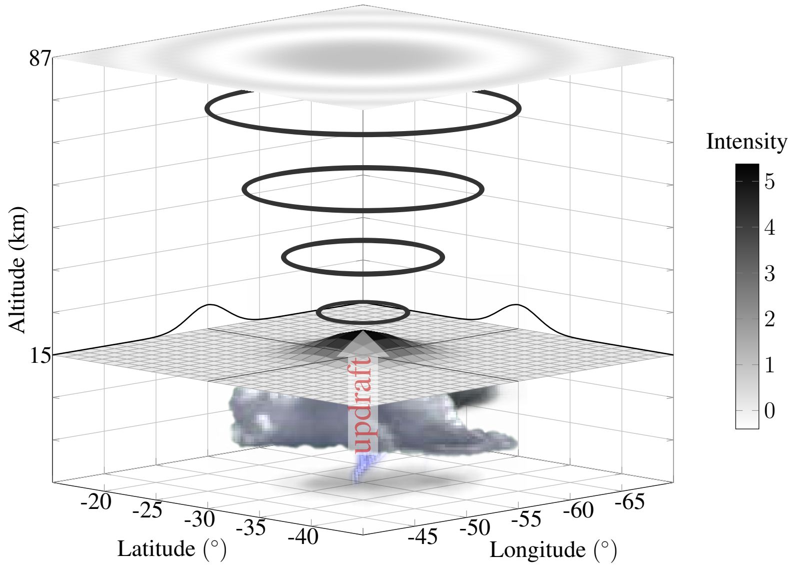

Source: Nyassor et al. (2021).

---

[1] This Chapter is an adapted version of a published paper: Nyassor, P. K., Wrasse, C. M., Gobbi, D., Paulino, I., Vadas, S. L., Naccarato, K. P., et al. (2021). Case studies on concentric gravity waves source using lightning flash rate, brightness temperature and backward ray tracing at São Martinho da Serra (29.44°S, 53.82°W). **Journal of Geophysical Research: Atmospheres**, 126, e2020JD034527. https://doi.org/10.1029/2020JD034527

When an upward moving air or updraft (indicated by the upward arrow labeled “updraft”) in a plume (or cloud) overshoots the tropopause and pushes stably stratified stratospheric air upwards, CGWs are generated as shown in Figure 6.1. Here, the tropopause is set at 15 km and is denoted by the stretched gray mesh. The overshot region of the tropopause by the plume is indicated by the dark-bulge region at the tip of the arrow. This dark-bulge region is analogous to the coldest cloud top temperature region in a GOES infrared CTBT image. Concentric waves are generated after the overshoot region is pulled down by gravity. These waves then propagate upward with increasingly larger concentric rings with altitude (the black circles). The concentric patterns are observed in a 2D projection in the OH emission layer (87 km) as the grey and white concentric rings. Figure 6.1 is centered at the geographic location of São Martinho da Serra.

Besides the observation of CGWs in São Martinho da Serra being a motivation of this work, factors such as the frequent occurrence of intense deep convection and associated lightning activity have as well motivated this work. Since this study aims to relate observed CGWs parameters to an observable parameter of the source, deep convections and their associated lightning activities present the needed basis for such research. For this reason, lightning was included in Figure 6.1 to conceptualized graphically deep convection, updraft, lightning, and overshooting being directly related to the convective sources of the observed CGWs. The inclusion of lightning in this study is based on the direct relation between lightning activity and convective updrafts during severe weather, such as thunderstorms reported in literature (DEIERLING; PETERSEN, 2008; BEDKA et al., 2010; JURKOVIĆ et al., 2015).

Therefore, in case study one, the potential spatial and temporal propagation path leading to the source positions and times of the CGW generation are determined using backward ray tracing. The characteristics of the sources were determined using the CTBT images from the GOES satellite and lightning activity from BrasilDAT lightning sensors. The CTBT images and spatial distribution of the lightning density were used to determine possible overshooting tops by updrafts. On the other hand, the frequency of overshooting by updrafts was estimated from the lightning flash rate.

6.2 Observation and methodology

The observation schemes and methodologies employed in the work of Nyassor et al. (2021), follow a similar description given in the observation, instrumentation, and models chapter (i.e., Chapter 3) and general methodology chapter (i.e., Chapter 4). The specific observation schemes and methodologies employed in Nyassor et al. (2021) are summarized in Table 6.1.

Table 6.1 - Summary of observation and methodology described in Chapter 4 employed in Nyassor et al. (2021).

Phenomena	Observation	Chapter	Methodology	Chapter
CGWs	All-sky imager	3.2.1	Image preprocessing	4.1.1
			Spectral analysis	4.1.2
			Ray tracing	4.2
			CGWs Center	4.4
CTBT	GOES	3.2.6	Overshooting tops	4.5.1
Lightning activities	BrasilDAT	3.2.4	Lightning densities	4.6.1
			Lightning flash rate	4.6.2

6.3 Results and discussion

6.3.1 The observed CGWs cases

The observed CGW on October 1, 2017 (hereafter Case 1) propagated approximately an hour and a half starting 06:44:27 UT, whereas the CGW events on March 24, 2018 (hereafter Case 2) and October 18, 2018 (hereafter Case 3) propagated for about 40 minutes. The Case 2 waves were visible in the all-sky images between 02:29:34 UT and 03:10:06 UT and for Case 3, they were visible between 05:36:10 UT and 06:16:48 UT. In Figure 6.2, the unwarped OH images of Cases 1, 2, and 3 are shown in the left, middle, and right panels, respectively. The location of the observation site is shown by the white triangle at the center of each image. In Table 6.2 the parameters of the CGW events are presented.

Table 6.2 - Concentric gravity waves parameters of the selected case studies at São Martinho da Serra.

Wave Parameters		**Case 1**	**Case 2**	**Case 3**
		10/01/2017	**03/24/2018**	**10/18/2018**
λ_H	(km)	48.20	31.32	44.90
ϕ	(°)	48.60	95.50	105.30
c_{obs}	(m/s)	60.20	72.50	76.10
τ_{obs}	(min)	13.30	07.20	09.80

Source: Nyassor et al. (2021).

To locate the source locations of these gravity waves in the troposphere, a ray tracing model was used to calculate the propagation paths of the gravity waves backward in space and time. The results obtained from the ray tracing for each CGWs event are shown in

Figure 6.2 - Unwarped hydroxyl (OH) images of the concentric gravity wave events observed at the Southern Space Observatory (SSO) of the National Institute for Space Research (INPE) in São Martinho da Serra.

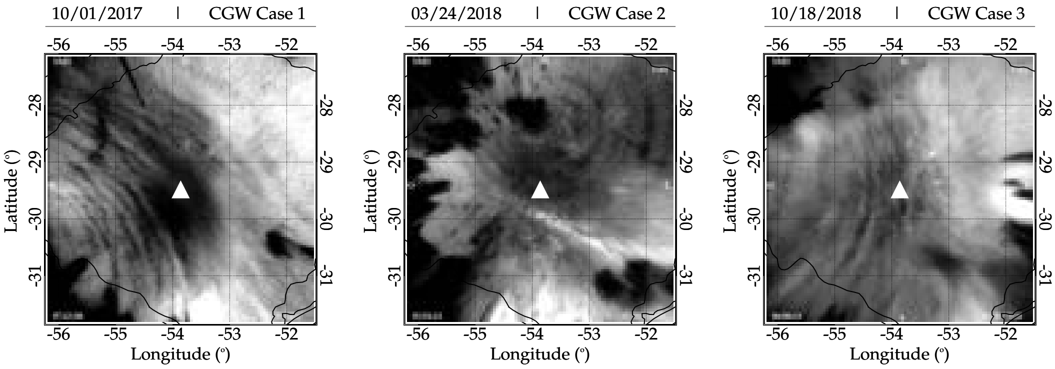

The white triangle shows the location of the SSO/INPE observatory. The state borders of Rio Grande do Sul are the black solid lines extending across the corners of each image.
Source: Nyassor et al. (2021).

Figure 6.3. For each event, the zero wind ray path is depicted by the red solid line, while the blue solid line is the model wind path of the wave as presented in Section 4.3.

The position and time where and when the ray paths stopped are depicted by the red and blue filled circles. The possible location (longitude and latitude) closest to the tropopause and the nearest time of overshooting each GW may have been generated from are indicated by the black asterisks over-plotted on the zero and model wind ray paths. The location (longitude, latitude) and altitude where the ray tracing began is presented by the black plus sign. The black triangle shows the center of the image and the location of the observation site, whereas the center of the first concentric gravity wave crest on the image (represented by a red dashed circle) is represented by the black diamond. In the upper panels, the OH airglow emission altitude is depicted by the black dotted lines. It has been reported in literature (ALEXANDER; PFISTER, 1995; HOLTON; ALEXANDER, 1999; SONG et al., 2003; VADAS et al., 2009a; YUE et al., 2009; XU et al., 2015; AZEEM et al., 2015) that high frequency concentric gravity waves are excited by convective overshooting by strong updrafts during thunderstorms. Since overshooting is indicated by the minimum temperature region in CTBT images, the position and time when the ray path of the wave reached the tropopause was used to obtain the nearest CTBT images. In the lower panels of Figure 6.3, the CTBT for each CGW event was over-plotted together with the ray paths on the map.

Two wind models used in the ray tracing showed when and where the ray path of each

Figure 6.3 - Ray tracing results of the three concentric gravity wave events presented in Figure 6.2.

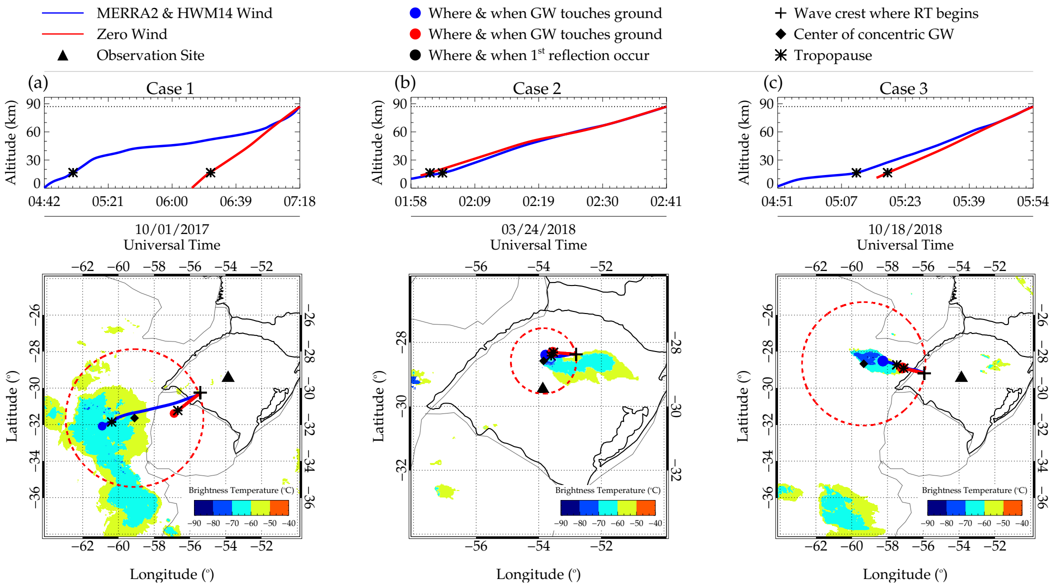

The temporal variations of the zero and model wind ray paths of the gravity wave with altitude are shown in the upper panels. In the lower panels, the spatial variations in longitude and latitude of the ray paths are shown. Panels (a), (b), and (c) represent the CGW Cases 1, 2, and 3, respectively. Source: Nyassor et al. (2021).

gravity wave stops. The ray paths of the zero and model winds for Case 2 and Case 3 ended below the tropopause except for Case 1. A summary of the tropopause altitude locations of the GWs adapted from Nyassor et al. (2021) is presented in Table 6.3. These locations indicate where the GWs may have been possibly excited from.

Table 6.3 - Locations of the CGWs at the tropopause altitude from reverse ray tracing.

Wind Models	**Case 1**		**Case 2**		**Case 3**	
	Lon	Lat	Lon	Lat	Lon	Lat
1	56.68°W	31.23°S	53.61°W	28.42°S	57.10°W	28.91°S
2	60.37°W	31.86°S	53.61°W	28.42°S	57.48°W	28.73°S

Source: Nyassor et al. (2021).

Here, the model winds ray paths are considered first. Since variation in the propagation path of a wave is mainly controlled by the background wind, variation in the ray traced path is expected (VADAS et al., 2009b; WRASSE et al., 2006; WRASSE et al., 2006). Previous studies (VADAS et al., 2009b; YUE et al., 2009; VADAS et al., 2012; XU et al., 2015) have shown that CGWs can propagate to the mesopause region without significant filtering and wavefront distortion effects if the background wind is smaller than 30 m/s. The propagation paths of CGW Cases 2 and 3 showed that the background winds during these events were weak. However, Case 1 showed otherwise with the magnitude of the zonal wind varying between 12 m/s west to 52 m/s east. The differences between the zero and model winds ray paths explain the observed weak winds during Cases 2 and 3. Also, it was observed that the tropopause positions of the model wind ray paths were consistent with the locations of the thunderstorms (shown by the CTBT images overplotted in lower panels of Figure 6.3). As a result of these consistencies, these waves were presumed to be excited just above the tops of the clouds and propagated up to the mesosphere.

As mentioned earlier, the main determining factor of GW propagation is the background wind. However, for all three CGW events under study, the magnitudes of the winds in all directions are smaller than the horizontal phase speeds of the waves. To further explore the effect of the wind on the propagation of the wave, a blocking diagram was used (TAYLOR et al., 1993).

The construction of the blocking diagram follows the procedure of Taylor et al. (1993), where the intrinsic frequency of the wave was defined as,

$$\Omega = \omega - k_H U_H = \omega\left[1 - \frac{U_H}{c_H}\right], \tag{6.1}$$

where ω is the observed frequency of the wave, k_H is the magnitude of the horizontal wave vector, U_H is the wind along the wave propagation direction (ϕ), and c_H is the observed horizontal phase speed of the wave. To obtain the zonal (U_x) and meridional (U_y) components of the horizontal wind (U_H), the right-hand side of Equation 6.1 was expanded to yield:

$$\Omega = \omega\left[1 - \frac{U_x \cos\phi + U_y \sin\phi}{c_H}\right]. \tag{6.2}$$

As discussed in Chapter 2, when U_H approaches c_H, the wave is said to be approaching a critical level. As a result, the intrinsic frequency Ω of a wave under such conditions, in turn, approaches zero. Therefore, as a wave approaches a critical level, Equation 6.2 then becomes:

$$c_H = U_x \cos\phi + U_y \sin\phi. \quad (6.3)$$

In a polar plot representation as shown in Figure 6.4, Equation 6.3 represents c_H for every known azimuth of U_x and U_y. In Figure 6.4, a 2D blocking diagram using the model wind from each CGW event is presented.

Figure 6.4 - Blocking diagram showing the magnitude and direction of the wind from the model wind used in the ray tracing for the three concentric gravity wave (CGW) events.

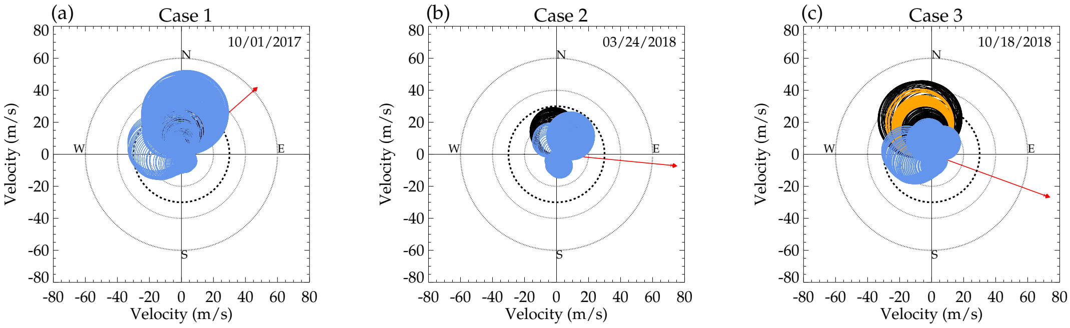

The magnitude and direction of the wave are depicted by the red arrows. The black and light blue rings represent the magnitudes and directions of the winds below the tropopause and above the tropopause, respectively. In panel (c), the orange rings represent the magnitude and directions of the wind from the altitude of the tropopause to 30 km. In each panel, the dotted circles indicate velocity intervals at each 20 m/s. The black dashed circles show the velocity in intervals of 30 m/s. Source: Nyassor et al. (2021).

The magnitude and direction of the phase speed of the wave are represented by the red arrows. Wind profiles from the ray tracing paths were used to construct the blocking diagrams. It is important to mention that the spatial and temporal variation in the wind profiles follows the dynamics of the ray paths. The forbidden regions (i.e., regions where GW are not likely permitted to propagate) from the Earth's surface to the tropopause are depicted by the black rings. The light blue rings show the forbidden regions between the tropopause and mesopause. The dashed circle in each panel is used to indicate a 30 m/s velocity mark of the wind. This 30 m/s mark is used as a standard to differentiate between weak and strong winds (VADAS et al., 2012). The dotted circles are used to indicate the velocities at 20, 40, and 60 m/s.

From panel (a), a maximum northward wind speed of ~50 m/s was observed for CGW Case 1, whereas the phase speed of this wave was 60 m/s. However, the blocking diagram between the northeastern and southwestern directions showed that the speed of the wind was less than 30 m/s. Here, it can be observed that the wave might propagate through part of the forbidden region and might suffer some degree of absorption as a result. The effect of the absorption on the vertical propagation of the wave could be the reason for a shallower horizontal propagation path observed in the ray tracing result of this case in the lower panel (a) of Figure 6.3.

Similar behavior of the Case 1 blocking diagram was seen in the Case 3 blocking diagram except for the propagation direction of the wave being opposite to the forbidden region. The forbidden region was strong in the northwestern direction with a maximum wind magnitude of ∼45 m/s, whereas the wave propagated southeastward at 76.1 m/s. The blocking diagrams of Cases 1 and 3 showed that these waves did not suffer significant filtering and structure distortion effect. This explains the vertical propagation of the concentric waves to the OH emission altitude. The opposite propagation directions of the Case 3 wave and the wind, and also the propagation of Cases 1 and 3 waves through some part of the forbidden region favored a longer horizontal propagation. This was evident in their respective ray tracing results.

As mentioned earlier, the model winds used to construct the blocking diagram of CGW Case 2 were less than 30 m/s from the surface of the Earth to the OH emission altitude and in all directions. For this reason, almost a 360° concentric wavefront was observed in the middle panel of Figure 6.2. A concentric wavefront of such a configuration showed that little or no filtering and wavefront distortion occurred. However, part of the concentric wavefronts was not clear due to the coverage of the cloud across the field of view of the all-sky imager (YUE et al., 2009; XU et al., 2015), whereas other parts were due to dissipation. The cloud coverage, on the other hand, affected the contrast of the image. It is important to mention here that the estimated center and the tropopause positions of the ray paths used to determine the source location of this wave located almost the same position as shown in panel (b) of Figure 6.3. Besides the two methods used to determine the source location pointed to a similar location which signifies weak winds, these weak winds were also affirmed by the tropopause positions of the zero and model winds ray paths. The effect of the wind during this night on the CGW Case 2 is in agreement with previous modeled work by Vadas et al. (2009b) and Vadas et al. (2012), where almost 360° concentric patterns were seen when the wind was less than 30 m/s.

Convective overshooting of the tropopause is known to be the main excitation mechanism of the CGWs. However, for concentric waves to be excited, the overshooting of the tropopause must extend vertically into the stratosphere by 1 to 3 km (YUE et al., 2009;

VADAS et al., 2009b; NYASSOR et al., 2021). For CGW Cases 1, 2, and 3, the vertical extent by which the tropopause was overshoot was estimated to investigate whether or not overshooting was the likely excitation mechanism. To determine the overshooting extent, the tropopause altitude and temperature must first be determined. Radiosonde measurements from the nearest (i.e., longitude and latitude) radiosonde launch sites were used to determine the tropopause temperatures and altitudes. The locations of the launch sites for Cases 1, 2, and 3 were Cordoba (64.21°W, 31.30°S), Santa Maria (53.87°W, 29.48°S), and Uruguaiana (57.03°W, 29.78°S), respectively. Using the lapse rate tropopause definition, the tropopause altitudes were estimated to be 17.12, 16.33, and 16.39 km for Cordoba, Santa Maria, and Uruguaiana, respectively. The corresponding minimum CTBT values for each CGW event (shown in Figure 6.2) are plotted in Figure 6.5.

Figure 6.5 - The minimum cloud top brightness temperature (CTBT) distribution, the tropopause positions of the ray paths, and final positions.

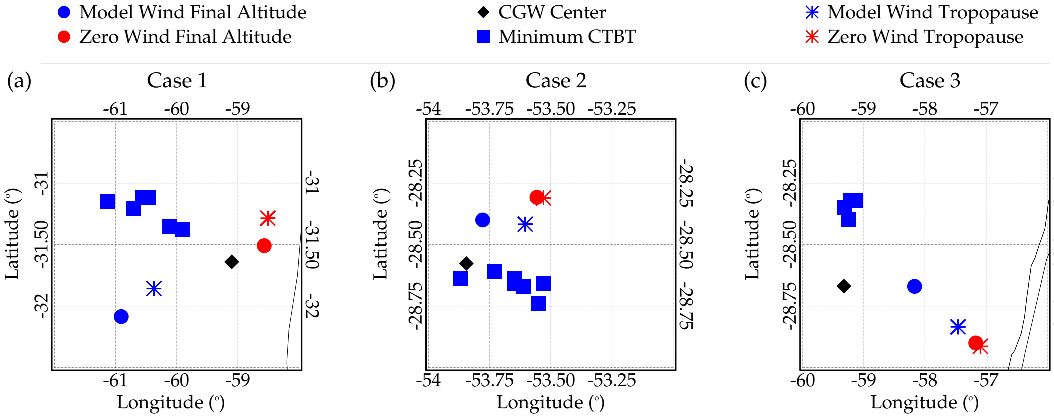

The position of each minimum CTBT is depicted by the blue squares. The red and blue filled circles show the final ray path positions of the zero and model winds, whereas the tropopause positions from the zero and model winds ray paths are depicted by red and blue asterisks.
Source: Nyassor et al. (2021).

A summary of the locations of the radiosonde launch sites, the tropopause altitudes, tropopause temperatures, the wave excitation times, the excitation times determined from Equation 6.4, CAPE, and temperature range of the CTBT are presented in Table 6.4.

To obtain the CTBT images corresponding to the possible excitation positions and times, the wind model ray path positions and times of the CGWs at the tropopause were used. Furthermore, to determine the exact positions of the overshooting tops, the longitudes and latitudes of the minimum CTBT (i.e., the proxy for identifying overshooting tops (BLUESTEIN et al., 2019)) were determined 30 minutes before and after the wave exci-

Table 6.4 - Summary of the radiosonde measurements, time of wave excitation determined by the ray tracing and the minimum CTBT (proxy of the overshooting tops).

Gravity Wave Event		**Case 1**	**Case 2**	**Case 3**
Latitude	(°S)	31.30	29.48	29.78
Longitude	(°W)	64.21	53.87	57.03
Trop. Alt	(km)	17.12	16.30	16.39
Excitation time	Zero wind (UT)	06:24	02:01	05:19
	Model wind (UT)	05:00	02:03	05:12
Equation 6.4	(UT)	04:24	02:01	04:34
Trop. Temp	(°C)	-65.30	-65.32	-77.00
CAPE	(J/kg)	767 - 877	1887 - 2064	2554 - 2779
CTBT Range	(°C)	-74 to -70	-76 to -71	-85 to -86

CAPE - Convective Available Potential Energy
CTBT - Cold Top Brightness Temperature

Source: Nyassor et al. (2021).

tation estimated times, determined by the model wind ray paths. These determined positions are shown in Figure 6.5. The blue squares show the overshooting tops in Figure 6.5, whereas the positions of the determined centers of the CGWs are depicted by the diamonds. The final and tropopause positions of the zero and model wind ray paths are indicated by the blue and red filled circles, and blue and red asterisks, respectively. GW generation by overshooting has been extensively investigated (LANE, 2015). The main source mechanisms of primary GWs with concentric structures observed in the middle and upper atmosphere were found to be point-like convective overshooting tops (YUE et al., 2009; YUE et al., 2013; YUE et al., 2014; XU et al., 2015). In most reported observed CGW events, CTBT images showed very cold cloud top temperatures before the CGW events (YUE et al., 2009; YUE et al., 2013; YUE et al., 2014; XU et al., 2015).

The distribution of the minimum CTBT in space suggests that the most likely source of these CGWs is through the overshooting of the tropopause. The tropopause locations of the model winds ray paths and the overshooting tops were found to be close, especially for Case 1 and Case 2 of Figure 6.5. The distance between the model winds ray paths tropopause positions and the closest minimum CTBT for Cases 1 and 2 are ∼73 km and ∼25 km, respectively. On the other hand, the tropopause position (blue asterisk) of Case 3 was found to be ∼212 km away from the central CTBT region (panel (c)). This difference in the two positions can be related to the MERRA-2 winds below 70 km and the HWM14 climatology winds above 70 km (monthly averages). These winds may differ from the actual winds during the event. A clear indication of the occurrence of the convective overshooting is that the minimum temperatures of the CTBT are colder than the tropopause temperatures.

Apart from using the ray tracing model to determine the excitation time of the observed GWs, the time the GW propagated from the tropopause to the OH emission altitude assuming zero background wind was also estimated using (VADAS et al., 2009b):

$$\Delta t = \frac{2\pi R^2 \left(1 + \Delta z^2 / R^2\right)^{3/2}}{N \Delta z \lambda_H}, \tag{6.4}$$

where Δt is the time the wave takes to propagate from the altitude of excitation (tropopause) to the observation altitude, R is the radius of the CGWs, Δz is the distance between the tropopause altitude and observation altitude, N is the Brunt Väisälä frequency, and λ_H is the horizontal wavelength of the CGW.

From Equation 6.4, the estimated excitation times for Cases 1 and 3 were found to be 4 hours before the observation of the CGW events. However, the ray tracing estimated excitation times were 2 hours and 45 minutes earlier, respectively. The difference in the estimated excitation times from the ray tracing and Equation 6.4 occur because Equation 6.4 is a theoretical estimate which assumes weak or zero background wind. However, this assumption is invalid for these cases since the background wind is greater than 30 m/s (see panels (a) and (c) of Figure 6.4).

On the other hand, the estimated excitation time of CGW Case 2 using Equation 6.4 and ray tracing showed that this CGW was excited ~40 minutes earlier before the observation of the wave in the OH emission altitude. Since the background wind was small, the tropopause position of zero and model winds ray paths, and the estimated radius all pointed to nearly a similar source location. As a result, this similarity in the estimated excitation time from the two approaches was expected. Also, the wind used in the blocking diagram showed magnitudes less than 30 m/s (found within the black dashed circle shown in panel (b) of Figure 6.4) in all directions during the wave event. This result is in good agreement with published results (VADAS et al., 2009b; YUE et al., 2009). Also, in Table 6.4, the excitation times are presented.

6.3.2 Tropospheric source

Gravity waves are generated when an updraft overshoots the tropopause by 1 - 3 km (LANE et al., 2001). It is, therefore, necessary to know the vertical extent to which the tropopause was overshot into the stratosphere to determine the altitude of the overshooting top (OT).

However, no observational data were available to determine the OT, hence, we adapted the method of OT estimation defined by Equation 6.5 from Griffin et al. (2016). Since the coldest region on GOES CTBT infrared image indicates overshooting top (BEDKA et al., 2010), it is expected that the tropopause must be warmer than the overshot region.

$$OT_{Height} = H_{Trop} + \frac{OT_{BT} - T_{Trop}}{OT_{LR}}, \tag{6.5}$$

where H_{Trop} is the tropopause height, OT_{BT} is the brightness temperature of the OT, T_{Trop} is the tropopause temperature and OT_{LR} is the OT lapse rate. The OT lapse rate is taken to be -7.34 K/km.

To estimate the OT height using Equation 6.5, the input parameters are the tropopause height and temperature from radiosonde measurements and minimum CTBT from GOES infrared images. All these parameters are presented in Table 6.4. From Equation 6.5, the estimated average OT showed that the tropopause was overshoot by 1.0, 1.2, and 1.3 km for CGW Cases 1, 2, and 3, respectively. The individual OTs corresponding to each minimum CTBT, the average OT, and the tropopause height are presented graphically in Figure 6.6. In each panel of Figure 6.6, the individual minimum CTBT, the average OT altitude, and the tropopause altitude are depicted by the blue square, the red dashed line, and the black line.

Figure 6.6 - The estimated overshooting tops (minimum cloud top brightness temperature (CTBT)) altitude for the three concentric gravity wave (CGW) events.

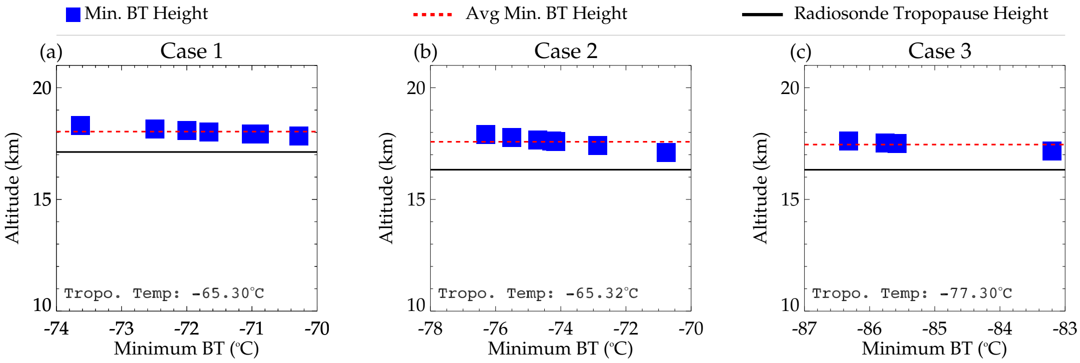

The blue square, the red dashed line, and the black solid line represent the overshooting top (OT) altitude for each minimum CTBT, the mean OT altitude, and the tropopause altitude, respectively. Source: Nyassor et al. (2021).

Furthermore, before the excitation (overshooting) time, the CAPE derived from radiosonde measurement showed values high enough to produce strong maximum updraft velocities that can lead to overshootings. The CAPE values presented in Table 6.4 were used to estimate the maximum updraft velocities, $w \sim \sqrt{2.CAPE}$ (HOLTON, 1992). For Case 1, Case 2, and Case 3, their estimated maximum updraft velocities range between 39 - 42 m/s, 61 - 64 m/s, and 71 - 75 m/s, respectively.

Previous studies (HOLTON, 1992; VADAS et al., 2012), estimated the vertical velocity of the updrafts in the convection region using CAPE. In relation to GWs, Vadas and Fritts (2009) estimated the amplitudes of GWs excited by updrafts. Also, CAPE can indicate the size of hail (BLUESTEIN, 1993) and the intensity of lightning (BEDKA et al., 2010). Stronger updrafts yield larger hail since these updrafts can hold the hail up longer in the updraft before the hail succumbs to gravity and falls out of the updraft. During the CGWs event on September 8 - 9, 2005 at Colorado, hail of different sizes were observed with their sizes related to the updraft (VADAS et al., 2012). The authors further showed that the locations of the hail and convective overshoot were within a similar region. On the other hand, strong lightning activity close to the location of convective overshooting tops had been reported by Bedka et al. (2010).

Owing to this, lightning activity was investigated within the time range of the CTBT image prior to the time of observation of the wave event. The lightning data were obtained from the Brazilian lightning detection network (BrasilDAT) sensors. Lightning data within a radius of ~1,000 km around the SMS observatory was considered. This range was chosen due to the maximum distance of the model wind ray path of the wave from the tropopause. Further information on the instrumentation of BrasilDAT lightning sensors can be found in Section 3.2.4. To extract the necessary information from the lightning data, two main analyses were performed: (a) determination of the spatial distribution of lightning and (b) the estimation of the lightning flash rate. The spatial distribution of the lightning was determined by binning in $0.06° \times 0.06°$ grid boxes in longitude and latitude. On the other hand, the lightning flash rate was estimated by computing the lightning flashes per minute for the entire time range considered. In panels (a), (b), and (c) of Figure 6.7(iii), the spatial distribution of the lightning densities and the CTBT of CGW Cases 1, 2, and 3 are presented, respectively, with the zoomed region denoted by the dashed-dotted lines in the right-hand panels.

Figure 6.7 - The comparison between the spatial distribution of lightning density and overshooting tops (minimum CTBT).

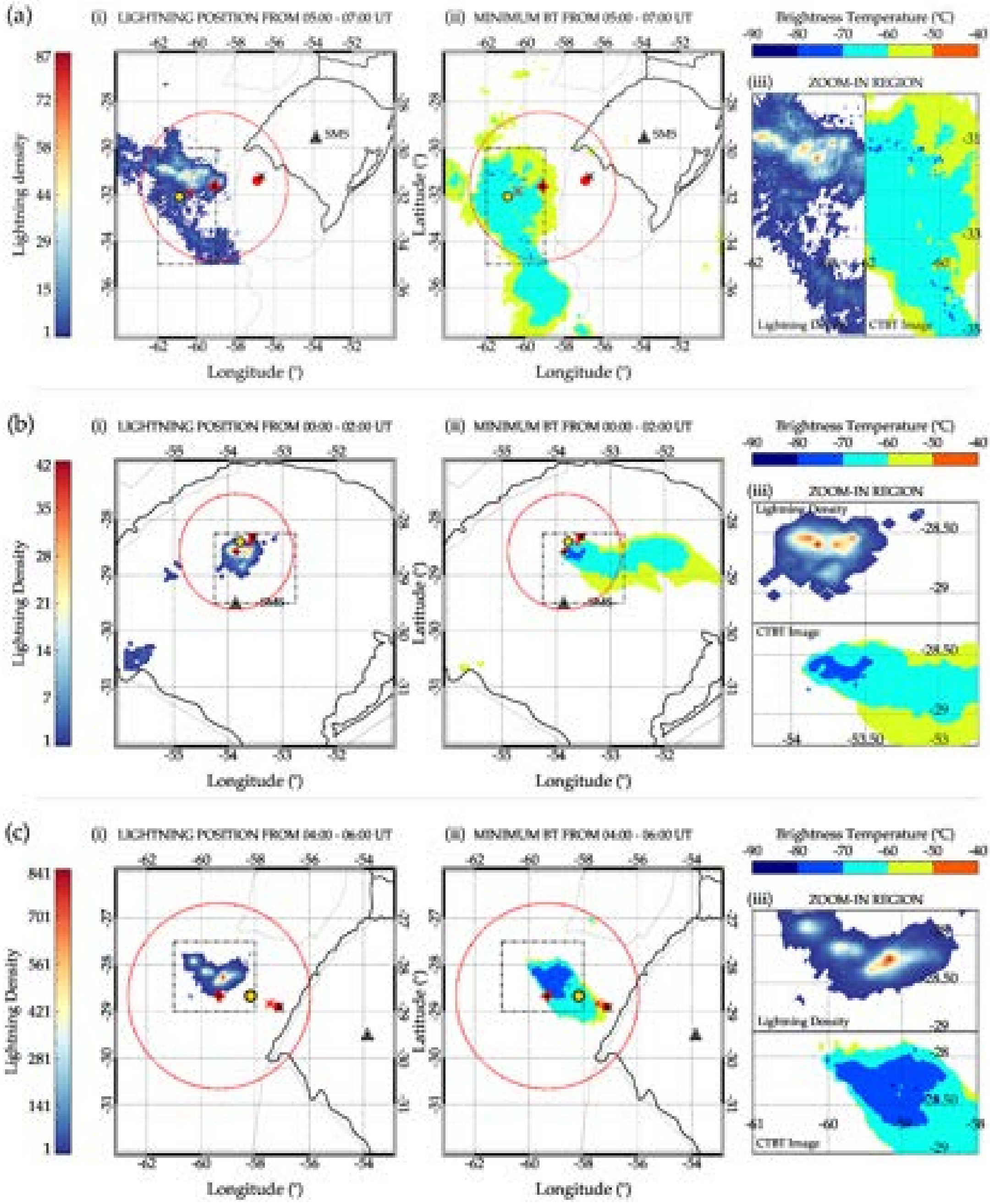

Panel (a), (b), and (c) represent CGW Case 1, Case 2, and Case 3, respectively. (i) of each panel represents the spatial distribution of the density of lightning flashes, whereas (ii) shows the overshooting tops (coldest BT region). The gold filled circle with black outline depicts the final position of the model wind ray path and the red filled circle shows the final position of the zero wind ray path. The center of the red dashed circle is indicated by the red star with black dot. The asterisks beside each final ray path position are the tropopause locations. (iii) in each panel shows the zoom-in of the area depicted by black dashed-dotted lines in (i) and (ii). The red dashed circle is the same as in Figure 6.3.

Source: Nyassor et al. (2021).

In all the three CGW events, it is clear that the positions of the highest lightning densities in Figure 6.7 agree well with the regions with minimum CTBT (OTs). The results also agree with previous works (BEDKA et al., 2010; JURKOVIĆ et al., 2015) that related OTs (minimum CTBT) to intensive lightning activity. Bedka et al. (2010) in their observational studies, showed a considerable amount of occurrence of lightning activity around OTs. The authors further showed that colder CTBT (>200 K or <-73.15°C) identified by satellite images had high occurrence of lightning within 10 km radius around the overshooting tops. In central Europe, Jurković et al. (2015) related lightning, OTs, and hails to strong convective storms. They further observed a significant increase in the lightning strokes at the time of overshooting. In one of the cases studied by Jurković et al. (2015), they observed production of hail and at the same time a jump in the lightning flash rate from 25 to 92 strokes per minute. Such a drastic change in strokes per minute indicates a strong updraft (SCHULTZ et al., 2009; EMERSIC et al., 2011). Similar behavior of the lightning activity analysis for the three CGW cases was observed, with the highest lightning activity showing a significant amount of high densities in the region of the OTs especially for Case number 3.

Similarly, the spatial and temporal distribution of OTs in the BT plot (Figure 6.7(ii)) agrees well with the spatial and temporal distribution of the lightning strokes density (Figure 6.7(i)). In Figure 6.7, the stopping position of the model wind ray path, the tropopause position of the model wind ray path, and the determined center are close to the region of high lightning density and the OTs (minimum BT regions). Lightning jumps were also observed exactly at the times of the coldest region. This coldest region is indicated by blue small structures on the CTBT images with temperature range between -70°C and -80°C for Cases 1 and 2, whereas -80°C to -90°C for Case 3.

To relate the lightning activity to OTs and then to the observed wave periods, the temporal variations in the lightning flash rate were used. To determine the lightning flash rate, the number of lightning flashes per minute was computed for both total and intracloud (IC) lightning by tracking the thunderstorm cell based on the GOES-16 imagery. Also, the window within the lightning was counted, while moving together with the storm. Lightning jumps, which are an indication of a change in the updraft were observed in the lightning flash rate variation (BEDKA et al., 2010; JURKOVIĆ et al., 2015). The times of occurrence of the lightning jumps were identified in the lightning flash rates time series (shown in Figure 6.8) and then compared to the times when minimum CTBT (or OTs) were seen in the GOES-16 infrared CTBT images.

Figure 6.8 - The comparison between image sequence of GOES-16 and the time series of lightning strokes per minutes.

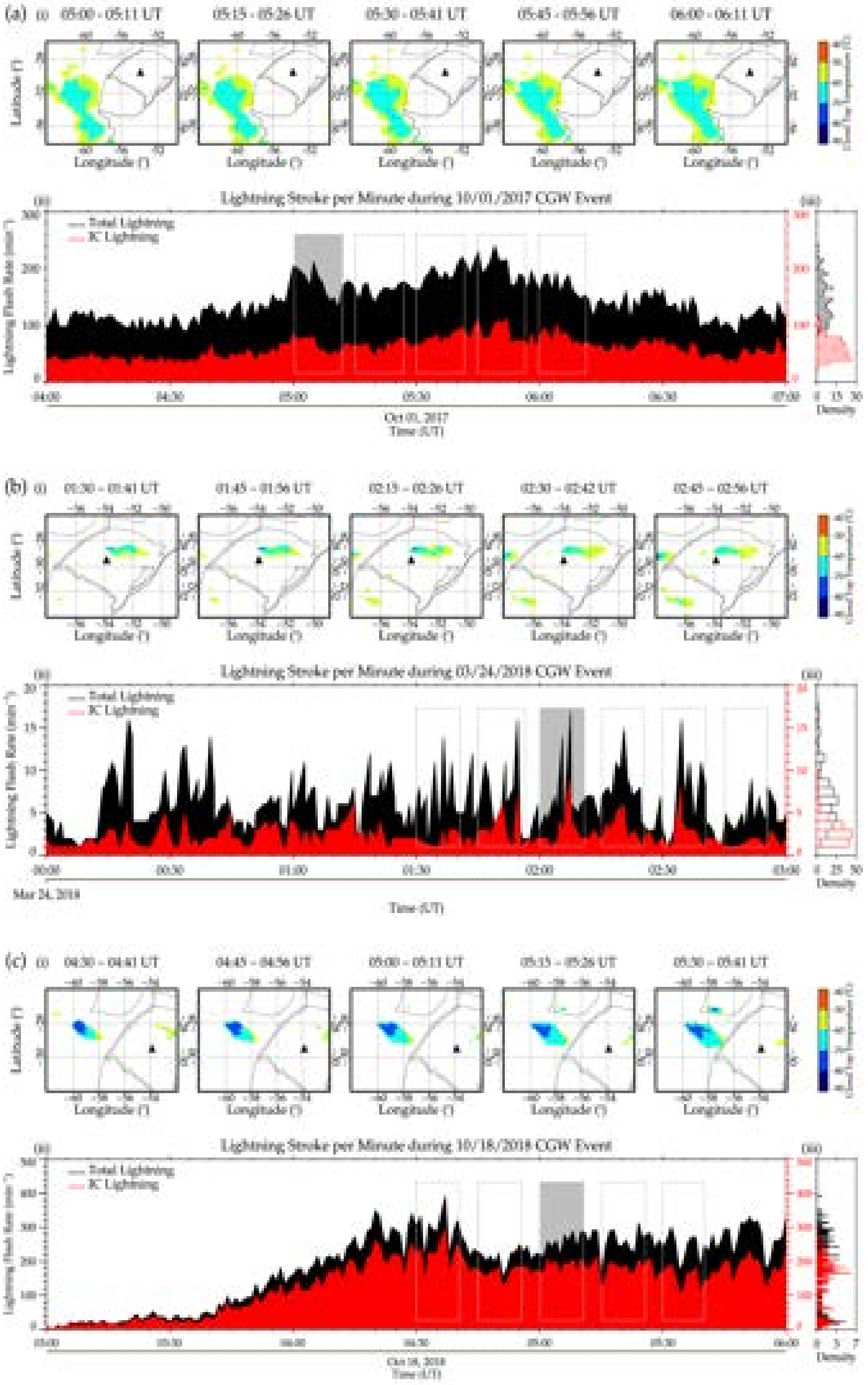

The upper (a), middle (b), and lower (c) panels represent the concentric gravity wave (CGW) events for Cases 1, 2, and 3, respectively. For each case, (i) represents image sequence of cloud top brightness temperature (CTBT) within the time range of the lightning time series, (ii) shows the time series, and (iii) the densities of the lightning rate of both total and intracloud lightning. The rectangles sequentially represent the CTBT GOES-16 images in (i). The gray shaded region depicts the time when the wave ray path reaches the tropopause which is considered to be the likely excitation time.

Source: Nyassor et al. (2021).

A time series image was constructed including the images that corresponded to the estimated wave excitation time obtained from the ray tracing results in order to follow the evolution of the OTs in time using CTBT images. In Figure 6.8, each rectangle on the time-lightning stroke plot corresponds to their respective CTBT image within the same time interval. The estimated time of the wave excitation (at the tropopause) by the ray tracing model is represented by the gray shaded regions. Several lightning jumps were observed in the lightning rate for all 3 events presented. A significant jump occurred ∼05:00 UT with the second one occurring ∼5 minutes later for the CGW Case 1. These two jumps occurred within the shaded region that is the estimated time for wave excitation. However, other jumps were also observed with the highest being within the time frame of 05:45 - 05:56 UT.

The Case 3 ray tracing result indicated that this gravity wave was excited ∼40 minutes (i.e., around 05:12 UT) before the observation time (see the upper panel of Figure 6.3c). The lower panel of the same figure, on the other hand, showed that the estimated excitation location was ∼212 km from the minimum CTBT image that corresponds to the time of excitation from the upper panel of Figure 6.3c. The positions of the estimated OTs corresponding to the minimum CTBT from 05:00 - 05:46 UT showed that no significant overshootings occurred. Also, no significant jump was seen during the estimated excitation time; instead, the jump was observed between ∼04:30 and 04:41 UT. However, the wind speed from the tropopause to ∼30 km altitude was between 29 and 38 m/s (the orange regions in Figure 6.4c) in the northwestern direction. As mentioned earlier, the model wind used in the ray tracing includes climatology winds above 70 km, which only give a guide of the winds that evening.

Even though the lightning rate values of the CGW Case 2 were not as large as that of Case 1, a lot of lumps were observed with a peak at ∼02:07 UT. However, no CTBT image was available at this time. Also, no significant displacement was observed in the position of the convective plume (cloud) within the set time frame. According to Cooney et al. (2018), the lifetime of an overshooting event spans ∼5 - 10 minutes. The ray tracing indicated that the estimated excitation time (the gray shaded region in panel (b(ii)) of Figure 6.8) of the wave corresponded to the CTBT time frame of 02:00 UT - 02:11 UT, if there was an observation. Schultz et al. (2009), Bedka et al. (2010), and Jurković et al. (2015) also referred to lightning jump as a consequence of the change in the updraft and overshooting event (BEDKA et al., 2010; JURKOVIĆ et al., 2015), therefore, in the absence of CTBT image during this jump yet having 4 minutes difference in time between the images, it is possible that this jump could have been captured by the overshooting event in the image before, hence the image before the jump was used as a reference. As stated earlier, the actual winds may differ from the HWM14 climatology winds above 70 km during this event, therefore the results obtained are likely within the error bars of the uncertainties in the wind.

According to Lane et al. (2001), and Vadas et al. (2009b), the width and depth of a convective plume are related to the horizontal and vertical wavelengths of the dominant excited GWs by a plume. So, the intrinsic period of the dominant characteristic wave generated by convective plume can be estimated using (VADAS et al., 2009b):

$$\tau_c = \tau_b \sqrt{\left[\frac{\mathcal{D}_H}{\mathcal{D}_Z}\right]^2 + 1}, \tag{6.6}$$

where the characteristic period is τ_c, the buoyancy period, $\tau_b = 2\pi/N$, the width of the plume is given as $\mathcal{D}_H$, and the depth of the plume as $\mathcal{D}_Z$. Because the depths and widths are similar, the GW generated by convective plume have periods ranging between 5 and 15 minutes, which is close to the Brunt Väisälä frequency, similar to Lane et al. (2001).

The widths of the plumes (the region of GOES-16 infrared CTBT images with the coldest brightness temperature) in this work were determined and found to range between 14 and 25 km. These values agreed well with the typical horizontal extent of convective plume reported by Vadas et al. (2012). Here, two images before the image corresponding to the time when the model wind ray path reached the tropopause were considered. Taking the depth of the plume to be 10 km (VADAS et al., 2009b) and using Equation 6.6, the characteristic periods of the waves range from 8 to 14 minutes. The range of periods of the gravity waves estimated in this study is similar to the periods reported by Vadas et al. (2009b). The periods in the lightning flash rate oscillations are computed next.

Williams et al. (1999) mentioned that lightning jumps indicate updraft. Also, updraft leads to convective overshooting (JURKOVIĆ et al., 2015) that consequently generate GWs, therefore lightning jumps may indicate gravity wave generation. One can then say that if all or a majority of lightning jumps occur when updrafts overshot the tropopause, then the frequency of the jumps can be related to the frequency of the updraft as well as the frequency of the generated gravity wave. Further analyses were performed on the time series of the lightning flash rate within the set of time intervals presented in Figure 6.8 to determine periodicities. The periodicities in the lightning rate were determined using Lomb Scargle periodogram (ZECHMEISTER; KÜRSTER, 2009) and wavelet analysis (TORRENCE; COMPO, 1998).

Before the application of the Lomb Scargle periodogram and wavelet analysis, the lightning rate time series was first fitted using least squares fitting. The fitting was done using frequencies above 30 minutes after which the fit was subtracted from the time series of the lightning jump to obtain the residual. Frequencies above 30 minutes were used due to the frequency range of the wave and also to eliminate periods longer than 30 minutes from the lightning flash rate. Besides considering the time when the ray path of the wave reached the tropopause as indicated by the ray tracing result, we also considered the time the lightning jumps occurred since: (a) lightning jump is the best early indicator of a strengthening updraft within a thunderstorm (SCHULTZ et al., 2009; CAREY et al., 2019) and (b) the time of the jump agree well with the overshooting time (JURKOVIĆ et al., 2015). In Figure 6.9, the result of the Lomb Scargle periodogram and wavelet analysis of the lightning flash rate are presented.

The time series of the total lightning and its residual are presented with the identified lightning jumps (LJ) labeled in Figure 6.9(i). In Table Table 6.5, the times of occurrence of the identified jumps and corresponding BT images are shown. A good agreement was observed in the times of the lightning jumps and the time the minimum CTBT images were captured. As shown in Figure 6.7, the minimum CTBT (OT) locations also coincide with the spatial lightning distribution with highest density. Since lightning activities (lightning jumps) are directly related to updraft and overshooting (JURKOVIĆ et al., 2015), such a result is expected. Using modeling, several studies (LANE et al., 2001; VADAS et al., 2009b) showed the direct relationship between the frequency of the source and the observed gravity waves. Since the temporal variation in updraft and overshoot can be inferred from lightning flash rate variations (DEIERLING; PETERSEN, 2008; BEDKA et al., 2010) as demonstrated in Figure 6.9, for the first time, lightning rate frequency (period) is related to the frequency (period) of the gravity waves generated using observational data.

Table 6.5 - The summary of CTBT image in relation to lightning jumps, their respective time of occurrence and change in rate for all the CGWs events.

BT Image Frame	Case 1			Case 2			Case 3		
	Jump Label	Time (UT)	Rate (min^{-1})	Jump Label	Time (UT)	Rate (min^{-1})	Jump Label	Time (UT)	Rate (min^{-1})
Frame 1	LJ$_1$ LJ$_2$	4:59-5:00 5:04-5:05	140-205 169-213	LJ$_3$	1:35-1:36	3-14	LJ$_1$	4:20-4:21	288-339
Frame 2	LJ$_3$ LJ$_4$	5:11-5:12 5:16-5:17	131-168 146-171	LJ$_4$	1:53-1:54	8-16	LJ$_2$	4:27-4:28	185-297
Frame 3	LJ$_5$ LJ$_6$	5:31-5:32 5:40-5:41	164-184 186-221	LJ$_5$	2:06-2:07	3-17	LJ$_3$	4:35-4:36	274-376
Frame 4	LJ$_7$ LJ$_8$	5:44-5:45 5:49-5:50	191-231 200-241	LJ$_6$	2:33-2:34	3-16			

Source: Nyassor et al. (2021).

Figure 6.9 - The periodicities in the lightning flash rate.

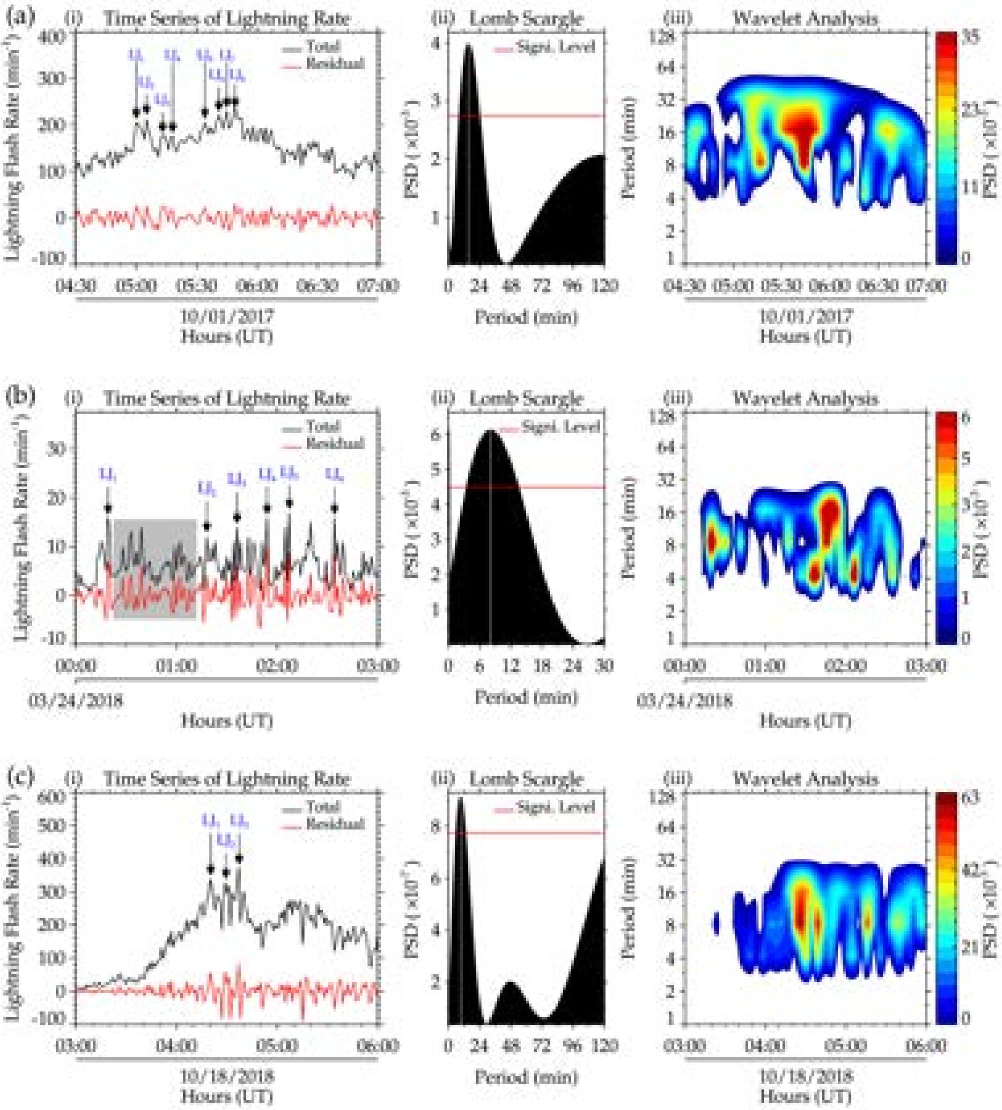

The top (a), middle (b), and bottom (c) panels represent the concentric gravity wave (CGW) events of Cases 1, 2, and 3, respectively. Panel (i) represent the time-lightning rate plot, whereas (ii) represents the Lomb Scargle Periodogram and (iii) showed the wavelet analysis result.
Source: Nyassor et al. (2021).

After the application of the Lomb Scargle periodogram to both total lightning flash rate and its residual, similar periodicities were observed. The Lomb Scargle periodogram results are shown in Figure 6.9(ii). Similarities were observed in the peak periods obtained by the Lomb Scargle periodogram and the wavelet analysis. In Table 6.6, the summary of the comparison between the periodicities in the lightning rate and the observed wave periods is presented. It is observed that the period of the gravity wave and those obtained from the lightning flash rate using Lomb Scargle periodogram and wavelet analysis are similar.

Table 6.6 - Comparison between the periods of the CGWs and oscillations obtained from the lightning flash rate data.

Gravity Wave Event			**Case 1**	**Case 2**	**Case 3**
Period (min)	Gravity Wave		13.30	07.20	09.80
	Lightning Rate	Lomb Scargle	15.60	08.10	09.60
		Wavelet	16.40	08.20	08.35

Source: Nyassor et al. (2021).

6.4 Conclusion

In this study, three concentric gravity waves (CGWs) observed in the OH emission layer using an all-sky imager in São Martinho da Serra (SMS) were presented. Using backward ray tracing, the source locations of the CGW events were determined. For all CGW cases presented in this work, the tropopause positions of the model winds ray paths coincides with nearby active convective systems, thereby suggesting these convective systems are the possible sources of the observed CGWs.

The wind profiles obtained from the model wind ray paths were used to investigate the background atmosphere condition relative to the wave propagation. Averagely, the winds during the three CGW cases were relatively weak, thereby permitting wave propagation without significant filtering and concentric wavefront distortion effect. However, the wind during CGW Case 2 was less than 30 m/s and this has permitted the propagation of the CGW thereby maintaining almost the 360° concentric wavefront.

The determined sources were further investigated to affirm that these waves were excited by the located convective system. The estimated overshooting tops for all the cases were greater or equal to 1 km which shows that these waves were most likely excited through overshooting by those systems. Besides using the overshootings to confirm the sources of the CGWs, lightning activity within the window of the convective systems was also used.

The spatial distribution of the lightning activity showed high densities in the region where the overshooting tops were observed in the CTBT images. Also, using the lightning flash rate within the set of time intervals considered for each case, the periodicities in the lightning flash rate were similar to the periods of the observed waves. This further strengthens the result that the observed CGWs were excited by the convective systems located by the backward ray tracing. Therefore, perturbations in lightning flash rate can most likely be used to estimate the frequency spectrum of excited gravity waves by convective overshoot. It is hereby, concluded based on this work that the lightning flash rate is a good indicator of gravity wave generation.

7 CONCENTRIC GRAVITY WAVES GENERATED BY A MOVING MESOSCALE CONVECTIVE SYSTEM IN SOUTHERN BRAZIL[1]

7.1 Introduction

Investigation on the source of three different concentric gravity waves on the night of October 2, 2019 was conducted. Prior to the observation of the CGWs, a moving Mesoscale Convective System (MCS) with several convective regions was seen transitioning from southeastern Argentina through Uruguay towards the Atlantic ocean. To know the source of the observed CGWs, the position and time where and when the wave was excited were determined using a ray tracing model. As the MCS and convective regions are moving, the overshootings from the convective regions within a certain spatial and temporal margin around the convective regions were tracked in space and time. These spatial and temporal margins were centered around the position and time the ray tracing indicated the wave was excited. Also, during this CGW event, other convection-related phenomena such as lightning was observed. Detailed discussions are given in the subsequent subsections.

7.2 Observation and methodology

The observation schemes and methodologies employed in this work are similar to the description given in the observation, instrumentation, and models chapter (i.e., Chapter 3) and general methodology chapter (i.e., Chapter 4). Table 7.1 presents the employed specific observation schemes and methodologies in the work of this chapter.

Table 7.1 - Summary of observation and methodology described in Chapter 4 employed in this work.

Phenomena	Observation	Chapter	Methodology	Chapter
CGWs	All-sky imager	3.2.1	Image preprocessing	4.1.1
			Spectral analysis	4.1.2
			Ray tracing	4.2
			CGWs Center	4.4
CTBT	GOES	3.2.6	Overshooting tops	4.5.1
				4.5.2
Lightning activities	BrasilDAT	3.2.4	Lightning densities	4.6.1
			Lightning flash rate	4.6.2

---

[1] This Chapter is an adapted version of a manuscript submitted for publication: P. K. Nyassor, C. M. Wrasse, I. Paulino, E. F. M. T. São Sabbas, J. V. Bageston, D. Gobbi, K. P. Naccarato, T. T. Ayorinde, H. Takahashi, C. A. O. B. Figueiredo, and D. Barros. Concentric Gravity Waves Generated by a Moving Mesoscale Convective System in Southern Brazil. **Under Revision**

7.3 Results and discussion

7.3.1 Characteristics of observed concentric waves

Between the hours of 00:13 UT and 04:15 UT on October 2, 2019, curved-like structures were observed originating from the southwestern part of the OH images captured by the SMS OH all-sky imager. After preprocessing the images (described in Section 4.1.1), three different concentric wavefronts with different epicenters, which occurred at different times were observed in the unwarped images. In Figure 7.1, the unwarped images of each concentric wavefront are presented, with the red rectangles emphasizing the regions where the concentric structures are visible. The white triangle indicates the center of the image and the location of the observation site as well. In Table 7.2, the times at which the CGWs first appeared in the airglow images, the estimated centers (in longitude, latitude), and the parameters of the waves are summarized.

Figure 7.1 - Example of unwarped images of each concentric gravity wave (CGWs) event observed at São Martinho da Serra on October 1 - 2, 2019.

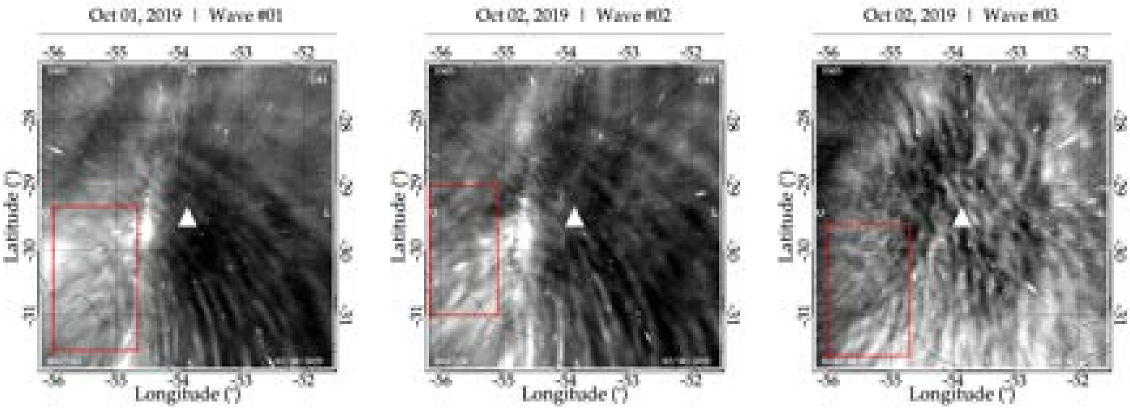

The left panel is Wave #01 observed at 00:27 UT, the middle panel is Wave #02 at 00:57 UT, and the right panel is Wave #03 at 04:04 UT. The white triangle shows the center of the image (which is also the location of the SMS observatory). The red rectangles emphasize the regions of the CGWs events.

7.3.2 Ray tracing results

The ray tracing model was used to investigate the propagation of the three CGWs and to determine the source location. In Figures 7.2, 7.3, and 7.4, the ray tracing results of Waves #01, #02, and #03 are presented, respectively. The longitudinal and latitudinal variations in the ray path for each CGW event are shown in panel (a) of Figures 7.2, 7.3, and 7.4. In panel (b), the temporal variations with altitude are presented. The variation in

Table 7.2 - Parameters of Excited Waves during the October 1 - 2, 2019 CGW Events.

Wave Parameters		**Wave #01**	**Wave #02**	**Wave #03**
Obs. Time (UT)		00:27:53	00:55:56	04:04:50
λ_H(km)		50.30±04.60	54.90±05.00	30.50±04.10
τ (min)		11.40±01.90	10.00±03.00	07.00±00.80
c_H (m/s)		73.90±10.60	91.00±09.00	72.90±08.60
ϕ (°)		31.60	90.00	89.50
CGWs Center	Lon	55.0°W	55.5°W	55.9°W
	Lat	30.8°W	29.29°W	30.9°W
CGWs Radius (km)		154.21	139.23	119.40

Source: Nyassor et al. (2021).

the cloud top temperature of GOES IR CTBT is depicted by the color bars. The cross, star, triangle, diamond, blue-filled, and red-filled circles represent the first visible concentric crest of the wave, tropopause height, observation site, center of CGW (dotted-dashed circle), and the stopping points of each ray path, respectively. In the upper left corner of the panel (a) (i.e., the cut-out region demarcated by the red dotted square), the distribution of the overshooting tops (OTs) in space around the determined center and the tropopause position of the ray paths are shown. The blue solid lines and the red dashed lines represent the model wind (i.e., MERRA-2 and HWM14) and the zero wind ray paths.

The GOES IR cloud top brightness temperatures images are overplotted on the map in panel (a) to reflect the status of the MCS closest to the time when the wind model ray paths reached the tropopause (excitation altitude). The coldest CTBT regions have been used to identify convective overshooting tops (BEDKA et al., 2010; JURKOVIĆ et al., 2015) and the possible source of the CGWs (YUE et al., 2009; VADAS; LIU, 2009; YUE et al., 2014; AZEEM et al., 2015; XU et al., 2015; NYASSOR et al., 2021). The backward ray tracing began at the OH emission altitude, that is, ∼87 km. The black dotted line in panel (b) of Figures 7.2, 7.3, and 7.4 indicate the OH emission altitude. The tropopause altitude which was obtained from the radiosonde measurement and considered as the excitation altitude is represented by the black dashed line.

Figure 7.2 - Ray tracing results of concentric gravity waves (CGWs) event one (#01) on October 1 - 2, 2019.

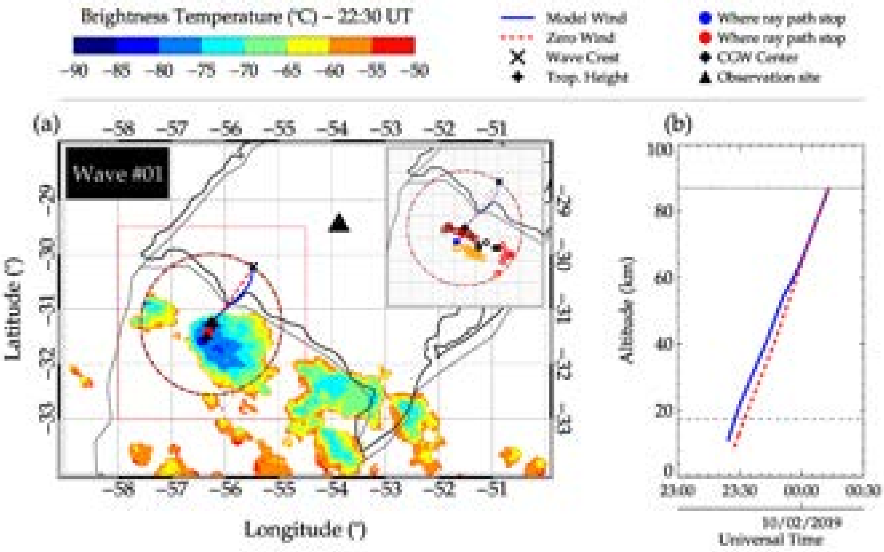

In panel (a), the individual path of the wave trajectory of the CGW and the MCS image at the time the ray path reached the tropopause are presented. The temporal variation with altitude of the ray path is shown in panel (b). The cross, star, triangle, diamond, blue-filled, and red-filled circles represent the wave crest, tropopause height, observation site, CGW center (of the dotted-dashed circle), and the stopping points of each ray path, respectively. The blue solid line and the red dashed lines represent the ray paths calculated with the model and zero winds, respectively. The zoom-in region in the upper-right corner of panel (a) is depicted by the red-dotted square. The color bars show the temperature scale of the cloud top.

Figure 7.3 - Ray tracing results of concentric gravity waves (CGWs) case two (#02) on October 2, 2019 with the same symbols as defined in Figure 7.2.

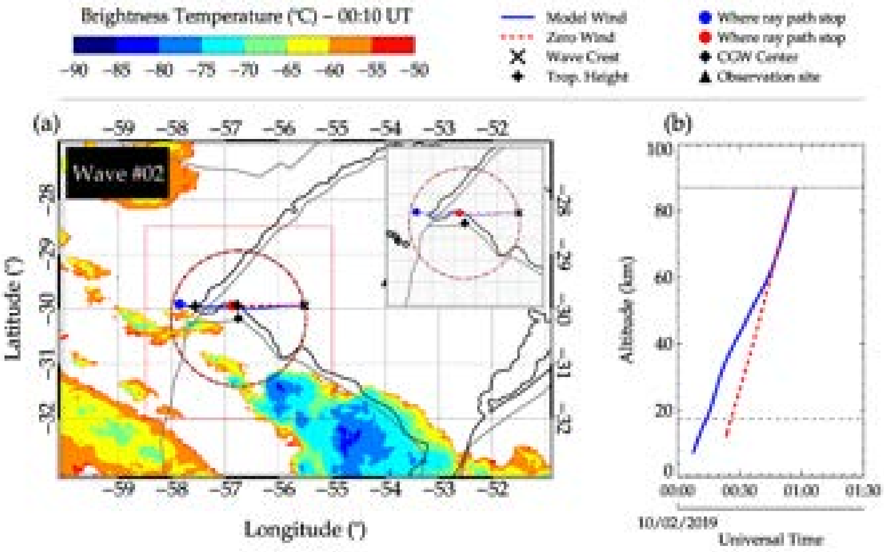

Figure 7.4 - Ray tracing results of concentric gravity waves (CGWs) case two (#03) on October 2, 2019 with the same symbols as defined in Figure 7.2.

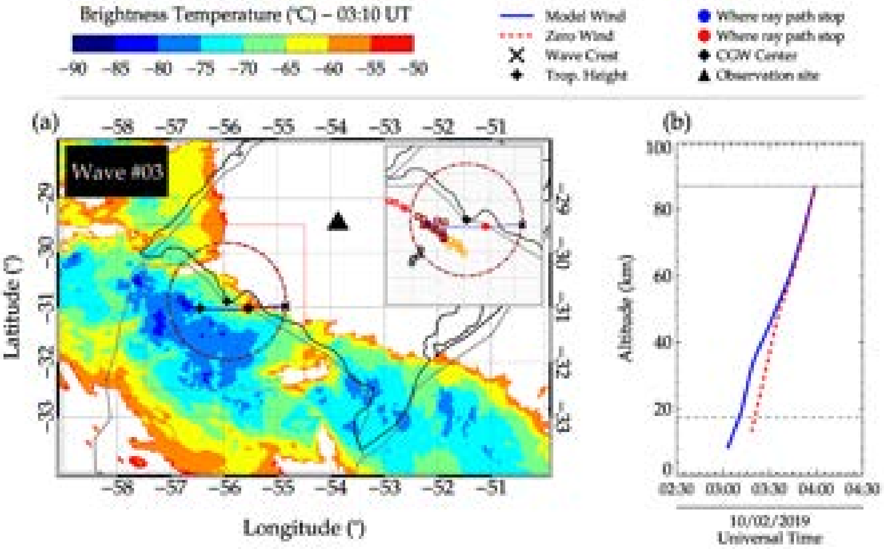

7.3.3 Effect of background wind on the wave propagation

The influence of the wind on the CGW propagation is investigated using blocking diagram. In the left panel of Figure 7.5 is the 3D blocking diagram, whereas, in the right panel, its 2D projection is presented. The construction of the blocking diagram follows the procedure of Taylor et al. (1993) described Section 6.3.1 using Equations 6.1, 6.2, and 6.3. In Figure 7.5, the red, light blue, and green rings show the characteristics of the winds between the altitude of 0 - 17 km, 18 - 87 km, and 87 - 100 km, respectively. The blue arrows extending from the origin of the 2D blocking diagram (right panel) show the magnitude and directions of the horizontal phase speeds of the CGW. The altitude ranges defined using the colors are the same for both panels. The thick black dashed circle is set at 30 m/s, whereas, the dotted circles are in an interval of 25 m/s. The average model winds between the hours of 21:00 UT on October 1, 2019, to 05:00 UT on October 2, 2019 were used to construct the blocking diagrams.

Figure 7.5 - 3D and 2D wind blocking diagram for the night of October 1 - 2, 2019.

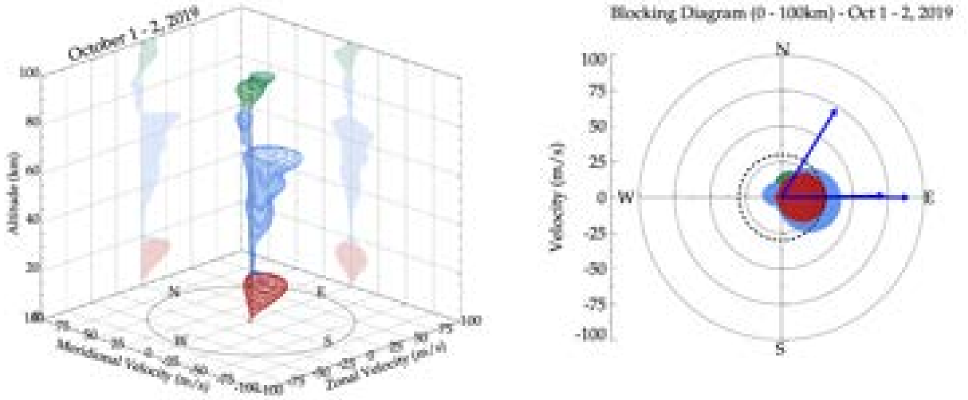

3D wind blocking diagram for the night of October 1 - 2, 2019 in the left panel and its 2D projection in a polar plot in the right panel. In the same panel, the magnitude and direction of the CGWs are indicated by the blue arrows. In both blocking diagrams, the red rings represent the magnitude and direction of the wind from 0 to 17 km which is the tropopause, the light blue rings, which extend from 18 to 87 km represent the wind above the tropopause up to the OH emission layer altitude (i.e., 87 km). The green rings represent the winds above 87 km. The thick dashed circle is set to 30 m/s whereas, the dotted circles are in an interval of 25 m/s.

Weak winds were observed below the mesosphere (i.e., 87 km). From the 2D projection in the right panel of Figure 7.5, it was observed that the magnitude of the wind between the ground and the OH emission altitude did not exceed 45 m/s even though there were variations in the profile. Note that among the three events presented in this work, the minimum phase speed of the CGWs was higher than the maximum wind. Generally, as shown in the right panel, the average wind profile was mainly within the north-eastern to the southeastern direction.

The filtering and wavefront distortion effects of the wind on the CGWs were investigated using the blocking diagrams. It was observed that the forbidden regions, that is, the regions where wave propagation is not permitted, presented a directional anisotropy, mainly between north to east directions. The magnitude of the wind was less than 45 m/s within the stratosphere and mesosphere and between northeast and southeast. Comparison between the wave phase speed (blue arrows in the right panel) and the wind (rings in both panels) revealed little or no wave filtering. It is important to mention that such wind magnitudes relative to the phase speed of the wave cannot significantly distort the concentric wavefronts. From the ray tracing results presented in Figures 7.2, 7.3, and 7.4, small variations were observed in the zero and model winds ray paths. These small variations suggest that the background winds were relatively weak during the three events, especially during

Wave #01 and #03.

7.3.4 Convective sources

To investigate whether convective overshooting of the tropopause by 1 - 3 km is the source of these CGWs, the CTBT IR images from GOES-16 were used to identify the convective overshooting tops. Numerous studies (SENTMAN et al., 2003; VADAS et al., 2009b; YUE et al., 2009; NYASSOR et al., 2021) associated mesospheric CGWs with overshooting convective cores in a thunderstorm. CTBT estimated from the GOES-12 IR images by Bedka et al. (2010) was used to determine overshooting tops. Also, the Next Generation Weather Radar (NEXRAD), Yue et al. (2009) was used to identify simultaneously two regions of convective overshooting and attributed them to be the sources of the two interfering CGWs they studied. They observed that the thunderstorm was active with strong convective activity 3 - 4 hours prior to the CGW observations.

At ∼18:40 UT on October 1, 2019, a warm cloud band began to develop convective regions around 32.0°S, 55.0°W in the GOES-16 IR images. As time progresses, the warm cloud band develops into a large Mesoscale Convective System (MCS) that extends from the northwestern to the southeastern part of São Martinho da Serra, Brazil, and into the Northern part of Uruguay. At 19:40 UT, the cloud top temperatures reached about -65°C, showing an extremely fast vertical growth which indicates strong updrafts activity. Half an hour later (i.e., 20:10 UT), the temperature of the cloud top was about -70°C, which is a characteristic of intense convection. The system afterward gradually began to organize into a multicell MCS. Figure 7.6 shows the convective cloud cover with the main part of the system over Uruguay at 22:40 UT.

To estimate the vertical extent of the overshooting, it is necessary to know the altitude and temperature of the tropopause. During the night of these CGW events, the tropopause temperature was colder than what was usually reported in literature. As a result, the tropopause temperature and altitude of days before and after the night of the CGWs events were considered in order to investigate the impact of the MCS on the tropopause. Some studies (SHERWOOD et al., 2003; KIM et al., 2018) attributed colder tropopause to the presence of extreme active deep convection since it appears to cool the layer near the cloud top. Therefore, tropopause height and temperature obtained from radiosonde measurements taken at Santa Maria (29.69°S, 53.81°W) from September 29, 2019 to October 10, 2019 at every 00:00 UT and 12:00 UT were considered in this analysis. In Figure 7.7, the tropopause altitude and temperature variations for all the days considered in this analysis are shown. On the night of the CGW event, the CAPE derived from the radiosonde measurement was ∼1500 J/kg (maximum updraft of ∼54.45 m/s). Also, hail events were

Figure 7.6 - GOES-16 IR image taken at 22:40 UT showing the MCS over Uruguay.

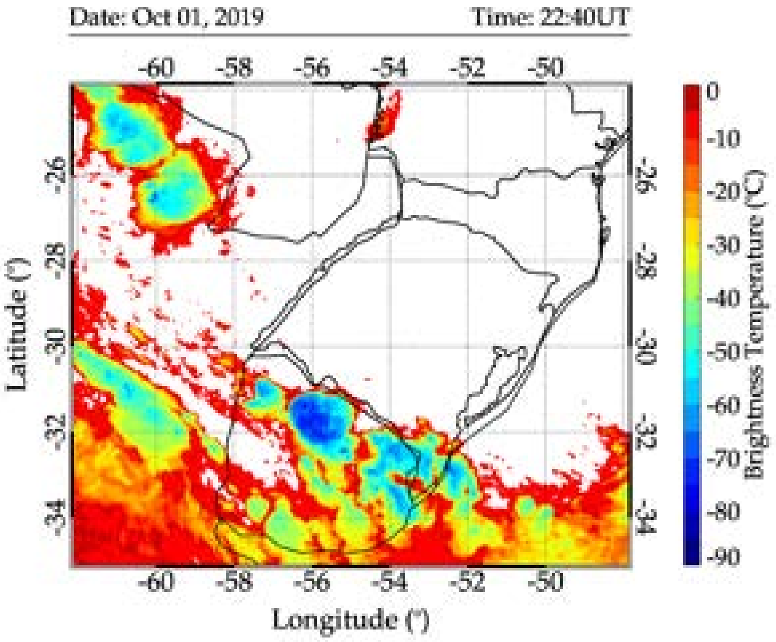

reported by Globo News (2019) which according to the source, began in the late hours on October 1, 2019, to the early hours of October 2, 2019.

In Figure 7.7(a), the tropopause temperature variations are presented. The temperature range of the cloud top for each day is indicated by the grayscale background regions with the label "T (°C)". A decrease in the tropopause temperature was observed during the days when the deep convection was present with very cold cloud top brightness temperatures, suggesting the presence of the deep convection further cools the tropopause (KIM et al., 2018). The decrease was observed to begin from 12:00 UT on September 30, 2019 to 12:00 UT on October 3, 2019 when the cloud top temperature was between -40°C and -90°C. The tropopause temperature began increasing as the deep convection dissipates as shown in the temperature variations from 12:00 UT on October 3, 2019, to October 10, 2019. On average, as shown in Figure 7.7(b), the variations in the tropopause altitude were centered around 17.5 km.

As demonstrated in Figure 7.7 that the presence of the active deep convection influenced the tropopause temperature, the averages of the tropopause temperature and altitude were computed and used in the estimation of the overshooting tops. The average tropopause temperature was found to be -74°C, whereas the average tropopause altitude was 17 km.

Employing the two overshooting tops estimation methods of Griffin et al. (2016) and

Figure 7.7 - Tropopause temperatures and altitudes variations at Santa Maria, RS, Brazil, from September 29 to October 10, 2019, obtained from radiosonde sounding measurements at 00:00 UT and 12:00 UT.

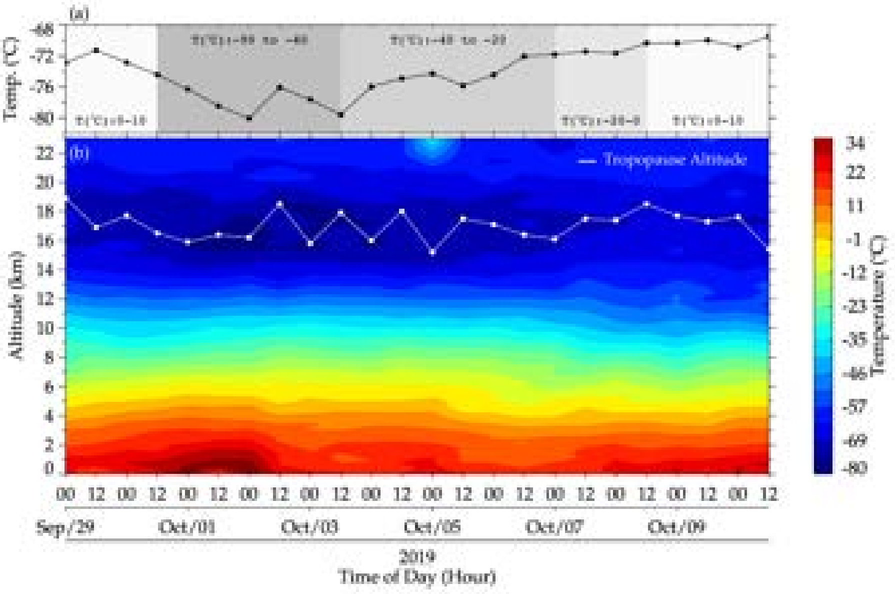

In panel (a), the variations of the tropopause temperature (black solid line with dots) along the days are presented. The grayscale regions with the label “T(°C)" represent the cloud top temperature range. The contour plot in panel (b) shows the temperature profile from 0 - 23 km at each 1 km along the days considered. The white solid line with dots shows the variations of the tropopause altitude with their respective temperatures shown in (a).

São Sabbas et al. (2009) described in Section 4.5, overshooting tops were estimated. In Figure 7.8, the results of the overshooting tops are estimated using the method of Griffin et al. (2016) for the overshooting convective cores (C #01,.., #04), determined to be the source of Waves #01, #02, and #03 is presented.

The model and zero winds ray paths of Wave #01 reached the tropopause at 23:27 UT and 23:32 UT, respectively, according to the ray tracing result. These times are considered to be the launch time of Wave #01. Considering the time when the model wind ray path indicates Wave #01 was launched, four different vigorous convective cores were observed. Among these four, only C #03 and C #04 fell within the time range when the ray path reached the tropopause. It is important to note that the maximum error in time estimated for the ray paths of Wave #01 from the OH emission layer altitude to the tropopause altitude was ±24 minutes. In the estimation of the error, three different ray tracing paths from three different starting positions on the first visible CGW crest were used. Three different starting positions were considered in order to study the effect of the wind on each ray path in several directions, thereby giving a general idea of the possible wave source locations.

Figure 7.8 - Tracking of overshooting in time.

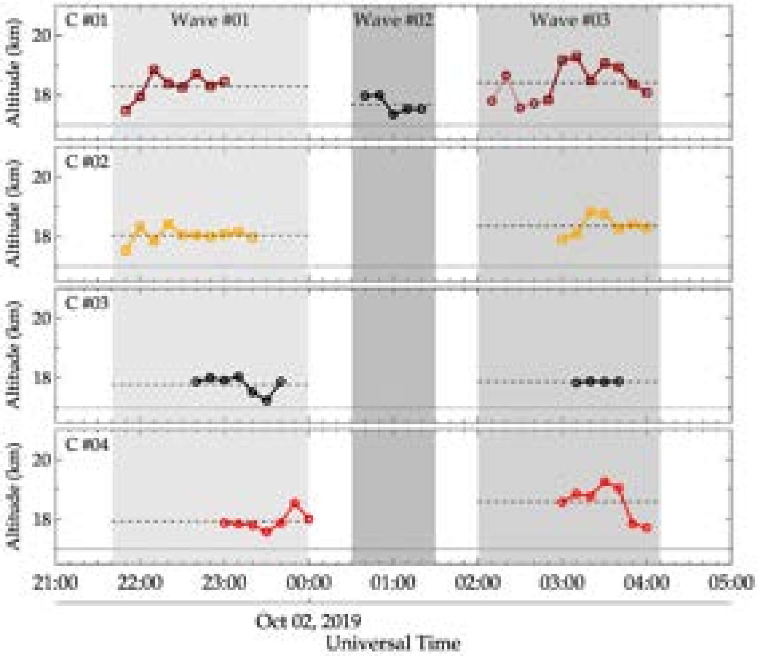

Panels (a), (b), (c), and (d) show the temporal variation of the overshooting of convective cores (C): #01, #02, #03, and #04 for the three concentric gravity waves (CGWs), Wave #01, Wave #02, and Wave #03. The greyscale regions demarcate the regions for each wave event. The dashed lines show the mean overshooting top altitude for each convective core, whereas the dotted lines show the mean tropopause altitude between September 29 to October 10, 2019.

Taking into account the error, three CTBT images before and after the estimated launch time of Wave #01 (i.e., 23:27 UT) were used to track the overshooting in time, unless there is a rapid dissipation of the core being tracked. This rapid convective core dissipation within the given time range was seen in C #03, where after 23:40 UT, no overshooting was observed. In such a case, the remaining 20 minutes in the forward tracking time was added to the reverse tracking time, thereby setting the reverse tracking time to 22:40 UT. A summary of the overshooting tops: wave number, number of convective cores, average overshooting top heights, peak overshooting top heights, and the time of the overshooting are given in Table 7.3. The results from both methods of Griffin et al. (2016) (M #01) and São Sabbas et al. (2010) (M #02) are presented in Table 7.3 with the comparison between the peak OT altitude of the two method graphically represented by Figure 7.9.

The comparison between the peak OT altitudes for the two methods was made and the result showed that the method of São Sabbas et al. (2010) agrees well with that of Griffin et al. (2016), since the error bars overlap with each other. This error analysis used to

Table 7.3 - Characteristics of Overshooting Tops (OTs) of the Convective Cores (C) during the October 1 - October 2, 2019 CGW events.

Wave #	**Trop Height (km)**	**Convective Core (C)**	**Mean OT (km)**		**Peak OT (km)**		**Peak OT Time**
			M #01	**M #02**	**M #01**	**M #02**	
01	17.00	#01	18.30	19.10	18.85 ± 0.39	19.98 ±0.80	22:10
		#02	18.04	18.68	18.42 ± 0.31	19.28 ± 0.50	22:20
		#03	17.78	18.26	18.05 ± 0.12	18.69 ± 0.30	23:10
		#04	17.93	18.49	18.54 ± 0.27	19.48 ± 0.50	23:50
02	17.00	#01	17.68	18.10	18.00 ± 0.17	18.61 ± 0.40	00:50
03	17.00	#01	18.42	19.28	19.29 ± 0.45	20.70 ± 1.00	03:10
		#02	18.36	19.19	18.83 ± 0.39	19.93 ± 0.70	03:20
		#03	17.87	18.40	17.88 ± 0.90	18.43 ± 0.30	03:10
		#04	18.58	19.50	19.25 ± 0.29	20.64 ± 0.90	03:30

Figure 7.9 - Comparison between the two OT altitude estimation methods.

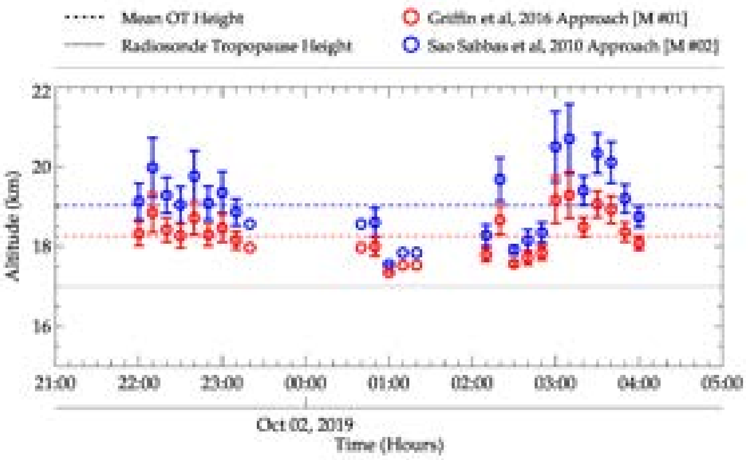

The open red circle with the error bar represents the Griffin et al. (2016) method, whereas the open blue circle with the error bars indicates the São Sabbas et al. (2010) method. The black dotted lines indicate the radiosonde tropopause height. The red and blue dashed lines represent the mean OT height for Griffin et al. (2016) and São Sabbas et al. (2010) methods, respectively.

plot the error bars follows the propagation error analysis by Bevington and Robinson (2003). The maximum estimated error for the method of Griffin et al. (2016) (M #01) is ∼ ±0.6 km whereas, the method of São Sabbas et al. (2010) (M #02) is ∼ ±0.9 km.

The occurrence time of the peak OTs of C #03 and C #04 of Wave #01 are within the error range of Wave #01. However, it was observed that the positions of the overshooting tops of C #03 and C #04 were more than 50 km from the determined center (black diamond) and the tropopause (asterisks) when the OTs were tracked in space. It is worth noting that before the airglow observation began this night, Wave #01 was already propagating in the OH airglow images, implying Wave #01 have already reached the OH airglow emission layer. As a result, the exact time when the first concentric wavefront appeared in the OH image could not be obtained. This makes it difficult to identify the approximate source position and time from the ray tracing model.

Since this system is moving, it is necessary to define a region within which the overshooting convective cores will be considered. This region was estimated using the average tropopause position of three different zero wind ray paths starting from three different positions on the first visible concentric crest and the error in the spatial variations of the ray paths. Wave #01 was used in this estimation, as shown in Figure 7.10.

Figure 7.10 - Description of how the region where overshooting convective cores were considered to determine the overshooting tops tracked in space and time.

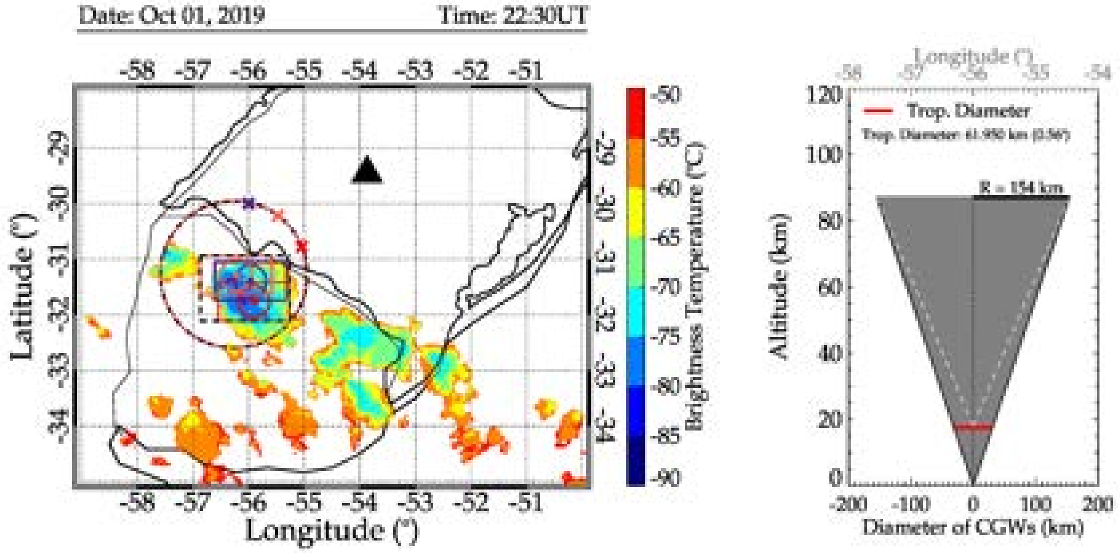

The black triangle, cross symbols (‘×’), and dashed-dotted circle are the same as defined in Figure 7.2. Each color of the ‘×’ corresponds to their respective solid circles, filled circles, and rectangles. The black dashed triangle was constructed from the extreme positions of the three rectangles. In the right panel of Figure 7.10 is the pictorial description of how the diameter of the tropopause was estimated. The red horizontal line depicts the tropopause diameter. The black vertical dashed lines depict the height of the cone with radius (R). The vertical slanted dashed lines at either side of the black vertical dashed lines show the propagation of the CGWs after the tropopause has been overshoot.

The map of the CTBT at 22:30 UT, similar to Figure 7.2 is presented in the left panel of Figure 7.10. The positions where the three ray tracing began are represented by the cross (×), whereas, the first visible concentric crest to appear in the OH image is depicted by the dark red dashed-dotted circle. The colors of '×' correspond to the same colors of the circles and the rectangles, implying that the ray trace starting position of the red '×' corresponds to the red circle with a red center, and the red rectangle. These circles were constructed from the tropopause diameters, whereas the rectangles were constructed from the tropopause diameter and the estimated errors in longitude and latitude in the model and zero winds ray paths. The extreme positions of the purple, light red, and red rectangles, were used to construct the black dashed rectangle. In the right panel of Figure 7.10, the description of the determination of the tropopause diameter is pictorially illustrated. The radius "(R) = 154 km" of the 2D cone at the OH emission altitude is the black horizontal solid line that extends from the middle, that is, the vertical dotted line. The height of the cone is represented by the black dotted vertical lines. The radius used here is the radius of the first visible concentric wavefront of Wave #01 in the OH images. The tropopause diameter which was determined from the ideal cone constructed using the radius of the concentric wavefront of Wave #01 is depicted by the red horizontal solid line. The conical propagation of the CGWs above the tropopause after the overshooting is represented by white vertical slanted dashed lines.

To determine the tropopause diameter, the concept of a conical propagation configuration of CGWs (VADAS et al., 2009b; NYASSOR et al., 2021) was employed. The radius of the CGWs (i.e., 154 km for Wave #01) was used as the radius of the base of the cone. Next, to determine the radius (diameter) at each altitude (every 1 km), the slant path of the cone was followed until the vertex of the cone. The vertex of the black solid slanted path is at the ground, whereas that of the white dashed path is above the tropopause. At the radius (i.e., the red horizontal line in the right panel of Figure 7.10) of the black slanted path at the tropopause is ∼31 km (∼62 km in diameter). From Vadas et al. (2009b) and Vadas et al. (2012), a typical diameter of a convective plume is 15 - 20 km. Also, considering the dome-like protrusion shooting out of the anvil of the convective core, the diameter of the overshooting region was set to the diameter of the tropopause.

The rectangle around each circle in the left panel of Figure 7.10 was constructed using the diameter of the tropopause. The widths of the rectangles were then constructed by adding the maximum error in longitude to the east and west sides of the circle. The maximum errors in latitude were further added to the north and south sides of the circles and used to construct the lengths of the rectangle. The maximum errors in longitude and latitude for Wave #01 are 40 km and 7 km, respectively. Next, the extreme positions of the purple, light red, and red rectangles were then used to construct the black dashed rectangle. All overshooting convective cores found within the black dashed rectangle were then tracked in space and time to determine the source position of Wave #01. This procedure was applied to Wave #02 and Wave #03 using their respective radii and maximum errors in longitude and latitude.

As stated earlier, before observation began this night, Wave #01 had already reached the OH emission layer altitude. Also, in the CTBT image, the observed overshooting convective cores at the time when the ray paths reached the tropopause were quite far. No significant variations were observed (see Figure 7.8) in the OTs of C #03 (black circles) unless between the hours of 23:10 UT and 23:40 UT. Between 23:30 UT and 23:50 UT, no variations were observed in the OTs of C #04 (red circles). Even though C #03 and C #04 overshot the tropopause more than 1 km, the exact time when the wave first appeared in the OH image is not known, therefore these OTs might not be the most likely source of the observed Wave #01. Furthermore, for C #04 the peak OT occurred after the estimated time the ray paths of Wave #01 reached the tropopause. This shows that even if Wave #01 should appear first in the OH images at 00:27 UT, C #04 (black circle) cannot be the source of Wave #01 since the distribution of C #04 in space is quite far from the determined source location.

Since Wave #01 was present in the OH emission before the start of the observation, the OTs (convective cores) were tracked further back in time to verify whether or not there were overshootings. Between 21:50 UT and 23:00 UT, and 21:50 UT and 23:20 UT, convective cores: C #01 (dark red square in Figure 7.8) and C #02 (orange squares in Figure 7.8) were observed with higher OTs, respectively. During the entire time range of C #01, large OT variations were observed with a peak OT at 22:10 UT and an altitude of 18.85 km. Also, OT variations were seen in C #02, particularly within 21:50 UT to 22:30 UT, with a peak OT at 22:40 UT and an altitude at 18.42 km. Following C #01 and C #02 in space, their distribution showed that the OTs of these two cores, especially C #01 were near the source location of Wave #01. Considering C #01 and C #02 OT characteristics, that is, peak OT altitudes and time of peak OT in Figure 7.8, and their spatial distributions around the estimated source locations in Figure 7.11, either of these two convective cores is the most likely source of Wave #01. Interestingly, no active convective cores were seen within the black dash rectangle (i.e., the region within which the overshooting cores were considered for Wave #01).

The convective cores of Wave #03 are examined. Similar to Wave #01, four convective cores; C #01, C #02, C #03, and C #04 were observed and tracked in space and time. In Figure 7.8, OT variations were observed for C #01, C #02, and C #04 with peak OT altitudes at 19.29, 18.83, and 19.25 km, and 03:10, 03:20, and 03:30 UT, respectively.

Figure 7.11 - Tracking of overshooting in space for each concentric gravity wave (CGWs).

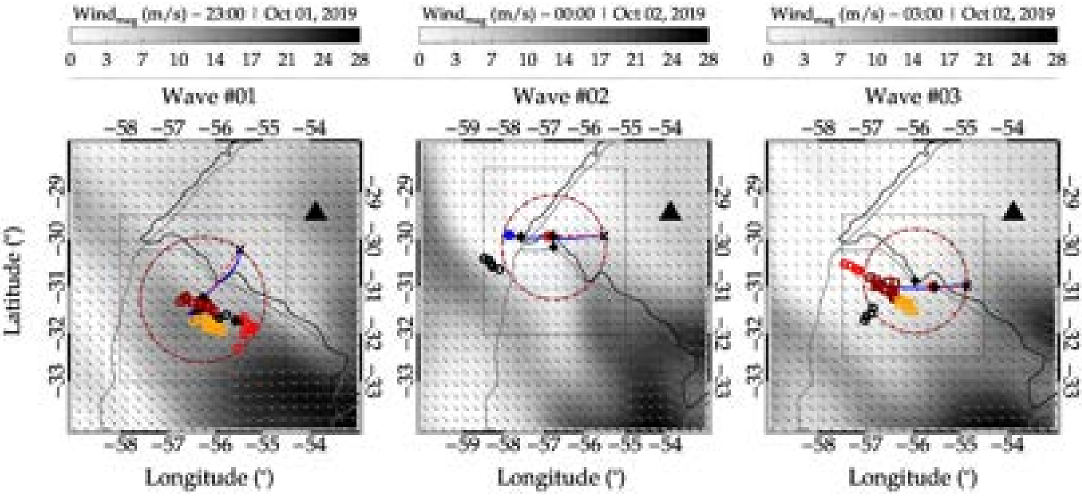

In the left, middle and right panels, the positions of the overshooting tops in space for Wave #01, Wave #02, and Wave #03, are presented, respectively. All symbols have the same meaning as in Figures 7.2, 7.3, and 7.4. Overplotted in this figure is the ECMWF Reanalysis 5th Generation (ERA5) wind vector plot at the 17 km, i.e., near the tropopause, at the time when the ray paths reached the tropopause.

Interestingly, the estimated excitation times for both zero and model winds ray path was 03:10 and 03:20 UT. These times coincide with the times the highest OT altitudes were observed for C #01 and C #02 of Wave #03. The distributions of C #01 (dark red squares) and C #02 (orange squares) in space are shown in the right panel of Figure 7.11. Their distributions revealed that the OT locations were close to the ray traced identified source locations and the determined center, especially for C #01.

For C #04 (red circles in Figure 7.8) of Wave #03, the time of the peak OT altitude was within the error range but its spatial distribution was outside: (i) the first visible concentric crest and (b) the set spatial region (determine using similar procedure describe for Wave #01) where the convective cores will be considered. As a result, C #04 is less likely to be the source of Wave #03. Also, the spatial distribution of C #03 (black circles in Figure 7.8) was outside the set spatial region where the convective cores will be considered. However, the OT temporal variation presented a peak OT altitude at 17.88 km around 03:20 UT but the peak altitude of C #03 occurred at the same time as that of C #02. Since the peak OT altitude of C #02 is ∼0.93 km higher than that of C #03 and also being closer to the source location, the overshooting from C #03 cannot generate Wave #03.

The first appearance of Wave #02 in the OH airglow images was at 00:55 UT. Twelve minutes later (i.e., around 01:07 UT) it disappeared. According to the ray tracing result, the time of excitation (the time the model wind ray path reached the tropopause) of this wave was around 00:50 UT and ∼140 km away from the closest overshooting convective core (C #01). Also, the determined center of the first visible concentric crest was ∼220 km away from the closest overshooting convective core. For C #01 of Wave #02 presented in Table 7.3, a peak OT altitude of 18.00 km at 00:50 UT was observed. Comparing the time of peak OT altitude with the time when Wave #02 was first visible in the OH image (i.e., 00:55 UT), it is not possible for Wave #02 with such characteristics to propagate to the OH emission layer within 5 minutes from the top of the cloud. However, no significant overshooting was observed around the possible source location within the excitation time. Also, no active convective cores were observed ±30 minutes within the region considered for the tracking of the convective cores. This suggests that the convective overshooting mechanism could not be the underlying excitation mechanism of Wave #02. Here, the body force mechanism is most likely the possible mechanism that could be used to justify the origin of Wave #02 but time factor did not permit further studies on this mechanism. Therefore, Wave #02 is left for further investigation in future work.

The tracking of convective core approach was employed in this case study to identify the most likely convective core that overshot to generate these three CGWs because of the moving MCS (together with the convective cores) (SÃO SABBAS et al., 2009). Averagely, the MCS was moving at a speed of ∼0.1°/10 min (11 km / 10 min). In Figure 7.11, the vector plot of the wind (the gray arrows) at the tropopause shows that the wind was southeastward throughout the entire period of the CGW events. The magnitudes of the winds are presented in the grey contour with the color bars showing their respective scales for each event.

7.3.5 Severe weather associated events

The CGW generating MCS was also accompanied by other severe weather-associated events. Events such as intense lightning, and hail were observed. The observation of the lightning activities was carried out by the Brazilian Lightning Detection Network (BrasilDAT) sensors. By employing a similar methodology described in Section 4.6 and also in the first case study, the locations with the highest lightning densities were obtained and found to agree well with the location of the overshooting top in the coldest region of the CTBT images. The result of the lightning density and the CTBT images are shown in Figure 7.12.

Besides relating the spatial distribution of the lightning strikes (i.e., the lightning densities) to the CTBT, the lightning flash rate oscillations were also determined, after which

Figure 7.12 - Comparison between the spatial distribution of lightning density and composite GOES-16 IR cloud top brightness temperature images from 22:00 UT on October 1, 2019 to 04:00 UT on October 2, 2019.

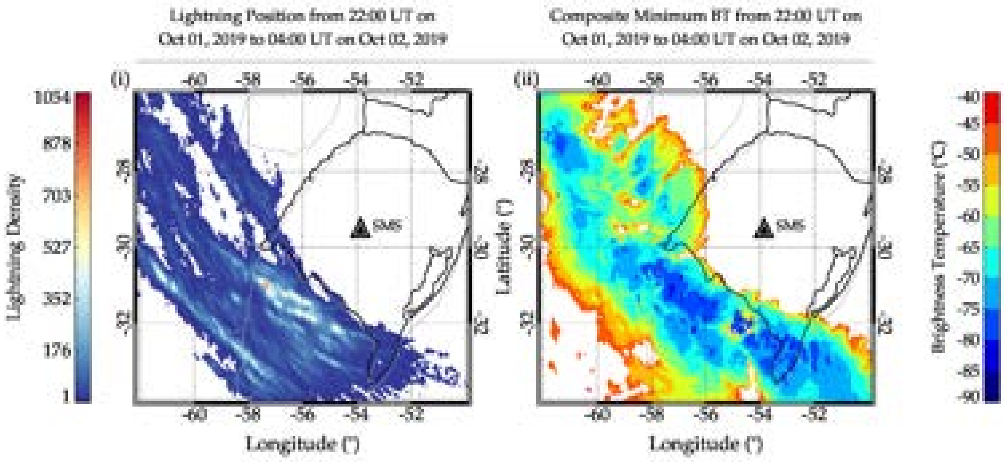

The position of the Southern Space Observation site is depicted by the black filled triangle with a white triangle.

the periodicities in the lightning flash rate oscillation were computed. The lightning flash rate was estimated for each CGW within the region, the overshooting convective cores were tracked. Also, the time range of the lightning flash rate was the same as that of the CTBT images. From the estimation of the lightning flash rate periodicities discussed in Sections 4.6.2 and 6.3.2, the estimated periods in the lightning flash rate agree well with observed periods of the CGWs. The results of the comparison between the estimated periods are summarized in Table 7.4.

Table 7.4 - Comparison between observed wave periods and lightning flash rate periods.

	Periods (min)	
CGWs Case	**Observed Wave**	**Lightning Flash Rate**
Wave #01	11.40±1.90	10.01±2.20
Wave #02	10.00±2.36	16.00±1.89
Wave #03	07.00±0.80	08.00±1.00

From Table 7.4, similar periods were observed in the lightning flash rate oscillation and the observed wave periods for Wave #01 and Wave #03. However, the lightning flash rate period for Wave #02 was not in agreement with the period of the observed wave. This further emphasizes the fact that the ray traced identified convective core was possibly not the source of Wave #02.

7.4 Conclusion

Three different concentric gravity waves generated by different overshooting convective cores in a moving Mesoscale Convective System (MCS) were presented. All the observed concentric waves have partial concentric wavefronts. The source locations of these CGWs were determined using backward ray tracing. The model wind showed weak winds during the ray tracing of the CGW event. The identified source locations for Waves #01 and #03 were close to overshooting convective cores. For Wave #02, no active overshooting convective cores were observed at the position and time the ray tracing indicated this wave was excited.

To determine the overshooting tops, the tropopause temperature and altitude are necessary. However, during this event, the tropopause temperature was colder than those presented in the literature. As a result, a study was conducted to investigate whether the presence of the MCS was the reason for the colder tropopause. This was done using observed tropopause temperatures and altitudes of days before and days after the CGWs event and from which their averages were used to estimate the overshooting top. Since the MCS was moving, the overshooting convective cores were tracked in space and time in order to determine the most likely cores that excited the observed waves. Two methods of the overshooting tops estimation were used and their results compared well with each other.

Severe weather-associated events, that is, lightning, and hail were observed as well. From the spatial analysis of the lightning, the distribution of the lightning densities in space coincides with the overshooting tops in the CTBT images. Furthermore, the temporal analysis showed that the periodicities in the lightning flash rate are similar to the observed periods of Waves #01 and #03. The lightning flash rate further showed that Wave #02 was not excited by the located convective core since the observed wave period and that of the lightning rate were not similar. The lightning, hail, and the sprite associated with the CGW generating MCS serve as a measure of the severity of the MCS.

8 INVESTIGATIONS ON CONCENTRIC GRAVITY WAVE SOURCES OVER THE BRAZILIAN EQUATORIAL REGION [1]

8.1 Introduction

Sources of GWs are very vital in the study of the dynamics of the atmosphere. CGWs is a kind of GWs that gives direct information on the possible source mechanism. Convective GWs with concentric wavefronts have been reported to be directly associated with tropospheric convections (VADAS et al., 2009b; YUE et al., 2009; XU et al., 2015). However, the observation of CGW can also indicate a different source mechanism besides the well-known tropospheric mechanical oscillator mechanism. Vadas et al. (2003) and Vadas et al. (2018) showed that concentric gravity waves are also excited by body forces created during the dissipation or breaking of primary gravity waves. These CGWs generated by body forces are known as secondary CGWs.

Therefore, in this case study, the sources of three concentric gravity wave events will be investigated. Using an all-sky imager, these waves were observed in the OH emission layer over São João do Cariri in the Brazilian equatorial region. The wave events have different concentric wavefront configurations. To determine the possible source locations of the concentric waves, backward ray tracing was used. The ray tracing result revealed that two of the CGW events were most likely excited by a nearby active convective system. On the other hand, the tropopause and the stopping positions of the wind model ray path of the remaining CGW event had no nearby and active convective system, suggesting this wave was most likely, generated in-situ. Detailed discussions on this case study are given in the subsequent subsections.

8.2 Observation and methodology

The observation schemes and methodologies employed in this work are similar to the description given in the observation, instrumentation and models chapter (i.e., Chapter 3) and general methodology chapter (i.e., Chapter 4). In Table 8.1, the employed specific observation schemes and methodologies employed in the work of Nyassor et al. (Under Review).

---

[1] This Chapter is an adapted version of a manuscript submitted to AGU: P. K. Nyassor, C. M. Wrasse, I. Paulino, D. Gobbi, H. Takahashi, P. P. Batista, R. A. Buriti, A. R. Paulino, E. Yiğit, K. P. Naccarato, D. Barros, and C. A. O. B. Figueiredo. Investigations on Concentric Gravity Wave Sources over the Brazilian Equatorial Region. **Under Review in Journal of Geophysical Research: Atmospheres**.

Table 8.1 - Summary of observation and methodology described in Chapter 4 employed in Nyassor et al. (Under Review).

Phenomena	Observation	Chapter	Methodology	Chapter
CGWs	All-sky imager	3.2.1	Image preprocessing	4.1.1
			Spectral analysis	4.1.2
			Ray tracing	4.2
			CGWs Center	4.4

8.3 Results

8.3.1 Gravity wave characteristics

In Figure 8.1, the unwarped, time-difference (TD) images of the three selected gravity waves are presented. The parameters of the three CGW events are summarized in Table 8.2.

Figure 8.1 - Samples of unwarped, time-difference (TD) images of each CGW event observed over São João do Cariri.

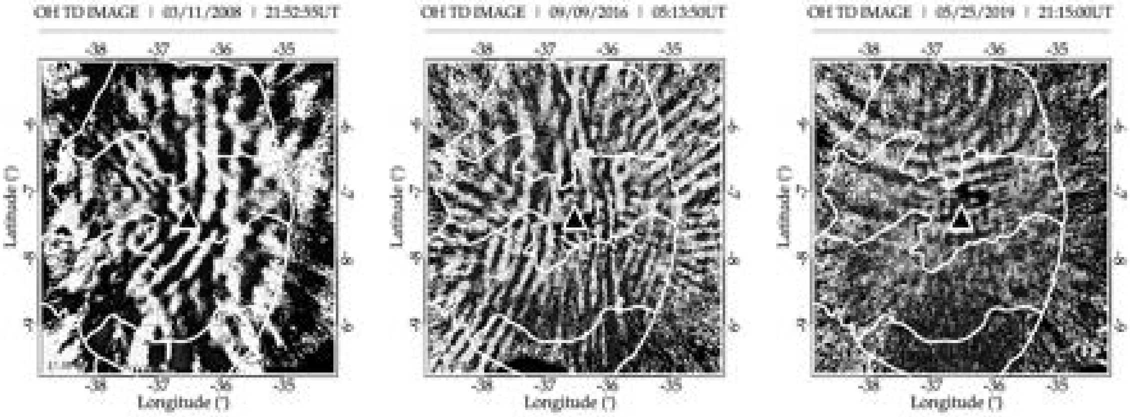

The left, middle, and right panels represent the CGW events on March 11, 2008, September 9, 2016, and, May 25, 2019, respectively. The black triangle with a white outline represents the São João do Cariri observatory. The white lines show the borders of Brazilian states.
Source: Nyassor et al. (Under Review).

8.3.2 Determination of source location

The three selected CGWs were backward ray traced to determine the source location using concatenated MERRA-2 and HWM14 model wind. Comparisons between the ray tracing determined source location and the geometrically determined CGW centers were made. The differences in these approximations were then used to investigate the effect of the

Table 8.2 - Concentric gravity waves parameters observed at São João do Cariri.

Wave Parameters	**03/11/2008**	**09/09/2016**	**05/25/2019**
λ_H (km)	31.90	42.50	30.90
τ (min)	10.80	12.30	07.00
c_H (m/s)	49.20	57.60	74.10
ϕ (°)	86.40	85.20	160.60
Radius (km)	200.00	460.00	Major: 150 Minor: 90

Source: Nyassor et al. (Under Review).

wind on the GWs propagation. The zero wind ray path determined source location and the determined center are considered to be a zeroth-order approximation.

Figure 8.2 presents the ray tracing result of the three selected CGW events for this case study. Panels (i) show the Convective Available Potential Energy (CAPE) maps. With a similar spatial range of the map as panels (i), the horizontal backward ray paths along longitude and latitude for the model wind (MW) together with the overplotted CTBT map are presented in Figure 8.2(ii). The temporal variation of the ray path with altitude and the profile of the horizontal wind along the ray path are presented in Figures 8.2(iii) and 8.2(iv), respectively. For each panel, the location of the observation site is represented by the black triangle and the position of the first visible concentric crest where the ray tracing began is denoted by the plus symbol. The centers of the concentric wavefronts, that is, the red dashed circles and the ellipse are indicated by black diamond. The blue solid lines represent the model winds ray paths of the waves, whereas the blue filled circles indicate the stopping position and time of the GWs ray paths. The tropopause altitudes are represented by an asterisk in the middle panels.

Figure 8.2 - The backward ray tracing results of the three selected CGW events observed at São João do Cariri.

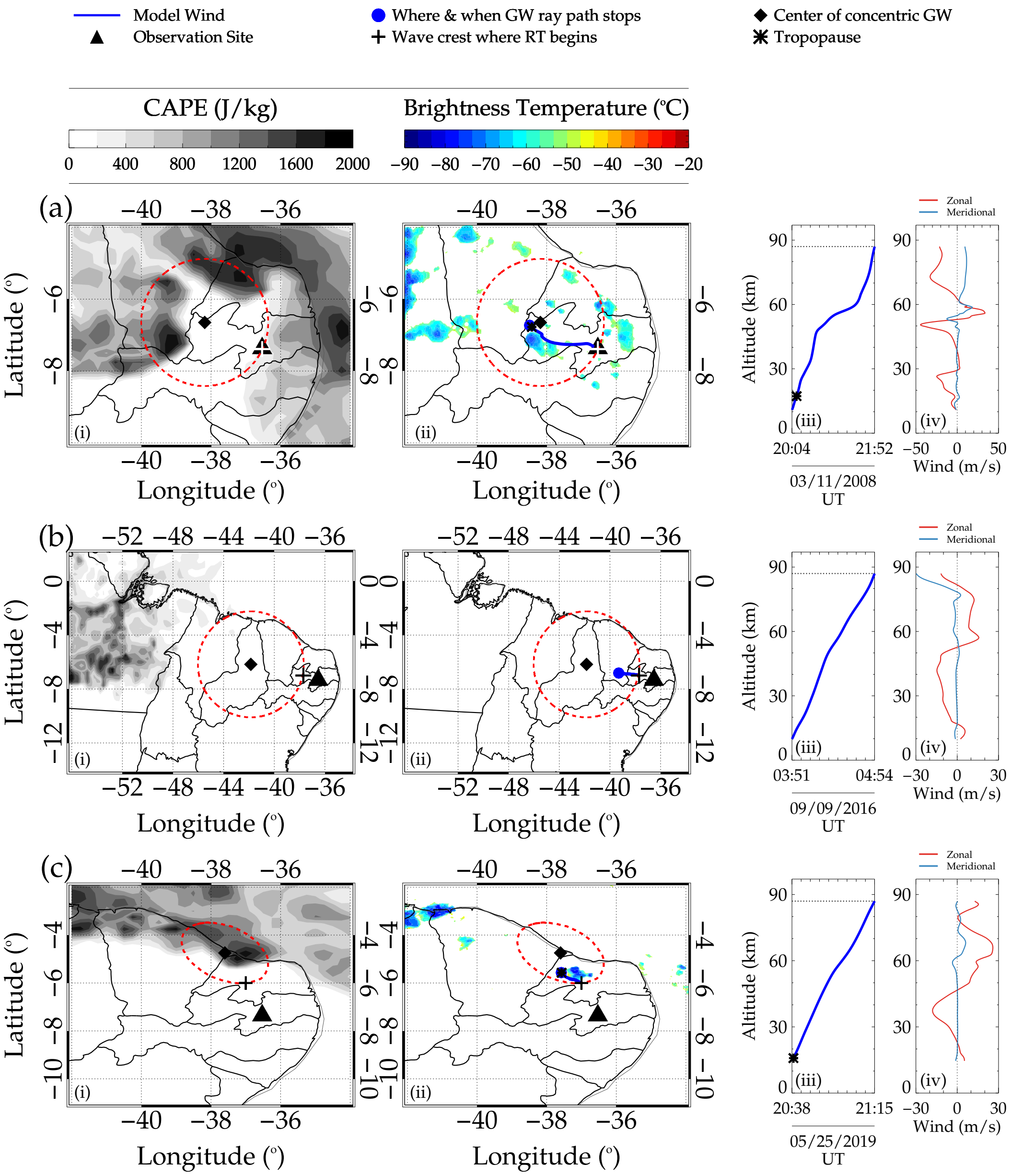

Panels a, b, and c, represent the CGW events on March 11, 2008, September 9, 2016, and May 25, 2019, respectively. In panels (i), the CAPE maps of the hour within which each of the CGWs were excited are shown. In panels (ii), the ray path for model winds and CTBT image over the map are presented. The temporal variations in the wind model ray paths with altitude are shown in panels (iii). In panels (iv), the vertical profile of the zonal (light red solid line) and meridional (light blue solid line) are presented.
Source: Nyassor et al. (Under Review).

The tropopause and stopping positions of the ray paths of the CGW events on March

11, 2008 and May 25, 2019 were close to nearby deep convective systems. The cloud top brightness temperature (CTBT) infrared images during these events indicated very cold cloud top temperature (signifying convective overshooting). This suggests that these waves were most likely generated by these convective systems. The color bars show the temperature scale of the CTBT in degrees Celcius. Figure 8.2(i) shows the convective available potential energy (CAPE) maps of the hour within which each of the waves was excited. The CAPE maps were used to provide information on the stability of the troposphere during the CGWs events. CAPE gives a measure of the quantity of energy available for convection. Also, CAPE is directly related to the maximum updraft velocity; thus the higher CAPE the greater possibility of severe weather (HOLTON, 1992). The CAPE maps presented in Figure 8.2(i) were obtained from the European Centre for Medium-Range Weather Forecasts (ECMWF) Reanalysis version 5 [ERA5] CAPE data. Details on how to access and process CAPE data are given by Hersbach et al. (2018).

The existence of convective systems was further proven using observed precipitation data. Daily precipitation data from the Center for Weather Forecasting and Climate Studies (CPTEC) of the National Institute for Space Research (INPE) were used. These data were obtained for each day of the CGW event. The data is a combination of precipitation products obtained from satellite and ground-based observations. The satellite observations were obtained from the Tropical Rainfall Measuring Mission (TRMM). On the other hand, the ground-based observations were obtained from a set of rain gauges distributed over South America. The two observations are combined to attained higher spatial distributions and also, fill gaps in the data in regions where one of the instruments does not have coverage. The method used to combined these two measurements is known as MERGE. Details on the precipitation datasets and the MERGE technique can be found in Rozante et al. (2010) and Rozante et al. (2020). For each CGW event, the precipitation data were selected such that if the wave was observed at the end of the day, such as the events of March 11, 2008, and May 25, 2019, the precipitation data for the same day was used. However, in the case where the wave was observed in the early hours of the day, for instance, the September 9, 2016 event, the precipitation of the previous day was used. Note that no precipitation was observed in the early hours of September 9, 2016 (i.e., 00:00 - 06:00 UT). In Figure 8.3(i), the spatial distributions of precipitation are presented. Figure 8.3 is similar to Figure 8.2 except for the replacement of the CAPE maps in panels (i) of Figure 8.2 with the observed precipitation map.

Figure 8.3 - Same as Figure 8.2 but with spatial distribution of precipitation in panels (i) instead of CAPE.

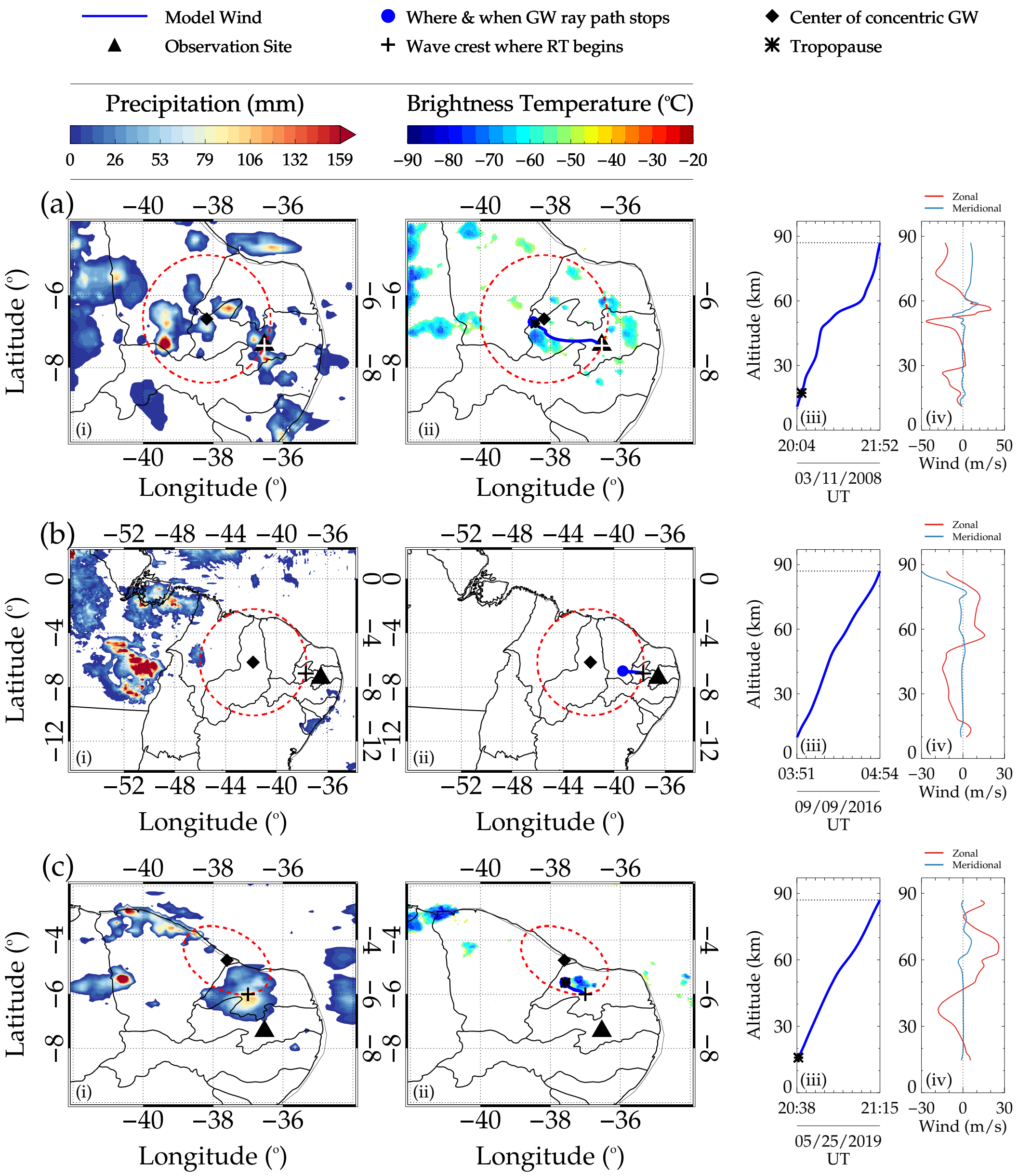

Source: Nyassor et al. (Under Review).

Studies by Dare-Idowu et al. (2020) used active deep convection with minimum cloud top brightness temperatures corresponding to the time when the ray path reached the tropopause to locate potential source positions of small-scale GWs. In Figures 8.2 and 8.3, the March 11, 2008 event has an arc-like wavefront, whereas that of May 25, 2019 has a semi-elliptical wavefront. These events have convective systems that were active at the time the model wind ray path reached the tropopause. The first visible concentric wavefront on the first OH image of each event is the red-dashed circle/ellipse in the respective sub-figures.

The stable and unstable state of the troposphere in connection to deep convection which is the possible source of CGWs was studied using CAPE. Here, high CAPE values close to the vicinity of the source locations (panels a(i) of Figures 8.2(a) and 8.2(c)) of March 11, 2008 and May 25, 2019 CGW events were observed. Between the hours of 18:00 UT - 23:00 UT on March 11, 2008 and May 25, 2019, CAPE values ranges between 1000 to 2000 J/kg. On the other hand, low CAPE values were observed close to the center and also the stopping position of the ray paths of the September 9, 2016 CGW event. To define the stability and instability condition of the troposphere, the definition of the Storm Prediction Center (SPC) of the National Oceanic and Atmospheric Administration (NOAA) was adopted in this work. According to the definition of SPC/NOAA, CAPE values $<$ 1000 J/kg are considered as weak instability, between 1000 J/kg $<$ CAPE $<$ 2500 J/kg as moderate instability, 2500 J/kg $<$ CAPE $<$ 4000 J/kg as strong instability, and CAPE $>$ 4000 J/kg as extreme instability (NOAA, 2021a). It is important to note that these definitions are dependent on location and time of year. The maximum updraft velocities ($w \sim [2CAPE]^{1/2}$) (HOLTON, 1992) determined from these CAPE values ranged from 44.72 to 63.25 m/s for the events of March 11, 2008 and May 25, 2019.

Vadas et al. (2009a) and Xu et al. (2015) observed high CAPE (updraft) either before or during the time of the CGWs events reported in their work. During a CGW event on the night of October 1, 2005 reported by Vadas and Liu (2009), they observed a maximum CAPE value of 600 - 800 J/kg (∼35 - 40 m/s) in the vicinity of the wave generating storm. Also, during a three-year study of CGWs over China, using a network of airglow all-sky imagers, Xu et al. (2015) reported high CAPE values near convective storms present. Using CAPE data obtained from ECMWF, the authors observed high CAPE values during the summer months where the occurrence of CGWs events was also frequent. In their work, they used an average CAPE value of 2500 J/kg (w ∼70 m/s) as the criteria for strong instability which was considered to lead to the formation of thunderstorms and consequently overshooting of the tropopause. Vadas and Fritts (2009) used a simulation study to establish a relationship between updraft estimated from CAPE and excited gravity waves by the updraft through overshooting of the tropopause. They found that the amplitudes of the excited GWs were related to the vertical updraft velocities. In this work, apart from using CAPE to investigate the stability of the troposphere, precipitation was also used to further prove the presence of convective systems. A good agreement was observed between the spatial distributions of the CAPE, precipitation, and convective systems for each event. This correlation further affirms that convective systems were present during the CGW events studied in this work.

Using the determination of the geometric center of the concentric wavefronts which is a complementary method, the likely source locations of CGWs were determined. The effect of the wind on the Doppler shifting of the position of wave sources relative to their propagation and also the distortion of the concentric wavefronts have been addressed by Vadas et al. (2009b) using a simulation. Weak winds, that is, < 30 m/s (VADAS et al., 2009b; VADAS et al., 2012; YUE et al., 2009), little or no significant displacement of the source position determined by the ray tracing and the geometrically determined center is expected. Also, no significant distortion of the CGW wavefronts is expected when the wind is weak. For instance, in panel (a) of Figures 8.2(ii) and 8.3(ii), the stopping point of the ray path of both zero wind (not shown) and model wind, and the geometrically determined center were close to each other, indicating weak background wind relative to the phase speed of the CGWs. On the other hand, with strong winds, that is, >30 m/s (VADAS et al., 2009b), significant concentric wavefront distortion and displacement in the source location relative to the CGW center is expected. In the case of the May 25, 2019 CGW event (as shown in panel (c) of Figures 8.2(ii) and 8.3(ii)): (1) the stopping/tropopause position of the ray path of the wave was far from the geometrically determined center, and (2) the wavefront of the CGWs was distorted (elliptical). In an ideal situation, without significant concentric wavefront distortion, CGWs must appear to have 360° complete circular wavefronts.

However, September 9, 2016 had no convective system present within the stated time when the model wind ray path reached the tropopause. The nearest active convective system during this event was within a distance of more than 1000 km westward the observation site. Also, as shown in panel (b(ii)) of Figures 8.2 and 8.3, the position of the geometrically determined center is $\sim$300 km away from the final/tropopause position of the ray path. No profound difference can be observed in the variation in time of the ray paths with altitude for zero (not shown) and model winds.

8.4 Discussion

8.4.1 Discussion on March 11, 2008 and May 25, 2019 CGWs events

All the three CGW selected for this case study were visible in the OH images for approximately an hour. The position and time, where and when the ray paths of March 11, 2008 and May 25, 2019 CGWs event reached the tropopause agree well with the position of convective systems at the time the systems were active. The tropopause position of the zero wind ray path of the March 11, 2008 event (not shown) and the position of the geometrically determined center were close, that is, 6.59°S, 37.94°W for zero wind and 6.65°S, 38.18°W for the determined center. The propagation time of the zero wind ray path of the March 11, 2008 event from the tropopause to the OH emission altitude was 1 hour:23 minutes. Using Equation 6.4, the propagation time for this CGW event was 1 hour:42 minutes. On the other hand, the wave propagation relative to the model wind in the ray tracing model reached the tropopause at 6.77°S, 38.43°W in 1 hour:42 minutes.

As observed in Figures 8.2 and 8.3, the May 25, 2019 CGW event had a difference between the model wind ray path stopping position and the center of the elliptical wavefront. As stated earlier, the first evidence of a relatively strong and varying wind is the observed elliptical wavefront. Also, it was observed that the estimated center of the ellipse was $\sim$107 km away from the tropopause and stopping position of the model wind ray path. This is because the stopping position of the model wind ray path was located at 5.57°S, 37.74°W and the center of the ellipse was at 4.60°S, 37.57°W. Using the major radius of the ellipse, the estimated propagation time was $\sim$50 minutes, and the propagation time of the model wind ray path was $\sim$35 minutes. However, the ray path of the zero wind stopped at $\sim$70 km, due to the violation of $m^2 \ll \frac{1}{4H^2}$ or $\lambda_z < 4\pi H$ condition in the anelastic dispersion relation (VADAS; FRITTS, 2005; VADAS, 2007).

Here, the effect of the wind on the wave propagation and wavefronts of the CGWs events of March 11, 2008 and May 25, 2019 are investigated. The vertical profiles of the zonal (light red solid line) and meridional (light blue solid line) winds in panels (a), (b), and (c) of Figures 8.2(iv) and 8.3(iv) were used. It was observed that the magnitudes of the meridional winds for these two events were lower than 20 m/s. On the other hand, the zonal winds for March 11, 2008 and May 25, 2019 CGWs events varied between 45 m/s west and 34 m/s east and 18 m/s west and 26 m/s east, respectively. In particular, the variations of the CGW event of March 11, 2008 zonal wind was mainly westward. This has significantly altered both the horizontal (see panel (a) of Figure 8.2(ii)) and vertical (see panel (a) of Figure 8.2(iii)) propagation of the wave. For the May 25, 2019 CGW event slight variations in the horizontal and vertical propagation were observed with the zonal wind being mainly eastward above 48 km. Despite these variations in the zonal wind, the phase speed of the May 25, 2019 wave was higher than the magnitude of the maximum horizontal wind. The elliptical wavefronts indicate strong wind (VADAS et al., 2009b; XU et al., 2015), however, the magnitude of the model wind was less than 30 m/s during the entire propagation of the wave; hence the model wind cannot explain the observation. Therefore, the observed meteor radar winds during this event will be used to explain this observation.

As mentioned earlier, strong and varying wind filter some spectrum of the waves and also, shift and distort wavefronts as shown in the simulation result of Vadas et al. (2009b) and observed by Xu et al. (2015). For the May 25, 2019 event, besides the semi-elliptical wavefronts, differences in the positions of the determined center, convective system, and tropopause position of the model wind ray path were observed. Using observed wind from meteor radar measurements, these differences were explained. This was done using a vector plot and a hodograph of the meteor radar wind as shown in Figure 8.4.

Figure 8.4 - The mesospheric wind characteristics during the May 25, 2019 CGW event.

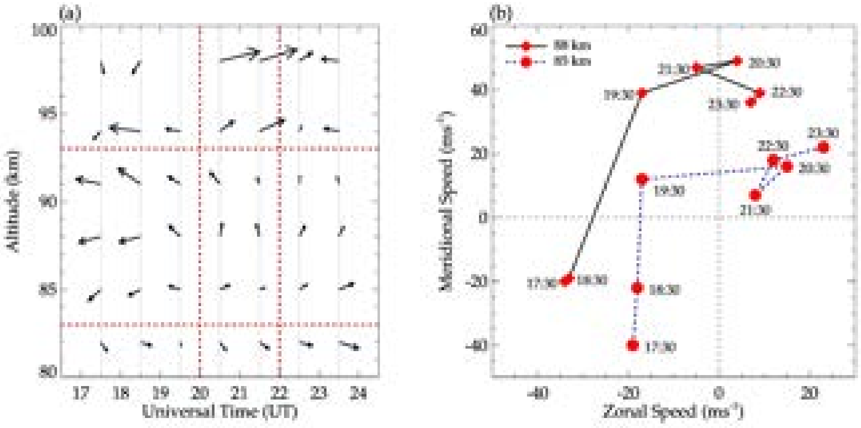

In panel (a) is the vector plot of the horizontal wind component, whereas, in panel (b), the hodograph of the wind at altitude 88 km (solid black lines with red diamonds) and 85 km (dark blue dashed lines with red dots) are shown. The red vertical dashed lines in panel (a) emphasize the time range within which the wave was excited to the time of observation, whereas the horizontal dashed lines indicate the altitude range between 83 to 95 km.
Source: Nyassor et al. (Under Review).

The meteor radar used in this work is installed at the same location as the airglow imager. It operated at a frequency of 35.24 MHz, with a 12 kW transmitter power. Wind velocities are measured between the altitudes of 82 and 100 km at each 3 km and a temporal resolution of 1 hour. In Figure 8.4(a), the altitude range of the vector plot is 83 to 98 km and from 17:30 to 23:30 UT. The two red dashed vertical lines were used to indicate the time range of 20:00 - 22:00 UT, which is the time interval within which the wave was excited to the time it was observed. On the other hand, the two horizontal lines are used to indicate the altitude range between 83 and 93 km. This is used to emphasize the wind characteristics in the mesopause region.

Between the hours of 17:30 UT and 18:30 UT, the wind vector was mostly westward within 85 to 95 km. A rotation in the wind towards the north was observed around

19:30 UT and between the altitude of 85 and 88 km, the wind was mainly northwestward. The northwestward shifting of the center of the May 25, 2019 CGW event relative to the possible source (i.e., the convective system) can be related to the northwestward rotation within the mesosphere. However, a change in direction between 19:30 and 21:30 UT was observed in the hodograph between 85 km and 88 km. The compression at the sides of the concentric wavefronts in the direction of the wind could be the main factor contributing to the formation of an elliptical wavefront. Xu et al. (2015) also used mesospheric wind with such characteristics to explain the elliptical wavefront reported in their work.

Background wind distorts wavefronts of CGWs, thereby making them appear squash circle or elliptical (VADAS et al., 2009b). On the night of August 13 - 14, 2013, near the Shuozhou (39.8°N, 112.1°E) station, Xu et al. (2015) observed GW with an elliptical wavefront. Between 20:00 LT on August 13, 2013, to 04:00 LT on August 14, 2013, meteor radar wind measurement at every 2 km in altitude and 1 hour, was used to study the wind characteristics. The authors constructed a hodograph of the wind at 87 km (see figure 11 of Xu et al. (2015)) and found that the direction of the wind was southeastward between 20:00 - 03:00 LT. At 20:00 LT the wind was 58 m/s and was 10 m/s at 04:00 LT. The wind characteristics during the time of this event were consistent with the distortion feature of their observed elliptical GW.

The three CGW events presented in this case study were propagating either towards the east or southeast. For instance, the propagation of the CGW events on March 11, 2008 and May 25, 2019 was eastward and southeastward suggesting these waves were excited in the western and northwestern parts of the observation site, respectively. For these two events, the tropopause position determined from the ray tracing coincides with intense and active convective systems. These propagation directions of the waves can be explained using the presence of a convective system during the event and also the season within which the waves were observed. The season within which the CGWs were observed corresponds to the season where the Intertropical Convergence Zone (ITCZ) is near the equator. Dare-Idowu et al. (2020) observed eastward and southeastward propagating GWs and attributed the propagation direction to the presence of deep convection sources to the west and northwest during the season of ITCZ. Previous studies (ESSIEN et al., 2018; DARE-IDOWU et al., 2020) and the current identified GWs sources were observed within the months of autumn, which are in agreement with the times of the action of ITCZ in Brazil, as shown by Utida et al. (2019).

The ray traced identified source locations of March 11, 2008 and May 25, 2019, CGWs events were found close to active convective systems suggesting these CGW events were most likely generated by the nearby convective systems. The CAPE maps that are shown in panels a(i) and c(i) of Figure 8.2 and precipitation in panels a(i) and c(i) of Figure 8.3 prior to the observation of these events, respectively, showed high values of CAPE and precipitation near the estimated source locations. The ray tracing estimated source location for March 11, 2008 CGW event, and its geometrically determined center were close to this active convective system. Also, the propagation time estimated by ray tracing and Equation 6.4 was similar. Having similar: (a) estimated source location using ray tracing and determined center and (b) estimated propagation time using ray tracing and Equation 6.4, implies the nearby active deep convection is the source of the March 11, 2008 CGW event.

On the other hand, May 25, 2019 CGW event presented a different propagation characteristic from the first visible crest to the geometric determined center and the source location. Despite the inability of the model wind to explain the propagation and observation of this wave, it gave an idea of the state of the wind on this night and also the propagation of the observed CGW. As stated earlier, a point-like overshooting of the tropopause is known to be the source of primary CGWs (YUE et al., 2009; XU et al., 2015), and strong and varying winds are indicated by elliptical wavefronts of CGWs (VADAS et al., 2009b; XU et al., 2015). Based on these characteristics, the May 25, 2019 CGW is most likely excited by the nearby active convective system. Hence, suggesting it is a primary gravity wave.

8.4.2 September 9, 2016 CGWs event

Even though the wind was weak during the entire propagation of the September 9, 2016 event, no convective systems were seen near the tropopause position of the wind model ray path. Variations in the horizontal wind were observed. The meridional wind increase from 0 m/s at $\sim$78 km to 30 m/s southward at 87 km, whereas the zonal winds varied between 16 m/s west and 16 m/s east. The variations in the vertical profile of the wind were mostly westward below 52 km. From the ray tracing results, it was observed in Figures 8.2 and 8.3 that the wind could not alter much the horizontal propagation of the wave trajectory.

For the September 9, 2016 CGW event, no active convective system was present near the tropopause position of the model wind ray path or the determined center of the concentric wavefront. As presented in Figure 8.2(b), the absence of a nearby convective system suggests that this wave might be: (i) generated by a remote convective system and propagated through a duct to the field of view of the all-sky imager or (ii) excited during the breaking or dissipation of a primary wave excited by a remote convective system. Before this event, convective systems with cloud top brightness temperature between -60°C to -70°C were observed between 22:00 UT on September 8, 2016 and 04:00 UT on September 9, 2016. These systems were more than 1000 km away from the observation site and centered around 51°W, 9°S and 48°W, 2°S. The 30 minutes resolution infrared CTBT images within this time range showed no significant spatial displacement. In the subsequent subsections, the two proposed generation and propagation conditions of this wave will be discussed.

8.4.3 Propagation of the observed CGWs in a duct condition

To explore the possibility of ducting, the condition of the background atmosphere was investigated using SABER temperature profiles. During this night, between 02:00 and 05:00 UT, eight temperature profiles were obtained from the TIMED/SABER satellite. Three of the soundings were close to the convective system within 02:52 UT to 02:56 UT on September 9, 2016. The other three soundings were close to the observation site between 04:31 UT and 04:33 UT. In Figure 8.5(a), the kinetic temperature profiles of each set of the three soundings are presented. In panel (b), the composite plot of the convective system with the corresponding sounding positions of each profile in panel (a) are shown.

Figure 8.5 - Panel (a) shows the temperature profiles from six SABER soundings (the position of each profile is shown by the corresponding squares).

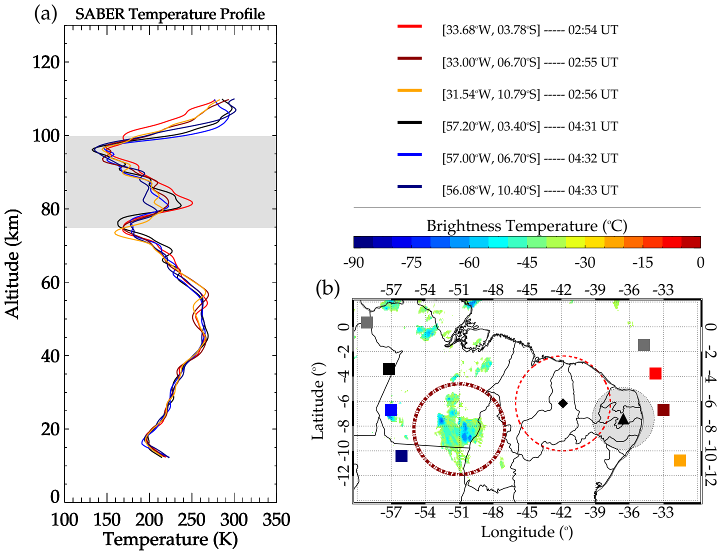

Active convective system during September 9, 2016 event shown in (b). The regions with convective systems considered as the possible source are emphasized by the dark red dashed-dotted circle. The sounding positions and times are defined in the legends. In panel (a), the gray squares are not considered in the temperature profile.
Source: Nyassor et al. (Under Review)

The sounding positions close to either the convective system or the observation site are depicted by the squares. The corresponding colors of the sounding times are defined in the legends. In Figure 8.5(b), the two gray squares were not considered in the profiles. This is because they are far away from the convective system and the observation site. In Figure 8.5(a), the gray shaded region between 75 and 100 km emphasizes the temperature inversion layer in the temperature profiles. The six selected profiles showed temperature inversion layers between ~75 km and ~95 km with the peak inversion altitude around 83 km and a mean temperature value of ~230 K (~-45°C).

The background investigation of September 9, 2016, CGW event is shown in Figure 8.6. The temperature (T), potential temperature (θ), Brunt Väisälä frequency square (N^2), wind in the direction along which the wave parameters were obtained, the square of vertical wavenumber (m^2) and the OH volume emission rate (VER) were considered to study the propagation conditions of the wave. These background profiles were obtained from the ray tracing results shown in panel (b) of Figure 8.2. In Figure 8.6(a), the kinematic temperature profile of the blue solid line corresponding to the blue square in Figure 8.5(b) is presented. This is the closest sounding profile (57.00°W, 6.70°S at 04:32 UT) to the convective system. The estimated potential temperature profile (dotted line) is also presented in the same plot. In panel (b), the profile of the Brunt Väisälä frequency squared is presented. In panel (c), the profile of the wind in the propagation direction of the wave is presented. This wind was obtained from ray tracing, which is the model (concatenated MERRA-2 and HWM14) wind. The spatial and temporal resolution of the wind depends on the step size (in time and space) during the ray tracing iteration. The vertical dotted line at zero acts as a reference to the wind variation.

To study the propagation of gravity waves in a real atmosphere, gradients in wind and temperature profiles cannot be neglected. For this reason, the vertical wavenumber square (m^2) was estimated using Equation 4.12, that is, the anelastic dispersion relation of gravity waves (VADAS; FRITTS, 2005; VADAS, 2007) defined in Section 4.3. Panel (d) of Figure 8.6 shows the profile of m^2 in a solid line with the horizontal dotted lines indicating the $m^2 > 0$ and $m^2 < 0$ regions. The error range of the wind in panel (c) and m^2 in panel (d) are indicated by the light-gray shaded region around the profiles. The wind and m^2 profiles have a maximum errors of $\sim\pm 13$ m/s and $\sim\pm 1.2\times10^{-7}$m^{-2} for m^2, respectively. The 1.6 μm OH normalized volume emission rate (VER) profile measured by the TIMED/SABER satellite is shown in panel (e). The horizontal dashed lines in all sub-figures show the top and bottom of the temperature inversion layer in the mesopause region. The gray shaded regions emphasize the altitude range between 12 and 100 km.

The peak VER of the 1.6 μm OH profile during this wave event was around 83 km which is

Figure 8.6 - Background atmosphere analysis during the September 9, 2016 CGW event over São João do Cariri.

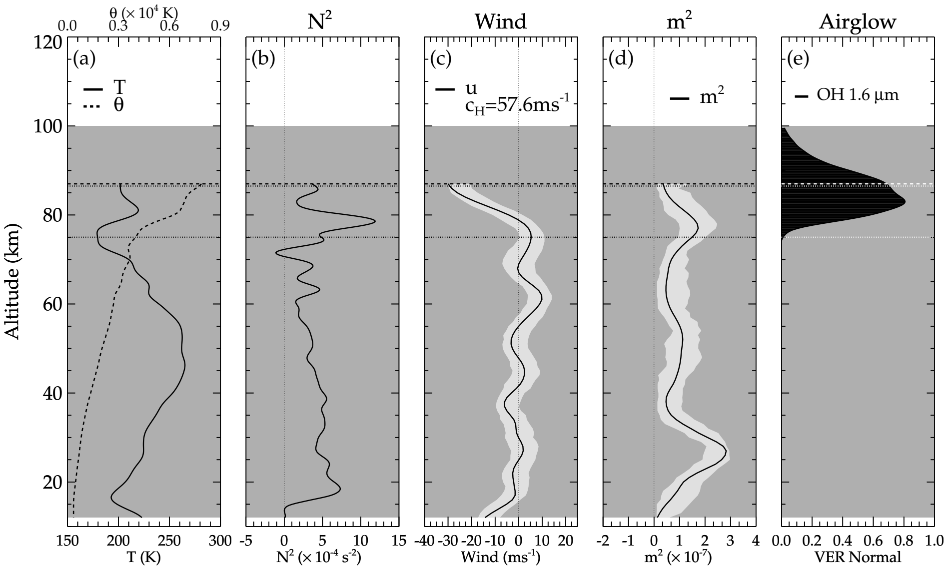

The profiles of the kinematic temperature (solid line) measured by the TIMED/SABER satellite and its corresponding estimated potential temperature (dotted line) are shown in panel (a). The squared of Brunt-Väisälä frequency profile is shown in panel (b) and in panel (c), the wind in the propagation direction of the wave (solid line) is presented. The vertical wavenumber squared (m^2) and the 1.6 μm normalized OH volumetric emission rate (VER) profiles are shown in panels (d) and (e), respectively.
Source: Nyassor et al. (Under Review).

also the altitude of the peak inversion layer in the temperature profile. The profiles used in this plot are below 87 km because this study focuses on the propagation characteristics of the wave between the excitation and observation altitudes. It was observed that despite the inversion layer in the temperature profile between 75 and 87 km, no effect of the inversion layer was seen in the m^2 profile. Throughout the entire altitude range considered in this analysis, the m^2 was positive ($m^2 > 0$) suggesting the CGW was propagating (GOSSARD; HOOKE, 1975).

Ducting and propagation of gravity waves are mainly controlled by background winds. However, during this CGW event, the effect of the temperature inversion in a form of a duct could not be seen in the ray tracing result. Note that the winds used, that is, MERRA-2 winds below 70 km and the HWM14 climatology winds above 70 km (monthly averages) may differ from the actual winds. During this event no observed winds were available. The importance of winds in the formation of Doppler duct at mesospheric heights has been demonstrated by previous studies (SNIVELY et al., 2007; SIMKHADA et al., 2009; FECHINE et al., 2009; BAGESTON et al., 2011; CARVALHO et al., 2017). The presence of ducts at these heights allows long-distance horizontal propagation of gravity waves. On the other hand, thermal ducts have a similar effect on the propagation of waves as shown by Bageston et al. (2011). Even though no ducting of CGW was observed in the ray tracing result, the possibility of ducting especially the Doppler duct cannot be totally excluded (KOGURE et al., 2020).

8.4.4 Observed gravity waves generated by convective system

During this CGW event, medium-scale gravity waves (MSGWs) have been observed as well. Two groups of the MSGWs were backward ray traced to determine their source locations. The grouping of the MSGWs was based on their propagation directions. Figure 8.7 shows the ray tracing results of the two groups of MSGWs.

Figure 8.7 - The ray tracing result of two groups of medium-scale gravity waves (MSGWs).

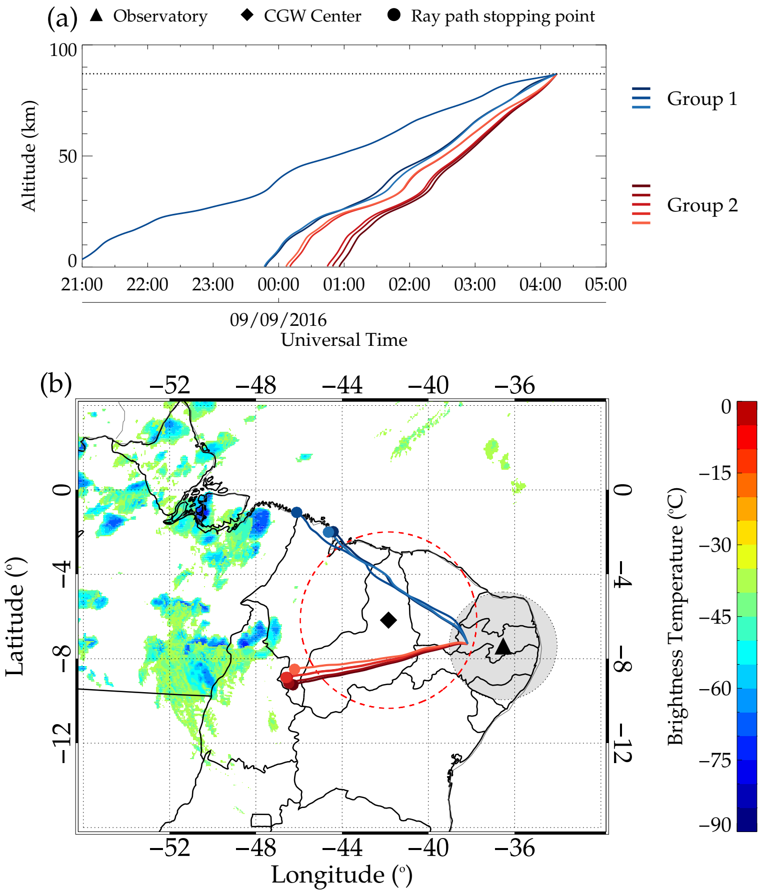

In panel (a), the time-altitude variations of the model wind ray paths are presented whereas, the longitude and latitude variations of the model wind ray paths are shown in panel (b).
Source: Nyassor et al. (Under Review).

The temporal variations of the model wind ray paths with altitude are shown in Figure 8.7(a) whereas, the longitudinal and latitudinal variations of the model wind ray paths are shown in Figure 8.7(b). The color bar shows the temperature scale of the cloud top brightness temperature (CTBT) image overplotted in Figure 8.7(b). The triangle, diamond, and filled circles have a similar meaning as those defined in Figures 8.2 and 8.3. Also, the first visible crest of the concentric wavefront is indicated by the red dashed circle. The field of view of the all-sky imager is represented by the grey filled circular region with a dotted circle. The initial time of the ray tracing for all the waves is 04:15 UT. This time was chosen since these waves were observed between 03:00 and 04:30 UT. The color range of each ray path shows the MSGWs groups that are being ray traced. The wave propagation directions are the basis of the grouping. In Table 8.3, the summary of the range of propagation directions of the MSGWs and their corresponding horizontal wavelengths are presented.

Table 8.3 - Groups of Medium-Scale Gravity Waves (MSGWs) backward ray traced.

Group	ϕ **Range (°)**	λ_H **Range (km)**
1	110 - 120	168 - 200
2	80 - 85	210 - 310

Source: Nyassor et al. (Under Review).

The propagation direction of the ray traced MSGWs agrees with the locations of the convective systems relative to the location of the observation site as observed in Figure 8.7 and Table 8.3. From the ray tracing results, it is clear that the MSGWs in groups 1 and 2 were most likely generated by the convective systems. Since model winds were used in the ray tracing, this could only give us an idea about the state of the atmosphere. Furthermore, by adopting the approach of Vadas and Crowley (2010), the horizontal propagation distance of these MSGWs was estimated. In this estimation, the maximum propagating period (τ), of 60 minutes, from MSGWs groups 1 and 2 were chosen while the Brunt Väisälä period (τ_B) was taken to be 5 minutes. The tropopause altitude this night obtained from the radiosonde measurement was 17 km, implying the vertical distance (Δz) between the top of the cloud and the observation altitude at 87 km is 70 km. Using the τ, τ_B, (Δz) as input parameters, the horizontal propagation distance ΔX_H of the MSGWs is

$$\Delta X_H = \Delta z \frac{\tau}{\tau_B}. \tag{8.1}$$

The estimated average horizontal distance traveled by the 60 minute wave using Equation 8.1 was ∼840 km. In Figure 8.8 (not drawn to scale), the geometry of the horizontal distance the wave traveled relative to the convective system is shown.

Figure 8.8 - The geometry of horizontal distance traveled by medium-scale gravity wave (MSGW) Group 1 (MSGW$_{G_1}$) and medium-scale gravity wave Group 2 (MSGW$_{G_2}$) with respect to the convective systems (CS) 1 and 2.

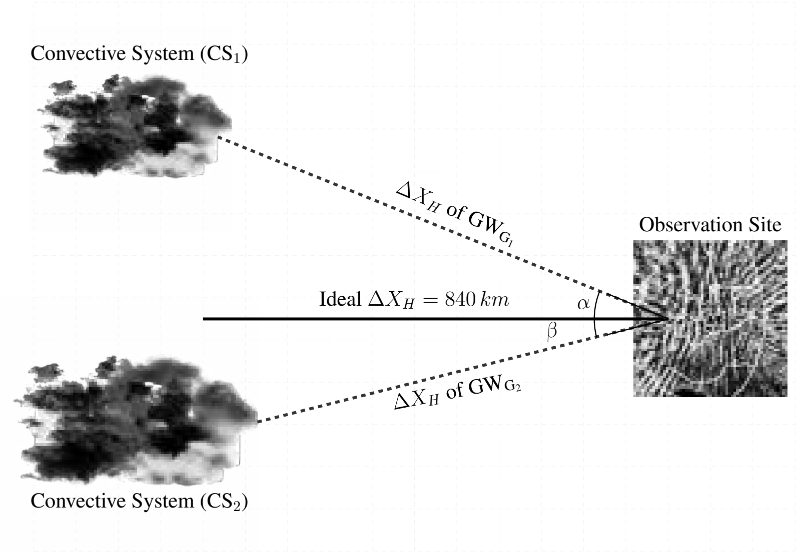

Source: Nyassor et al. (Under Review).

It was observed that the Groups 1 and 2 MSGWs traveled horizontally at an angle (α and β) relative to the “ideal ΔX_H” as shown in Figure 8.8. So taking the mean angles of α and β to be 30° and 5°, respectively, the ΔX_H traveled by the MSGWs relative to the convective systems were estimated. The Group 1 MSGWs propagated ∼1127.30 km horizontally at 30° towards the convective system 1 whereas, Group 1 MSGWs propagated ∼985.90 km at 5° relative to the convective system 2. These propagation distances agree with the distance between the positions of the convective systems and the observation sites. The estimation of the horizontal distance traveled by the MSGWs is to show that during this event, the deep convection generated other spectra of waves that propagated to São João do Cariri observation site. Since the ray tracing result of the September 9, 2016 CGW event did not stop close to any convective system which can be related as the source, it is possible that other waves generated by this system, can break to generate the CGW.

8.4.5 Source location of observed September 9, 2016 CGW event

As observed in the ray tracing result in panel (b(ii)) of Figures 8.2 and 8.3, neither the ray tracing tropopause nor stopping position was close to any nearby active convective system. Inferring from the ray tracing result, this wave was most likely not excited by a convective system, therefore the only possible source that can be considered is the body forces created through momentum and energy deposition of primary gravity waves generated by either convective systems 1 or 2. As shown earlier, the temperature inversion could not create a thermal duct that could enhance long-distance horizontal propagation. Also, no wind shear was observed in the model winds used, therefore, whether or not there was a Doppler duct, the model wind cannot be used to make such a conclusion. Without an actual background wind, ducting of the wave or the waves being generated by body force is a question to be answered in future work.

Since no conclusion could be drawn from the observations, the horizontal propagation analogy discussed in Section 8.4.4 was employed to investigate the propagation of the concentric wave. Here, it is assumed that the source of the CGW was either CS_1 or CS_2. Considering that the CGW was excited at 17 km and propagated to the OH emission altitude ($\sim$87 km), Δz $\sim$70 km. Taking τ_B $\sim$5 minutes, τ $\sim$12 minutes, and using Equation 8.1, $\Delta X_H \sim$ 172.2 km. Using the same analogy of the angles the CGW propagated relative to the observation site from CS_1 and CS_2, the estimated ΔX_H were $\sim$200 and $\sim$173 km, respectively. The distance between the center of the CGW to a central excitation/source point of both systems at longitude -48° is $\sim$550 km. This implies the CGW cannot propagate even half the distance between longitude -48° and the CGW center before reaching the OH emission altitude.

This analogy shows that a wave with such characteristics cannot propagate to the field of view of the imager without a duct. Even though temperature inversion was observed, the background study presented in Figure 8.6 showed no characteristics of a duct. Also, the spatial distribution of precipitation before or during the September 9, 2016 CGW event confirmed that no convective systems were around the center of the CGW. This leads to the suggestion that the only possible source mechanisms for this CGW are body forces created through the dissipation/breaking of primary waves as reported by Kogure et al. (2020) and reference therein. Since: (a) ray tracing result showed that this wave is not excited by a nearby convective system, (b) background study showed no duct, and (c) the estimated horizontal propagation distance showed that the CGW cannot propagate directly to the field of view of the imager from the convective systems, further investigation is needed. This will include a detailed study on the propagation and dissipation of

GWs generated by the convective systems using simulation. With the current evidence available, this CGW is not directly excited by the convective system to the west of the observation site. It is important to note here that there were no observed GWs activities at the source location or along the ray paths of the primary GWs and for that reason, only simulation can be used. However, due to time constraints on the doctorate work, the simulation study will be done in the near future.

8.5 Conclusion

Three concentric gravity waves (CGW) events observed in São João do Cariri. Using ray tracing, the source locations of the CGW events were determined. Among the three events, the tropopause and stopping position of the model wind ray paths of the CGW events on March 11, 2008 and May 25, 2019 were close to nearby active convective systems. The CGW event of September 9, 2016, on the other hand, had no convective system at the tropopause or stopping position of the ray path.

The stability condition of the troposphere and the state of convection before and during the wave events were investigated. Using CAPE maps, high CAPE values were observed during the hours within which the March 11, 2008 and May 25, 2019 CGW events were excited. Also, precipitation data were used to further prove the existence of convective systems before and during the excitation time of these waves. On the other hand, CAPE map and precipitation showed no activity of convection near the tropopause and stopping positions of the September 9, 2016 CGW ray path, further strengthen the fact that convective system might not be the source.

The model winds used in the ray tracing for all the events were weak which explains the observation of the CGW event in the OH emission altitude. However, for the observed elliptical case, the model wind could not be used to explain the observation. Therefore, mesospheric wind from meteor radar measurement available during the night of the May 25, 2019 CGW event was used to explain the elliptical wavefront and also, the shifting of the center of the ellipse from the source position. The meteor radar wind during this night was consistent with the observed CGW.

In conclusion, the CGW events on March 11, 2008 and May 25, 2019 are most likely excited by the nearby active convective system located by the ray tracing. The ray tracing result, the background study, and the estimated horizontal propagation distance show that the September 9, 2016 CGW event was not directly excited by the convective system more than 1000 km west of the observation site. To further draw a solid conclusion on the source of the September 9, 2016 CGW event a simulation study will be conducted shortly.

9 GENERAL CONCLUSION

In this chapter, the general conclusions of the work will be summarized. Also, future works that could be carried out using the techniques developed, used, and presented in this thesis will be suggested.

A broad study on (a) the characteristics of concentric gravity waves (CGWs), (b) their propagation in the atmosphere, and (c) investigation of their possible sources were carried out. The general conclusions of this work are summarized below:

1. Thirty-eight (38) CGWs events from three (3) observation sites were observed. Thirty (30) events were classified, analyzed, and characterized, in which nine (9) CGWs were selected for further investigation.
2. Among the 9 CGWs:
    a. one (1) CGW had almost complete circular wavefronts;
    b. one (1) CGW had a semi-elliptical wavefront, and
    c. the remaining CGWs had arc-like wavefronts.
3. Ray tracing model was used to investigate the propagation of the nine (9) CGWs in the atmosphere and also determine the location of the possible source of these waves. The background wind and temperature used in the ray tracing were obtained from the HWM14, MERRA-2, and NRLMSIS-00 models. TIMED/SABER temperatures and meteor radar winds were used when available.
4. The backward ray tracing result showed that:
    a. seven (7) of the selected CGWs events were most likely excited by a nearby deep convective system whereas;
    b. for the other two CGWs, no convective systems were located nearby where the ray traced paths stopped.
5. It was observed that the positions of the centers of the CGWs excited by deep convective systems agree well with the tropopause and stopping positions determined by the ray tracing for CGWs with background wind less than 30 m/s for waves studied in this work.
6. The deep convective systems near the stopping positions of the ray tracing, which were considered to be the sources of the CGWs were used to:

    a. determine the overshooting tops and the extent of overshooting and;
    b. relate the source parameters, particularly the frequency of overshooting to the period of the observed wave using lightning activity.

7. The estimated periods in the lightning flash rate of the deep convection system observed over São Martinho da Serra were compared with the periods of the observed CGWs. The periods of the observed CGW that were excited by the deep convective systems located near the stopping positions of the ray tracing agree with the periods found in the lightning flash rate. The agreement of the periods of the observed CGW and the lightning rate further strengthened the result that these CGWs were excited by the deep convective systems located near the stopping positions of the backward ray tracing.

This established relationship between the periods of the observed CGWs and the lightning flash rate is the major and novel contribution from this work to literature (NYASSOR et al., 2021).

9.1 Future work

The methodologies and numerical tools developed during this doctoral thesis were used to solve some of the research questions this work aims to answer. However, some of these questions remained unanswered due to time constraints, and as a result, future work is needed to address these questions in order to contribute to scientific advances in this area.

The first possibility would be to modify the current ray tracing model to investigate the body force (VADAS et al., 2018; KOGURE et al., 2020) source mechanisms of the CGW events without deep convection as their source. Gravity waves with a direct link to tropospheric sources are known as primary gravity waves. As primary waves propagate vertically, at certain altitudes they break or dissipate due to instabilities, and as a result, they deposit their momentum and energy to the background atmosphere. This deposited momentum and energy, in turn, accelerate or decelerate the mean flow, thereby creating body forces. These body forces excite a new spectrum of gravity waves known as secondary waves. As reported by Vadas et al. (2018) and Kogure et al. (2020), secondary gravity waves can have concentric wavefront, therefore the modified ray tracing would study the propagation and dissipation of the CGW events without deep convective sources to determine the altitude at which these waves dissipate to create the body force that may have excited the secondary waves.

As stated earlier, the CGW events in Cachoeira Paulista have not been studied in this work not only because of time but also because of the absence of an active deep convective system during those events. It is, for this reason, the propagation and dissipation of these events will also have to be investigated whether or not they are primary or secondary gravity waves.

Also, since the previous study by Tsunoda (2010) showed that ESF can be seeded by LSWS with more emphasis on GWs with concentric phase fronts, it is intended to investigate this possibility in the future. Studies by Vadas et al. (2018) and Kogure et al. (2020) explained the mechanism of secondary CGWs excitation mechanism, so conducting similar studies in the Brazilian sector (as mentioned earlier) will help explore the aspect of the ESF and related phenomena as well.

REFERENCES

ADLER, R. F.; FENN, D. D. Thunderstorm intensity as determined from satellite data. **Journal of Applied Meteorology and Climatology**, v. 18, n. 4, p. 502–517, 1979. 116

ADLER, R. F.; MARKUS, M. J.; FENN, D. D. Detection of severe midwest thunderstorms using geosynchronous satellite data. **Monthly Weather Review**, v. 113, n. 5, p. 769–781, 1985. 42

ALEXANDER, M. J.; PFISTER, L. Gravity wave momentum flux in the lower stratosphere over convection. **Geophysical Research Letters**, v. 22, n. 15, p. 2029–2032, 1995. 132

ALEXANDER, M. J.; ROSENLOF, K. H. Nonstationary gravity wave forcing of the stratospheric zonal mean wind. **Journal of Geophysical Research: Atmospheres**, v. 101, n. D18, p. 23465–23474, 1996. 32

AUMANN, H. H.; CHAHINE, M. T.; GAUTIER, C.; GOLDBERG, M. D.; KALNAY, E.; MCMILLIN, L. M.; REVERCOMB, H.; ROSENKRANZ, P. W.; SMITH, W. L.; STAELIN, D. H. Airs/amsu/hsb on the aqua mission: design, science objectives, data products, and processing systems. **IEEE Transactions on Geoscience and Remote Sensing**, v. 41, n. 2, p. 253–264, 2003. 30

AZEEM, I.; YUE, J.; HOFFMANN, L.; MILLER, S. D.; STRAKA, W. C.; CROWLEY, G. Multisensor profiling of a concentric gravity wave event propagating from the troposphere to the ionosphere. **Geophysical Research Letters**, v. 42, n. 19, p. 7874–7880, 2015. 132, 153

BAGESTON, J.; WRASSE, C.; GOBBI, D.; TAKAHASHI, H.; SOUZA, P. Observation of mesospheric gravity waves at comandante ferraz antarctica station (62 s). **Annales Geophysicae**, v. 27, n. 6, p. 2593–2598, 2009. 33, 53

BAGESTON, J.; WRASSE, C. M.; BATISTA, P.; HIBBINS, R.; FRITTS, D. C.; GOBBI, D.; ANDRIOLI, V. Observation of a mesospheric front in a thermal-doppler duct over king george island, antarctica. **Atmospheric Chemistry and Physics**, v. 11, n. 23, p. 12137–12147, 2011. 183, 184

BAGESTON, J. V. **Caracterização de ondas de gravidade mesosféricas na Estação Antártica Comandante Ferraz**. Tese (Doutorado em Geofísica Espacial) — Instituto Nacional de Pesquisas Espaciais (INPE), São José dos Campos, 2010. 33, 72

BATISTA, P.; TAKAHASHI, H.; GOBBI, D.; MEDEIROS, A. First airglow all sky images at 23Â° s. **Advances in Space Research**, v. 26, n. 6, p. 925–928, 2000. Available from: <`https://www.sciencedirect.com/science/article/pii/S0273117700000314`>. 33

BEDKA, K.; BRUNNER, J.; DWORAK, R.; FELTZ, W.; OTKIN, J.; GREENWALD, T. Objective satellite-based detection of overshooting tops using infrared window channel brightness temperature gradients. **Journal of Applied Meteorology and Climatology**, v. 49, n. 2, p. 181–202, 2010. 4, 42, 43, 116, 130, 140, 141, 143, 145, 147, 153, 157

BEVINGTON, P.; ROBINSON, D. **Data Reduction and Error Analysis for the Physical Sciences.** [S.l.]: McGraw-Hill, 2003. 161

BLOOMFIELD, P. **Fourier analysis of time series: an introduction**. [S.l.]: John Wiley & Sons, 2004. 77

BLUESTEIN, H. B. **Synoptic-dynamic meteorology in midlatitudes. Volume II. Observations and theory of weather systems**. [S.l.]: New York, NY (United States); Oxford University Press, 1993. 141

BLUESTEIN, H. B.; LINDSEY, D. T.; BIKOS, D.; REIF, D. W.; WIENHOFF, Z. B. The relationship between overshooting tops in a tornadic supercell and its radar-observed evolution. **Monthly Weather Review**, v. 147, n. 11, p. 4151–4176, 2019. 137

BOVIK, A. C. **The essential guide to image processing**. [S.l.]: Academic Press, 2009. 90

BROWNING, K. A.; BLYTH, A. M.; CLARK, P. A.; CORSMEIER, U.; MORCRETTE, C. J.; AGNEW, J. L.; BALLARD, S. P.; BAMBER, D.; BARTHLOTT, C.; BENNETT, L. J. The convective storm initiation project. **Bulletin of the American Meteorological Society**, v. 88, n. 12, p. 1939–1956, 2007. 1

BRUNNER, J. C.; ACKERMAN, S. A.; BACHMEIER, A. S.; RABIN, R. M. A quantitative analysis of the enhanced-v feature in relation to severe weather. **Weather and Forecasting**, v. 22, n. 4, p. 853–872, 2007. 42

BURITI, R. **Estudo de parâmetros de ondas de gravidade por medidas simultâneas de radar MU e fotômetro em Shigaraki (35 N, 136 L), Japão. São José dos Campos**. Tese (Doutorado em Geofísica Espacial) - Instituto Nacional de Pesquisas Espaciais — Instituto Nacional de Pesquisas Espaciais, São José dos Campos, 1997. 27

BURITI, R.; TAKAHASHI, H.; GOBBI, D. First results from mesospheric airglow observations at 7.5 ° s. **Revista Brasileira de Geofísica**, v. 19, n. 2, p. 169–176, 2001. 33

CAREY, L. D.; SCHULTZ, E. V.; SCHULTZ, C. J.; DEIERLING, W.; PETERSEN, W. A.; BAIN, A. L.; PICKERING, K. E. An evaluation of relationships between radar-inferred kinematic and microphysical parameters and lightning flash rates in alabama storms. **Atmosphere**, v. 10, n. 12, p. 796, 2019. 147

CARVALHO, A.; PAULINO, I.; MEDEIROS, A. F.; LIMA, L. M.; BURITI, R. A.; PAULINO, A. R.; WRASSE, C. M.; TAKAHASHI, H. Case study of convective instability observed in airglow images over the northeast of Brazil. **Journal of Atmospheric and Solar-Terrestrial Physics**, v. 154, p. 33–42, 2017. 183

CHAMBERLAIN, J. W. **Physics of the Aurora and Airglow**. [S.l.]: Elsevier, 2016. 27

CHAPMAN, S. Some phenomena of the upper atmosphere. **Proceedings of the Physical Society. Section B**, v. 64, n. 10, p. 833, 1951. 27

CLEMESHA, B.; BATISTA, P.; SIMONICH, D. Simultaneous measurements of meteor winds and sporadic sodium layers in the 80–110 km region. **Advances in Space Research**, v. 27, n. 10, p. 1679–1684, 2001. 54

COLE, H.; OYJ, V.; DABBERDT, W.; SHELLHORN, R.; COLE, H.; PAUKKUNEN, A.; ANTIKAINEN, V. Radiosonde. **Elsevier**, 2003. 59

COONEY, J. W.; BOWMAN, K. P.; HOMEYER, C. R.; FENSKE, T. M. Ten year analysis of tropopause-overshooting convection using gridrad data. **Journal of Geophysical Research: Atmospheres**, v. 123, n. 1, p. 329–343, 2018. 145

CRAMER, G. **Introduction a l'analyse des lignes courbes algebriques par Gabriel Cramer.** [S.l.]: Chez les Freres Cramer & Cl. Philibert, 1750. 112

CRAWFORD, J.; ROTHWELL, P.; WELLS, N. Simulating experiments for spacelab: Airborne television observations of airglow clouds in the near infrared. **Nature**, v. 257, n. 5528, p. 650–651, 1975. 28

DARE-IDOWU, O.; PAULINO, I.; FIGUEIREDO, C. A.; MEDEIROS, A. F.; BURITI, R. A.; PAULINO, A. R.; WRASSE, C. M. Investigation of sources of gravity waves observed in the Brazilian equatorial region on 8 april 2005. **Annales Geophysicae**, v. 38, n. 2, p. 507–516, 2020. 174, 179

DEIERLING, W.; PETERSEN, W. A. Total lightning activity as an indicator of updraft characteristics. **Journal of Geophysical Research: Atmospheres**, v. 113, n. D16, 2008. 4, 43, 130, 147

DEWAN, E.; PICARD, R.; O'NEIL, R.; GARDINER, H.; GIBSON, J.; MILL, J.; RICHARDS, E.; KENDRA, M.; GALLERY, W. Msx satellite observations of thunderstorm-generated gravity waves in mid-wave infrared images of the upper stratosphere. **Geophysical Research Letters**, v. 25, n. 7, p. 939–942, 1998. 26

DROB, D. P. et al. An empirical model of the earth's horizontal wind fields: Hwm07. **Journal of Geophysical Research: Space Physics**, v. 113, n. A12, 2008. 71

____. An update to the horizontal wind model (hwm): The quiet time thermosphere. **Earth and Space Science**, v. 2, n. 7, p. 301–319, 2015. 46, 71, 81

EARTHNETWORKS. **Earth Networks Lightning Sensor Technical and Installation Manual @ONLINE**. 2021. 60

EMERSIC, C.; HEINSELMAN, P.; MACGORMAN, D.; BRUNING, E. Lightning activity in a hail-producing storm observed with phased-array radar. **Monthly Weather Review**, v. 139, n. 6, p. 1809–1825, 2011. 143

ESSIEN, P.; PAULINO, I.; WRASSE, C. M.; CAMPOS, J. A. V.; PAULINO, A. R.; MEDEIROS, A. F.; BURITI, R. A.; TAKAHASHI, H.; AGYEI-YEBOAH, E.; LINS, A. N. Seasonal characteristics of small-and medium-scale gravity waves in the mesosphere and lower thermosphere over the Brazilian equatorial region. **Annales Geophysicae**, v. 36, n. 3, p. 899–914, 2018. 179

FECHINE, J.; WRASSE, C. M.; TAKAHASHI, H.; MEDEIROS, A. F.; BATISTA, P.; CLEMESHA, B.; LIMA, L. M.; FRITTS, D.; LAUGHMAN, B.; TAYLOR, M. J. et al. First observation of an undular mesospheric bore in a doppler duct. **Annales Geophysicae**, v. 27, n. 4, p. 1399–1406, 2009. 183

FRITTS, D. C.; ALEXANDER, M. J. Gravity wave dynamics and effects in the middle atmosphere. **Reviews of Geophysics**, v. 41, n. 1, 2003. 1, 18, 21, 23, 24, 35, 107

GARCIA, F.; TAYLOR, M. J.; KELLEY, M. Two-dimensional spectral analysis of mesospheric airglow image data. **Applied Optics**, v. 36, n. 29, p. 7374–7385, 1997. 72, 73

GELARO, R. et al. The modern-era retrospective analysis for research and applications, version 2 (merra-2). **Journal of Climate**, v. 30, n. 14, p. 5419–5454, 2017. 46, 81

GLICKMAN, T.; WALTER, Z. **Glossary of meteorology. Amer. Meteor. Soc., 855 pp**. [S.l.]: American Meteorological Society, 2000. 42

GLOBO NEWS. **RS registra granizo e rajadas de vento de mais de 100 km/h**. 2019. Available from: <`https://g1.globo.com/rs/rio-grande-do-sul/noticia/2019/10/02/rs-registra-granizo-e-rajadas-de-vento-de-mais-de-100-kmh.ghtml`>. 158

GOSSARD, E.; HOOKE, W. **Waves in the Atmosphere**. [S.l.]: Elsevier, New York, 1975. 1, 9, 15, 17, 19, 183

GRIFFIN, S. M.; BEDKA, K. M.; VELDEN, C. S. A method for calculating the height of overshooting convective cloud tops using satellite-based ir imager and cloudsat cloud profiling radar observations. **Journal of Applied Meteorology and Climatology**, v. 55, n. 2, p. 479–491, 2016. xxx, 113, 140, 158, 159, 160, 161

HAPGOOD, M.; TAYLOR, M. J. Analysis of airglow image data. **Annales de Geophysique**, v. 38, p. 805–813, 1982. 73

HARGREAVES, J. K. **The solar-terrestrial environment: an introduction to geospace-the science of the terrestrial upper atmosphere, ionosphere, and magnetosphere**. [S.l.: s.n.], 1992. 17

HEDIN, A. E. et al. Empirical wind model for the upper, middle and lower atmosphere. **Journal of Atmospheric and Terrestrial Physics**, v. 58, n. 13, p. 1421–1447, 1996. 70

HERSBACH, H. et al. **ERA5 hourly data on single levels from 1979 to present, Copernicus Climate Change Service (C3S) Climate Data Store (CDS)**. 2018. 173

HERSÉ, M. Atmospheric physics and earth observations: waves in the oh emissive layer. **Science**, v. 225, n. 4658, p. 172–174, 1984. 28

HEYMSFIELD, G. M.; JR, R. H. B. Satellite-observed characteristics of midwest severe thunderstorm anvils. **Monthly Weather Review**, v. 116, n. 11, p. 2200–2224, 1988. 116

HINES, C. O. Internal atmospheric gravity waves at ionospheric heights. **Canadian Journal of Physics**, v. 38, n. 11, p. 1441–1481, 1960. 14

HOCKING, W.; FULLER, B.; VANDEPEER, B. Real-time determination of meteor-related parameters utilizing modern digital technology. **Journal of Atmospheric and Solar-Terrestrial Physics**, v. 63, n. 2-3, p. 155–169, 2001. 54

HOLTON, J. **An introduction to dynamic meteorology**. [S.l.]: Academic Press, 1992. 40, 141, 173, 175

HOLTON, J. R.; ALEXANDER, M. J. Gravity waves in the mesosphere generated by tropospheric convention. **Tellus B**, v. 51, n. 1, p. 45–58, 1999. 132

HOLTON, J. R.; HAKIM, G. J. **An introduction to dynamic meteorology**. [S.l.: s.n.], 2012. 37, 38, 40

HORENSTEIN, H. **Black and white photography: a basic manual**. [S.l.]: Little Brown & Company, 2005. 49

HORINOUCHI, T.; NAKAMURA, T.; KOSAKA, J.-i. Convectively generated mesoscale gravity waves simulated throughout the middle atmosphere. **Geophysical Research Letters**, v. 29, n. 21, 2002. 2, 41

ISLER, J. R.; TAYLOR, M. J.; FRITTS, D. C. Observational evidence of wave ducting and evanescence in the mesosphere. **Journal of Geophysical Research: Atmospheres**, v. 102, n. D22, p. 26301–26313, 1997. 20

JURKOVIĆ, P. M.; MAHOVIĆ, N. S.; POČAKAL, D. Lightning, overshooting top and hail characteristics for strong convective storms in central europe. **Atmospheric Research**, v. 161, p. 153–168, 2015. 4, 130, 143, 145, 146, 147, 153

KEOSCIENTIFIC. **Keo Sentry Imagers for Airglow Research@ONLINE**. 2018. 52

KIM, J.; RANDEL, W. J.; BIRNER, T. Convectively driven tropopause-level cooling and its influences on stratospheric moisture. **Journal of Geophysical Research: Atmospheres**, v. 123, n. 1, p. 590–606, 2018. 157, 158

KIM, Y.-J.; ECKERMANN, S. D.; CHUN, H.-Y. An overview of the past, present and future of gravity-wave drag parametrization for numerical climate and weather prediction models. **Atmosphere-Ocean**, v. 41, n. 1, p. 65–98, 2003. 1, 35

KOGURE, M.; YUE, J.; NAKAMURA, T.; HOFFMANN, L.; VADAS, S. L.; TOMIKAWA, Y.; EJIRI, M. K.; JANCHES, D. First direct observational evidence for secondary gravity waves generated by mountain waves over the Andes. **Geophysical Research Letters**, v. 47, n. 17, p. e2020GL088845, 2020. 26, 28, 184, 187, 190, 191

KOTSOVINOS, N. E. Axisymmetric submerged intrusion in stratified fluid. **Journal of Hydraulic Engineering**, v. 126, n. 6, p. 446–456, 2000. 41

KUNDU, P. K.; COHEN, I. M. **Fluid mechanics 3.ed**. [S.l.]: Elsevier, 2004. 9, 10

KUNDU, P. K.; COHEN, I. M.; DOWLING, D. R. **Fluid mechanics 6.ed.** [S.l.]: Elsevier, 2016. 103

LANE, T. P. **Gravity waves| convectively generated gravity waves**. [S.l.]: Elsevier, 2015. 138

LANE, T. P.; REEDER, M. J.; CLARK, T. L. Numerical modeling of gravity wave generation by deep tropical convection. **Journal of the Atmospheric Sciences**, v. 58, n. 10, p. 1249–1274, 2001. 35, 36, 41, 139, 146, 147

LANE, T. P.; REEDER, M. J.; GUEST, F. M. Convectively generated gravity waves observed from radiosonde data taken during mctex. **Quarterly Journal of the Royal Meteorological Society**, v. 129, n. 590, p. 1731–1740, 2003. 23, 35, 36, 41, 42

LANE, T. P.; SHARMAN, R. D. Gravity wave breaking, secondary wave generation, and mixing above deep convection in a three-dimensional cloud model. **Geophysical Research Letters**, v. 33, n. 23, 2006. 2, 23, 35, 36

LEAN, H. W.; ROBERTS, N. M.; CLARK, P. A.; MORCRETTE, C. The surprising role of orography in the initiation of an isolated thunderstorm in southern england. **Monthly Weather Review**, v. 137, n. 9, p. 3026–3046, 2009. 1

LIGHTHILL, M. **Waves in fluids**. Cambridge University Press, 1978. ISBN 9780521216890. Available from: <`https://books.google.com.br/books?id=oVXTngEACAAJ`>. 95

LILIENTHAL, F.; YIĞIT, E.; SAMTLEBEN, N.; JACOBI, C. Variability of gravity wave effects on the zonal mean circulation and migrating terdiurnal tide as studied with the middle and upper atmosphere model (muam2019) using a whole atmosphere nonlinear gravity wave scheme. **Frontiers in Astronomy and Space Sciences**, v. 7, p. 88, 2020. 15

LIMA, L. **Observações de ondas planetárias na região da mesopausa equatorial e de baixas latitudes do hemisfério sul**. [S.l.]: São José dos Campos: INPE, 2004. 56

LIU, A. Z.; SWENSON, G. R. A modeling study of o2 and oh airglow perturbations induced by atmospheric gravity waves. **Journal of Geophysical Research: Atmospheres**, v. 108, n. D4, 2003. Available from: <`https://doi.org/10.1029/2002JD002474`>. 107

LIU, C.; HECKMAN, S. Total lightning data and real-time severe storm prediction. In: WMO TECHNICAL CONFERENCE ON METEOROLOGICAL AND ENVIRONMENTAL INSTRUMENTS AND METHODS OF OBSERVATION, 2012. **Proceedings...** [S.l.]: ICI/IFSA, 2012. 60

LIU, N.; LIU, C.; HAYDEN, L. Climatology and detection of overshooting convection from 4 years of gpm precipitation radar and passive microwave observations. **Journal of Geophysical Research: Atmospheres**, v. 125, n. 7, p. e2019JD032003, 2020. Available from: <`https://doi.org/10.1029/2019JD032003`>. 114

MAEKAWA, R. **Observations of gravity waves in the mesopause region by multicolor airglow imaging**. Thesis (Master) — University of Kyoto, Kyoto, 2000. 72, 73, 79

MARKS, C. J.; ECKERMANN, S. D. A three-dimensional nonhydrostatic ray-tracing model for gravity waves: formulation and preliminary results for the middle atmosphere. **Journal of Atmospheric Sciences**, v. 52, n. 11, p. 1959–1984, 1995. 16

MEDEIROS, A.; FECHINE, J.; BURITI, R.; TAKAHASHI, H.; WRASSE, C.; GOBBI, D. Response of oh, o_2 and oi5577 airglow emissions to the mesospheric bore in the equatorial region of Brazil. **Advances in Space Research**, v. 35, n. 11, p. 1971–1975, 2005. 45

MEDEIROS, A.; TAKAHASHI, H.; BATISTA, P.; GOBBI, D.; TAYLOR, M. J. Observations of atmospheric gravity waves using airglow all-sky ccd imager at Cachoeira Paulista, Brazil (23 s, 45 w). **Geofísica Internacional**, v. 43, n. 1, p. 29–39, 2004. 33

MEDEIROS, A.; TAYLOR, M. J.; TAKAHASHI, H.; BATISTA, P.; GOBBI, D. An investigation of gravity wave activity in the low-latitude upper mesosphere: propagation direction and wind filtering. **Journal of Geophysical Research: Atmospheres**, v. 108, n. D14, 2003. 21, 33, 34

MEDEIROS, A. F. **Observações de ondas de gravidade através do imageamento da aeroluminescência**. Tese (Doutorado em Geofísica Espacial) — Instituto Nacional de Pesquisas Espaciais, São José dos Campos, 2001. Available from: <`http://mtc-m16.sid.inpe.br:80/rep/sid.inpe.br/jeferson/2005/02.15.14.39`>. 4, 72, 73

MEDEIROS, A. F. **Observações de ondas de gravidade através do imageamento da aeroluminescência**. Tese (Doutorado em Geofísica Espacial) — Instituto Nacional de Pesquisas Espaciais, São José dos Campos, 2001. Available from: <`http://mtc-m16.sid.inpe.br:80/rep/sid.inpe.br/jeferson/2005/02.15.14.39`>. 27, 33

MEDVEDEV, A. S.; YIĞIT, E.; HARTOGH, P. Ion friction and quantification of the geomagnetic influence on gravity wave propagation and dissipation in the thermosphere-ionosphere. **Journal of Geophysical Research: Space Physics**, v. 122, n. 12, p. 12–464, 2017. 15

MEINEL, A. O_2 emission bands in the infrared spectrum of the night sky. **The Astrophysical Journal**, v. 112, p. 464, 1950. 27

MERTENS, C. J.; MLYNCZAK, M. G.; LÓPEZ-PUERTAS, M.; WINTERSTEINER, P. P.; PICARD, R.; WINICK, J. R.; GORDLEY, L. L.; III, J. M. R. Retrieval of mesospheric and lower thermospheric kinetic temperature from measurements of co2 15 μm earth limb emission under non-lte conditions. **Geophysical Research Letters**, v. 28, n. 7, p. 1391–1394, 2001. 64

MIDGLEY, J. E.; LIEMOHN, H. Gravity waves in a realistic atmosphere. **Journal of Geophysical Research**, v. 71, n. 15, p. 3729–3748, 1966. 15

MILLER, S. D.; MILLS, S. P.; ELVIDGE, C. D.; LINDSEY, D. T.; LEE, T. F.; HAWKINS, J. D. Suomi satellite brings to light a unique frontier of nighttime environmental sensing capabilities. **Proceedings of the National Academy of Sciences**, v. 109, n. 39, p. 15706–15711, 2012. 2

MIYOSHI, Y.; YIĞIT, E. Impact of gravity wave drag on the thermospheric circulation: implementation of a nonlinear gravity wave parameterization in a whole-atmosphere model. **Annales Geophysicae**, v. 37, n. 5, p. 955–969, 2019. 15

MOREELS, G.; HERSE, M. Photographic evidence of waves around the 85 km level. **Planetary and Space Science**, v. 25, n. 3, p. 265–273, 1977. 28

NACCARATO, K. P.; PINTO, O.; SLOOP, C. D.; HECKMAN, S.; LIU, C. Evaluation of brasildat relative detection efficiency based on lis observations and a numeric model. In: INTERNATIONAL CONFERENCE ON LIGHTNING PROTECTION, 2014. **Proceedings...** [S.l.]: IEEE, 2014. 60, 61

NAPPO, C. J. **An introduction to atmospheric gravity waves**. [S.l.]: Academic Press, 2013. 1, 20, 24

NOAA. **Storm prediction center**. July 2019. Available from: <https://www.spc.noaa.gov/sfctest/sfcoa.html>. 38

____. **Explanation of SPC Severe Weather Parameters - NOAA**. 2021. Available from: <https://www.spc.noaa.gov/exper/mesoanalysis/help/begin.html>. 175

____. **GOES-R series instruments overview**. Feb. 2021. Available from: <https://www.nasa.gov/content/goes-r/index.html>. 65

NYASSOR, P. K.; BURITI, R. A.; PAULINO, I.; MEDEIROS, A. F.; TAKAHASHI, H.; WRASSE, C. M.; GOBBI, D. Determination of gravity wave parameters in the airglow combining photometer and imager data. **Annales Geophysicae**, v. 36, n. 3, p. 705–715, 2018. 45, 52, 53

NYASSOR, P. K.; WRASSE, C. M.; GOBBI, D.; PAULINO, I.; VADAS, S. L.; NACCARATO, K. P.; TAKAHASHI, H.; BAGESTON, J. V.; FIGUEIREDO, C. A. O. B.; BARROS, D. Case studies on concentric gravity waves source using lightning flash rate, brightness temperature and backward ray tracing at São Martinho da Serra (29.44°s, 53.82°w). **Journal of Geophysical Research: Atmospheres**, v. 126, n. 10, p. e2020JD034527, 2021. xxi, 26, 34, 128, 129, 130, 131, 132, 133, 135, 136, 137, 138, 140, 142, 144, 147, 148, 149, 153, 157, 163, 190

NYASSOR, P. K.; WRASSE, C. M.; PAULINO, I.; GOBBI, D.; TAKAHASHI, H.; BATISTA, P. P.; BURITI, R. A.; R., P. A.; NACCARATO, K. P.; BARROS, D.; FIGUEIREDO, C. A. O. B. Investigations on concentric gravity wave sources over the Brazilian equatorial region. Under Review. xxii, 34, 128, 169, 170, 171, 172, 174, 178, 181, 183, 184, 185, 186

NYASSOR, P. K.; WRASSE, C. M.; PAULINO, I.; SABBAS, E. F. M. T. S.; BAGESTON, J. V.; GOBBI, D.; NACCARATO, K. P.; AYORINDE, T. T.; TAKAHASHI, H.; FIGUEIREDO, C. A. O. B.; D., B. Concentric gravity waves generated by a moving mesoscale convective system in southern Brazil. Under Revision. 34, 128

PAULINO, I. **Estudo da propagação de ondas de gravidade na termosféra-ionosféra**. Tese (Doutorado em Geofísica Espacial) — Instituto Nacional de Pesquisas Espaciais, São José dos Campos, 2012. Available from: <http://mtc-m16.sid.inpe.br:80/rep/sid.inpe.br/jeferson/2005/02.15.14.39>. 18, 19, 20, 21, 28, 33, 34, 36, 45, 52, 63, 88, 97, 98, 104, 109, 110

PAULINO, I.; TAKAHASHI, H.; INPE; VADAS, S. L.; WRASSE, C. M.; BURITI, R.; MEDEIROS, A.; GOBBI, B. D. Reverse ray-tracing of medium-scale gravity waves observed in northeast of Brazil during the 2009 spread F experiment. In: COSPAR SCIENTIFIC ASSEMBLY, 39., 2012. **Proceedings...** [S.l.]: COSPAR, 2012. p. 1470. 36

PAULINO, I.; TAKAHASHI, H.; VADAS, S.; WRASSE, C.; SOBRAL, J.; MEDEIROS, A.; BURITI, R.; GOBBI, D. Forward ray-tracing for medium-scale gravity waves observed during the copex campaign. **Journal of Atmospheric and Solar-Terrestrial Physics**, v. 90, p. 117–123, 2012. 33, 98

PEDOE, D. **Circles: a mathematical view**. [S.l.]: Cambridge University Press, 1995. 110

PERWITASARI, S.; SAKANOI, T.; NAKAMURA, T.; EJIRI, M.; TSUTSUMI, M.; TOMIKAWA, Y.; OTSUKA, Y.; YAMAZAKI, A.; SAITO, A. Three years of concentric gravity wave variability in the mesopause as observed by imap/visi. **Geophysical Research Letters**, v. 43, n. 22, p. 11–528, 2016. 1, 3, 26

PETERSON, A.; KIEFFABER, L. Infrared photography of oh airglow structures. **Nature**, v. 242, n. 5396, p. 321–322, 1973. 28

PETERSON, A. W.; ADAMS, G. W. Oh airglow phenomena during the 5–6 july 1982 total lunar eclipse. **Applied Optics**, v. 22, n. 17, p. 2682–2685, 1983. 28

PIANI, C.; DURRAN, D.; ALEXANDER, M.; HOLTON, J. A numerical study of three-dimensional gravity waves triggered by deep tropical convection and their role in the dynamics of the qbo. **Journal of the Atmospheric Sciences**, v. 57, n. 22, p. 3689–3702, 2000. 41

PICONE, J.; HEDIN, A.; DROB, D. P.; AIKIN, A. Nrlmsise-00 empirical model of the atmosphere: statistical comparisons and scientific issues. **Journal of Geophysical Research: Space Physics**, v. 107, n. A12, p. SIA–15, 2002. 46, 67, 81

PIERCE, A.; CORONITI, S. A mechanism for the generation of acoustic-gravity waves during thunderstorm formation. **Nature**, v. 210, n. 5042, p. 1209–1210, 1966. 1

PITTEWAY, M.; HINES, C. The viscous damping of atmospheric gravity waves. **Canadian Journal of Physics**, v. 41, n. 12, p. 1935–1948, 1963. 13, 15

RADIOSONDE. **Radiosonde Online Image@ONLINE**. 2021. Available from: <`https://www.leggo.it/photos/HIGH/40/64/1504064_20160124_whatisaradiosonde-692x1024.jpg`>. 59

ROZANTE, J. R.; GUTIERREZ, E. R.; FERNANDES, A. d. A.; VILA, D. A. Performance of precipitation products obtained from combinations of satellite and surface observations. **International Journal of Remote Sensing**, v. 41, n. 19, p. 7585–7604, 2020. 173

ROZANTE, J. R.; MOREIRA, D. S.; GONCALVES, L. G. G. de; VILA, D. A. Combining trmm and surface observations of precipitation: technique and validation over south america. **Weather and Forecasting**, v. 25, n. 3, p. 885–894, 2010. 173

SALLY, J. D. **Roots to research: a vertical development of mathematical problems**. [S.l.]: American Mathematical Society., 2007. 112

SÃO SABBAS, F. et al. Observations of prolific transient luminous event production above a mesoscale convective system in Argentina during the sprite2006 campaign in Brazil. **Journal of Geophysical Research: Space Physics**, v. 115, n. A11, 2010. 160, 161

SÃO SABBAS, F.; RAMPINELLI, V.; SANTIAGO, J.; STAMUS, P.; VADAS, S.; FRITTS, D.; TAYLOR, M.; PAUTET, P.; NETO, G. D.; PINTO, O. Characteristics of sprite and gravity wave convective sources present in satellite ir images during the spreadfex 2005 in Brazil. **Annales Geophysicae**, v. 27, n. 3, p. 1279–1293, 2009. xxx, 113, 115, 159, 166

SCHMIT, T. J.; GURKA, J.; GUNSHOR, M. M.; MENZEL, W.; LI, J. The advanced baseline imager (abi) on geostationary operational environmental satellites (goes)-r. In: INTERNATIONAL CONFERENCE ON INTERACTIVE INFORMATION PROCESSING SYSTEMS (IIPS) FOR METEOROLOGY, OCEANOGRAPHY, AND HYDROLOGY, 21., 2005. **Proceedings...** [S.l.], 2005. 66

SCHULTZ, C. J.; PETERSEN, W. A.; CAREY, L. D. Preliminary development and evaluation of lightning jump algorithms for the real-time detection of severe weather. **Journal of Applied Meteorology and Climatology**, v. 48, n. 12, p. 2543–2563, 2009. 143, 145, 147

SENTMAN, D.; WESCOTT, E.; PICARD, R.; WINICK, J.; STENBAEK-NIELSEN, H.; DEWAN, E.; MOUDRY, D.; SABBAS, F. S.; HEAVNER, M.; MORRILL, J. Simultaneous observations of mesospheric gravity waves and sprites generated by a midwestern thunderstorm. **Journal of Atmospheric and Solar-Terrestrial Physics**, v. 65, n. 5, p. 537–550, 2003. 1, 4, 26, 157

SHERWOOD, S. C.; HORINOUCHI, T.; ZELEZNIK, H. A. Convective impact on temperatures observed near the tropical tropopause. **Journal of the Atmospheric Sciences**, v. 60, n. 15, p. 1847–1856, 2003. 157

SIMKHADA, D.; SNIVELY, J.; TAYLOR, M. J.; FRANKE, S. Analysis and modeling of ducted and evanescent gravity waves observed in the hawaiian airglow. **Annales Geophysicae**, v. 27, n. 8, p. 3213–3224, 2009. 183

SMITH, V. H.; MOBBS, S. D.; BURTON, R. R.; HOBBY, M.; AOSHIMA, F.; WULFMEYER, V.; GIROLAMO, P. D. The role of orography in the regeneration of convection: A case study from the convective and orographically-induced precipitation study. **Meteorologische Zeitschrift**, v. 24, n. 1, p. 83–97, 2015. 1

SNIVELY, J. B.; PASKO, V. P.; TAYLOR, M. J.; HOCKING, W. K. Doppler ducting of short-period gravity waves by midlatitude tidal wind structure. **Journal of Geophysical Research: Space Physics**, v. 112, n. A3, 2007. 183

SONG, I.-S.; CHUN, H.-Y.; LANE, T. P. Generation mechanisms of convectively forced internal gravity waves and their propagation to the stratosphere. **Journal of the Atmospheric Sciences**, v. 60, n. 16, p. 1960–1980, 2003. 132

SUZUKI, S.; SHIOKAWA, K.; OTSUKA, Y.; OGAWA, T.; KUBOTA, M.; TSUTSUMI, M.; NAKAMURA, T.; FRITTS, D. C. Gravity wave momentum flux in the upper mesosphere derived from oh airglow imaging measurements. **Earth, Planets and Space**, v. 59, n. 5, p. 421–428, 2007. 1

TAKAHASHI, H.; BATISTA, P.; BURITI, R.; GOBBI, D.; NAKAMURA, T.; TSUDA, T.; FUKAO, S. Simultaneous measurements of airglow oh emissionand meteor wind by a scanning photometer and the muradar. **Journal of Atmospheric and Solar-Terrestrial Physics**, v. 60, n. 17, p. 1649–1668, 1998. 33

TAKAHASHI, H.; ONOHARA, A.; SHIOKAWA, K.; VARGAS, F.; GOBBI, D. Atmospheric wave induced O2 and OH airglow intensity variations: effect of vertical wavelength and damping. **Annales Geophysicae**, v. 29, n. 4, p. 631, 2011. 106

TAKAHASHI, H.; SAHAI, Y.; BATISTA, P. Airglow O2 (1σ) atmospheric band at 8645 Å and the rotational temperature observed at 23°s. **Planetary and Space Science**, v. 34, n. 3, p. 301–306, 1986. 33

TAKAHASHI, H.; WRASSE, C. M.; FIGUEIREDO, C. A. O. B.; BARROS, D.; ABDU, M. A.; OTSUKA, Y.; SHIOKAWA, K. Equatorial plasma bubble seeding by mstids in the ionosphere. **Progress in Earth and Planetary Science**, SpringerOpen, v. 5, n. 1, p. 1–13, 2018. 2, 4

TAYLOR, M. J. A review of advances in imaging techniques for measuring short period gravity waves in the mesosphere and lower thermosphere. **Advances in Space Research**, v. 19, n. 4, p. 667–676, 1997. 28

TAYLOR, M. J.; HAPGOOD, M. Identification of a thunderstorm as a source of short period gravity waves in the upper atmospheric nightglow emissions. **Planetary and Space Science**, v. 36, n. 10, p. 975–985, 1988. 26

TAYLOR, M. J.; HAPGOOD, M.; ROTHWELL, P. Observations of gravity wave propagation in the oi (557.7 nm), na (589.2 nm) and the near infrared oh nightglow emissions. **Planetary and Space Science**, v. 35, n. 4, p. 413–427, 1987. 28

TAYLOR, M. J.; PAUTET, P.-D.; MEDEIROS, A.; BURITI, R.; FECHINE, J.; FRITTS, D.; VADAS, S.; TAKAHASHI, H.; SABBAS, F. S. Characteristics of mesospheric gravity waves near the magnetic equator, Brazil, during the spreadfex campaign. **Annales Geophysicae**, v. 27, n. 2, p. 461, 2009. 21

TAYLOR, M. J.; RYAN, E.; TUAN, T.; EDWARDS, R. Evidence of preferential directions for gravity wave propagation due to wind filtering in the middle atmosphere. **Journal of Geophysical Research: Space Physics**, v. 98, n. A4, p. 6047–6057, 1993. 134, 155

TIMED/SABER. **SABER Online Image@ONLINE**. 2021. Available from: <`https://www.upload.wikimedia.org/wikipedia/commons/c/c4/TIMED.jpg`>. 62

TORRENCE, C.; COMPO, G. P. A practical guide to wavelet analysis. **Bulletin of the American Meteorological Society**, v. 79, n. 1, p. 61–78, 1998. 146

TRISHCHENKO, A. P. Solar irradiance and effective brightness temperature for swir channels of avhrr/noaa and goes imagers. **Journal of Atmospheric and Oceanic Technology**, v. 23, n. 2, p. 198–210, 2006. Available from: <`https://journals.ametsoc.org/view/journals/atot/23/2/jtech1850_1.xml`>. 28

TSUDA, T. Characteristics of atmospheric gravity waves observed using the mu (middle and upper atmosphere) radar and gps (global positioning system) radio occultation. **Proceedings of the Japan Academy, Series B**, v. 90, n. 1, p. 12–27, 2014. 35

TSUNODA, R. T. On seeding equatorial spread f: Circular gravity waves. **Geophysical Research Letters**, v. 37, n. 10, 2010. 2, 4, 191

UNIVERSITY OF WYOMING. **Radiosonde sounding**. 2019. Available from: <`http://weather.uwyo.edu/upperair/sounding.html`>. Access in: August 2021. 58, 59

____. **Sounding station parameters and indices**. 2021. Access in: August 2021. 58

UTIDA, G. et al. Tropical south atlantic influence on northeastern brazil precipitation and itcz displacement during the past 2300 years. **Scientific Reports**, v. 9, n. 1, p. 1–8, 2019. 179

VADAS, S.; FRITTS, D. Reconstruction of the gravity wave field from convective plumes via ray tracing. **Annales Geophysicae**, v. 27, n. 1, p. 147, 2009. 22, 25, 41, 42, 108, 141, 175

VADAS, S.; YUE, J.; NAKAMURA, T. Mesospheric concentric gravity waves generated by multiple convective storms over the north american great plain. **Journal of Geophysical Research: Atmospheres**, v. 117, n. D7, 2012. 3, 4, 26, 35, 36, 129, 133, 135, 136, 141, 146, 163, 176

VADAS, S. L. Horizontal and vertical propagation and dissipation of gravity waves in the thermosphere from lower atmospheric and thermospheric sources. **Journal of Geophysical Research: Space Physics**, v. 112, n. A6, 2007. 9, 10, 34, 98, 102, 103, 104, 105, 106, 177, 182

VADAS, S. L.; AZEEM, I. Concentric secondary gravity waves in the thermosphere and ionosphere over the continental united states on 25-26 march 2015 from deep convection. **Journal of Geophysical Research: Space Physics**, p. e2020JA028275, 2020. 2, 26

VADAS, S. L.; BECKER, E. Numerical modeling of the generation of tertiary gravity waves in the mesosphere and thermosphere during strong mountain wave events over the southern andes. **Journal of Geophysical Research: Space Physics**, v. 124, n. 9, p. 7687–7718, 2019. 2

VADAS, S. L.; CROWLEY, G. Sources of the traveling ionospheric disturbances observed by the ionospheric tiddbit sounder near wallops island on 30 october 2007. **Journal of Geophysical Research: Space Physics**, v. 115, n. A7, 2010. 185

VADAS, S. L.; FRITTS, D. C. Thermospheric responses to gravity waves arising from mesoscale convective complexes. **Journal of Atmospheric and Solar-Terrestrial Physics**, v. 66, n. 6-9, p. 781–804, 2004. 2, 4, 23, 24, 25, 41

____. Thermospheric responses to gravity waves: Influences of increasing viscosity and thermal diffusivity. **Journal of Geophysical Research: Atmospheres**, v. 110, n. D15, 2005. 9, 15, 34, 95, 96, 106, 109, 177, 182

____. Influence of solar variability on gravity wave structure and dissipation in the thermosphere from tropospheric convection. **Journal of Geophysical Research: Space Physics**, v. 111, n. A10, 2006. 10, 106

VADAS, S. L.; FRITTS, D. C.; ALEXANDER, M. J. Mechanism for the generation of secondary waves in wave breaking regions. **Journal of the Atmospheric Sciences**, v. 60, n. 1, p. 194–214, 2003. 2, 169

VADAS, S. L.; LIU, H.-l. Generation of large-scale gravity waves and neutral winds in the thermosphere from the dissipation of convectively generated gravity waves. **Journal of Geophysical Research: Space Physics**, v. 114, n. A10, 2009. 153, 175

VADAS, S. L.; LIU, H.-l.; LIEBERMAN, R. Numerical modeling of the global changes to the thermosphere and ionosphere from the dissipation of gravity waves from deep convection. **Journal of Geophysical Research: Space Physics**, v. 119, n. 9, p. 7762–7793, 2014. 1

VADAS, S. L.; TAYLOR, M. J.; PAUTET, P.-D.; STAMUS, P.; FRITTS, D. C.; LIU, H.-L.; SABBOS, F. S.; BATISTA, V.; TAKAHASHI, H.; RAMPINELLI, V. Convection: the likely source of the medium-scale gravity waves observed in the oh airglow layer near brasilia, brazil, during the spreadfex campaign. **Annales Geophysicae**, v. 27, p. 231, 2009. 35, 36, 106, 107, 108, 109, 132, 175

VADAS, S. L.; YUE, J.; SHE, C.-Y.; STAMUS, P. A.; LIU, A. Z. A model study of the effects of winds on concentric rings of gravity waves from a convective plume near fort collins on 11 may 2004. **Journal of Geophysical Research: Atmospheres**, v. 114, n. D6, 2009. 1, 2, 3, 4, 24, 28, 29, 30, 42, 43, 129, 133, 136, 137, 139, 146, 147, 157, 163, 169, 176, 177, 178, 179, 180

VADAS, S. L.; ZHAO, J.; CHU, X.; BECKER, E. The excitation of secondary gravity waves from local body forces: Theory and observation. **Journal of Geophysical Research: Atmospheres**, v. 123, n. 17, p. 9296–9325, 2018. 2, 169, 190, 191

VARGAS, F.; GOBBI, D.; TAKAHASHI, H.; LIMA, L. Gravity wave amplitudes and momentum fluxes inferred from oh airglow intensities and meteor radar winds during spreadfex. **Annales Geophysicae**, v. 27, n. 6, p. 2361, 2009. 33

VARGAS, F.; SWENSON, G.; LIU, A.; GOBBI, D. O (1s), oh, and o2 (b) airglow layer perturbations due to agws and their implied effects on the atmosphere. **Journal of Geophysical Research: Atmospheres**, v. 112, n. D14, 2007. 72

VARGAS, F. A. **Estudo do espectro das ondas de gravidade observadas em Cachoeira Paulista (23ºS)**. Dissertação (Mestrado em Geofísica Espacial) — Instituto Nacional de Pesquisas Espaciais, São José dos Campos, 2003. Available from: <`http://mtc-m16.sid.inpe.br:80/rep/sid.inpe.br/jeferson/2003/02.15.14.39`>. 72

VARGAS, F. A. **Investigação do fluxo de momento das ondas de gravidade na alta atmosfera através da aeroluminescência**. Tese (Doutorado em Geofísica Espacial) — Instituto Nacional de Pesquisas Espaciais (INPE), São José dos Campos, 2007. 33, 107

VOLLAND, H. **Handbook of atmospheric electrodynamics, volume I**. [S.l.: s.n.], 2017. 39

WALTERSCHEID, R.; SCHUBERT, G.; BRINKMAN, D. Small-scale gravity waves in the upper mesosphere and lower thermosphere generated by deep tropical convection. **Journal of Geophysical Research: Atmospheres**, v. 106, n. D23, p. 31825–31832, 2001. 42

WEEKS, A. R. **Fundamentals of electronic image processing**. [S.l.]: SPIE Optical Engineering Press Bellingham, 1996. 72

WIENS, K. C.; RUTLEDGE, S. A.; TESSENDORF, S. A. The 29 june 2000 supercell observed during steps. part ii: lightning and charge structure. **Journal of the Atmospheric Sciences**, v. 62, n. 12, p. 4151–4177, 2005. 43

WILLIAMS, E.; BOLDI, B.; MATLIN, A.; WEBER, M.; HODANISH, S.; SHARP, D.; GOODMAN, S.; RAGHAVAN, R.; BUECHLER, D. The behavior of total lightning activity in severe florida thunderstorms. **Atmospheric Research**, v. 51, n. 3-4, p. 245–265, 1999. 146

WRASSE, C. **Estudo de geração e propagação de ondas de gravidade atmosféricas**. Tese (Doutorado em Geofísica Espacial) — Instituto Nacional de Pesquisas Espaciais (INPE), São José dos Campos, 2004. 33, 49, 50, 51, 52, 72, 76, 109

WRASSE, C. et al. Reverse ray tracing of the mesospheric gravity waves observed at 23 s (brazil) and 7 s (indonesia) in airglow imagers. **Journal of Atmospheric and Solar-Terrestrial Physics**, v. 68, n. 2, p. 163–181, 2006. 133

WRASSE, C. M.; NAKAMURA, T.; TSUDA, T.; TAKAHASHI, H.; GOBBI, D.; MEDEIROS, A. F.; TAYLOR, M. J. Atmospheric wind effects on the gravity wave propagation observed at 22.7°s-Brazil. **Advances in Space Research**, v. 32, n. 5, p. 819–824, 2003. 4

WRASSE, C. M. et al. Mesospheric gravity waves observed near equatorial and low–middle latitude stations: wave characteristics and reverse ray tracing results. **Annales Geophysicae**, v. 24, n. 12, p. 3229–3240, 2006. 33, 133

WRASSE, C. M.; RODRIGUES, I. Programa de calibração de images all-sky. 2008. 72

WRASSE, C. M.; TAKAHASHI, H.; GOBBI, D. Comparison of the oh (8-3) and (6-2) band rotational temperature of the mesospheric airglow emissions. **Revista Brasileira de Geofísica**, v. 22, n. 3, p. 223–231, 2004. 33, 35, 97

XIAN, T.; HOMEYER, C. R. Global tropopause altitudes in radiosondes and reanalyses. **Atmospheric Chemistry and Physics**, v. 19, n. 8, p. 5661–5678, 2019. Available from: <`https://acp.copernicus.org/articles/19/5661/2019/`>. 114

XU, J. et al. Concentric gravity waves over northern china observed by an airglow imager network and satellites. **Journal of Geophysical Research: Atmospheres**, v. 120, n. 21, 2015. 1, 3, 4, 26, 29, 30, 43, 132, 133, 136, 138, 153, 169, 175, 177, 178, 179, 180

XU, S.; YUE, J.; XUE, X.; VADAS, S. L.; MILLER, S. D.; AZEEM, I.; III, W. S.; HOFFMANN, L.; ZHANG, S. Dynamical coupling between hurricane matthew and the middle to upper atmosphere via gravity waves. **Journal of Geophysical Research: Space Physics**, v. 124, n. 5, p. 3589–3608, 2019. 1, 4

YEE, J.-H.; TALAAT, E. R.; CHRISTENSEN, A. B.; KILLEEN, T. L.; RUSSELL, J. M.; WOODS, T. N. Timed instruments. **Johns Hopkins APL Technical Digest**, v. 24, n. 2, p. 156–164, 2003. 62

YIĞIT, E.; AYLWARD, A. D.; MEDVEDEV, A. S. Parameterization of the effects of vertically propagating gravity waves for thermosphere general circulation models: sensitivity study. **Journal of Geophysical Research: Atmospheres**, v. 113, n. D19, 2008. 15

YIĞIT, E.; MEDVEDEV, A. S. Internal wave coupling processes in earth's atmosphere. **Advances in Space Research**, v. 55, n. 4, p. 983–1003, 2015. 1

____. Role of gravity waves in vertical coupling during sudden stratospheric warmings. **Geoscience Letters**, SpringerOpen, v. 3, n. 1, p. 1–13, 2016. 1

YIĞIT, E.; MEDVEDEV, A. S.; AYLWARD, A. D.; HARTOGH, P.; HARRIS, M. J. Modeling the effects of gravity wave momentum deposition on the general circulation above the turbopause. **Journal of Geophysical Research: Atmospheres**, v. 114, n. D7, 2009. 1

YIĞIT, E.; MEDVEDEV, A. S.; ERN, M. Effects of latitude-dependent gravity wave source variations on the middle and upper atmosphere. **Frontiers in Astronomy and Space Sciences**, v. 7, p. 117, 2021. Available from: <`https://www.frontiersin.org/article/10.3389/fspas.2020.614018`>. 15

YUE, J.; HOFFMANN, L.; ALEXANDER, M. J. Simultaneous observations of convective gravity waves from a ground-based airglow imager and the airs satellite experiment. **Journal of Geophysical Research: Atmospheres**, v. 118, n. 8, p. 3178–3191, 2013. 1, 32, 138

YUE, J.; MILLER, S. D.; HOFFMANN, L.; STRAKA, W. C. Stratospheric and mesospheric concentric gravity waves over tropical cyclone mahasen: Joint airs and viirs satellite observations. **Journal of Atmospheric and Solar-Terrestrial Physics**, v. 119, p. 83–90, 2014. 1, 2, 26, 28, 30, 31, 32, 43, 138, 153

YUE, J.; VADAS, S. L.; SHE, C.-Y.; NAKAMURA, T.; REISING, S. C.; LIU, H.-L.; STAMUS, P.; KRUEGER, D. A.; LYONS, W.; LI, T. Concentric gravity waves in the mesosphere generated by deep convective plumes in the lower atmosphere near fort collins, colorado. **Journal of Geophysical Research: Atmospheres**, v. 114, n. D6, 2009. 1, 2, 3, 4, 26, 43, 129, 132, 133, 136, 137, 138, 139, 153, 157, 169, 176, 180

ZECHMEISTER, M.; KÜRSTER, M. The generalised lomb-scargle periodogram-a new formalism for the floating-mean and keplerian periodograms. **Astronomy & Astrophysics**, v. 496, n. 2, p. 577–584, 2009. 146

ZIEGLER, C. L.; MACGORMAN, D. R. Observed lightning morphology relative to modeled space charge and electric field distributions in a tornadic storm. **Journal of Atmospheric Sciences**, v. 51, n. 6, p. 833–851, 1994. 43

APPENDIX A - BACKGROUND PROFILES AND RAY PATH OF ESTIMATED PARAMETERS

The purpose of this Appendix is to present the profiles of background atmospheric parameters and the estimated parameters along the ray paths of the ray tracing results shown in Figure 4.20 of Section 4.3.

A.1 Background atmosphere parameter

The vertical profiles of the measured, model, and derived background atmosphere parameters are presented in Figure A.1

Figure A.1 - The profiles of background atmosphere parameters along the ray path of the March 24, 2018 CGW event.

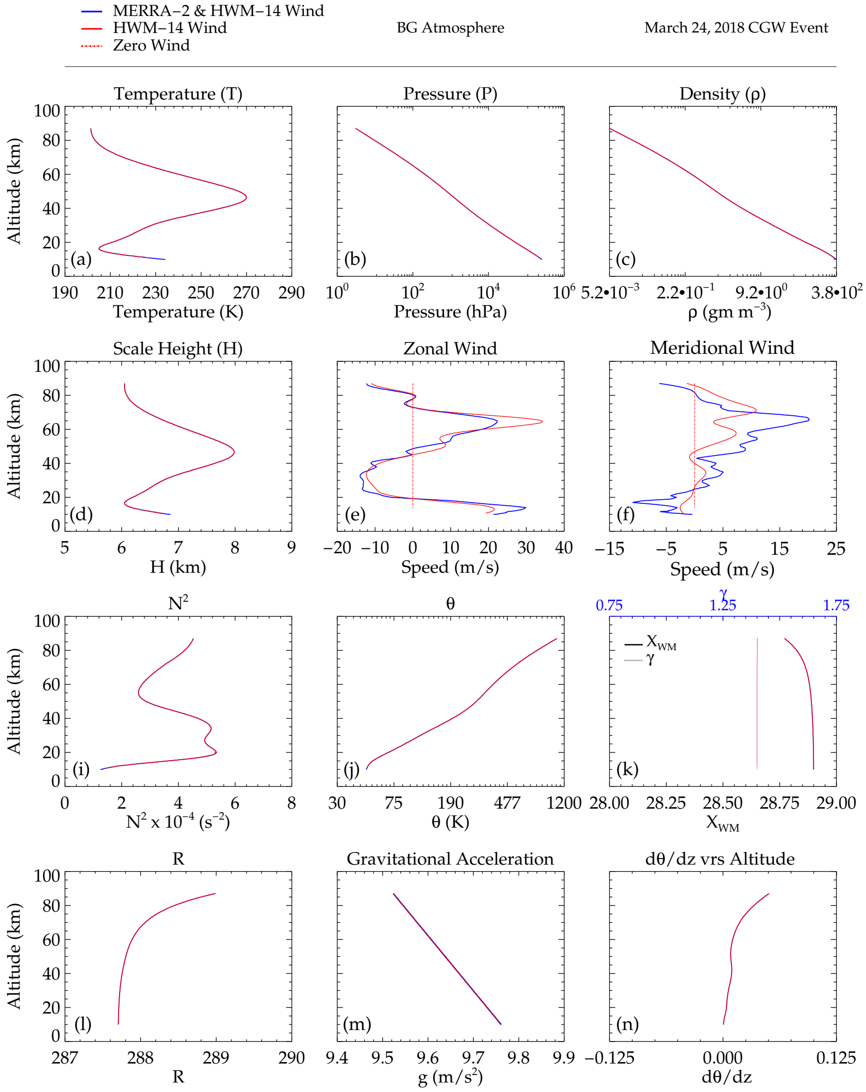

In panels (a), (b), (c), (d), (e), (f), (g), (h), (i), (j), (k), (l), (m), and (n), the profiles of temperature (T), pressure (P), density (ρ), scale height (H), zonal wind, meridional wind, Brunt Väisälä frequency, potential temperature (θ), ratio of specific heats (γ), molar mass of the atmospheric particles (X_{WM}), specific gas constant (R), acceleration due to gravity (g) and the derivative of potential temperature with respect to altitude, along the ray paths of March 24, 2018 CGW event are shown respectively.

A.2 Ray path of estimated parameter

The vertical profiles of the estimated parameters along the ray path of the CGW are shown in Figure A.2.

The parameters of the wave along the ray path are determined using the ray tracing model. Figure A.2 presents these characteristic parameters for the concentric gravity wave event of March 24, 2018. Variations are observed in the path of the wave along longitude and latitude below 70 km. In general, these observed variations are small for the entire profile.

The variations in the path of the wave along latitude and longitude can be associated mainly with the variations in the zonal (Figure A.2(c)) and meridional (Figure A.2(f)) wind. These variations as a function of altitude can be due to the Brunt Väisälä frequency square presented in Figure A.2(k) and also the temperature shown in Figure A.2(n) Between the altitudes of 20 and 70 km, variations were observed in the wind, especially in the concatenated MERRA-2 and HWM-14 model wind, which shows a maximum value at ∼65 km. Likewise, the meridional wind component also showed a maximum at ∼65 km for the MERRA-2 whereas, for HWM-14 the maximum occurred at ∼65.

In general, the magnitude of the wind was less than 30 m/s except for the HWM-14 zonal wind. The effect of the variations in the Brunt-Väisälä frequency influences the profiles of intrinsic frequency and the vertical group velocity of the wave and also the vertical wavelength, especially between 20 - 60 km altitude. These variations in the background conditions of the atmosphere can explain the existence of the variations observed in the trajectory of the waves.

Figure A.2 shows the logarithmic profile of the momentum flux with altitude. From Equation 2.33, a very important term in the estimation of momentum flux is the imaginary part of the intrinsic frequency. In Figure A.2, the vertical profile of the imaginary part of the intrinsic frequency is shown. Below 70 km, the imaginary component of the intrinsic frequency is constant, whereas, above 70 km, it increases steadily. Other profiles such as the GW amplitudes in atmospheric fields, for instance, horizontal wind, temperature, and

Figure A.2 - The profiles of estimated parameters along the ray path of the March 24, 2018 CGW event.

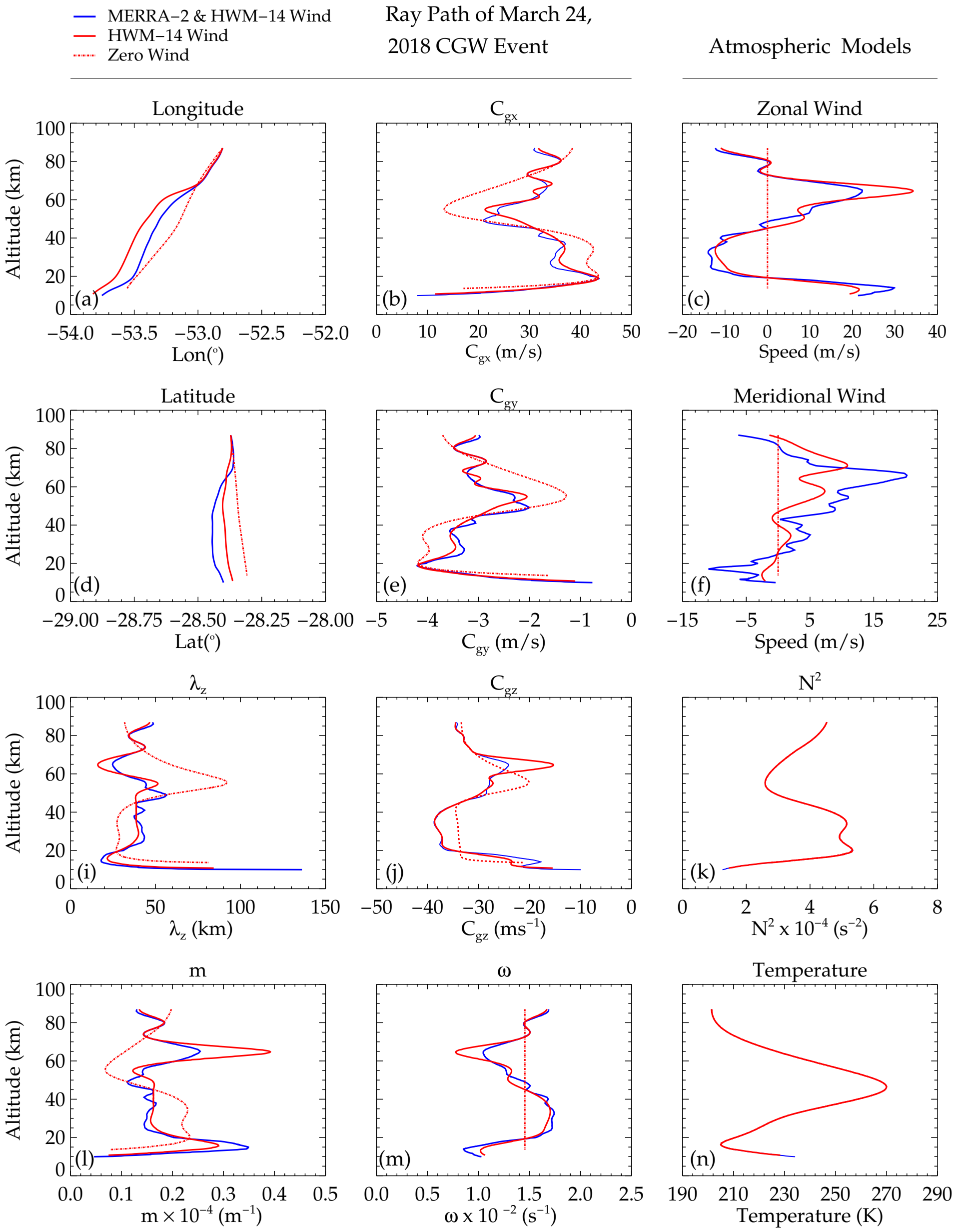

(continue on next page)

density described in Section 4.3.4 are also shown.

Figure A.2 - Conclusion

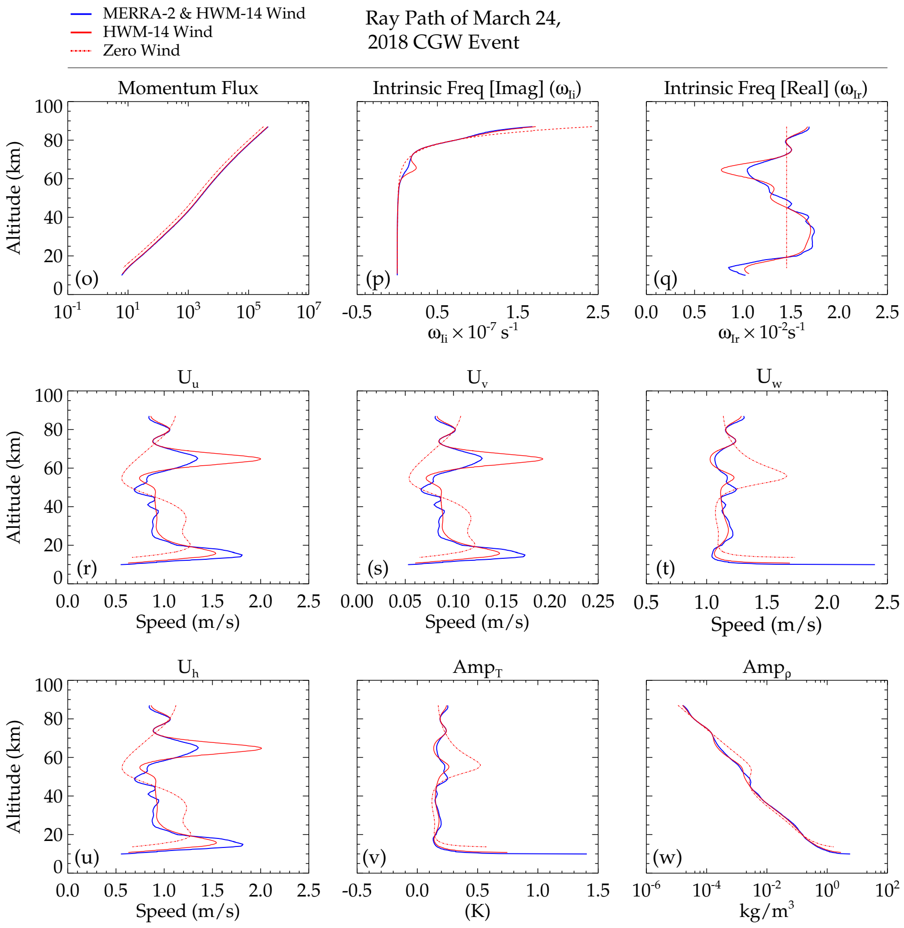

The vertical profile of the background wind perturbation: $\tilde{u}$, $\tilde{v}$, $\tilde{w}$, and u'_H (as defined in Section 4.3.4), represented by $\mathrm{U_u}$, $\mathrm{U_v}$, $\mathrm{U_w}$, and $\mathrm{U_h}$ in panels (r), (s), (t), and (u) of Figure A.2, respectively. Also, the GW amplitudes of temperature ($\tilde{T}$) and density ($\tilde{\rho}$) are presented in panels (v) and (w) as $\mathrm{Amp_T}$ and Amp_ρ, respectively in Figure A.2.

It can be observed that the zonal (panel (r)) and meridional (panel (s)) wind perturbation are similar to that of the horizontal wind (panel (u)) except that the magnitude of the meridional is small. The profile of the vertical wind perturbations (panel (t)) is, however, different from the horizontal component.